Thermal transport in a two-dimensional Kitaev spin liquid

DISSERTATION
zur Erlangung des akademischen Grades
Doctor rerum naturalium
(Dr. rer. nat.)

vorgelegt
der Fakultät Mathematik und Naturwissenschaften der
Technischen Universität Dresden

von

Angelo Pidatella

geboren am 23.08.1991 in Catania, Italien

eingereicht am 27.06.2019

verteidigt am 02.09.2019

Erstgutachter: Prof. Dr. Matthias Vojta
Zweitgutachter: Prof. Dr. Wolfram Brenig

To my family

Abstract

Quantum spin liquids represent a novel phase of magnetic matter where quantum fluctuations are large enough to suppress the formation of local order parameters, even down to zero temperature. Quantum spin liquid states can emerge from frustrated quantum magnets. These states show several peculiar properties, such as topological order, fractional excitations, and long-range entanglement.

The Kitaev spin model on the honeycomb lattice is one of the few models proposed which can exactly show the existence of a $\mathbb{Z}_2$ quantum spin liquid. The model describes spins featuring frustrated compass interactions, and it exhibits a quantum spin liquid ground state.

The model's ground state can be found exactly by representing spins in terms of Majorana fermions. It turns out that spin excitations fractionalize into two degrees of freedom: spinless matter fermions and flux excitations of the emergent $\mathbb{Z}_2$ gauge theory.

Recently, possible solid-state realizations of Kitaev quantum spin liquids have been proposed in a class of frustrated Mott insulators. Unfortunately, experiments can not unambiguously identify quantum spin liquids, due to their elusive nature. Nevertheless, indirect observations on a spin liquid state can be done by looking at its excitations. Along this line, thermal transport investigations provide for an option to study heat-carrying excitations, and thus the properties of the related spin liquid state.

In this doctoral thesis work, I performed a study of longitudinal thermal transport properties in the two-dimensional Kitaev spin model. This study aims to advance the understanding of transport in prototypical frustrated quantum magnets that might harbor Kitaev physics, and in particular quantum spin liquid states. For this purpose, I explored the model for varying exchange coupling regimes – to underline the impact of anisotropy on transport – and I studied transport over a wide range of temperatures.

Transport properties have been explored within the formalism of the linear response theory. Based on the latter, thermal transport coefficients can be evaluated by calculating dynamical energy-current auto-correlation functions.

First, I performed an analytical study of the uniform gauge sector of the model – where excitations of gauge degrees of freedom are neglected. Analytical findings for the energy-current correlations, and their related transport coefficients, imply a finite-temperature ballistic heat conductor in terms of free matter fermion excitations – independent of exchange couplings.

Second, thermal transport has been studied at finite temperatures, considering thermal gauge excitations off the uniform gauge sector. For this purpose, I made use of two complementary numerical methods able to treat finite-temperature systems.

On the one hand, I resorted on the exact diagonalization of the Kitaev Hamiltonian given in terms of fermions and a real-space dependent $\mathbb{Z}_2$ gauge potential, to study relatively small systems.

On the other hand, I used an approximate method based on a mean-field treatment of thermal gauge fluctuations. The method allowed to extend the study of thermal transport to systems with up to $\sim \mathcal{O}(10^4)$ spinful sites. It made possible the computation of correlation functions by reducing the exact trace over all gauge states to an average over dominant gauge states suited to a given temperature range.

The reliability of the method has been checked by comparing to numerically exact thermodynamics of systems. Based on the thermodynamic analysis, the method has been restricted to a temperature range where the mean-field treatment of gauge fluctuations is acceptable. Within such temperature range, the method succeeded in well reproducing exact results. The prime advantage of this method is its capability to reveal important features in the energy-current correlation spectra, not captured by the exact diagonalization approach because of finite-size effects.

I found that the energy-current correlation spectra, in the presence of thermal gauge excitations, show clear signatures of spin fractionalization. In particular, the low-energy part of spectra displays features arising from a temperature-dependent matter-fermion density relaxation off an emergent thermal gauge disorder. This static gauge disorder also leads to the appearance of a pseudogap in the zero-frequency limit, which closes in the thermodynamic limit. The extracted dc heat conductivity is consequently influenced by this interplay between matter fermions and gauge degrees of freedom.

The anisotropy in the exchange couplings moves Kitaev systems through gapless and gapped phases of the matter fermion sector.

Effects of anisotropy are visible in the dc conductivities which display a low-temperature dependence crossing over from power-law to exponentially activated behavior upon entering the gapped phase.

Therefore, I found that in the thermodynamic limit, two-dimensional Kitaev systems feature dissipative transport, regardless of exchange couplings.

This finding is in contrast to the ballistic transport found discarding gauge excitations in the uniform gauge sector, which underlines the relevance of gauge degrees of freedom in thermal transport properties of Kitaev systems.

Keywords— Thermal conductivity, frustrated magnetism, antiferromagnetism, spin-orbit coupling, spin liquid, fractionalization, magnetotransport, topological phases of matter, Kitaev model

Contents

CHAPTER 1

Introduction

Magnetism is a well-developed field of physics with a long history of discoveries. Magnetic materials have provided a prolific field for the production of models that can be explored experimentally. The recent possibility to synthesize low-dimensional magnetic materials opened the way to many unconventional phenomena led by enhanced quantum effects. Along this path, instances in which theories predict novel phases of matter continuously intrigue the condensed matter community, which also tries to find appropriate experimental conditions to observe them. In this context, the so called *quantum spin liquid* (QSL) phase is a not-entirely explored territory with extraordinary properties. Theoretically predicted by P. W. Anderson in 1973 [1], it represents an elusive quantum state of matter not yet conclusively verified by experiments.

To understand the peculiarity of this exotic phase − which is related to the core of this work − it is useful to give a basic idea of the concept of phase and phase transition based on local symmetry. This concept relies on Landau symmetry-breaking theory [2]. Its fundamental principle is that different orders are related to different symmetries − according to which the microscopic degrees of freedom arrange. This order can be described by a *local* order parameter which is able to distinguish different phases from each other. A standard example of an order parameter is given by the average magnetization of a ferromagnetic material, $M = \langle S_i \rangle$. S_i is the local degree of freedom, or spin, located at the i^{th} site of a lattice, and can either points up or down. The system can exist in two different phases depending on the temperature. Below a critical temperature T_c, a ferromagnetic interaction between nearest neighbor spins selects the same direction, breaking the spin rotational symmetry, and giving rise to a permanent magnetization $M > 0$. Above T_c, thermal fluctuations of S_i lead to a zero magnetization, $M = 0$. Thus, the local order parameter $M(T)$ discriminates in the phase transition − occurring at $T = T_c$ − between the ferromagnetic ($M > 0$) and the paramagnetic phase ($M = 0$). The distinction of phases in terms of order parameters is only dictated by the symmetry group of the Hamiltonian considered for the problem, regardless of its microscopic details. Such a theory, based on a mean-field order parameter, was later improved taking also into account fluctuations of the order parameter, within the so called Ginzburg-Landau theory [3]. In the end, the Ginzburg-Landau theory was thought able to describe all phases of matter and transitions.

However, as it frequently happens, experiments push theory to the brink. In the 80's a discovery related to a system of electrons confined in two dimensions − what is known as a 2-dimensional electron gas (2DEG) − was reported. This 2DEG, subject to a strong magnetic field at very low temperatures was observed to form a new kind of order [4], with a state of matter turning into an incompressible quantum liquid [1]. These states are labeled by a quantity named filling fraction $\nu = nhc/eB$, related to the ratio of electron density n, and flux quanta of the applied magnetic field B. States having a fractional ν were observed, and called Fractional Quantum Hall (FQH) states. A theoretical study of the FQH states was reported by Laughlin [5]. These states show internal orders which do not have any connection with any kind of local symmetries − or the breaking of them − resulting in exotic phases beyond the Ginzburg-Landau scheme.

The idea of *topological order* [6] was provided to describe the new order in FQH states. Even though there is no rigorous definition of topological order in the literature, some important physical features of FQH states can give an idea of it. First, FQH states show a ground state degeneracy which only depends on the topology of the space [7], with a degeneracy of q^g, where $q = 1/\nu$ and g is the genus of the manifold the system is embedded into (e.g. $g = 1$ for a Torus). Second, excitations of these states show typical properties as the *fractionalization* of the charge [2]. Finally, these excitations from FQH states obey unconventional mutual exchange statistics, named *anyonic*, which interpolates continuously between bosonic and fermionic statistics. In fact, exchanging two quasiparticles − dubbed *anyons* − the related quantum state acquires a phase $e^{i\theta}$, with $\theta \in [0, \pi]$ [8, 9]. Interestingly, topological order describes also other states of matter, for instance QSL states. Hence, unconventional properties together with the absence of any local order parameter for topologically ordered states should give an idea about how challenging is the study and the detection of the QSL phase in experiments.

Moreover, topological states are interesting in the quest for decoherence-protected qubits − in the context of quantum computation. Qubits are the basic units of quantum information, and they consist of two-state quantum-mechanical systems. Computation processes require coherence among these states, which is, however, undermined by quantum decoherence introduced via their excitation spectrum [10]. Highly-degenerate states are preferred to preserve the coherence of states, and one may rely on topology to provide physically protected degeneracies. Topological degenerate states are gapped and robust against *local* perturbations [11] − in other words, they are locally indistinguishable and do not couple with each other. These features allow to use these states to generate coherent qubits. Basic elements for quantum computation are provided by operations on the excitations of these topological states, i.e., anyons, introducing to what is called *topological quantum computation* [12].

In the pursuit of phases of matter showing topological excitations, A. Kitaev has contributed extensively. He introduced one of the simplest examples of exactly solvable lattice model displaying topological order and Abelian excitations, namely the Toric Code model [13]. Furthermore, he developed a 2D quantum spin model on the honeycomb lattice [14] which has recently been subject of great interest. This latter model is analytically solvable and describes a QSL state. It allows to further understand the properties of the QSL phase, such as the emergence of fractional excitations, non-Abelian statistics, and topological edge modes. In this context, theoretical and experimental efforts have been spent looking for evidence of Kitaev physics in real materials.

---

[1] The term *liquid* indicates degrees of freedom arranged in a strongly correlated state with no static order. For an *incompressible* fluid follows that $\partial n/\partial \mu = 0$, with μ the chemical potential, i.e., no particles can be injected/taken out from the state.

[2] For FQH states, which elementary constituents are electrons of charge e, the excitations carry a charge that is a fraction of e.

A promising route in the quest for topologically ordered QSL states is provided by the study of *frustrated* magnetic materials [15]. The term “frustrated” indicates the impossibility to satisfy simultaneously all the competing exchange processes involved in the Hamiltonian of a system [16]. Frustration usually counteracts order based on symmetry breaking. Thus, it can be assumed as a mechanism-guide to select systems that might be good candidates for QSLs.

An important and difficult question is the experimental synthesis and characterization of QSLs. About this last point, several experimental techniques are employed to probe QSL physics indirectly. These techniques, such as inelastic neutron scattering [17, 18], Raman scattering [19], μSR [20], NMR [21, 22], and also thermal transport measurements [23, 24], look at the elementary magnetic excitations of a QSL state. In particular, thermal transport is phenomenologically related to the thermodynamics, the energy dispersion, and the relaxation time of excitations involved in heat transport. It represents a powerful tool able to discriminate scattering mechanisms in quantum magnets — see Hess [25] for a review.

The prime goal of this thesis is to perform a theoretical study of the dynamical thermal transport for a two-dimensional QSL system. Here, the model considered is the aforementioned Kitaev model on the honeycomb lattice. This study aims to advance the understanding of transport in prototypical frustrated quantum magnets that might harbor QSL states. To stay in the QSL phase predicted by plain Kitaev physics, this work neglects other possible competing interactions in the model. In this context, it is possible to study the contribution of arising fractional excitations to the heat conductivity.

1.1 Outline

The thesis is organized in the following way. In the present chapter, I proceed by first introducing the concept of frustrated magnetism and quantum spin liquid. I close the chapter with some examples of experimental techniques to explore QSLs. In chapter 2, I first introduce theoretical aspects of thermal transport. Second, I present some selected experimental results for thermal transport measurements in low-dimensional spin systems. In chapter 3, I provide a description of the Kitaev spin model on the honeycomb lattice. The ground state of the model can be exactly found. I present and discuss the solution obtained, which describes a quantum spin liquid ground state hosting two fractional excitations: spinless matter fermions coupled with emergent flux excitations of $\mathbb{Z}_2$ gauge field. The solution can be obtained via several possible representations of the spin model in terms of fermions. In particular, I describe both a Majorana representation of spins, and a representation based on a Jordan-Wigner transformation − which has been employed in this thesis. In chapter 4, I present both the analytical and numerical methods used to compute heat transport coefficients by evaluating the energy-current auto-correlation function. Specifically, I show an analytical approach employed to study system in the uniform gauge sector. Moreover, I present numerical methods to deal with systems in excited-gauge sectors. These methods consist of the exact diagonalization method, and of a phenomenological mean-field treatment of thermal gauge fluctuations. In chapter 5, I show the results obtained for thermal transport in the Kitaev honeycomb model. These results are based on a complementary use of the formal developments introduced in the preceding chapters. Findings for the energy-current auto-correlation function, as well as for the transport coefficients, are presented in a wide range of temperatures − which allows to study the role of thermal gauge disorder in the heat transport − and for several sets of exchange couplings − to study the impact of anisotropic interactions. Finally, I conclude the thesis by summarizing the work carried out and discussing the results obtained. Various technical details are provided in the respective appendices.

1.2 Frustrated magnets

To introduce the concept of frustration in magnetic materials it is useful to recall the behavior of *unfrustrated* magnetic systems. For most of the unfrustrated magnets, spin fluctuations lead to a paramagnetic phase above a critical temperature T_c. These fluctuations become smaller by going below T_c, where systems develop some kind of long-range magnetic order. Consider the spin-$\frac{1}{2}$ Heisenberg model on a simple cubic lattice,

$$\mathcal{H} = \sum_{\langle ij \rangle} J_{ij} \mathbf{S}_i \cdot \mathbf{S}_j. \tag{1.1}$$

In a classical description, $\mathbf{S}_i=\{S_i^x, S_i^y, S_i^z\}$ refers to the 3-components spin vector located at the i^{th} site. These local degrees of freedom interact via the nearest-neighbor exchange coupling J_{ij}. In the ordered phase of the model, the classical ground states are Néel states. These states are unique up to global spin rotations, that are a symmetry of the model. The phase transition from a high-temperature paramagnet to a low-temperature antiferromagnet is described within the Landau theory. The staggered magnetization $M(T)$ is the local order parameter, which quantifies the breaking of spin rotational symmetry in ground states.

Magnets hosting *frustration* do not behave according to this conventional scheme. Frustrated magnets counteract the usual tendency towards the symmetry-breaking order below a critical temperature. The term frustration refers to the impossibility to satisfy simultaneously competing interactions of the system. For instance, considering the model in (1.1) – e.g., put on a different lattice, or adding next nearest-neighbors interactions – frustration would mean that there exists no state in which each local energy cost J_{ij} can be minimized. As a consequence, a large number of low-energy configurations arise due to frustrated interactions, and they lead to large low-energy fluctuations. These fluctuations contribute to evade the classical long-range order. Thus, a frustrated system may either be characterized by a strongly reduced ordering temperature, or to lead to an exotic liquid phase [3], not ordered at all. Indeed, the classical ground state degeneracy of these systems is not due to symmetry arguments but is accidental. So the spectrum of fluctuations varies around each ground state. Consequently, ground states with the lowest excitation energies can be selected, because they have the largest entropy and the smallest zero-point energy. This mechanism — known as *order-by-disorder* — is common in frustrated systems and allows for ordered states driven by thermal (quantum) fluctuations.

Generally, one distinguishes two prototypical forms of magnetic frustration. First, *geometrical* frustration on non-bipartite lattices with only nearest-neighbor interactions. The 2D antiferromagnetic Ising model [4] on a triangular lattice is an example (see Fig. 1.1(a)). For this type of frustration, all exchange bonds cannot be simultaneously satisfied due to local geometrical constraints. Second, *interaction* frustration led by competing longer range or anisotropic exchange interactions also on bipartite lattices. The $J_1 - J_2$ Heisenberg model on a square lattice can be an example (see Fig. 1.1(b))

$$\mathcal{H} = J_1 \sum_{\langle ij \rangle} \mathbf{S}_i \cdot \mathbf{S}_j + J_2 \sum_{\langle\langle ij \rangle\rangle} \mathbf{S}_i \cdot \mathbf{S}_j. \tag{1.2}$$

---

[3] For a physical understanding of these exotic liquid phases, I refer the reader to Sec. 1.3.

[4] The Ising spin Hamiltonian is given by $\mathcal{H} = -J \sum_{\langle ij \rangle} \sigma_i \sigma_j$ with $\sigma_i = \pm 1$.

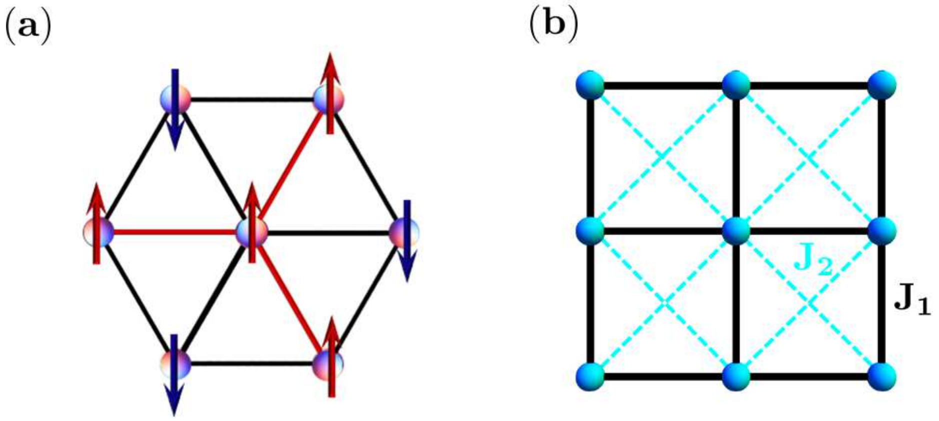

Figure 1.1: (a) Ising spins (arrows) interacting antiferromagnetically on a triangular lattice. The red bond indicates the geometrically frustrated one. (b) $J_1 - J_2$ Heisenberg model on a square lattice. Nearest-neighbor J_1 and next nearest-neighbor J_2 interactions are shown with black and blue bonds, respectively.

In (1.2) $\langle \cdots \rangle$ and $\langle\langle \cdots \rangle\rangle$ are nearest-neighbors and next nearest-neighbors bonds, respectively. The classical ground state of this model depends on the ratio $r = J_2/J_1$. For $r < \frac{1}{2}$ the ground state shows a conventional Néel order on the bipartite lattice. If $r > \frac{1}{2}$ the system yields a ground state with decoupled Néel sublattices [26]. The fully frustrated condition $r = \frac{1}{2}$ provides a large amount of classical degenerate ground states, including any state with a zero total spin per elementary square. Quantum corrections to the order parameter have been considered for this case, providing, for each of these states, the suppression of a possible order. This latter likely because of the presence of large low-energy fluctuations [26]. Recently discovered quasi-2D materials, such as Li_2VOSiO_4 and Li_2VOGeO_4 are possible realization of the model of (1.2) [27].

It is worth introducing – for the purpose of this work – a case of frustration led by the *entanglement* of spin and orbital degrees of freedom. The sensitivity of orbital interactions to the spatial orientation of orbitals generally gives rise to highly anisotropic Hamiltonians, and to frustrated states. Transition-metal (TM) compounds with partially filled d-levels are an example of systems with an intricate interplay of electronic, orbital, and spin degrees of freedom.

In particular, one can consider TM oxides formed by magnetic ions in a d^5 electronic configuration. A large set of d^5 materials including iridates – typically with a $\mathrm{Ir}^{4+}(5d^5)$ valence – exists. Ruthenium-based compounds with a $\mathrm{Ru}^{3+}(4d^5)$ valence can be also included in this d^5-materials set . Degeneracy of d levels can be lifted due to the crystal-field potential. Levels split into threefold-degenerate t_{2g} states and twofold-degenerate e_g states. Then, five electrons with magnetic moment $s = \frac{1}{2}$ lie in the lower-energy t_{2g} orbitals with orbital moment $\ell = 1$. In the limit of strong spin-orbit (SO) coupling the system results in a fully filled $j = \frac{3}{2}$ band and a half-filled $j = \frac{1}{2}$ band. This SO interaction gives rise to a reduction of the effective electronic bandwidth even in the presence of moderate electronic Coulomb repulsion. Thus it allows for the opening of a Mott insulating gap. This is why these $j = \frac{1}{2}$ Mott materials are usually referred to as *spin-orbit assisted Mott insulators* [28]. Figure 1.2 guides through the formation of SO entangled $j = \frac{1}{2}$ moments for typical Ir^{4+} or Ru^{3+} ions in a d^5 electronic configuration. To appreciate the importance of these systems in the context of frustration, it

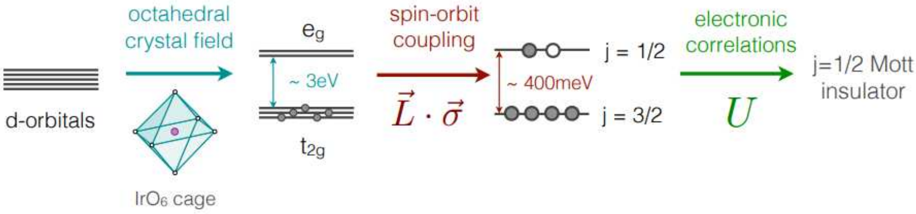

Figure 1.2: Scheme of lifting *d*-orbitals degeneracy driven by crystal-field splitting, spin-orbit coupling, and electronic correlation, producing $j = \frac{1}{2}$ for ions as Ir^{4+} or Ru^{3+}. Figure taken from Ref. [28].

is useful to provide a microscopic description of them.

A recent work [29] has studied magnetic interactions in these SO coupled Mott insulators. In these systems, the orbital, spin, and geometrical frustration are shown to be superimposed via the SO entanglement. Moreover, the symmetry of low-energy Hamiltonians considered is strongly dependent on the lattice geometry. This aspect offers a promising route to design exotic spin models like *quantum compass* models [30] — including the Kitaev's honeycomb model [14].
In particular, Jackeli and Khaliullin [29] formulate a superexchange theory to describe magnetic interactions of Ir^{4+}. The model considers a superposition of spin and orbital states led by strong SO coupling. Such a *mixing* gives rise to isospin states with a real-space density profile as in Fig. 1.3(a). This specific distribution of states plays a key role in determining the form of the exchange Hamiltonian. This latter will depend on bond geometry via such a density profile. Two possible TM-O-TM geometries are considered in their work. One of these is a 90°-bond formed by edge-sharing octahedra — see Fig. 1.3(b). With this particular arrangement, the Hamiltonian of the system has exchange interactions that depend on the spatial orientation of the active-orbital bonds

$$\mathcal{H}_{ij}^{\gamma} = -J S_i^{\gamma} S_j^{\gamma}, \tag{1.3}$$

where ij labels a γ-bond living in a plane perpendicular to the $\gamma(= x, y, z)$ axis.
Equation (1.3) is analogous to a quantum compass model. Their work also outlines how to engineer the Kitaev compass model in 90° TM-O-TM Mott insulators. The model (1.3) can be implemented on triangular lattices for magnetic ions in layered compounds ABO_2 — with A and B alkali and TM ions, respectively. The triangular lattice of magnetic ions in an ABO_2 structure can be depleted down to a honeycomb lattice, obtaining $\mathrm{A}_2\mathrm{BO}_3$ layered compounds. For this latter structure, there are three not equivalent bond-interactions which reproduce the frustrated bond-dependent couplings in the Kitaev model. In Figs. 1.3(c,d) examples of triangular and honeycomb structures, as well as the corresponding spin-orbit patterns are shown, respectively.

1.2.1 Signatures of frustration

Frustrated magnets tend to evade the magnetic order. Considering this property, a quantity which can characterize the amount of frustration in a system is provided by Ramirez [31]. The magnetic susceptibility $\chi(T)$ at high temperature obeys the Curie-Weiss law

$$\chi(T) \propto \frac{1}{T - \Theta_{CW}} \; . \tag{1.4}$$

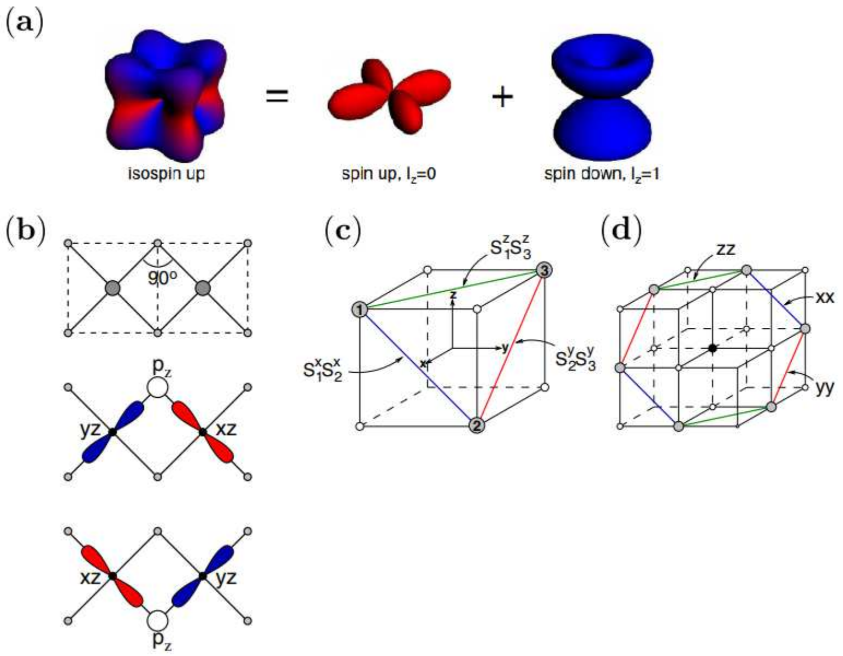

Figure 1.3: (a) Density profile of one of the two isospin states considered in Ref. [29]. It is a superposition of a spin up density in $|xy\rangle$-orbital with $\ell_z = 0$, and a spin down density in $(|yz\rangle + i|xz\rangle)$ state with $\ell_z = 1$. (b) TM-O-TM 90°-bond formed by edge-sharing octahedra, with active orbitals laying on these bonds. Large (small) dots indicate the transition metal (oxygen) ions. Examples of 90°-bonds TM-O-TM structures and corresponding interaction patterns. Grey (white) circles stand for magnetic ions sites (oxygen sites). (c) Triangular unit cell for ABO_2-type compounds. The model (1.3) here realizes a quantum compass model on a triangular lattice, with bond 1-2 being perpendicular to the x-axis. (d) Hexagonal unit cell for A_2BO_3-type compounds. Here magnetic ions are located on a honeycomb lattice. The model (1.3) is identical to the Kitaev model. Figures adapted from Ref. [29].

The Curie-Weiss temperature in (1.4) — $\Theta_{CW}<0$ if the exchange is antiferromagnetic, $\Theta_{CW}>0$ if ferromagnetic — refers to the energy scale of exchange interactions. Above $|\Theta_{CW}|$ the system is in a paramagnetic regime because of thermal fluctuations. In unfrustrated systems, at $T \lesssim \Theta_{CW}$ magnetic moments start to order, reported by a cusp in $\chi(T = T_c \sim \Theta_{CW})$. By contrast, frustrated systems do not show any feature in $\chi(T \sim \Theta_{CW})$. Here the paramagnetic phase is extended to lower temperatures, meaning that $T_c \ll \Theta_{CW}$. Thus, ordering may occur at a lower T_c than usual or may be prevented even at $T = 0$. Ramirez introduces the ratio

$$f = \frac{|\Theta_{CW}|}{T_c} \tag{1.5}$$

as a measure for the degree of frustration. Materials with a large value of f are usually referred to as frustrated — see Chalker [32] and Balents [15] for some examples of frustrated real materials and the corresponding value of f.

Furthermore, in some geometrically frustrated systems, there is a large number Γ of degenerate classical ground states. This leads to an extensive residual entropy $S_0 = k_B \ln(\Gamma)$. The 2D Ising model on a triangular lattice of Fig. 1.1(a) is an example. Its ground-state manifold counts at least $\Gamma = 2^{N/3}$, where N is the number of lattice (spins) sites. Γ results from all the possible ways to arrange spins pointing either up or down with one unsatisfied bond

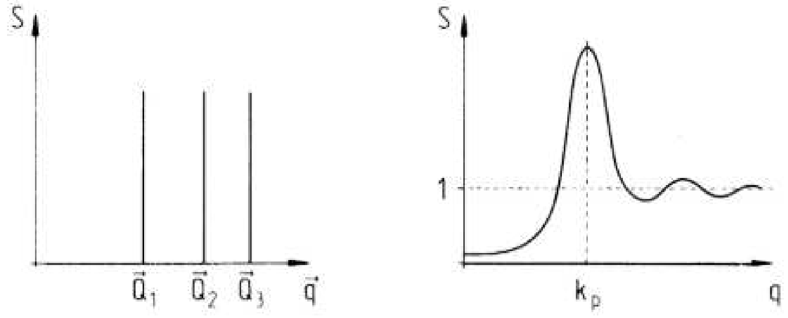

Figure 1.4: Left. Bragg peaks of an ideal crystal for specific ordering vectors $\mathbf{Q}_i$ in the reciprocal space. Right. Example of typical structure factor of a liquid in the reciprocal space. Features of correlated local degrees of freedom exist in the short-range distance of the real space. Figure taken from Ref. [34].

per triangle. Thus, in this system the residual entropy per site is $S_0/N \geq k_B \frac{1}{3} \ln 2 \sim 0.210 k_B$. Wannier studied the model in 1950 [33] and he exactly calculated an $S_0/N \sim 0.3230 k_B$.

1.3 Quantum spin liquids

Frustration represents a suitable context for the development of novel states of matter. In particular, the existence of *spin liquid* states has been predicted for frustrated spin systems. P. W. Anderson introduced the concept of spin liquids in 1973 [1]. He discussed the possible existence of *disordered* ground states beyond conventional long-range ordered Néel states, for 2D quantum frustrated antiferromagnets.
The term spin liquid is intended to draw an analogy between possible phases of a magnet and the canonical three-phases of *water*. To identify these phases one can study the spin-spin correlation function $\langle \mathbf{S}_j \cdot \mathbf{S}_k \rangle$, and in particular the static structure factor

$$S(\mathbf{q}) = \frac{1}{N} \sum_{j \neq k} \langle \mathbf{S}_j \cdot \mathbf{S}_k \rangle e^{i\mathbf{q}(\mathbf{r}_j - \mathbf{r}_k)} \,, \tag{1.6}$$

with $\mathbf{S}_j$ the spin operator on the j^{th} lattice site, $\langle \cdots \rangle$ indicating an ensemble average, and $\mathbf{q}$ the momentum vector in the reciprocal space. Neglecting finite temperature effects, it is reasonable to see a paramagnet as behaving like a gas, since both phases have *uncorrelated* degrees of freedom . This results in a $S(\mathbf{q}) \to 0$ for $|\mathbf{r}_j - \mathbf{r}_k| \to \infty$ that is featureless. In contrast, it is appropriate to think of a Néel state as a solid. Here, $S(\mathbf{q}) \propto \delta(\mathbf{q} - \mathbf{Q}_i)$ describes the periodic pattern of a long-range ordered system, with $S(\mathbf{q})$ consisting of Bragg peaks at all ordering vectors $\mathbf{Q}_i$. For a liquid, $S(\mathbf{q})$ is a smooth function with no sharp peaks, whose structure describes instead the short-range order of such a system — see Figs. 1.4.

Therefore, a spin liquid here stands for a state with short-range correlated spins preventing any form of long-range magnetic order. Despite this analogy with conventional fluids, spin liquids can exhibit much more exotic phenomena. Many models in literature describe either classical or quantum spin liquids [15, 35]. Because the content of this work deals with quantum models, I will refer to quantum spin liquids (QSLs) in the remainder of this thesis. The term *quantum spin liquid* is not unambiguously defined in the literature. For this purpose, in the following I will discuss three possible definitions of QSLs commonly used.

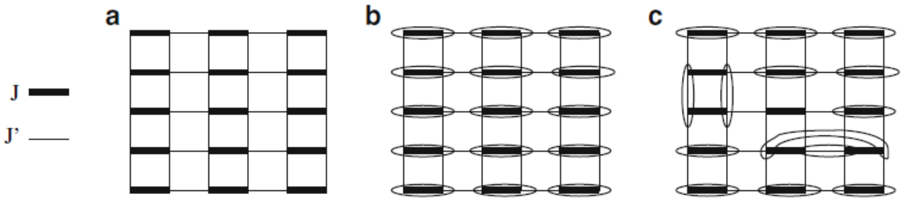

Figure 1.5: (a) Dimerized $J - J^{'}$ Heisenberg model on a square lattice. (b) Limit of $J^{'} = 0$ where the ground state is trivially a product of spin singlets (ellipses) on J bonds. (c) Small $J^{'} \neq 0$ produces other possible VB patterns which can contribute to the ground-state wavefunction. Figure taken from Ref. [38].

(a) A QSL can be defined as *a state without magnetic long-range order, meaning that* $\langle \mathbf{S}_j \cdot \mathbf{S}_k \rangle$ *decays to zero for* $|\mathbf{r}_j - \mathbf{r}_k| \to \infty$.

According to (a), any system with continuous spin-rotation symmetry and dimensionality $d \leq 2$ at finite temperature is a spin liquid (Mermin-Wagner theorem [36]). Spin-$\frac{1}{2}$ $J_1 - J_2 - J_3$ Heisenberg model on the hexagonal lattice studied by Fouet *et al.* [37] can be somewhat also included in (a). Many phases of this latter model have been found, depending on the degree of frustration. In particular, Néel order or ferromagnetism disappears around the points of maximum classical frustration leading to phases with spin-gap and short-range spin-spin correlations.

Further examples can be related to systems where SU(2) spin symmetry is not broken in the ground state due to quantum effects. One way to think of this is given by pairing spins in rotationally invariant valence bonds (VBs). The VB states are singlet states which connect two spin-$\frac{1}{2}$ at site i and j of a lattice, indicated as $|vb\rangle_{i,j}$ later on. A dimerized model, such as the $J - J^{'}$ Heisenberg model shown in Fig. 1.5, can give an idea about a possible VB configuration. Here a non-magnetic VB ground-state wavefunction is a direct product of $|vb\rangle_{i,j}$ covering all the lattice sites. The columnar dimer state of Fig. 1.5 provides an example of what is called valence bond crystal (VBC). More general than the columnar dimer state of Fig. 1.5, a VBC can be thought as a state where spins group themselves spontaneously into small clusters arranged in a spatially regular pattern. Each cluster contains spins forming singlets. Interestingly, there exists one type of VBC in which the energetically optimal VB pattern is unique − the state in Fig. 1.5 is an example of this type − and there also exists a second type of VBC having several degenerate VB patterns, related by symmetry. While both types of VBC do not break the SU(2) symmetry, and have no long-range spin correlations [38] − hence belonging to the spin liquid definition (a) − the second type of VBC has certain features of a conventional crystal. It shows a long-range order in the dimer-dimer correlation, and spontaneous breakdown of some discrete lattice symmetries.

(b) A QSL can be also defined as *a state without any spontaneously broken symmetry.*

This definition excludes − as in (a) − magnetically ordered states that break SU(2) spin symmetry. But (b) also rules out the VBC above discussed which breaks lattice symmetries.

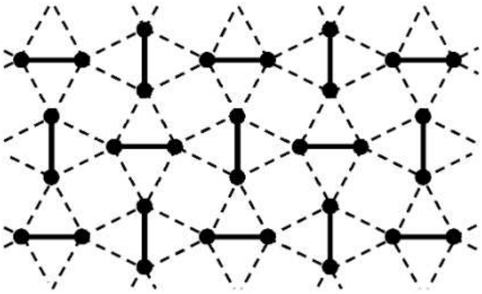

Figure 1.6: Lattice structure of the Cu^{2+} spins of $SrCu_2(BO_3)_2$. Bold-solid bonds represent the nearest-neighbor interactions, where dashed bonds indicate the next-nearest-neighbor coupling. Figure taken from Ref. [41].

Moreover the conjectured chiral spin liquids − that break the time-reversal symmetry − are also ruled out by (b). There are nevertheless few cases of magnetic insulators without any obvious broken symmetry. The 2D quantum spin system $SrCu_2(BO_3)_2$ is an example of a system with an exact dimer ground state − no spontaneously breaking of symmetries − and gapped excitations [39], see Fig. 1.6. The spin system may be described by the 2D Heisenberg model on a square lattice with some diagonal bonds [5]. This latter is referred to as the Shastry-Sutherland [40] model. This system obeys definition (b).

A third possible definition for a QSL may follow from the Anderson's idea of a *resonating valence bonds* (RVB) state [1, 42]. The RVB state is a linear superposition of a very large number of possible valence-bond coverings $|c\rangle$ of a lattice. If each VB configuration contributes equally to the RVB state, its ground-state wavefunction can be written as $|\Phi\rangle_{\mathrm{RVB}} = |c_1\rangle + |c_2\rangle + \cdots + |c_n\rangle = \sum_i |c_i\rangle$. In contrast with a VBC which shows a preferred ordering pattern, an RVB state resonates between an extensive fraction of the manifold of VB configurations. This results in a lacking long-range order, with an RVB state behaving as a spin liquid. Rokhsar and Kivelson [43] discovered an RVB liquid phase in connection to cuprates by studying the quantum dimer model (QDM) on a square lattice. However, they found that except for a critical point − where a gapped short-ranged RVB liquid exists − the model exhibits only VBC phases. The first example of a model describing a short-ranged RVB liquid state is provided by the QDM on a triangular lattice [44] − see Fig. 1.7.

Several properties of this RVB liquid that highlight general aspects of a QSL can be contrasted to the discussed VBCs:

- Such a resonating state $|\Phi\rangle_{\mathrm{RVB}}$ made of dimer coverings shows no long-range order in any spin, dimer, or higher-order correlation functions, unlike VBCs.
- A VBC has gapped, integer spin excitations obtained by breaking dimers. In contrast, this RVB liquid has spin-$\frac{1}{2}$ *fractional* excitations, called *spinons*. These magnetic excitations are created in pairs − since $S^z_{tot} = \pm 1$ − and can propagate independently carrying a fraction of the energy and momentum. Spinons cannot exist in a VBC, because to liberate two free spin-$\frac{1}{2}$ objects, the dimer ordered pattern is perturbed, leading to an unfavorable energy cost paid for this excited state. Such a cost refers to a *string* connecting misaligned dimers between the two spinons. This energy cost

---

[5] The Hamiltonian is $\mathcal{H} = J \sum_{\langle i,j \rangle} \mathbf{S}_i \cdot \mathbf{S}_j + J' \sum_{\langle\langle i,j \rangle\rangle} \mathbf{S}_i \cdot \mathbf{S}_j$, with J and J' nearest- and next-nearest-neighbor interactions

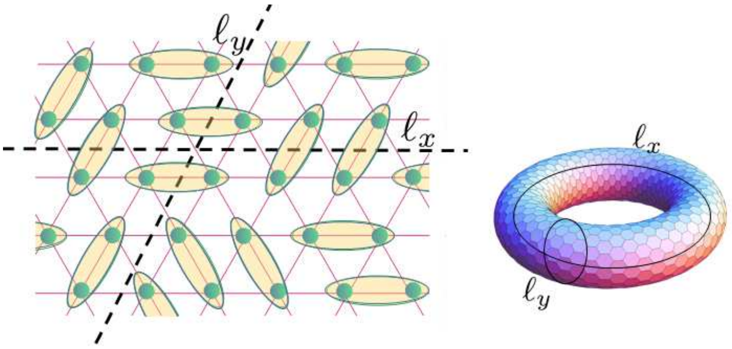

Figure 1.7: One of the possible VB configurations for the triangular QDM. A superposition of resonating VB pattern – similar to that one depicted – leads to an RVB state on a triangular lattice. Ellipses refer to singlet valence-bonds. The figure also depicts the partitioning of the QSL ground states into topological sectors by means of the two reference lines ℓ_x, ℓ_y wrapping around the torus (right bottom) of the triangular lattice with periodic boundary conditions. The parity resulting from the number of dimers crossed by ℓ_x, ℓ_y is invariant under local transformations of dimers arrangement.

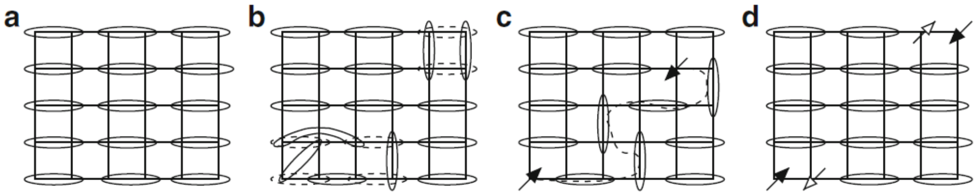

Figure 1.8: (a) Scheme of a columnar VBC on a square lattice. (b) Possible fluctuations in the VBC wavefunction shown as variations of the VB parent arrangement in (a). (c) Representation of the confinement experienced in the short-range distance by two test-spinons in a VBC. (d) At larger distances – with the energy cost compared to the spin gap – another dimer is broken leading to two extra spin-$\frac{1}{2}$ entities. These extra entities screen out (dress) the test-spinons and restore the regular favored pattern in a VBC. Figure taken from Ref. [38].

is proportional to the length of the string, which leads to a long-range potential that forbids an infinite separation of the two excitations, i.e., they are *confined* – see Fig. 1.8. By contrast in an RVB liquid – due to the absence of a preferred VB pattern – the string of rearranged dimers between two spinons only reshuffles dimer configurations which already contribute to the ground state [15]. Thus that energy cost is finite as the separation distance goes to infinity, and spinons are said to be *deconfined*.

- The ground state degeneracy in a VBC is related to a spontaneous symmetry breaking of lattice symmetries. Differently, the ground state degeneracy in an RVB liquid depends on the genus of the underlying lattice, hence on its *topology*. *Topological order* introduced for FQH states [7] is also a key concept here. Indeed, changing locally a dimer configuration requires a reordering of a certain number of other dimers. It is possible to show that there exist loop operators which are invariant under local transformations of dimers. Thus the possible ground states can be separated into different *sectors* not connected by any local flipping of dimers, but only by global rearrangements of them. For instance, one can imagine to place the triangular QDM on a torus, as shown in Fig. 1.7. Let us consider the two reference lines ℓ_x, ℓ_y that form winding loops on the torus. A sector is given by two winding numbers $(W_x, W_y) = (-1^{n_x}, -1^{n_y})$ with n_x, n_y counting the number of valence bonds crossed by ℓ_x, ℓ_y. Each sector leads to a ground-state wavefunction $|\Phi\rangle_{\mathrm{RVB}}$. More generally 2^{2g} topologically distinct sectors arise for surfaces with genus g – where $g = 0(1)$ for a sphere (torus). These sectors are locally equivalent. This means that no local order parameters can discriminate them [45]. Therefore, an RVB liquid has as many ground states as it has topological sectors.

- A VBC is given by a direct product of VB states, representing a *short-range entangled* (SRE) system. This short-range RVB liquid instead is made of a superposition of VB configurations, resulting in a *long-range entangled* (LRE) system. The LRE has been shown to be strictly connected to the presence of topologically ordered ground states and their related fractional excitations – see more details in the work by Kitaev and Preskill [46]. One way to explore entanglement is via the von Neumann entropy. In the context of a triangular RVB state, dividing it into two spatial regions, A and B, one can trace out the spins in the region B and obtain the reduced density matrix $\rho_A = \mathrm{Tr}_B\,|\Phi\rangle\langle\Phi|$, with $|\Phi\rangle$ the ground-state wavefunction. The von Neumann entropy of A, $S_A = -\,\mathrm{Tr}_A\,\rho_A \log \rho_A$, captures the entanglement between A and B degrees of freedom. S_A vanishes if the ground state is a direct product, i.e., $|\Phi\rangle = |\Phi_A\rangle \otimes |\Phi_B\rangle$. A fundamental feature of the entanglement entropy is that for gapped quantum matter it is expected to obey the so called *area law*, $S_A \sim \alpha L - \gamma$, see Fig. 1.9. The first term describes the local entanglement between A and B separated by the boundary of length L, with a non-universal behavior. The second term, γ is believed to provide a universal characterization of the entanglement of topologically ordered states, which does not depend on the local physics near the boundaries. Recently the γ contribution to S_A for such a short-range gapped RVB system [47] has been investigated and found consistent with that expected for a gapped QSL.

To summarize, an RVB state is one of the systems closest to the realization of a QSL. The properties above listed can be then used to characterize at least some types of QSLs. The element that connects these properties is the massive entanglement [35] of RVB ground states, which has an important role in producing topologically ordered ground states supporting non-local fractional excitations. In view of this, the third definition of a QSL follows as

(c) A QSL is *a state with long-range entanglement.*

Although all the definitions (a), (b), and (c) somewhat include QSLs, I will consider (c) as a useful working definition of a QSL in the remainder of this thesis.

1.3.1 Experimental techniques

It is currently challenging to probe non-local features or measure the degree of entanglement – which are hallmarks of QSLs. However conventional experimental techniques can be adapted to probe QSL physics indirectly. Definitive proofs of QSL are nevertheless difficult to obtain. Thus, it is necessary to combine different observations via complementary techniques to have a complete picture of potential QSL systems. In the following, I want to mention only some of the experimental techniques used to investigate potential QSL systems – for a review see Savary and Balents [35].

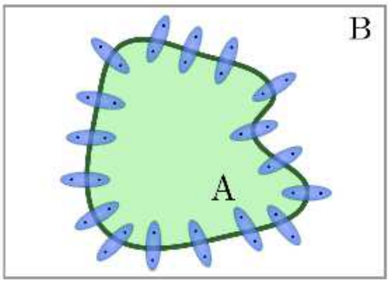

Figure 1.9: Schematic picture of the division of space into a region A and its complement B. The contribution to the area law given by the term αL arises from the sum of local contributions due to entangled singlets spanning the boundary. Figure adapted from Ref. [35].

- *Inelastic neutron scattering.* It offers access to the dynamic spin-spin correlation function $S(\omega, \mathbf{q}) \sim \langle \mathbf{S}_{-\mathbf{q},-\omega} \cdot \mathbf{S}_{\mathbf{q},\omega} \rangle$ of a system, with ω and $\mathbf{q}$ the energy and momentum transfers, respectively. The inelastic signal provided at $\omega \sim J$ – where J is the spin exchange scale – reveals excitations with energy ω and momentum $\mathbf{q}$. Due to their non-local nature, QSL excitations arise in pairs. This gives rise to a smooth signal where at each momentum $\mathbf{q}$, the signal intensity is spread out over a continuum of frequencies ω, with the constraint $\mathbf{q} = \mathbf{q_1} + \mathbf{q_2}$. This continuum spectrum exhibited by QSLs is in contrast to that one of ordinary magnets or SRE valence bond crystals. For the latter, peaked structures in the signal are expected, due to the elementary individual excitations produced by a spin flip of the ground state. However, even pairs of non-local excitations may form a bound state (local entity) that would contribute with a sharp peak in $S(\omega, \mathbf{q})$.

- *Specific heat.* It is one of the most important thermodynamic quantities to study quantum magnetism. Phase transitions of a system can be detected via specific heat $C(T)$ that shows a singularity around the transition temperature. It allows to study the spin entropy released, by means of standard thermodynamic relations. Moreover, it provides access to low energy excitations of quantum magnets. For instance, gapless states can lead to enhancement of power-law behavior in the low-temperature $C(T) \propto T^{\alpha}$ – directly related to the density of states of low-energy excitations. Various power laws are predicted for gapless QSL states. Unfortunately, specific heat does not discriminate different contributions arising from spin or lattice excitations. This because it is sensitive to any excitations.

- *Magnetic susceptibility.* The uniform dc magnetic susceptibility $\chi(T)$ typically shows a peak or cusp at a phase transition. From measurements of $\chi(T)$ one can determine the magnetic ordering temperature T_c, as well as the Curie-Weiss temperature Θ_{CW}. This allows to construct the frustration parameter f introduced in equation (1.5). As already mentioned, large values of f indicate the tendency to elude ordering, that might suggest a typical – but not definitive – signature for a QSL. As for the specific heat, $\chi(T)$ at low temperature can also be related to excitations of a system.

- *Heat conductivity.* Mobile excitations contribute to the heat conductivity in a system. Measurements of heat conductivity κ can determine if excitations are extended or localized. Excitations of a gapless QSL can contribute to κ, showing a change in the low-temperature power-law behavior – indicative of the type of low-energy excitations. These latter may significantly change the form of κ which would show anomalous contributions. However all the propagating excitations − phonons included − contribute to κ. This means that to observe the impact of QSL excitations on κ, one needs to disentangle the lattice contributions from the magnetic ones.

CHAPTER 2

Thermal transport

In this chapter, I will first give a brief introduction of transport theory within the framework of linear response theory. The transport coefficients – subjects of study in this work – are here derived and described. Particular attention will be paid on the thermal conductivity mediated via magnetic excitations of spin systems. In this context, I will conclude the chapter presenting a sample of experimental results for low-dimensional spin systems where magnetic heat transport largely contributes.

In a solid, the thermal conductivity is determined by mobile heat carriers. The simplest example of this is the thermal conductivity of a metal. Within the Drude model [48], the bulk thermal conductivity in a metal is due to the conduction electrons [1]. To define conductivity, one may consider a metal bar along which the temperature varies slowly. In the absence of source and sink at the end of the bar, which would maintain the temperature gradient ∇T, thermal energy flows in the direction opposite to the gradient. For small temperature gradients, one can define a *thermal current* density

$$\mathbf{j}^q = -\kappa \nabla T. \tag{2.1}$$

In (2.1) $\mathbf{j}^q$ is a vector parallel to the heat flow direction, whose magnitude returns the thermal energy per unit time crossing a unit area perpendicular to the flow. The proportionality variable κ is the so called *thermal conductivity.* A quantitative estimate of the thermal conductivity κ – based on the kinetic theory – can be provided by the equation [48]

$$\kappa = \frac{1}{d} c v \ell \,, \tag{2.2}$$

where d refers to the dimensionality of the system, c the specific heat, v the velocity, and ℓ the mean free path of the respective heat carriers. In metals, electrons have a specific heat which is proportional to $k_B T$. Considering the Fermi velocity v_F as the velocity of electrons, this yields $\kappa_{el} = \pi^2 n k_B^2 \ell T / 3 m v_F$, where n is the electron density and m the electron mass. From this estimate for κ_{el}, it is possible to retrieve the famous empirical Wiedemann-Franz law [2] [49, 50]. The same theory can be applied to *insulating* systems where heat is mostly carried by elementary excitations of the lattice – i.e., phonons. According to the Debye model, for

---

[1] In any solid system there will also be some amount of κ from structural vibrations of the material as well – the so called phonon thermal conductivity κ_{ph}.

[2] By substituting the relaxation time $\tau = \ell / v_F$ in favor of the related electrical conductivity $\sigma = ne^2\tau/m$, the Wiedemann-Franz law follows as $\frac{\kappa}{\sigma T} = \frac{\pi^2}{3}\left(\frac{k_B}{e}\right)^2 = 2.44 \times 10^{-8} \mathrm{W\Omega/K^2}$.

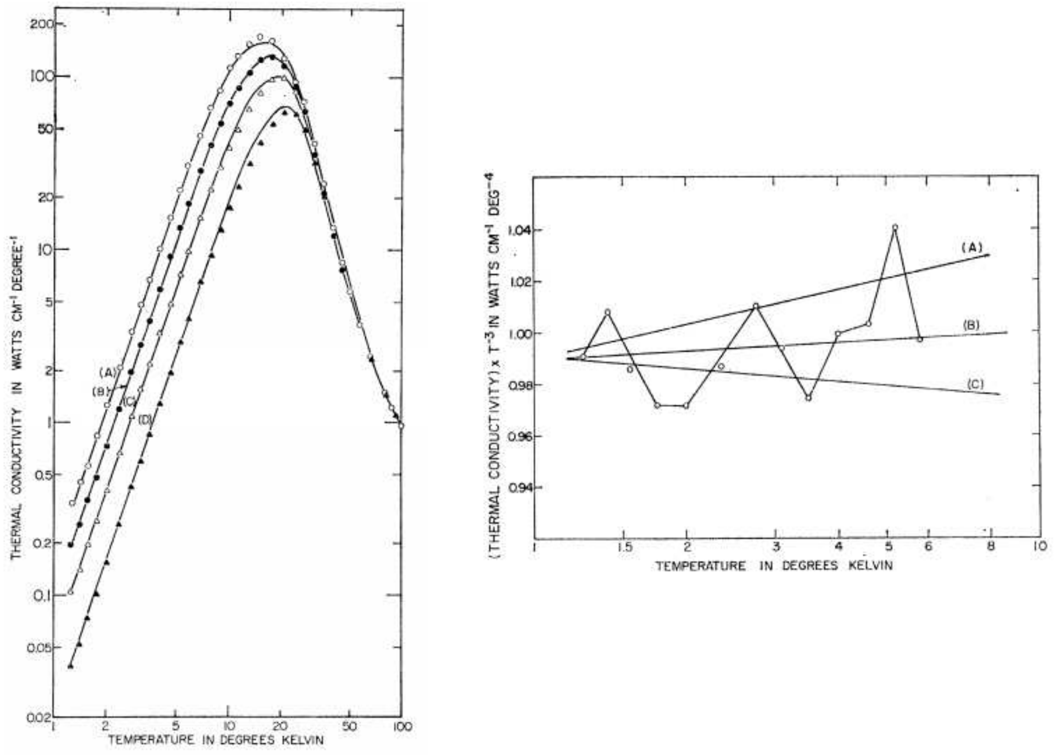

Figure 2.1: Left. Thermal conductivity of isotopically pure crystals of LiF for different mean crystal widths (A-D). It shows the general trend of κ_{ph} influenced by several scattering rates as in (2.3) : *boundary scattering* (below 10 K), arising of *Umklapp processes* (at intermediate temperatures), and *phonon-phonon scattering* (at high temperatures). Right. Low-temperature κ divided by T^3 and plotted against T. Figures taken from Ref. [52].

temperatures $T \ll \Theta_D$ – where Θ_D is known as Debye temperature – the contribution of phonons to the thermal conductivity κ from (2.2) can be written as [48]

$$\kappa_{ph} = \frac{k_B}{2\pi^2 v_{ph}} (\frac{k_B}{\hbar})^3 T^3 \int_0^{\Theta_D/T} \frac{x^4 e^x}{(e^x-1)^2} \tau(\omega, T) dx \ , \tag{2.3}$$

where $x = \hbar\omega/k_B T$, v_{ph} is the phonon velocity, and $\tau(\omega, T) = \ell/v_{ph}$ is a temperature and frequency dependent scattering time. Except for extremely low- or high-temperature regimes, the mean free path of heat-carrying excitations cannot be given as a constant. It rather depends on several scattering processes that are generally energy and temperature dependent. Thus, the importance of having introduced $\tau(\omega, T)$ in (2.3). Assuming that these scattering processes act independently from each other, one can write τ^{-1} as a sum of different scattering rates. These rates arise from possible boundary scatterings, point-defect scatterings, and Umklapp processes. For a detailed survey of the different scattering rates see e.g., Ref. [51]. The accuracy of the theory describing heat transport is thus largely dependent on a reliable estimate of all possible scattering rates involved in a specific system. Some typical measured thermal conductivities that illustrate the general trend for κ_{ph} as in (2.3) are reported in Fig. 2.1.

In principle – according to (2.2) – every excitation contributing to the specific heat, and that has a non-vanishing group velocity can contribute to heat transport. There are instances of *low-dimensional* magnetic insulators that show unusual contributions to κ arising from *spin excitations* [25]. These excitations represent another channel for the heat conductivity beyond the standard phonon one. Furthermore, they can interact with phonons, leading to additional scattering mechanisms. Similarly to the electronic and the phononic contribution, the magnetic thermal conductivity κ_{mag} can be estimated from (2.2). Therefore, by means of (2.2) one can study the properties of the low-energy heat-carrying magnetic excitations. In view of this, thermal transport becomes a powerful tool to investigate unconventional phenomena in low-dimensional spin systems.

2.1 Linear response theory

In linear response theory (LRT) every flux of a certain quantity (i.e., *currents* $\boldsymbol{j}_i$) within a system is given by a linear combination of related driving *forces* f_i acting on the same system. These forces might be temperature gradients ∇T, or electric fields $E = -\nabla V$. Linear response assumes that

$$\boldsymbol{j}_i = \sum_j \mathcal{L}_{ij} f_j \,, \tag{2.4}$$

where coefficients $\mathcal{L}_{ij}$ are measurable quantities that are defined via *correlation functions*, usually called *transport coefficients*. By means of (2.4) one can, for instance, recall the expression reported for the thermal current density in (2.1), with $f_j = -\nabla T$, and a certain coefficient $\mathcal{L}_{ij} = \kappa$.

In this section, I briefly introduce the formalism used to describe both spin and thermal transport coefficients in quantum magnets subject to magnetic field and thermal gradients [3] .

One may consider a system described by a Hamiltonian $\mathcal{H}_0$. The latter can be defined via a *local energy density* $h_0(\mathbf{r})$, as $\mathcal{H}_0 = \int d\mathbf{r} h_0(\mathbf{r})$. One can also assume the system to be in equilibrium with a locally varying and time-dependent inverse temperature $\beta + a(\mathbf{r},t) = \frac{1}{T} + (\frac{1}{T(\mathbf{r},t)} - \frac{1}{T})$, and an external magnetic field $B + b(\mathbf{r},t)$ that is coupled to the z-component of the spin density $S^z(\mathbf{r}) \equiv S(\mathbf{r})$. In this context, $a(\mathbf{r},t)$ and $b(\mathbf{r},t)$ are small perturbations of the total Hamiltonian, which effects can be treated in the linear response regime if $a(\mathbf{r},t) \ll \beta$ and $b(\mathbf{r},t) \ll B$ – fact which is assumed in the remainder of this section. The canonical statistical operator follows as

$$\begin{aligned} \rho &= \frac{1}{Z}\exp\{-\int d\mathbf{r}\big[\big(\beta + a(\mathbf{r},t)\big)\big(h(\mathbf{r}) - b(\mathbf{r},t)S(\mathbf{r})\big)\big]\} \\ &= \frac{1}{Z}\exp\{-\beta\big[\mathcal{H} + \int d\mathbf{r} h(\mathbf{r})\frac{a(\mathbf{r},t)}{\beta} - \int d\mathbf{r} b(\mathbf{r},t)S(\mathbf{r})\big]\} + \mathcal{O}(ab)\,, \end{aligned} \tag{2.5}$$

where $h(\mathbf{r}) = h_0(\mathbf{r}) - BS(\mathbf{r})$, Z is the partition function, and $\mathcal{H} = \mathcal{H}_0 - BS$. $S = \int d\mathbf{r} S(\mathbf{r})$ is the total z-magnetization.

Under conservation of the total energy $\mathcal{H}$ and magnetization S, two *currents* exist, $\boldsymbol{j}_h(\mathbf{r})$ and $\boldsymbol{j}_S(\mathbf{r})$, the *energy* and *spin* current, related to the energy density and the magnetization

---

[3] In the remainder of this section $\hbar = k_B = 1$, and Einstein's summation convention over pairwise equal indices is implied .

		$\mu = 1$	$\mu = 2$
Density operator	$d_\mu(\mathbf{r})$	$S(\mathbf{r})$	$h(\mathbf{r})$
Current operator	$j^l_\mu(\mathbf{r})$	$j^l_S(\mathbf{r})$	$j^l_h(\mathbf{r})$
Potentials	$\phi_\mu(\mathbf{r},t)$	$b(\mathbf{r},t)$	$-\frac{1}{\beta}a(\mathbf{r},t)$
Forces (1)	$g_{l\mu}(\mathbf{r},t)$	$\partial_l\phi_\mu(\mathbf{r},t)$	
Forces (2)	$f_{l\mu}(\mathbf{r},t)$	$\partial_l b(\mathbf{r},t)$	$\partial_l T(\mathbf{r},t)$

Table 2.1: Notation adopted to compute the linear response function to weak perturbations $a(\mathbf{r},t)$ and $b(\mathbf{r},t)$.

density, respectively. These currents satisfy equations of continuity

$$\begin{aligned} \partial_t h(\mathbf{r}) + \partial_l j^l_h(\mathbf{r}) &= 0 \\ \partial_t S(\mathbf{r}) + \partial_l j^l_S(\mathbf{r}) &= 0\,. \end{aligned} \tag{2.6}$$

In (2.6) $\partial_t \mathcal{C} = i\big[\mathcal{H},\mathcal{C}\big]$. It is possible to show that the energy current decomposes into $\boldsymbol{j}_h(\mathbf{r}) = \boldsymbol{j}_{th}(\mathbf{r}) - B\boldsymbol{j}_S(\mathbf{r})$. Here $\boldsymbol{j}_{th}(\mathbf{r})$ is the *thermal* current which is equal to the energy current in a system with zero magnetic field B. However, if B is finite, the energy current results in a spin (particle) part $\boldsymbol{j}_S(\mathbf{r})$ coupled with the thermal part $\boldsymbol{j}_{th}(\mathbf{r})$. In this context, B tunes the Zeeman energy per spin, or equivalently the chemical potential per particle. An alternative way to obtain the energy current expression of (2.6) is via the *polarization* operator $\mathbf{P} = \sum_{\mathbf{r}} \mathbf{r}h(\mathbf{r})$. Indeed, it is possible to show [53] that

$$\partial_t \mathbf{P} = i\big[\mathcal{H},\mathbf{P}\big] = \boldsymbol{j}_h(\mathbf{r}). \tag{2.7}$$

Without loss of generality, in the following I adopt the notation of Tab. 2.1 to discuss the time-dependent thermal average of the currents $\langle j^l_\mu(\mathbf{r},t)\rangle$ under perturbations $a(\mathbf{r},t)$ and $b(\mathbf{r},t)$. In particular, index $\mu = 1(2)$ here refers to the spin (energy) part. Let us consider time-dependent perturbations $W(t) = -d_\mu(\mathbf{r},t)\phi_\mu(\mathbf{r},t)$ of the total Hamiltonian, that are adiabatically switched on from $t = -\infty$ [4]. Thus, $\rho(-\infty)$ from (2.5) represents the equilibrium statistical operator − i.e., $\big[\rho(-\infty),\mathcal{H}\big] = 0$ − with $\rho_S(-\infty) = \rho_D(-\infty) = \rho(-\infty) \equiv \frac{1}{Z}\exp(-\beta\mathcal{H})$. Here indices S and D refer to the Schrödinger and Dirac time-evolution picture, respectively [5]. In the linear regime − i.e., for $||W|| \ll ||\mathcal{H}||$ − it follows that $\rho_D(t) - \rho(-\infty) = -i\int_{-\infty}^{t}\big[W_D(t'),\rho(-\infty)\big]dt' + \mathcal{O}(W^2)$. By using the latter expression, the time-dependent

---

[4] The total Hamiltonian is $H = \mathcal{H} + W(t)$, where $\mathcal{H}$ is the unperturbed term and $W(t)$ the time-dependent perturbation term. The latter is adiabatically switched on if $W(t \to -\infty) = 0$.

[5] In the Schrödinger picture of time evolution $\dot\rho_S(t) = -i\big[H,\rho_S(t)\big]$, with H the total Hamiltonian. In the Dirac picture $\dot\rho_D(t) = -i\big[W_D(t),\rho_D(t)\big]$, with $W(t)$ the time-dependent perturbation.

thermal average of currents is given by

$$\begin{aligned}
\langle j^l_\mu(\mathbf{r},t)\rangle &= \mathrm{Tr}\{j^l_{\mu D}(\mathbf{r},t)\big(\rho_D(t)-\rho(-\infty)\big)\}\\
&= -i\int_{-\infty}^{t}\mathrm{Tr}\{j^l_{\mu D}(\mathbf{r},t)\big[W_D(t'),\rho(-\infty)\big]\}dt'\\
&= i\int d\mathbf{r}'\int_{-\infty}^{t}\langle\big[j^l_\mu(\mathbf{r},t),d_\nu(\mathbf{r}',t')\big]\rangle_\rho\phi_\nu(\mathbf{r}',t')dt'\\
&= \int d\mathbf{r}'\int_{-\infty}^{t}\chi_{\mu\nu}(\mathbf{r},t;\mathbf{r}',t')\phi_\nu(\mathbf{r}',t')dt'\,.
\end{aligned}\tag{2.8}$$

In (2.8) the time-dependence of operators stems from the Dirac picture. The invariance under permutation of trace is used to go from the second to the third line of (2.8). The notation $\big[\cdot\big]$ refers to a commutator. The thermal average $\langle\cdot\rangle_\rho$ is evaluated at the equilibrium $\rho=\rho(-\infty)$. In the last line of (2.8), $\chi_{\mu\nu}(\mathbf{r},t;\mathbf{r}',t') = i\Theta(t-t')\langle\big[j^l_\mu(\mathbf{r},t),d_\nu(\mathbf{r}',t')\big]\rangle$ is the so called *response function*[6].

One may derive an alternative form of (2.8) performing some calculations. Starting from the third line of (2.8):

$$\begin{aligned}
\langle j^l_\mu(\mathbf{r},t)\rangle &= i\int d\mathbf{r}'\int_{-\infty}^{t}dt'\langle\big[j^l_\mu(\mathbf{r},t),d_\nu(\mathbf{r}',t')\big]\rangle_\rho\phi_\nu(\mathbf{r}',t')\\
(i) &= i\int d\mathbf{r}'\int_{-\infty}^{t}dt'\langle j^l_\mu(\mathbf{r},t)|Ld_\nu(\mathbf{r}',t')\rangle_\rho\phi_\nu(\mathbf{r}',t')\\
(ii) &= \int d\mathbf{r}'\int_{-\infty}^{t}dt'\langle j^l_\mu(\mathbf{r},t)|\partial_{t'}d_\nu(\mathbf{r}',t')\rangle_\rho\phi_\nu(\mathbf{r}',t')\\
(iii) &= -\int d\mathbf{r}'\int_{-\infty}^{t}dt'\langle j^l_\mu(\mathbf{r},t)|\partial_m j^m_\nu(\mathbf{r}',t')\rangle_\rho\phi_\nu(\mathbf{r}',t')\\
(iv) &= \int d\mathbf{r}'\int_{-\infty}^{t}dt'\langle j^l_\mu(\mathbf{r},t)|j^m_\nu(\mathbf{r}',t')\rangle_\rho g_{m\nu}(\mathbf{r}',t').
\end{aligned}\tag{2.9}$$

In (2.9) at step (*i*) the Kubo's identity [54] $\langle\mathcal{A}^\dagger|L\mathcal{B}\rangle = \langle\big[\mathcal{A}^\dagger,\mathcal{B}\big]\rangle$ has been used [7]. Step (*ii*) follows from the Liouville operator L acting on the density operator. Step (*iii*) makes use of the equations of continuity (2.6) where the time-derivative of the density operator is replaced by the gradient of the related current operator. In the end, at step (*iv*) an integration by parts is performed, returning the gradient of potentials $g_{m\nu}(\mathbf{r}',t)$ as defined in Tab. 2.1. From a Fourier transformation of (2.9) it follows

$$\langle j^l_\mu(\mathbf{q},\omega)\rangle = \mathcal{L}^{lm}_{\mu\nu}(\mathbf{q},\omega)f_{m\nu}(\mathbf{q},\omega)\,,\tag{2.10}$$

where $\mathcal{L}^{lm}_{\mu\nu}(\mathbf{q},\omega)$ refers to the *conductivity tensor*, expressed as a retarded *current relaxation function* via

$$\mathcal{L}^{lm}_{\mu\nu}(\mathbf{q},\omega+i0^+) = i\beta^p\langle j^l_\mu(\mathbf{q})|\frac{1}{\omega+i0^+-L}j^m_\nu(-\mathbf{q})\rangle.\tag{2.11}$$

Equation (2.11) − depending on $\mu\nu$ indices − indicates *spin* (11), *thermal* (22), and *magnetothermal* (12, 21) *conductivities.* These conductivities relate to the transport coefficients

---

[6] The step function $\Theta(t-t')$ takes into account the time causality of the response function.

[7] L represents the *Liouville* operator that describes the time-evolution of an operator $\mathcal{A}$, with $L\mathcal{A}_\mu(t) = \big[\mathcal{H},\mathcal{A}_\mu(t)\big]$, and $\dot{\mathcal{A}}_\mu(t) = iL\mathcal{A}_\mu(t)$.

introduced in (2.4). The change of notation of *forces* from $g_{m\nu}(\mathbf{q},\omega)$ in (2.9) to $f_{m\nu}(\mathbf{q},\omega)$ in (2.10) is a convention to fulfill *Onsager's* reciprocal relations [55], i.e., $T\mathcal{L}_{12} = \mathcal{L}_{21}$. Due to this change, equation (2.11) has the prefactor $\beta^p = (1/T)^p$, with $p = 1(0)$ for $\nu = 2(1)$ – see Tab. 2.1.

2.1.1 Transport coefficients

Spin and energy currents are thus related to the gradients $\nabla b(\mathbf{q},\omega)$ and $\nabla T(\mathbf{q},\omega)$ of the magnetic field b and temperature T, respectively, by

$$\begin{pmatrix} \mathcal{J}_1 \\ \mathcal{J}_2 \end{pmatrix} = \begin{pmatrix} \mathcal{L}_{11} & \mathcal{L}_{12} \\ \mathcal{L}_{21} & \mathcal{L}_{22} \end{pmatrix} \begin{pmatrix} \nabla b \\ -\nabla T \end{pmatrix} , \tag{2.12}$$

with $\mathcal{J}_\mu = \langle j_\mu \rangle$, and $\mathcal{L}_{\mu\nu}$ are the transport coefficients of Eqs. (2.10 ,2.11). In the following, the same notation of indices $\mu = 1(2)$ reported in Tab. 2.1 is used to indicate spin (energy) currents, respectively. For spin models, off-diagonal coefficients are only nonzero at finite magnetic fields. These cross coefficients are a measure for the coupling of the single transport phenomena within the system. A system with $\mathcal{L}_{12} = \mathcal{L}_{21} = 0$ consists of independent irreversible processes, where every driving force only affects its connected current flow. Transport coefficients can be measured via experiments [50]. First of all – the *spin* conductivity σ – measured for $\nabla T = 0$, is equal to $\mathcal{L}_{11}$. The *thermal* conductivity κ is usually measured under the condition of zero-particle flow, i.e., $\mathcal{J}_1 = 0$. Under such condition, it is then possible to show that $\kappa = \mathcal{L}_{22} - (\mathcal{L}_{21}^2 / T\mathcal{L}_{11})$, which reduces to $\kappa = \mathcal{L}_{22}$ for zero magnetic fields.

A *spectral representation* of coefficients $\mathcal{L}_{\mu\nu}$ in (2.12) can be derived from (2.11). With $z = \omega + i0^+$, one can write (2.11) as

$$\begin{aligned}
\mathcal{L}_{\mu\nu}^{lm}(\mathbf{q},\omega) &= \beta^p \int_{-\infty}^{0} dt \langle j_\mu^l(\mathbf{q}) | e^{-i(z-L)t} j_\nu^m(-\mathbf{q}) \rangle \\
(i) &= \beta^p \int_{-\infty}^{0} dt \int_0^\beta d\tau \langle j_\mu^l(\mathbf{q},\tau) e^{-i(z-L)t} j_\nu^m(-\mathbf{q}) \rangle \\
(ii) &= \beta^p \int_0^\beta d\tau \int_{-\infty}^{0} dt e^{-izt} \langle j_\mu^l(\mathbf{q},\tau) e^{iLt} j_\nu^m(-\mathbf{q}) \rangle \\
&= \beta^p \int_0^\beta d\tau \int_{-\infty}^{0} dt e^{-izt} \langle j_\mu^l(\mathbf{q},\tau) j_\nu^m(-\mathbf{q},t) \rangle .
\end{aligned} \tag{2.13}$$

In (2.13) at step (i) the notion of *Mori*'s scalar product [56] $\langle \mathcal{A}_\mu^\dagger | \mathcal{A}_\nu \rangle = \int_0^\beta d\tau \langle \mathcal{A}_\mu^\dagger(\tau) \mathcal{A}_\nu \rangle$ has been employed. Here, τ is the *imaginary* time that has units of β, and t refers to the *real* time. At step (ii) the Liouville operator L returns a time-dependent current operator $j_\nu^m(\mathbf{q},t)$. The last line of (2.13) clearly shows that the transport coefficients $\mathcal{L}_{\mu\nu}(\mathbf{q},\omega)$ follow from the time-dependent *current-current correlation functions*

$$C_{\mu\nu}^{lm}(\mathbf{q}, t + i\tau) = \langle j_\mu^l(\mathbf{q}) j_\nu^m(-\mathbf{q}, t + i\tau) \rangle . \tag{2.14}$$

By inserting complete sets of eigenstates[8] of $\mathcal{H}$, Eq. (2.13) reads

$$\begin{aligned}\mathcal{L}^{lm}_{\mu\nu}(\mathbf{q},\omega) &= \frac{\beta^p}{\Omega Z}\sum_{l'm'}\int_{-\infty}^{0} dt e^{-i(z+\varepsilon_{l'}-\varepsilon_{m'})t}\int_0^\beta d\tau e^{-\beta\varepsilon_{l'}} e^{(\varepsilon_{l'}-\varepsilon_{m'})\tau}\langle l'|j^l_\mu(\mathbf{q})|m'\rangle\langle m'|j^m_\nu(-\mathbf{q})|l'\rangle \\ &= \frac{\beta^p}{\Omega Z}\sum_{l'm'} e^{-\beta\varepsilon_{l'}}\frac{i}{z+\varepsilon_{l'}-\varepsilon_{m'}}\left(e^{(\varepsilon_{l'}-\varepsilon_{m'})\beta}-1\right)\frac{1}{\varepsilon_{l'}-\varepsilon_{m'}}\langle l'|j^l_\mu(\mathbf{q})|m'\rangle\langle m'|j^m_\nu(-\mathbf{q})|l'\rangle\end{aligned} \tag{2.15}$$

In (2.15) Z refers to the partition function, and Ω is the system size. Moreover, $\mathcal{L}^{lm}_{\mu\nu}(\mathbf{q},\omega)$ can be decomposed into real and imaginary parts to extract the spectrum of the conductivity. In particular, due to the imaginary unit i up front in (2.11), the spectral function is returned by the real part of (2.15), as

$$\mathbb{R}\mathrm{e}\{\mathcal{L}^{lm}_{\mu\nu}(\mathbf{q},\omega)\} = \frac{\pi\beta^p}{\Omega Z}\frac{1-e^{-\beta\omega}}{\omega}\sum_{l'm'} e^{-\beta\varepsilon_{l'}}\langle l'|j^l_\mu(\mathbf{q})|m'\rangle\langle m'|j^m_\nu(-\mathbf{q})|l'\rangle\delta(\omega+\varepsilon_{l'}-\varepsilon_{m'})\,, \tag{2.16}$$

where $\delta(\cdots)$ is the Dirac's delta function. Furthermore, the sum over states $l'm'$ in (2.16) can be split into two parts : a first contribution for $\varepsilon_{l'}=\varepsilon_{m'}$ and a second contribution for $\varepsilon_{l'}\neq\varepsilon_{m'}$, returning

$$\mathbb{R}\mathrm{e}\{\mathcal{L}^{lm}_{\mu\nu}(\mathbf{q},\omega)\} = D^{lm}_{\mu\nu}(\mathbf{q})\delta(\omega) + \mathcal{L}^{reg,lm}_{\mu\nu}(\mathbf{q},\omega)\,. \tag{2.17}$$

Equation (2.17) defines the zero-frequency transport coefficient, called *Drude weight* (DW) $D^{lm}_{\mu\nu}(\mathbf{q})$, and the finite-frequencies coefficient, called *regular part* $\mathcal{L}^{reg,lm}_{\mu\nu}(\mathbf{q},\omega)$. Equation (2.17) is usually considered in the long-wavelength limit, namely for $\mathbf{q}\to 0$, for which reason in the following one may consider simply $\mathbb{R}\mathrm{e}\{\mathcal{L}^{lm}_{\mu\nu}(\mathbf{q}=0,\omega)\} = \mathbb{R}\mathrm{e}\{\mathcal{L}^{lm}_{\mu\nu}(\omega)\}$. Expressions for $D^{lm}_{\mu\nu}$ and $\mathcal{L}^{reg,lm}_{\mu\nu}(\omega)$ can be read off from (2.16) as

$$D^{lm}_{\mu\nu} = \frac{\pi\beta^{p+1}}{\Omega Z}\sum_{\substack{l',m'\\ \varepsilon_{l'}=\varepsilon_{m'}}} e^{-\beta\varepsilon_{l'}}\langle l'|j^l_\mu(0)|m'\rangle\langle m'|j^m_\nu(0)|l'\rangle\,, \tag{2.18}$$

and

$$\mathcal{L}^{reg,lm}_{\mu\nu}(\omega) = \frac{\pi\beta^p}{\Omega Z}\frac{1-e^{-\beta\omega}}{\omega}\sum_{\substack{l',m'\\ \varepsilon_{l'}\neq\varepsilon_{m'}}} e^{-\beta\varepsilon_{l'}}\langle l'|j^l_\mu(0)|m'\rangle\langle m'|j^m_\nu(0)|l'\rangle\delta(\omega+\varepsilon_{l'}-\varepsilon_{m'})\,. \tag{2.19}$$

The physical meaning carried by $D^{lm}_{\mu\nu}$ of (2.18) and by $\mathcal{L}^{reg,lm}_{\mu\nu}(\omega)$ of (2.19) is a measure of *ballistic* and *dissipative* contribution to conductivities, respectively. Quantities usually interesting for transport studies are the DW and the zero-frequency limit of the regular part,

$$\mathcal{L}^{dc}_{\mu\nu} = \lim_{\omega\to 0}\mathcal{L}^{reg}_{\mu\nu}(\omega)\,, \tag{2.20}$$

called *dc conductivity.* In general, the way in which the dynamic current-current correlation functions in (2.13) decay, determines the ballistic or diffusive character of the energy and spin transport.

Figure 2.2 – for example – is a schematic representation of the typical behavior of $\mathbb{R}\mathrm{e}\{\mathcal{L}^{lm}_{\mu\nu}(\omega)\}$

---

[8] So that $\rho = \sum_{l'}\rho_{l'}|l'\rangle\langle l'|$, with $\rho_{l'} = \frac{1}{Z}e^{-\beta\varepsilon_{l'}}$ since $[\mathcal{H},\rho]=0$, and $\mathcal{H}|l'\rangle = \varepsilon_{l'}|l'\rangle$.

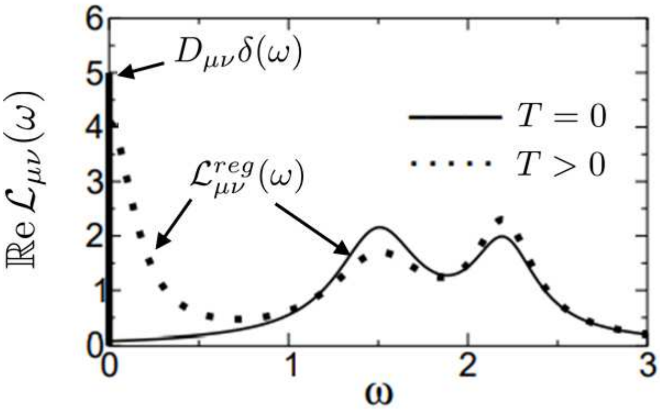

Figure 2.2: Real part of the conductivity $\mathcal{L}_{\mu\nu}(\omega)$ of a typical *clean* metal, as a function of frequency, at $T = 0$ (solid line) and finite-temperature $T > 0$ (dotted line). The singular Drude weight $D_{\mu\nu}\delta(\omega)$ at $T = 0$ is depicted by a thick solid line. The regular part $\mathcal{L}^{reg}_{\mu\nu}(\omega)$ is shown too. Figure adapted from Ref. [57].

as a function of frequency for a clean metallic system. Both the DW and the dc conductivity are shown also dependent on the temperature T. Based on a study of these latter, it is possible to discuss different scenarios for the conductivity.

For a *clean* system at $T = 0$, the Drude weight $D_{\mu\nu}(T = 0) \equiv D^0_{\mu\nu}$ only characterizes the system as a *conductor* (*metal*) $D^0_{\mu\nu} > 0$ – see $D^0_{\mu\nu}$ at $\omega = 0$ in Fig. 2.2 – or as an *insulator* $D^0_{\mu\nu} = 0$, since no dissipation is expected, i.e., $\mathcal{L}^{dc}_{\mu\nu}(T = 0) = 0$ [9].

At finite temperatures, the δ-function broadens to a Drude peak of width inversely proportional to a characteristic scattering time. The latter gives rise to a finite $\omega \to 0$ limit which implies a finite *dc* conductivity – shown in Fig. 2.2 with a finite value on y-axis. The scattering mechanisms – intrinsic (due to interactions), or extrinsic (due to coupling to other excitations) – lead typically to a vanishing $D_{\mu\nu}$ in the thermodynamic limit [10]. Physically this represents the scenario of a *dissipative* conductor.

Another possible scenario is the case where both $D_{\mu\nu}$ and $\mathcal{L}^{dc}_{\mu\nu}$ are zero at finite temperature. A *disordered* insulating system – provided that disorder is strong enough to produce localization – can belong to such a case. A system of this type can be called *ideal insulator.*

But it is also possible the case where $D_{\mu\nu}$ remains finite even at finite temperature, leading to a *ballistic* transport in the thermodynamic limit – regardless of $\mathcal{L}^{dc}_{\mu\nu}$. This kind of system is called *ideal conductor.* This latter case can be presented as a transport without dissipation of parts of the current. Differently speaking, in the time-domain, a part of the current will never decay. The phenomenon has been related to the existence of *conservation laws* [58], which influence on transport properties of low-dimensional quantum systems has been studied by Zotos *et al.* [59].

---

[9] In a system with disorder, the DW could vanish even at zero temperature and the dc residual conductivity is finite – provided the disorder is not strong enough to produce localization [57].

[10] There exist, however, systems showing anomalous (diverging) conductivity at $T > 0$, i.e., scattering mechanisms do not suppress $D_{\mu\nu}$ [57].

One example is spin transport in spin-$\frac{1}{2}$ Heisenberg XXZ [11] chain, where the spin current j_1 is not conserved for any nonzero anisotropic exchange coupling Δ. Although j_1 is not a conserved operator, other conserved observables can exist. To be more precise, given a set of these observables $\{\mathcal{A}_l\}$ [12] in the Liouville space, so that $L\mathcal{A}_l = \left[\mathcal{H}, \mathcal{A}_l\right] = 0$, and using the fact that $\langle\mathcal{A}_l^\dagger|\mathcal{A}_m\rangle$ has all the properties of a scalar product in this operator space, the related Drude weight $D_{11}(b,T)$ is given by the so called *Mazur's* inequality [60]

$$D_{11}^{lm}(b,T) \geq \frac{\pi}{\Omega}\sum_l \frac{\langle j_1^l(0)|\mathcal{A}_l\rangle\langle\mathcal{A}_l^\dagger|j_1^m(0)\rangle}{\langle\mathcal{A}_l^\dagger|\mathcal{A}_l\rangle} = \frac{\pi\beta}{\Omega}\sum_l \frac{\langle j_1^l(0)\mathcal{A}_l\rangle\langle\mathcal{A}_l^\dagger j_1^m(0)\rangle}{\langle\mathcal{A}_l^\dagger\mathcal{A}_l\rangle}. \tag{2.21}$$

In (2.21) $\langle\mathcal{A}_l^\dagger|\mathcal{A}_l\rangle = \beta\langle\mathcal{A}_l^\dagger\mathcal{A}_l\rangle$ has been used [56]. Its interpretation is that the Drude weight is finite whenever the currents $j_1^l(0)$ and $j_1^m(0)$ have a finite (Mori) projection onto a subset of conserved operators $\{\mathcal{A}_l\}$ of the system. Thus, (2.21) provides a lower bound for the Drude weight $D_{11}^{lm}(b,T)$. For instance, at finite magnetic fields b, one conserved operator that is often considered in (2.21) is the thermal current $\mathcal{A}_l = \boldsymbol{j}_{th}$, which has a finite overlap $\langle\boldsymbol{j}_1|\boldsymbol{j}_{th}\rangle > 0$ onto the spin current operator, with a resulting $D_{11}^{lm}(b,T) > 0$ [59].

2.2 Selected experimental results

Low-dimensional quantum spin systems have attracted particular attention in thermal transport investigations. The reason is that these systems often show peculiar ground states and unusual related excitations. These excitations can contribute to the thermal conductivity κ of the system. Studying this contribution to the heat transport one can characterize the spin excitations and the properties of the related spin system. Besides, there exists a beneficial interplay between theoretical predictions and experiments. In this context, one example is the *integrable* [13] spin-$\frac{1}{2}$ Heisenberg XXZ 1D chain model, for which a diverging κ has been predicted [59]. It would be interesting to contrast this theoretical prediction with experiments on 1D magnetic materials.

In the following, I present a selection of results from thermal transport measurements performed on low-dimensional systems. For the purpose of this work, I show some of the experiments carried out on either *unfrustrated* [61–72] or *frustrated* [23, 24, 73–75] low-dimensional quantum magnets.

2.2.1 Magnetic heat transport in unfrustrated systems

In this section, I focus on spin-$\frac{1}{2}$ antiferromagnetic Heisenberg (HAF) models on three different lattice structures: a 1D spin chain, a quasi-1D spin two-leg ladder, and a 2D square lattice. Because of the varying dimensionality, distinct properties and different kinds of excitations arise – from which predictions on thermal conductivity depend on.

Examples of materials described by the aforementioned models are $CaCu_2O_3$, $SrCuO_2$ and

---

[11] $\mathcal{H}_{\text{XXZ}} = -J\sum_i\left(S_i^xS_{i+1}^x + S_i^yS_{i+1}^y + \Delta(S_i^zS_{i+1}^z - \frac{1}{4})\right) - b\sum_i S_i^z$, with Δ the anisotropy parameter, and b the magnetic field.

[12] $\{\mathcal{A}_l\}$ are orthogonal to each other, $\langle\mathcal{A}_l\mathcal{A}_m\rangle = \langle\mathcal{A}_l^2\rangle\delta_{l,m}$.

[13] Most commonly, quantum systems are called integrable if an infinite set of conserved quantities $\{\mathcal{A}_l\}$ exists which are pairwise different [58] – see discussion in Sec. 2.1.1 about *conservation laws* and transport.

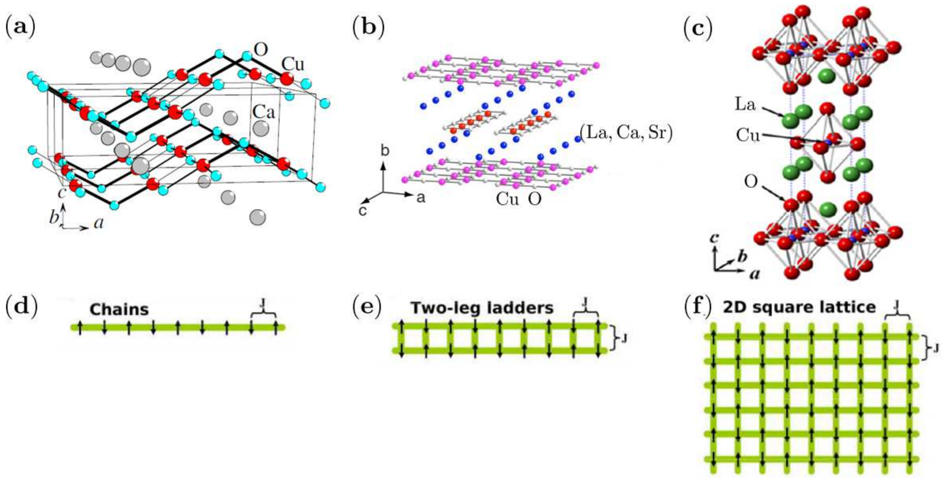

Figure 2.3: Crystal structures of (a) $CaCu_2O_3$, (b) $(Sr, La, Ca)_{14}Cu_{24}O_{41}$ compounds, and (c) La_2CuO_4. (d-f) Illustration of low-dimensional spin lattices related to (a-c) structures: (d) 1D spin chains, (e) quasi-1D two-leg spin ladders, and (f) 2D square lattice. Arrows indicate local moments of the CuO-arrangements in crystals (a-c). Exchange coupling J is antiferromagnetic. Figure (a) is taken from Ref. [76], (b) is adapted from Ref. [77], and (c) is adapted from Ref. [78]. Figures (d-f) are adapted from Ref. [25].

Sr_2CuO_3 (spin chains), $(Sr, La, Ca)_{14}Cu_{24}O_{41}$ (spin ladders), and La_2CuO_4 (2D square lattice) – see Fig. 2.3. These materials have common features: they all are copper oxides compounds – *cuprates* – and they are *electrically insulating* systems. Thus, it is reasonable to expect that the thermal conductivity for these systems is only carried by lattice and spin excitations, κ_{ph} and κ_{mag}, respectively.

Considering *pure* thermal transport – $\mathcal{J}_1 = 0$ in (2.12)– the energy current is $\mathcal{J}_2 = -\kappa\nabla T$, where the thermal conductivity is generally $\kappa = \mathcal{L}_{22} - (\mathcal{L}_{21}^2/T\mathcal{L}_{11})$. In the following, I refer to κ as in (2.17), with $\mathbb{R}\mathrm{e}\{\kappa(\omega)\} = D_{th}\delta(\omega) + \kappa^{reg}(\omega)$. The coefficient D_{th} is the *thermal* Drude weight, and $\kappa^{reg}(\omega)$ is the diffusive part.

The spin-$\frac{1}{2}$ 1D HAF chain model assumed for $CaCu_2O_3$ describes an integrable system. It is possible to show [79] that it features a Luttinger-liquid-like behavior [80], with fractionalized gapless *spinon* excitations. In particular, the system has been predicted to show ballistic heat transport – via spinons – with a diverging heat conductivity [59]. The latter can be expressed as $\mathbb{R}\mathrm{e}\{\kappa(\omega)\} = D_{th}\delta(\omega)$. Moreover, the temperature dependence of the thermal Drude weight D_{th} has been evaluated [81] *exactly* in the low-temperature limit **14**, where

$$D_{th} = \frac{(\pi k_B)^2}{3\hbar} vT \,, \tag{2.22}$$

with v the velocity of spinons in the long-wavelength limit. In a real material, scattering processes cause a broadening of the δ-peak into, e.g., a Lorentzian in frequency space with a width proportional to the scattering rate τ^{-1}. Thus the magnetic contribution κ_{mag} per single chain, is rendered finite, approximated by $\kappa_{mag} = D_{th}\tau/\pi$ [70], with $\ell_{mag} = v\tau$ the spinon mean free path. To show this, one may consider the kinetic model in one dimension of κ as in (2.2), to estimate κ_{mag} at low temperature. It is given – taken into account that

---

[14] Low temperatures here means that $T \lesssim 0.15\, J/k_B$, namely $T \lesssim 300\,\mathrm{K}$ for $J/k_B \sim 2000$.

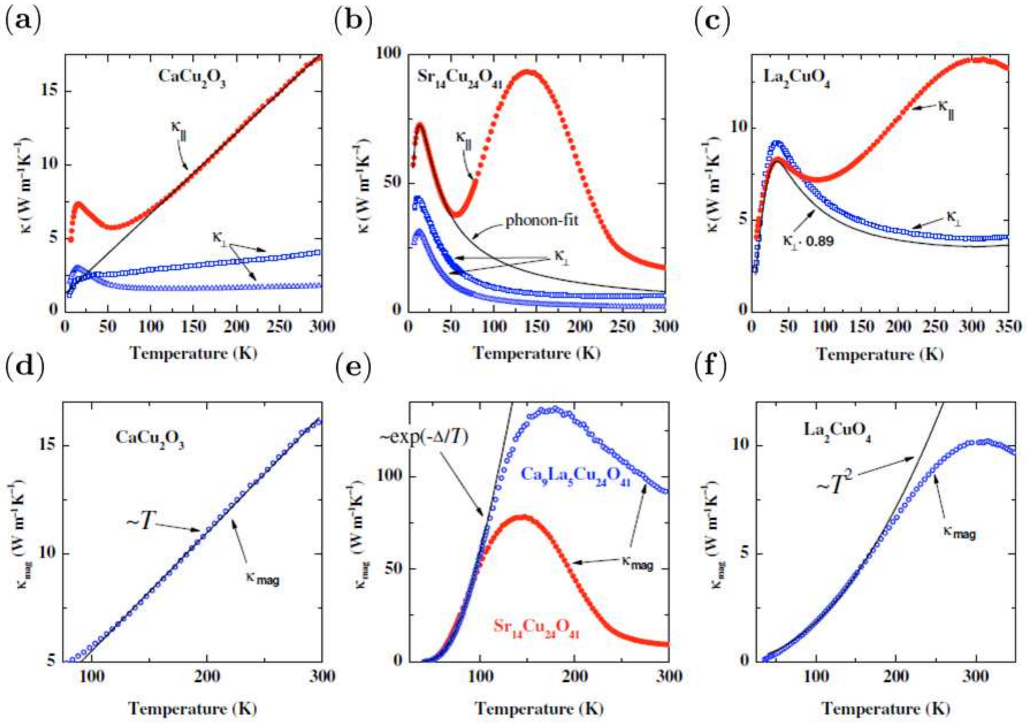

Figure 2.4: (a-c) Temperature dependence of thermal conductivity κ for different low-dimensional spin materials: (a) 1D spin-chain $CaCu_2O_3$, (b) quasi-1D two-leg spin ladder $Sr_{14}Cu_{24}O_{41}$, and (c) 2D-HAF on square lattice La_2CuO_4. Here, κ is split into $\kappa = \kappa_\parallel + \kappa_\perp$, which are the component parallel to the low-dimensional structure, and that one perpendicular, respectively (red • and blue ◦). Solid lines in (b,c) depict an estimate of phonon background, whereas solid line in (a) is a linear fit in a $T \geq 100\,\mathrm{K}$ range. (d-f) Magnetic thermal contribution to κ obtained subtracting the phonon term, κ_{ph}, as a function of temperature, of (d) $CaCu_2O_3$, (e) $Sr_{14}Cu_{24}O_{41}$ (red •) and $Ca_9La_5Cu_{24}O_{41}$ (blue ◦), and (f) La_2CuO_4. Solid lines represent the kinetic estimates for κ, with the low-temperature dependence reported beside. Figures are adapted from Refs. [70, 66, 69].

spinons obey the Fermi-Dirac statistics – by [65]

$$\kappa_{mag} = \frac{2k_B^2 n_S}{\pi\hbar} T\ell_{mag} \underbrace{\int_0^{\frac{\pi J}{2k_BT}} dx \frac{x^2 e^x}{(e^x+1)^2}}_{=\frac{\pi^2}{6} \text{ for } T\to 0} \overset{(2.22)}{\overbrace{=}} \frac{D_{th} n_s}{\pi v}\ell_{mag} = \frac{D_{th}\tau}{\pi} n_s \,, \tag{2.23}$$

with n_S the number of spin chains.

Figure 2.4(a) shows the thermal measurements carried out on $CaCu_2O_3$ [70]. In particular, the total thermal conductivity $\kappa = \kappa_{ph} + \kappa_{mag}$ is reported as a function of temperature. Experimentally, it is necessary to isolate the magnetic contribution κ_{mag} from the phonon term κ_{ph} [15]. Figure 2.4(d) shows the result of such a procedure, displaying $\kappa_{mag}(T)$. Experimental data remarkably confirm the theoretical estimate for $\kappa_{mag} \propto T$ as in (2.23). Other works on different spin-chain compounds [64, 72] have also related an unusual large heat contribution to spinon excitations. Effects of *purity* on the thermal conductivity of these compounds

---

[15] The extrapolation of the experimental κ_{mag} usually exploits its different properties with respect to κ_{ph}. For instance, while the former is usually anisotropic , i.e., $\kappa_{mag}^{\parallel} \neq \kappa_{mag}^{\perp}$, the latter is isotropic – see Hess [25] for further details on the experimental procedure.

have been also studied [71, 72]. In a high-purity sample, an extraordinary scattering length $\ell_{mag} \sim \mu$m is reported at low temperatures, limited only by impurities. This finding suggests that much larger ℓ_{mag} may be achieved in perfectly clean crystals, which corroborates the theoretical predictions for such systems.

The quasi-1D two-leg spin ladders system, as in $Sr_{14}Cu_{24}O_{41}$, is characterized by a singlet dimer ground state separated from the triplet excited state by an energy gap Δ_{tr}. These triplet excitations – or *triplons* – are dispersing modes, and hence it is expected that they contribute somehow to the thermal conductivity of the system [63, 66]. The prediction for κ_{mag}, similarly derived as in (2.23) according to (2.2), implies that due to the spin gap Δ_{tr}, $\kappa_{mag} \propto \exp(-\Delta_{tr}/(k_B T))$.
Further observations on the estimate of κ_{mag} have been reported in Refs. [63, 66]. The experimental data for κ_{mag} [66] of $Sr_{14}Cu_{24}O_{41}$ are in agreement with the expected temperature-dependent activation of triplons in the low-temperature range. The observed κ_{mag} follows an exponentially activated behavior as shown in Fig. 2.4(e). The data have been extrapolated from the total κ reported in Fig. 2.4(b) by means of standard procedures. Moreover, studies of the magnetic mean-free path ℓ_{mag} temperature dependence have been done. These lead to the conclusion that such a system is not expected to show ballistic transport, due to its non-integrability [59, 82]. However, the thermal conductivity looks anomalously large due to an experimental mean-free path much larger than the spin correlation length in the system [25].

For the 2D-HAF on square lattice – such as in La_2CuO_4 [83] – one expects a classical long-range ordered Néel ground state with *magnon* excitations. What is expected is that magnons contribute to the observed anomalous *in-plane* heat conductivity [68, 69, 84, 85]. Thus, a low-temperature estimate of κ_{mag} can be obtained as usual via the kinetic model of a 2D-κ using (2.2), and reading as [69]

$$\kappa_{mag} = \sum_{i=1}^{2} \frac{k_B^3 T^2 \ell_{mag}}{2\pi\hbar^2 v_0 c} \int_{\frac{\Delta_i}{k_B T}}^{\infty} dx x^2 \sqrt{x^2 - (\frac{\Delta_i}{k_B T})^2} \frac{e^x}{(e^x - 1)^2}. \tag{2.24}$$

In (2.24) the sum over i refers to a sum over the magnon dispersion relation $\varepsilon_{\mathbf{q}}$ of the two branches $i = 1, 2$. Its 2D expression [16] reads $\varepsilon_{\mathbf{q}} = \varepsilon_q = \sqrt{\Delta_i^2 + (\hbar v_0 q)^2}$. In (2.24) v_0 is the spin-wave velocity, c is the lattice constant perpendicular to the planes, while Δ_i denotes a small spin gap for each magnon branch [17]. The rough low-temperature estimate is then $\kappa_{mag} \propto T^2$. Remarkably, experimental data [69] for κ_{mag} of La_2CuO_4 reported in Fig. 2.4(f) are consistent with the theoretical estimate.

2.2.2 Magnetic heat transport in frustrated systems

Thermal transport measurements [23, 24, 73–75, 86] have been recently reported for frustrated materials which are possible candidates of quantum spin liquids. The problem of revealing such a phase of matter is an active subject in the condensed matter community. The combined use of conventional experimental techniques – spectroscopic, local resonance probe measurements – can help to unveil the properties of spin liquids having a look on their excitations. In this context, thermal transport works efficiently, being related to the properties of low-energy

---

[16] In real quasi 2D materials, exchange anisotropies cause the opening of gaps – see e.g., Ref. [83].
[17] Note that the spin gaps could be neglected without any large error.

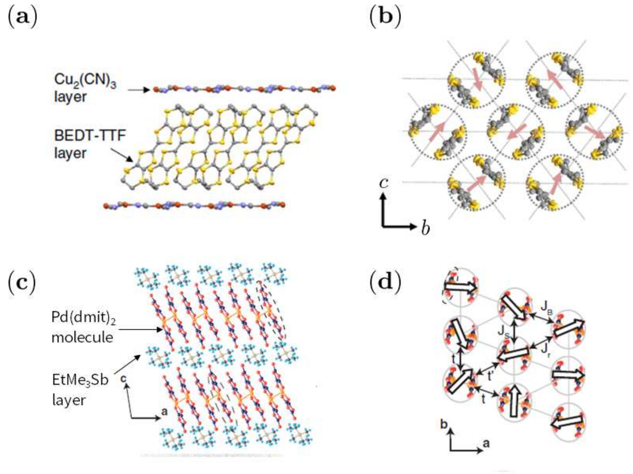

Figure 2.5: (a) Crystal structure of $\kappa-(\mathrm{BEDT-TTF})_2\mathrm{Cu}_2(\mathrm{CN})_3$ as a two-dimensional layered material. (b) Molecular arrangement in a two-dimensional magnetic layer. Ellipsis and arrows stand for $(\mathrm{BEDT-TTF})_2^+$ molecular dimers on a triangular lattice, and for spins-$\frac{1}{2}$ on dimers, respectively. (c) Crystal structure of $\mathrm{EtMe_3Sb[Pd(dmit)_2]_2}$. It consists of two-dimensional $\mathrm{Pd(dmit)_2}$ layers separated by layers of cation $\mathrm{EtMe_3Sb}$. (d) Sketch of the in-plane arrangement of spins on the $\mathrm{Pd(dmit)_2}$ layer. Encircled molecules stand for strongly dimerized $[\mathrm{Pd(dmit)_2}]_2^-$ units with spin-$\frac{1}{2}$. Nearest-neighbor interactions are indicated by $J_{B,S,r}$. Figures (a,b) are reproduced from Ref. [87], (c,d) are adapted from Ref. [88].

mobile excitations that carry heat.

In the following, I present some experimental results for either *organic* [23, 24] or *inorganic* [73, 75] materials, possibly hosting quantum spin liquid states.

Among organic frustrated compounds, $\kappa-(\mathrm{BEDT-TTF})_2\mathrm{Cu}_2(\mathrm{CN})_3$ and $\mathrm{EtMe_3Sb[Pd(dmit)_2]_2}$ [18] – shown in Fig. 2.5 – have been considered as possible realization of quantum spin liquids. Several observations [89, 90] have indeed reported suppression of the long-range magnetic order down to very low temperatures, $T \sim$ mK. The materials have 2D layers of dimerized molecules, where each dimer has one electron forming a half-filled Mott *insulating* system on a triangular lattice [24], as shown in Figs. 2.5 (b,d). Many models have been proposed to explain frustration and to justify the emergence of a spin liquid state [91–93] in these materials. Since they are insulators, κ is expected to be given in terms of phonons and possible spin excitations. At low temperatures, by using (2.2) one may assume $\kappa(T) \propto c(T)$, where $c(T)$ is the temperature-dependent specific heat. A term $\sim T^{\alpha-1}$ in κ/T – with α typically between 2 and 3 – relates to κ_{ph}. While, a residual term γ in κ/T could arise from mobile gapless magnetic excitations. Results from thermal conductivity measurements [23, 24] are shown in Fig. 2.6(a) for both compounds.

Figure 2.6(a) shows κ/T as function of T^2. In view of this, a finite intercept of the straight-line κ_{ph} would be an evidence of magnetic contributions.
The $\kappa-(\mathrm{BEDT-TTF})_2\mathrm{Cu}_2(\mathrm{CN})_3$ shows a convex and non-T^2 dependent κ/T. This fact has been related to the opening of a spin gap [23] with an expected thermally activated behavior

---

[18] $(\mathrm{BEDT-TTF})_2$ stands for *bis(ethylenedithio)-tethrathiafulvalene* and $\mathrm{EtMe_3Sb[Pd(dmit)_2]_2}$ contains abbreviation for dmit = 1, 3−dithiole−2−thione−4, 5−dithiolate, Me = $\mathrm{CH_3}$, and Et = $\mathrm{C_2H_5}$.

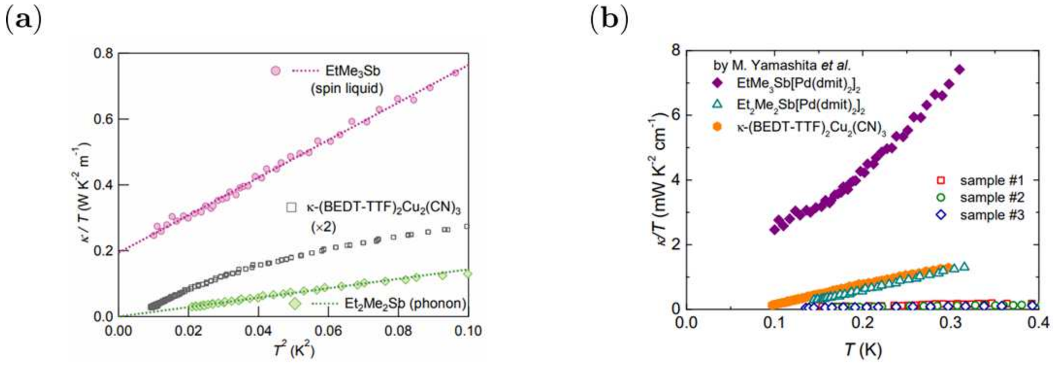

Figure 2.6: (a) Thermal conductivity κ/T vs. T^2 to reveal a residual of κ/T as intercept in the relation $\kappa = \gamma T + \alpha T^3$ (the term $\sim T^3$ is the phonon contribution). In EtMe$_3$Sb[Pd(dmit)$_2$]$_2$ a finite γ is shown in the $T \to 0$ limit. The nonmagnetic parent compound Et$_2$Me$_2$Sb[Pd(dmit)$_2$]$_2$ only shows the expected phonon contribution. On the contrary, $\kappa-$(BEDT$-$TTF)$_2$Cu$_2$(CN)$_3$ displays a convex and non-T^2 dependent κ/T. (b) Comparison of thermal conductivity κ/T vs. T for EtMe$_3$Sb[Pd(dmit)$_2$]$_2$ from Ref. [94] with data shown in (a) from Ref. [24]. Figure (a) is taken from Ref. [24], and figure (b) is taken from Ref. [94].

for κ. Thus, this material would provide an example of a *gapped* quantum spin liquid. Differently, EtMe$_3$Sb[Pd(dmit)$_2$]$_2$ has a κ/T with a finite intercept. This fact has been attributed to the existence of mobile gapless excitations of the related quantum spin liquid ground state [24]. A nonmagnetic parent compound is contrasted with the latter (green dots). For this material $\kappa = \kappa_{ph}$, and actually κ/T extrapolates to zero in the zero-temperature limit. Results on the existence of mobile gapless excitations in EtMe$_3$Sb[Pd(dmit)$_2$]$_2$ from Yamashita *et al.* [24] – shown in Fig. 2.6(a) – have been recently criticized by new experimental works [94, 95]. These works have studied the thermal conductivity of the same compound, and with samples prepared in similar conditions as in Ref. [24]. Results of κ/T as function of T for EtMe$_3$Sb[Pd(dmit)$_2$]$_2$ from Ni *et al.* are shown in Fig. 2.6(b). They are contrasted to those obtained in Ref. [24] and displayed in Fig. 2.6(a). The data for thermal conductivity κ/T reported in Ref. [94] and shown in Fig. 2.6(b) are well reproduced by a linear fitting, i.e., $\kappa/T \sim \gamma + bT$. Interestingly, a negligible residual term γ is observed, which is inconsistent with the existence of mobile gapless magnetic excitations, and thus also with the outcome of Ref. [24]. Both works in Refs. [94, 95] attribute the magnitude and behavior of κ/T in EtMe$_3$Sb[Pd(dmit)$_2$]$_2$ entirely to phonons, which can be possibly scattered by low-energy localized spin excitations of the spin liquid ground state [96]. The discrepancy of results on κ/T raises questions about the true ground state of this QSL candidate. Thus, the synthesis of gapless QSL with highly mobile excitations remains an open issue.

Among frustrated inorganic materials, particular attention has been paid to a ruthenium-based compound with Ru^{3+}($4d^5$) magnetic ions. The 2D-layered $\alpha-$RuCl$_3$ – subject of a very active interest – belongs to the so called $j = \frac{1}{2}$ spin-orbit assisted Mott insulators [99]. The interaction frustration that characterizes these systems arises from a strong spin-orbit coupling [28, 29] – that has been discussed in Sec. 1.2. In particular, $\alpha-$RuCl$_3$ shows peculiar features covered by a quantum spin liquid.

Figure 2.7(a) displays its crystal structure. Analogously to iridate compounds discussed in Ref. [29], the edge-sharing octahedra geometry of the crystal leads to anisotropic spin-orbit

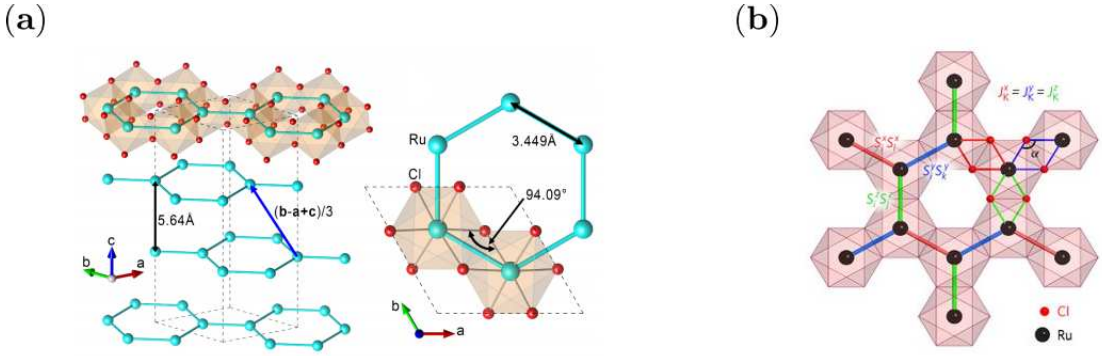

Figure 2.7: (a) (Left): Three-dimensional stacking of Ru^{3+} (cyan spheres) honeycomb layers. Each Ru-layer is in between of two Cl-layers (red spheres). (Right): Edge-shared $\mathrm{RuCl_6}$ octahedra form the Ru honeycomb layer. (b) Local Ru^{3+} ($j = 1/2, 4d^5$) hexagon structures arising from by the edge-shared $\mathrm{RuCl_6}$ octahedra, in the layered 2D $\alpha-\mathrm{RuCl_3}$. Ru−Cl−Ru superexchange paths mimic the Kitaev interactions [14] $J_K^\gamma S_i^\gamma S_j^\gamma$ between two nearest-neighbor magnetic spins, with $\gamma\{x, y, z\}$ indicating the bond direction. Figure (a) is adapted from Ref. [97], (b) is reproduced from Ref. [98].

interactions. These interactions are described via quantum compass models, and the material has been proposed [18, 21, 22, 97, 98] as a good candidate to embody a Kitaev quantum spin liquid [14] − see Fig. 2.7(b). However, a definitive realization of a quantum spin liquid in this compound is still argument of debate and research.

The $\alpha-\mathrm{RuCl_3}$ has been under intense scrutiny regarding measurements of the longitudinal thermal conductivity [73, 74, 86]. Among them, the experiment recently carried out by Hentrich *et al.* [73] has measured an highly unusual low-temperature heat conductivity κ.

Figure 2.8(a) shows κ as a function of temperature T at zero and finite magnetic fields B, for in-plane (left panel) and out-of-plane (right panel) measurements. The heat conductivity measurements are carried out in two magnetic field regimes: for $B < B_c$ (I), and for $B > B_c$ (II) − where $B_c \sim 7\,\mathrm{T}$ is the critical field for $\alpha-\mathrm{RuCl_3}$. In (I) and (II), magnetic ordered and spin liquid phases are expected, respectively.

The two panels show similar behavior for κ independent of (B, T) − i.e., κ is *isotropic*. This suggests that the field-induced low-temperature peak in κ can be hardly attributed to gapless Kitaev spin excitations in (II). Thus, a phonon-type heat transport is proposed for this system.
Nevertheless, the magnetic excitations of $\alpha-\mathrm{RuCl_3}$ have a relevant impact on heat transport because of scattering processes with phonons. This scattering is particularly strong in (I), while it is suppressed in (II), fact that would give rise to such a large low-temperature κ.
A theoretical interpretation of these distinct behaviors for κ has been provided. In (I) residual degrees of freedom − in Ref. [73] dubbed *Kitaev-Heisenberg paramagnons* − arise because of quantum fluctuations, even though in a magnetic ordered phase. At low temperatures, these paramagnons scatter off acoustic phonons (momentum $k \sim 0$), suggesting that only small-momenta paramagnons are relevant for scattering. The enhancement of κ in (II) instead relates to the opening of a field-induced gap in the paramagnons energy spectrum. Because of this energy gap, phonons are decoupled from paramagnons, and the scattering rate becomes extremely small.

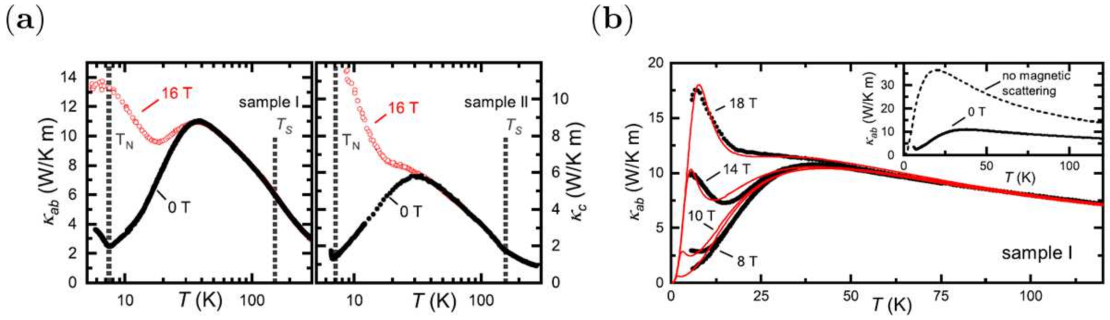

Figure 2.8: (a) Temperature dependence of heat conductivity of $\alpha-$RuCl$_3$ at finite magnetic field $B = 16\,$T (red-empty circle), and at zero field $B = 0\,$T (black-filled circle). The left (right) panel shows the in-plane κ_{ab} (out-of-plane κ_c) measurements. The magnetic ordering temperature, T_N, is displayed (black-dashed line). (b) Kinetic estimate of κ (red lines) including magnetic scattering are superimposed onto experimental data of κ_{ab} (black circles). Inset: zero-field κ_{ab} compared to the kinetic estimate of κ without magnetic scattering. Figure adapted from Ref. [73].

A kinetic estimate of κ according to (2.2) has been provided. It considers either only the phonon relaxation time τ_{ph}, or also includes a magnetic relaxation time τ_{mag}. The estimated κ are reported in Fig. 2.8(b) superimposed onto experimental data, showing the importance of magnetic excitations to explain heat transport in this material.

Another recent experiment performed by Kasahara *et al.* [75] has reported the observation of a half-integer *thermal quantum Hall effect* (TQHE) in $\alpha-$RuCl$_3$.

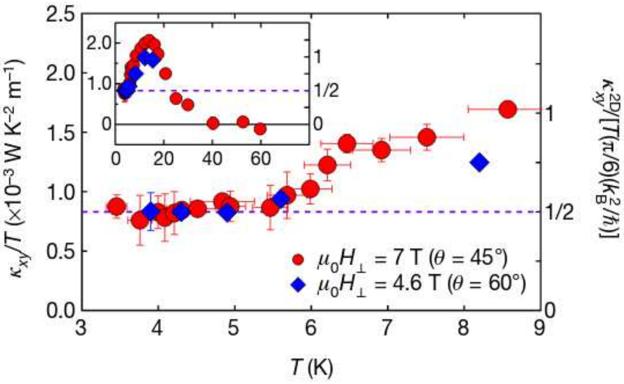

Figure 2.9: Experimental data of the thermal Hall conductivity κ_{xy}/T vs T for $\alpha-$RuCl$_3$. Two values of tilted magnetic fields with respect the plane are shown, $\theta = 45°, 60°$, for which quantized plateau are observed at low temperatures. The right-axis shows κ_{xy}/T in units of $(\pi k_B^2/6\hbar)$. Inset shows κ_{xy}/T in wider a temperature regime. Figure reproduced from Ref. [75].

This effect has been also suggested for topological superconductors and insulators [100, 101], and for certain quantum spin liquids [14, 102] under broken time-reversal symmetry. The TQHE can be related to the thermal Hall conductivity $\kappa_{xy} = \nu T(\pi k_B^2/6\hbar)$ [100] of topologically protected ballistic edge currents at finite magnetic fields. The value of ν represents a topological invariant number that can be integer or fractional. The latter relates to the

integer (fractional) nature of heat-carrying excitations.
In particular, observation of a *quantized* fractional thermal Hall conductivity would refer to topologically ordered states, having fractional excitations that obey *non-Abelian* anyonic statistics [100]. The Kitaev quantum spin liquid state speculated for $\alpha-$RuCl$_3$ implies the existence of both Abelian and non-Abelian excitations $-$ in terms of Majorana fermions [14]. At finite magnetic fields, *bulk* excitations are gapped, but chiral *gapless* Majorana edge modes flow and can carry energy at the edge of a sample.

Figure 2.9 shows the temperature dependence of κ_{xy}/T measured at finite magnetic fields for which a *small* plateau has been observed. This plateau is very narrow and limited in the temperature range, at a value of κ_{xy}/T around $(\pi k_B^2/12\hbar)$, i.e., for a half-integer $\nu = 1/2$. The latter may be a rather strong evidence for chiral non-Abelian Majorana edge modes with $\nu = 1/2$ $-$ predicted for Kitaev quantum spin liquids [14] $-$ as well as for a quantum spin liquid phase in $\alpha-$RuCl$_3$.

However, these results are still under debate due to experimental uncertainties on the observed “quantized” value of κ_{xy}. The latter remains hard to detect. In the work carried out by Kasahara *et al.* the quantized κ_{xy} is particularly limited in terms of temperatures and magnetic fields. Moreover, this first observation is not yet reproduced by any other experimental groups. Chiral magnon edge modes have been also suggested as possible explanation of the thermal Hall effect for the same material [103] which, however, would not lead to any quantization of κ_{xy}. Moreover, in a solid, the spin-phonon coupling plays a relevant role for the understanding of the thermal Hall effect $-$ aspect recently discussed in the literature [104, 105]. Thus, further investigations are required to draw definitive conclusions.

CHAPTER 3

Kitaev model

Topological order offers a new way, to see and to classify condensed matter systems, which goes beyond the order based on symmetry breaking. In this context, A. Kitaev has provided valuable contributions [13, 14] for exploring topological phases of matter. In a pioneering work in 2006, he introduced a two-dimensional (2D) quantum spin model, later called Kitaev honeycomb model [14]. The model exhibits distinct quantum spin liquid phases, with related quasiparticles that obey anyonic statistics.

These quasiparticles – or *anyons* – have unusual mutual exchange statistics [1] (neither Bose-Einstein nor Fermi-Dirac), and they can only occur in two dimensions. F. Wilczek began studying anyons [8]. He suggested a model based on $(2 + 1)$-dimensional electrodynamics. Two kinds of particles are considered: integer electric charges e and vortices v carrying magnetic flux (which is a real number defined up to an integer). The *braiding* (exchanging) of such particles along $(2 + 1)$-dimensional particle wordlines [2] leads to a nontrivial exchange phase $\theta = 2\pi ev$ [3]. Therefore, charge and vortices – when considered together – are anyons, as well as their composite objects (charge-vortex). Anyons can be *Abelian* (*non-Abelian*), depending on a one- (higher-) dimensional representation of the braid group. The braid group can be represented in terms of generators σ_i, which act on a N-particle wavefunction $\psi(r_1, \ldots, r_N)$ braiding the i^{th} particle with the $(i+1)^{\text{th}}$. Non-Abelian braiding statistics may follow for a degenerate set of g states, $\psi_\alpha(r_1, \ldots, r_N)$, with the same particle configuration, and $\alpha = 1, 2, \ldots, g$. The braiding generator σ_i is represented by a $g \times g$ matrix $\rho(\sigma_i)$, acting such that $\psi_\alpha \to \rho(\sigma_i)_{\alpha\beta}\psi_\beta$. The action of this g-dimensional operators defines unitary transformations within the subspace of degenerate states. Since $\rho(\sigma_1)\rho(\sigma_2) \neq \rho(\sigma_2)\rho(\sigma_1)$ do not necessarily commute – just as matrix multiplication does not – the particles obey non-Abelian statistics, which may cause not just a trivial phase change of ψ_α. Without degeneracy, the subspace is one-dimensional, and then all transformations commute – because they are just multiplications by a phase factor. The latter case describes Abelian braiding statistics [4] [8, 9, 14]. One important fact is that anyons exist as excitations in some condensed matter systems, as for instance in the aforementioned quantum spin liquids, but also in other topologically ordered states, e.g., the Laughlin state [108] in a fractional quantum Hall system at filling factor $\nu = 1/3$ – which carries Abelian anyons with $\theta = \pi/3$ and $e = \pm 1/3$. The concept of anyons implies that the underlying state has an energy gap (at least for topolog-

---

[1] Meaning that under quasiparticle exchange, $|\psi_{1,2}\rangle = e^{i\theta}|\psi_{2,1}\rangle$, with $\theta \in [0, \pi]$.

[2] A worldline is a time-like curve in spacetime. Each point of a worldline is an event that can be labeled with the time and the spatial position of the object at that time.

[3] The exchange phase θ has to be a rational multiple of 2π.

[4] I would refer to Refs. [106, 107] for a pedagogical review on anyons and their classification.

ically nontrivial quasiparticles). This because braiding may not be defined if excitations are not localizable.
As introduced in Chapter 1, anyons play an important role in the definition of logic processes in the context of topological quantum computation [12], where their related topologically ordered states are referred to as qubits.

In this chapter, I will present the 2D Kitaev model on the honeycomb lattice. For this purpose, it is instructive to briefly introduce another spin model, namely the 2D toric code [13], because some properties and physics of the toric code can be related to a limit case of the Kitaev model. The 2D Kitaev honeycomb model is exactly solvable, and the solution is obtained via a reduction to free real fermions [14], i.e., *Majorana* fermions [109]. I will present this solution and its related properties. To conclude, I will show another fermionization procedure able to solve the model which has been used in this work.

3.1 The two-dimensional toric code

The toric code (TC) [13] is an exactly solvable spin-1/2 model, typically defined on a 2D square lattice. Placing spins on the edges of a square lattice, the Hamiltonian reads

$$\mathcal{H}_{\mathrm{TC}} = -J_e \sum_s A_s - J_m \sum_p B_p \,, \tag{3.1}$$

where the star operator $A_s = \prod_{i\,\in\,\mathrm{star}\,(s)} \sigma_i^x$ couples the σ^x-component of all spins adjacent to a vertex s, and the plaquette operator $B_p = \prod_{i\,\in\,\partial p} \sigma_i^z$ couples the σ^z-component of all spins surrounding a plaquette p – as shown in Fig. 3.1(a). Operators in (3.1) are Hermitian and have eigenvalues ±1. Since any given pair of vertex and plaquette operators either share 0 or 2 bonds, A_s and B_p commute with one another, and thus the model can be solved exactly. Therefore, common sets of eigenstates $|\Psi\rangle$ for both A_s and B_p can be constructed. The ground state is returned by the so called "stabilizer conditions", $A_s|\Psi\rangle = B_p|\Psi\rangle = |\Psi\rangle \;\forall\, s, p$, with a ground-state energy $E_0 = -N(J_e + J_m)$, and N the number of lattice sites.

Embedding the model with periodic boundary conditions onto a *torus*, the sign of a vertex (plaquette) can only be flipped on an *even* number of vortices (plaquettes). This fact implies two overall constraints, i.e., $\prod_s A_s = \prod_p B_p = +1$, from which one can deduce the ground-state *degeneracy* on a torus. The total Hilbert space has 2^{2N} states, but due to the aforementioned constraints there are only $2N - 2$ independent choices of operators in (3.1). Thus, one has $2^{2N}/2^{2N-2} = 4$ ground states on a torus. This degeneracy can be also deduced using different arguments. Indeed, one may construct the ground-state wavefunction solving (3.1) in the σ^z basis states, that can be related to classical variables $z_i = \pm 1$. For each classical spin configuration $\mathbf{s} = \{z_i\}_{i=1}^{2N}$ it is possible to define a plaquette flux operator as

$$w_p(\mathbf{s}) = \prod_{i \in \partial p} z_i \,, \tag{3.2}$$

where $w_p = -1$ relates to a *vortex* on plaquette p. The stabilizer condition in a ground state $|\Psi_0\rangle$ of the TC implies no vortices, thus

$$|\Psi_0\rangle = \sum_{\{\mathbf{s}\,:\,w_p(\mathbf{s})=+1\,\forall p\}} \alpha_{\mathbf{s}} |\mathbf{s}\rangle \,. \tag{3.3}$$

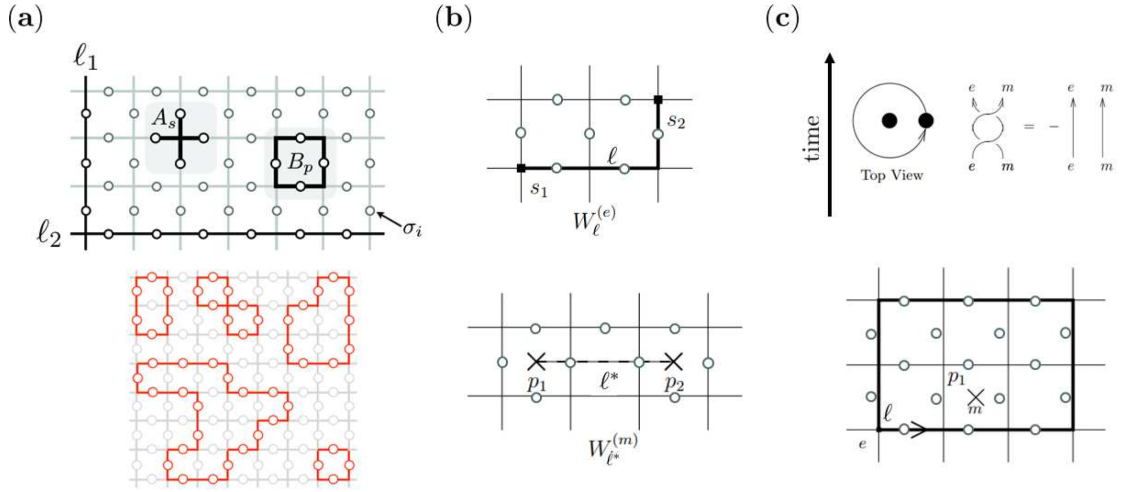

Figure 3.1: (a) The 2D toric code model. Spins-$\frac{1}{2}$ σ_i live on the edges of the square lattice. Spins adjacent to a star operator A_s and to a plaquette operator B_p are shown. Winding cycles on a torus $\ell_{1,2}$ are shown as well. Example of a loop gas (red line, edge spins $\sigma_i^z = -1$) is also displayed. (b) Excitations e (m) lying at the end of strings ℓ (ℓ^*) related to path operators $W_\ell^{(e)}$ $\left(W_{\ell^*}^{(m)}\right)$. (c) Full rotation of e around a magnetic charge m at p_1. Braiding operation leads to a nontrivial phase factor. Figure (a) is adapted from Castelnovo *et al.* in Ref. [110] and from Ref. [111]. Figures (b,c) are adapted from Ref. [10].

The group of star operators acts on $|\mathbf{s}\rangle$ by flipping spins. But the stabilizer condition holds if and only if all coefficients $\alpha_\mathbf{s}$ are equal for each *path* of the action of A_s. In view of this, the ground state – which is referred to as *quantum loop gas* – is a *resonant* superposition of vortex-free spin configurations (loops) – see Fig. 3.1(a). One can show the *four-fold* ground-state degeneracy on a torus by considering Wilson loop-like operators,

$$w_\ell(\mathbf{s}) = \prod_{i\in\ell} z_i. \tag{3.4}$$

When the loop ℓ is a *contractible* [5] loop, then the flux in (3.4) is given by the product of the plaquette fluxes w_p of (3.2) within the loop [6], and for each ground state $w_\ell = +1$. While if ℓ is one of the two nontrivial independent cycles on the square lattice wrapping the torus – which cannot be contracted – then $w_\ell(\mathbf{s}) = \pm 1 = (-1)^n$ relates to conserved winding number parity, with n the number of loop-bonds crossed by ℓ. Indeed, the latter remains preserved by any given A_s overlapping with ℓ, since the star operator overlaps it on 0 or 2 bonds. The two independent essential loops ℓ_1, ℓ_2 – shown in Fig. 3.1(a) – lead to four distinct *topological sectors* that give rise to four-fold degenerate ground states, labeled by $w_{\ell_1}(\mathbf{s}) = \pm 1$ and $w_{\ell_2}(\mathbf{s}) = \pm 1$. On a general manifold, one finds that the degeneracy increases as 2^{2g}, where g is the genus of the manifold.

Excitations in the TC model arise from violating one of the stabilizer conditions for the ground state. These excitations come in two varieties: *electric charges* e and *magnetic vortices* m of a $\mathbb{Z}_2$ gauge theory [7] [112] . To visualize these excitations, one can construct two

---

[5] If there exist a homotopy of a loop into a point, then the loop is said contractible.

[6] Reminiscent of Stokes' theorem.

[7] The TC can be seen as an Ising gauge theory. Degrees of freedom located on the edges of the lattice correspond to $\mathbb{Z}_2$ valued gauge potentials. Star operators A_s are gauge transformations, and

path operators for open loops,

$$W_\ell^{(e)} = \prod_{i\in\ell} \sigma_i^z \ , \quad W_{\ell^*}^{(m)} = \prod_{i\in\ell^*} \sigma_i^x \ . \tag{3.5}$$

In (3.5) ℓ (ℓ^*) indicates the path going from s_1 to s_2 (p_1 to p_2 on the dual lattice) – see Fig. 3.1(b). $W_\ell^{(e)}$ commutes with B_p's and A_s's – except for the end-string points s_1, s_2 where $W_\ell^{(e)}$ and $A_{s_{1,2}}$ anticommute. While, $W_{\ell^*}^{(m)}$ commutes with A_s's and B_p's – except for the end-string points p_1, p_2 where $W_{\ell^*}^{(m)}$ and $B_{p_{1,2}}$ anticommute. Thus, the state $|\Psi_{s_1,s_2(p_1,p_2)}\rangle = W_{\ell(\ell^*)}|\Psi\rangle$ is an eigenstate of the Hamiltonian with a pair of electric charges (magnetic vortices) located at s_1, s_2 (p_1, p_2) which energy cost is $4J_e$ ($4J_m$). While single e and m are *bosons* (considering the exchange among same particle type), it is possible to show that composite $e-m$ particles are *fermions* [10]. Even more, the *braiding* of e around m, in a full rotation (two exchanges) – see Fig. 3.1(c) – yields a phase of -1. Indeed, assuming $|\xi\rangle$ to be a state containing a vortex at p_1, the braiding operation is described by $W_\ell^{(e)}|\xi\rangle = \big(\prod_{i\in\ell}\sigma_i^z\big)|\xi\rangle = \big(\prod_{p\in\partial\ell}B_p\big)|\xi\rangle = B_{p_1}|\xi\rangle = -|\xi\rangle$ – accordingly to (3.5) and (3.4). This result is not consistent with either bosonic or fermionic statistics. In particular, excitations are *Abelian anyons.*
To conclude, the TC is one of the simplest quantum models leading to a topologically ordered quantum state. Topological order gives rise to a robust ground-state degeneracy, and massive, deconfined quasiparticles showing mutual anyonic statistics .

3.2 The two-dimensional honeycomb model

The two-dimensional Kitaev honeycomb (2D-KH) model [14] is an exactly solvable spin-1/2 model constructed on a 2D honeycomb lattice. It stands out as one of the few models in which a $\mathbb{Z}_2$ quantum spin liquid can be exactly shown to exist. The Hamiltonian is described in terms of *two*-body interactions, rather than *four*-body interactions as for the discussed $\mathbb{Z}_2$ toric code (TC). This latter fact favors the experimental synthesis of the 2D-KH model with respect to the TC, since a four-body interaction is harder to realize [8]. Possible experimental realizations of 2D-KH physics have been suggested in strong spin-orbit coupled compounds, usually dubbed *Kitaev materials* [28, 29]. In the following, I will show that the 2D-KH model exhibits *gapped* phases that are perturbatively related to the TC. Moreover, under time-reversal symmetry breaking, a new topological phase arises with distinct topological properties, and *non-Abelian* anyons.

The spin Hamiltonian introduced by A. Kitaev [14] reads

$$\mathcal{H} = -J_x \sum_{x\text{-bonds}} \sigma_i^x\sigma_j^x - J_y \sum_{y\text{-bonds}} \sigma_i^y\sigma_j^y - J_z \sum_{z\text{-bonds}} \sigma_i^z\sigma_j^z \ . \tag{3.6}$$

The degrees of freedom are localized spin-1/2 that live on the vertices of a bipartite honeycomb lattice. They interact via *bond*-dependent nearest-neighbor exchange interactions. In other words, the exchange coupling terms, J_{λ_i}, couple specific Pauli vector components, $\sigma_i^{\lambda_i}$, depending on the bond directions $\lambda_i = x, y, z$ – see Fig. 3.2(a). The model is clearly *frustrated* due to anisotropic exchange interactions in (3.6).

---

their commutation with the plaquette operators B_p leads to an overall gauge invariance.

[8] $\mathbb{Z}_2$-TC commonly discussed experimental setups involve polar molecules [113], optical lattices [114], and Josephson-junction arrays [115].

Kitaev provided an exact solution of the model based on an extensive number of integrals of motion, i.e., conserved plaquette operators

$$\hat{w}_p = \prod_{i\,\in\,\partial p} \sigma_i^{\lambda_i} = \sigma_1^y \sigma_2^z \sigma_3^x \sigma_4^y \sigma_5^z \sigma_6^x\,. \tag{3.7}$$

Let us consider a lattice with $2N$ sites, i.e., N unit cells. In (3.7) p refers to one of the N hexagonal plaquettes on the lattice. The plaquette operator $\hat{w}_p$ is defined as the product of the six spins on the plaquette's vertices. Since $\hat{w}_p^2 = 1$, it has eigenvalues ± 1. Its eigenvalues can be physically interpreted as the *magnetic flux* through the plaquette p. If $w_p = -1$ then the plaquette carries a *vortex* – somewhat reminiscent of equation (3.2). It is possible to show that operators $\hat{w}_p$ commute with $\mathcal{H}$, and also that different operators $\hat{w}_p$ commute with each other. In particular, $N-1$ conserved quantities exist [9], and thus common eigenstates $|\xi\rangle$ of $\mathcal{H}$ and $\hat{w}_p$ can be found. In view of this, one can divide the total Hilbert space $\mathfrak{L}$ into eigenspaces of $\hat{w}_p$, or *sectors*, as

$$\mathfrak{L} = \bigoplus_{w_1,\ldots,w_N} \mathfrak{L}_{w_1,\ldots,w_N} \quad \text{where} \quad |\xi\rangle \in \mathfrak{L}_w \iff \hat{w}_p|\xi\rangle = w_p|\xi\rangle \;\forall\, p\,, \tag{3.8}$$

with N the number of plaquettes. Each sector $\mathfrak{L}_{w_1,\ldots,w_N}$ in (3.8) relates to a choice of $w_p = \pm 1$ for each plaquette p. Therefore, one can solve for the eigenvalues of the Hamiltonian restricted to a particular sector $\mathfrak{L}_{w_1,\ldots,w_N}$. The total Hilbert space has 2^{2N} states, and since one has $N-1$ independent vortex sectors, it follows that the dimension of each sector is 2^{N+1}. Thus, splitting into sectors does not solve the problem yet, since it is still exponentially hard. However, it turns out that the spin Hamiltonian can be mapped onto a *real* Majorana fermion Hamiltonian. I will focus on such a mapping and on the related solution of the Hamiltonian in the next section.

3.3 Majorana representation

It is worth recalling what Majorana fermions are and how do they enter in the fermionic representation of spin degrees of freedom.

Introduced by Ettore Majorana in 1937 [109], they are particles that are their own antiparticles. In the second quantization language, this points out that creation and annihilation of Majorana fermions should be operated by the same operator, $\gamma_i^\dagger = \gamma_i$, from which follows $\gamma_i^2 = 1$, and the anticommutation relation $\{\gamma_i, \gamma_j\} = 2\delta_{ij}$. Each *complex* fermionic mode $d^{(\dagger)}$, can be thought as "composed" by two *real* Majorana fermions,

$$d = \frac{\gamma_1 + i\gamma_2}{2}\;,\; d^\dagger = \frac{\gamma_1 - i\gamma_2}{2}. \tag{3.9}$$

To solve the model, one may consider to represent the Pauli operators in (3.6) via some operators $\tilde{\sigma}^x, \tilde{\sigma}^y, \tilde{\sigma}^z$. These latter can be constructed via a collection of four Majorana operators, c, b^x, b^y, and b^z – see Fig. 3.3(a) – that act on a 4-dimensional Fock space $\mathfrak{F}$, and read as

$$\tilde{\sigma}^x = i b^x c\,, \tag{3.10a}$$

$$\tilde{\sigma}^y = i b^y c\,, \tag{3.10b}$$

$$\tilde{\sigma}^z = i b^z c\,. \tag{3.10c}$$

---

[9] In systems with periodic boundary conditions – of interest to this work – fluxes can only be created in pairs, hence the constraint $\prod_p w_p = 1$, from which only $N-1$ independent w_p follow.

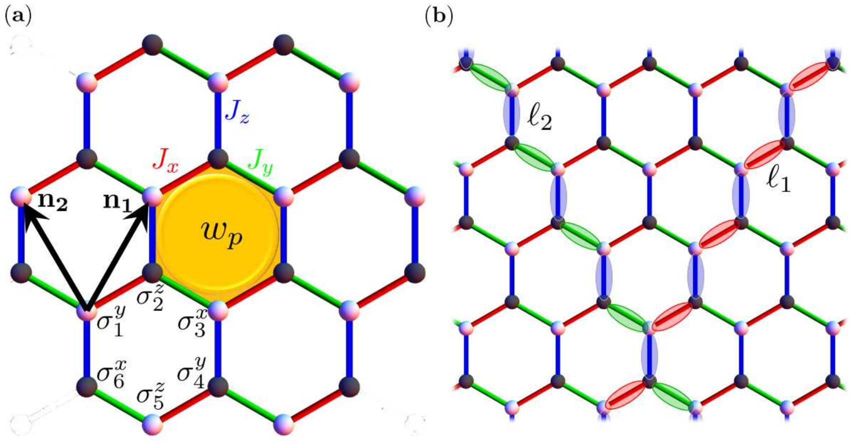

Figure 3.2: (a) The Kitaev model on the two-dimensional honeycomb lattice. The bond-directional dependent exchange interactions, J_x, J_y, and J_z, connect the two sublattices (light and dark bullets). Unit vectors are $\mathbf{n_1}$ and $\mathbf{n_2}$. Spins $\sigma_i^{\lambda_i}$ – with $\lambda_i = x, y, z$ – belonging to the same plaquette define the related plaquette operator $\hat{w}_p$ (yellowish hexagon). (b) Nontrivial loops ℓ_1 and ℓ_2 wrapping the torus which the model with boundary conditions is embedded onto.

Adopting this new representation causes an *enlargement* of the Hilbert space. Note that the Hilbert space of the spins is a 2-dimensional subspace $\mathfrak{L} \subset \mathfrak{F}$. A proper representation of spins in terms of Majorana fermions requires a restriction to the subspace $\mathfrak{L}$. This subspace is identified by states $|\xi\rangle$ that satisfy the constraint

$$|\xi\rangle \in \mathfrak{L} \qquad \Longleftrightarrow \qquad D|\xi\rangle = |\xi\rangle\,, \quad \text{where } D = -i\sigma^x\sigma^y\sigma^z = 1\,. \tag{3.11}$$

One may call $\mathfrak{L}$ and $\mathfrak{F}$ the *physical subspace* and the *extended space*, respectively. In the Majorana language, the operator D in (3.11) reads as $D = b^x b^y b^z c$, and can have eigenvalues ± 1. But the restriction to a physical eigenstate $|\xi\rangle$ imposes $D|\xi\rangle = |\xi\rangle$ as in (3.11). All the other eigenstates are unphysical [10] and must be discarded. Within $\mathfrak{L}$, the set of operators $\tilde{\sigma}^\lambda$ in (3.10) acts as σ^λ acts on spins, by enforcing the constraint of (3.11). In particular, two conditions need to be fulfilled for a proper representation:

(1) $\tilde{\sigma}^\lambda$ preserves the subspace $\mathfrak{L}$, which follows from $\left[\tilde{\sigma}^\lambda, D\right] = 0$.

(2) If restricted to $\mathfrak{L}$, $\tilde{\sigma}^\lambda$ obey the same algebraic relations as σ^λ, which is verified since $(\tilde{\sigma}^\lambda)^\dagger = \tilde{\sigma}^\lambda$, $(\tilde{\sigma}^\lambda)^2 = 1$, and $\tilde{\sigma}^x\tilde{\sigma}^y\tilde{\sigma}^z = (ib^x c)(ib^y c)(ib^z c) = ib^x b^y b^z c^3 = iD = i$.

3.3.1 Solving the model using Majoranas

The spin Hamiltonian $\mathcal{H}\{\sigma_j^{\lambda_j}\}$ in (3.6) can be written as a fermionic Hamiltonian $\tilde{\mathcal{H}}\{b_j^{\lambda_j}, c_j\} = \mathcal{H}\{\tilde{\sigma}_j^{\lambda_j}\}$ which is restricted to the physical subspace by the condition in (3.11), i.e., $D = D_j = b_j^x b_j^y b_j^z c_j$ for $j = 1, \ldots, 2N$. In the Majorana representation the Hamiltonian in (3.6) reads as

$$\tilde{\mathcal{H}} = \frac{i}{4}\sum_{\langle j,k\rangle} \hat{A}_{jk} c_j c_k \;\text{ where }\; \hat{A}_{jk} = \begin{cases} 2J_{\lambda_{jk}}\hat{\eta}_{jk} \;\Leftarrow (j,k) \\ 0 \quad \text{otherwise} \end{cases} \;\text{ with }\; \hat{\eta}_{jk} = i b_j^{\lambda_{jk}} b_k^{\lambda_{jk}}, \tag{3.12}$$

---

[10] The unphysical states belong to the extended Fock space $\mathfrak{F}$, but not to the physical subspace $\mathfrak{L}$.

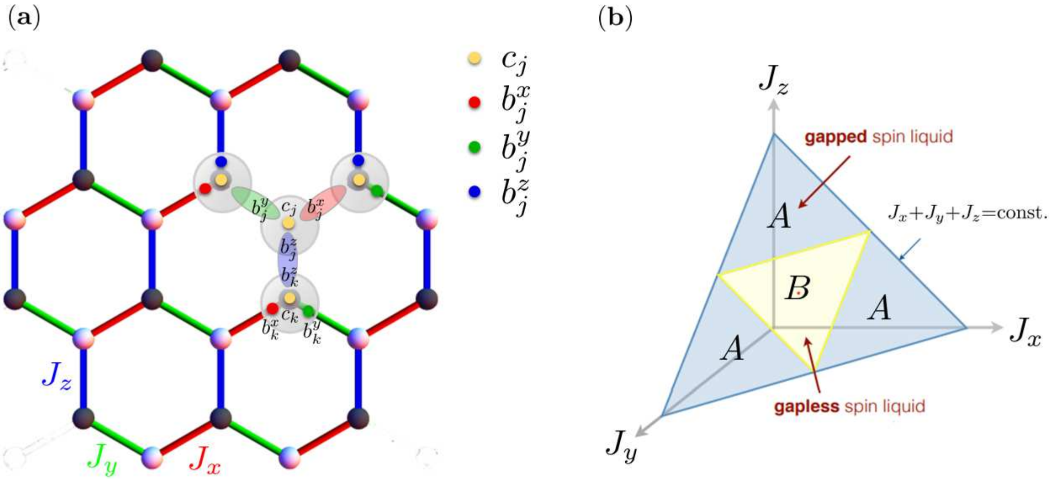

Figure 3.3: (a) Illustration of the 2D-KH model with the introduction of Majorana flavors c_j, b_j^x, b_j^y, b_j^z. Each grey bubble refers to a single spin σ_j. The static $\mathbb{Z}_2$ gauge fields are given by recombining bond-Majoranas, depicted as colored ellipsis. (b) Phase diagram of the model in the vortex-free sector, with $J_x + J_y + J_z = \text{const.}$. The gapped (gapless) spin liquid phases are shown as blue (yellow) shaded zones. Figure (b) is adapted from Ref. [28].

where $\lambda_{jk} = x, y, z$ indicates the direction of the (j,k) bond, as in Fig. 3.3. The Hamiltonian in (3.12) has a quartic form, because $\hat{A}_{jk}$ is not a simple matrix, but rather it is an operator depending on $\hat{\eta}_{jk}$. Fortunately, these bilinear operators commute with each other and with $\tilde{\mathcal{H}}$. Therefore, one can decompose the Fock space into common eigenspaces of $\hat{\eta}_{jk}$, which are labeled by its eigenvalues $\eta_{jk} = \pm 1$,

$$\mathfrak{F} = \bigoplus_{\eta} \mathfrak{F}_\eta \quad \text{where} \quad |\Psi\rangle \in \mathfrak{F}_\eta \iff \hat{\eta}_{jk}|\Psi\rangle = \eta_{jk}|\Psi\rangle \ \forall\, j,k\,. \tag{3.13}$$

Restriction of $\tilde{\mathcal{H}}$ in (3.12) to $\mathfrak{F}_\eta$ is obtained by replacing operators $\hat{\eta}_{jk}$ in favor of valued $\mathbb{Z}_2$ gauge fields $\eta_{jk} = \pm 1$. Thus, one can solve within each subspace $\mathfrak{F}_\eta$ the quadratic Hamiltonian

$$\tilde{\mathcal{H}}_{\{\eta\}} = \frac{i}{4} \sum_{\langle j,k \rangle} A_{jk} c_j c_k \quad \text{with} \quad A_{jk} = 2 J_{\lambda_{jk}} \eta_{jk}\ , \tag{3.14}$$

which now relates to a *free Majorana fermions* problem with static gauge fields. Decomposition in (3.13) has been similarly done as in (3.8) where the physical space $\mathfrak{L}$ is split into eigenspaces labeled by the eigenvalues of the plaquette operators, $w_p = \pm 1$. These two decompositions relate one to another by expressing operators $\hat{w}_p$ in terms of Majorana fermions, and noting that within the physical space $\mathfrak{L}$

$$\hat{w}_p = \prod_{\langle j,k \rangle \,\in\, \partial p} \hat{\eta}_{jk}. \tag{3.15}$$

From (3.15) thus follows that each eigenspace $\mathfrak{L}_w$ in (3.8) reads as

$$\mathfrak{L}_w = \prod_{\mathfrak{L}} \mathfrak{F}_\eta\,, \quad \text{where} \quad w_p = \prod_{\langle j,k \rangle \,\in\, \partial p} \eta_{jk}. \tag{3.16}$$

The *ground state* of the 2D-KH model can be found then via the following procedure:

(1) Fix a value of $w_p = \pm 1$ for all plaquettes.

(2) Step (1) implies to find η_{jk} which satisfy w_p in (3.16), taking care of the direction-dependence on the bond, since $\eta_{jk} = -\eta_{kj}$.

(3) Solve the quadratic Hamiltonian in (3.14) to find the energy spectrum $E[w(\eta)]$. However, the corresponding state $|\Psi_\eta\rangle$ is not gauge invariant since it belongs to $\mathfrak{F}_\eta$. Thus, to obtain the corresponding physical state one needs to symmetrize over all gauge transformations [11], by means of a projection of $|\Psi_\eta\rangle$ onto the physical space,

$$|\Psi_w\rangle = \prod_{j=1}^{2N} \underbrace{\left(\frac{1+D_j}{2}\right)}_{\equiv P_j} |\Psi_\eta\rangle \ \in \ \mathfrak{L}\,, \tag{3.17}$$

where P_j is the projector operator.

(4) Repeat the previous steps for all w_p and pick up the w_p-configuration which minimizes the energy $E[w(\eta)]$.

In particular, the energy minimum follows from a *vortex-free* field configuration, i.e., $w_p = 1$ for all plaquettes p [12] . It represents the ground state over all the vortex sectors. Its energy spectrum and its related phase diagram – shown in Fig. 3.3(b) – can be found analytically. Moreover, the ground state is topologically degenerate – similarly as in the TC. The ground state of the model with boundary conditions embedded onto a torus is four-fold degenerate. To visualize it, one may consider the two loops wrapping the torus in ℓ_1 and ℓ_2 directions – as shown in Fig. 3.2(b). Thus, one can construct *fermionic path operators* according to (3.7) in terms of spins or in terms of Majorana fermions as

$$\hat{w}_\ell(i_0,\ldots,i_n) = \sigma_{i_0}^{\lambda_{i_0}} \sigma_{i_1}^{\lambda_{i_1}} \cdots \sigma_{i_{n-1}}^{\lambda_{i_{n-1}}} \sigma_{i_n}^{\lambda_{i_n}} = \left(\prod_{i=1}^{n} -i\hat{\eta}_{i,i-1}\right) c_0 c_n\,, \tag{3.18}$$

where if $i_0 = i_n$ (closed loops $\ell_{1,2}$), c_0 and c_n cancel each other, leading to two Wilson loops, $\hat{w}_{\ell_1}$ and $\hat{w}_{\ell_2}$. These operators commute with the Hamiltonian in (3.6) as $\hat{w}_p$ in (3.7) do. Their eigenvalues can be ± 1 depending on the sign of the bond gauge variables η_{jk}. Physically, one may flip a chain of bonds – e.g., along ℓ_1. This *global* operation amounts to the creation of a pair of vortices ($w_p = -1$), with one of the two vortices winding around the torus before being annihilated with its partner. Because of such a process, there is a *flux* through one of the torus holes, which is measured by $w_{\ell_1} = \pm 1$. The topological character arises because gauge field configurations which correspond to the same vortex configuration are not related to each other by *local* gauge transformations $\eta_{jk} \to -\eta_{jk}$. Therefore, the four distinct topological sectors – labeled by $\{w_{\ell_1}, w_{\ell_2}\}$ – lead to four-fold degenerate ground states.

3.3.2 Vortex-free state spectrum

The energy spectrum is given by the eigenvalues of the matrix iA_{jk} in (3.14) for $w_p = 1\ \forall\, p$, which stands for the vortex-free configuration. One choice to be in the vortex-free state is

---

[11] The operator D_j can be seen as a *gauge transformation* for the $\mathbb{Z}_2$ group. Applying D_j to $|\Psi_\eta\rangle$ changes the values of η_{jk} on the bonds connecting j with three nearest vertices k, which however does not change the vortex sector, i.e., $|\Psi_w\rangle \ \in \ \mathfrak{L}$.

[12] Reminiscent of the stabilizer condition found for the TC ground state.

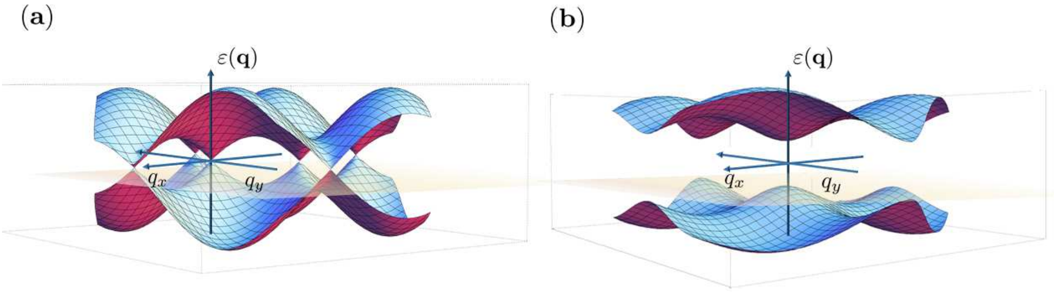

Figure 3.4: Vortex-free energy spectrum $\varepsilon(\mathbf{q}) = \pm|f(\mathbf{q})|$ (a) for the isotropic point in phase B, and (b) in the gapped phase A_z for $J_x = J_y = 0.5$, and $J_z = 2$.

given by $\eta_{jk} = 1$ for all bonds (j, k), with $j(k) \in$ even (odd) sublattice. Within the vortex-free state, the Hamiltonian is translational invariant. This means that the energy spectrum can be found analytically via Fourier transformation of (3.14),

$$c_{\mathbf{q},\mu} = \frac{1}{\sqrt{2N}} \sum_{\mathbf{r}} e^{-i(\mathbf{qr})} c_{\mathbf{r},\mu} \quad \Longrightarrow \quad i\tilde{A}(\mathbf{q}) = \begin{pmatrix} 0 & if(\mathbf{q}) \\ -if(\mathbf{q})^* & 0 \end{pmatrix}. \tag{3.19}$$

In (3.19) the index μ refer to the position of the site on the bipartite lattice, where $\mathbf{r}$ is the location of the unit cell. The 2×2 matrix $\tilde{A}$ is the Fourier transform of the related matrix in (3.14). The function $f(\mathbf{q}) = 2\big(J_x e^{i(\mathbf{qn_1})} + J_y e^{i(\mathbf{qn_2})} + J_z\big)$, with $\mathbf{n_1} = (\frac{1}{2}, \frac{\sqrt{3}}{2})$ and $\mathbf{n_2} = (-\frac{1}{2}, \frac{\sqrt{3}}{2})$ that represent the unit cell vectors chosen as in Fig. 3.2(a). One may introduce *complex* fermions $d_{\mathbf{q}} = \frac{1}{2}(c_{\mathbf{q},\mu} + ic_{\mathbf{q},\nu})$ according to (3.9). Substituting them to $c_{\mathbf{q},\mu}$ in (3.19), the Hamiltonian follows as

$$\tilde{\mathcal{H}}_{\{\eta=1\}} = \frac{1}{2} \sum_{\mathbf{q}} \begin{pmatrix} d^\dagger_{\mathbf{q}} d_{-\mathbf{q}} \end{pmatrix} \begin{pmatrix} e_{\mathbf{q}} & \Delta_{\mathbf{q}} \\ \Delta^*_{-\mathbf{q}} & -e_{-\mathbf{q}} \end{pmatrix} \begin{pmatrix} d_{\mathbf{q}} \\ d^\dagger_{-\mathbf{q}} \end{pmatrix}. \tag{3.20}$$

The Hamiltonian in (3.20) has the form of a BCS Hamiltonian for superconductors, with $\Delta_{\mathbf{q}} = i\,\mathbb{I}\mathrm{m}\, f(\mathbf{q})$, and $e_{\mathbf{q}} = \mathbb{R}\mathrm{e}\, f(\mathbf{q})$. To diagonalize (3.20), one can perform a Bogoliubov transformation – see further details on the transformation in the Appendix A.1. The transformation introduces a set of quasiparticles given by a superposition of creation and annihilation operators, i.e., $d_{\mathbf{q}} = \big(\cos(\phi_{\mathbf{q}})d'_{\mathbf{q}} + \sin(\phi_{\mathbf{q}})d'^{\dagger}_{-\mathbf{q}}\big)$ and $d^\dagger_{-\mathbf{q}} = \big(\sin(\phi_{\mathbf{q}})d'_{\mathbf{q}} - \cos(\phi_{\mathbf{q}})d'^{\dagger}_{-\mathbf{q}}\big)$, with $\tan(2\phi_{\mathbf{q}}) = \mathbb{I}\mathrm{m}\, f(\mathbf{q}) / \mathbb{R}\mathrm{e}\, f(\mathbf{q})$. The diagonalized Hamiltonian reads

$$\tilde{\mathcal{H}}_{\{\eta=1\}} = \sum_{\mathbf{q}} |f(\mathbf{q})| \Big(2d'^{\dagger}_{\mathbf{q}} d'_{\mathbf{q}} - 1\Big). \tag{3.21}$$

The energy spectrum $\varepsilon(\mathbf{q}) = \pm|f(\mathbf{q})|$ is shown in Fig. 3.4. The ground state energy is thus given by $E_0 = -\sum_{\mathbf{q}} |f(\mathbf{q})|$, while the *matter fermion* excitations have energy $E(\mathbf{q}) = 2|f(\mathbf{q})|$. The other kind of excitations are vortices, which have a finite energy gap Δ_w . The latter is the energy difference of a state with and without a vortex pair. The spectrum is either *gapless* – i.e., $f(\mathbf{q})$ is zero for some $\mathbf{q}^*$ – or *gapped*, depending on the anisotropy of the exchange couplings. The function $f(\mathbf{q})$ is zero if and only if the exchange couplings fulfill triangle inequalities [13], which mark the regions in the phase diagram of Fig. 3.3(b), i.e., the B gapless phase and three distinct A gapped phases. A special point in the phase B at $J_x = J_y = J_z$ (isotropic point) has two zeros which correspond to Dirac points, which merge and disappear at the transition to phases A.

---

[13] So that, $|J_x| \leq |J_y| + |J_z|$, $|J_y| \leq |J_x| + |J_z|$, and $|J_z| \leq |J_x| + |J_y|$ – see more in Ref. [14].

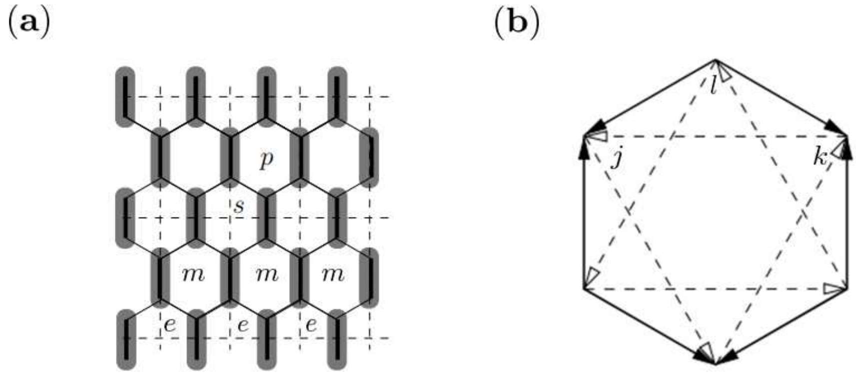

Figure 3.5: (a) Dimers (dark ovals) on z-bonds of the 2D-KH lying on the edges (dashed) of a square lattice (SL). Plaquettes of the 2D-KH on alternate rows relate to *stars* (s) and *plaquettes* (p) of the SL. (b) Scheme of the chiral interaction matrix in equation (3.24). Figures are adapted from Ref. [10].

3.3.3 Gapped phase A

In the gapped phase A, two quasiparticle types exist: gapped fermions and $\mathbb{Z}_2$ vortices ($w_p = -1$), the latter related to the $\mathbb{Z}_2$ gauge fields $\eta_{jk\in\partial p}$. When a fermion *braids* around a vortex, the related quantum state acquires a phase -1. This fact – as introduced in Sec. 3.1 – refers to quasiparticles called *Abelian anyons*. It turns out that there exists another type of anyon, which is a second type of vortex, degenerate with the first type, but distinct from it. To visualize it, one may consider (3.6) in the phase A_z [14] as $\mathcal{H} = \mathcal{H}_0 + V$, with $\mathcal{H}_0$ containing the z-bonds terms, whereas V contains x- and y-bonds terms. In the limit of $V = 0$, i.e., $J_{x,y} = 0$, $J_z > 0$ the system consists of a set of dimers, with a highly degenerate ground state, i.e., each two spins on z-bonds are aligned as effective spins $|\Uparrow\rangle = |\uparrow\uparrow\rangle$ or $|\Downarrow\rangle = |\downarrow\downarrow\rangle$ – as shown in Fig. 3.5(a). If one considers a small perturbation V, i.e., $J_x, J_y \ll J_z$, an effective Hamiltonian acting in the space of the effective spins can be obtained using *perturbation theory.* At 4th order of perturbation [15],

$$\mathcal{H}_{\text{eff}}^{(4)} = -\frac{J_x^2 J_y^2}{16|J_z|^3}\sum_p Q_p\,, \quad \text{with} \quad Q_p = \sigma^y_{\text{left}(p)}\sigma^y_{\text{right}(p)}\sigma^z_{\text{up}(p)}\sigma^z_{\text{down}(p)} = \left(\hat{w}_p\right)_{\text{eff}}\,, \tag{3.22}$$

where p runs over the plaquettes of the effective spin lattice – see Fig. 3.5(a), and Q_p is the plaquette operator acting on the effective spin space. It is possible to show that (3.22) can be mapped onto the TC Hamiltonian in (3.1), where the plaquettes of the effective spin lattice reduce to plaquettes p and vertices s of the TC lattice (square lattice with dashed lines in Fig. 3.5(a)). Therefore, *two* distinct kinds of vortices arise – analogously to electric charges e and magnetic charges m in the TC – living on *even* and *odd* rows of the honeycomb lattice. The set of quasiparticles is completed by fermions which, however, differ in energy from composite e–m fermions [16].

---

[14] This occurs when $|J_z| \gg |J_x| + |J_y|$.

[15] The 4th order refers to the first not constant term. I would refer for further details and explicit calculations to Ref. [14].

[16] The energy of a fermion is $\sim 2|J_z|$, while e–m composite fermions have an energy $\sim 4J_{\text{eff}}$.

3.3.4 Gapless phase B

Differently from phase A, phase B involves gapless fermions, and only one type of vortices with undefined statistics. To get a well-defined excitations statistics, the opening of a gap is required. In particular, one may open it under time-reversal symmetry (TRS) breaking, for instance by applying an external magnetic field $\mathbf{h} = (h_x, h_y, h_z)$. One can treat the problem by using perturbation theory, adding a perturbation $V = -\sum_j \left(h_x\sigma_j^x + h_y\sigma_j^y + h_z\sigma_j^z\right)$ to (3.6). Assuming for simplicity the isotropic point in the phase B, one may construct an effective Hamiltonian acting on the vortex-free state. The first nontrivial perturbative order breaking TRS is the 3$^{\text{rd}}$,

$$\mathcal{H}_{\text{eff}}^{(3)} \sim \frac{h_x h_y h_z}{J^2} \sum_{j,k,l} \sigma_j^x \sigma_k^y \sigma_l^z = iK \sum_{\langle\langle j,k \rangle\rangle} c_j c_k \quad \text{with} \quad K \sim \frac{h_x h_y h_z}{J^2}\,, \tag{3.23}$$

and

$$\mathcal{H}_{\text{eff}} = \frac{i}{4} \sum_{j,k} A_{jk} c_j c_k\,, \qquad \text{with} \qquad A_{jk} = 2J_{\langle j,k \rangle} + 2K_{\langle\langle j,k \rangle\rangle}. \tag{3.24}$$

Equation (3.23) introduces a next-nearest neighbors interaction (hopping), opening a gap in the fermionic spectrum – i.e., it includes nonzero diagonal terms in $\tilde{A}(\mathbf{q})$ in (3.19). The matrix elements in (3.24) includes either nearest J or (next-nearest) K neighbors hopping, illustrated with solid (dashed) arrows in Fig. 3.5(b). The spectrum follows from the eigenvalues of the modified matrix $i\tilde{A}(\mathbf{q})$, reading as $\varepsilon(\mathbf{q}) = \pm\sqrt{|f(\mathbf{q})|^2 + \Delta^2(\mathbf{q})}$, where $\Delta(\mathbf{q}) = 4K\big(\sin(\mathbf{q}\mathbf{n_1}) - \sin(\mathbf{q}\mathbf{n_2}) + \sin(\mathbf{q}(\mathbf{n_2} - \mathbf{n_1}))\big)$. Thus, in the presence of a magnetic field the phase B acquires a *mass*. Since *bulk* excitations are now gapped, their braiding rules must be well-defined. In particular, it turns out that vortices are *non-Abelian anyons*, based on the computation of a finite *odd* Chern number $\nu = \pm 1$ [116]. This topological invariant arises from the Berry flux of the fermionic spectral projector $P(\mathbf{q}) = \frac{1}{2}\big[1 - \text{sgn}\left(i\tilde{A}(\mathbf{q})\right)\big]$ **[17]**, given by $\nu = \frac{1}{2\pi i}\int d^2\mathbf{q} \left(\frac{\partial P(\mathbf{q})}{q_x} \times \frac{\partial P(\mathbf{q})}{q_y}\right) \cdot P(\mathbf{q})$ [14]. Because of $\nu = \pm 1$, it is possible to show that every vortex carries an *unpaired* Majorana mode. As a result of a *fusion* **[18]**, vortices can either annihilate (*vacuum*), or leave a *bulk* fermion due to pairing of Majorana modes [14]. Thus, the output of braiding two vortices depends on which of these sectors are produced, which is compatible with the non-Abelian anyons fusion and braiding rules [107]. Moreover, since ν is nonzero, the system has gapless edge modes described in terms of Majorana fermions. These edge modes can carry energy, leading potentially to measurable thermal transport.

3.4 Jordan-Wigner fermionization

In this section I present a solution of the 2D-KH model based on the Jordan-Wigner transformation (JWT) [117–119]. The transformation allows to represent spin-$\frac{1}{2}$ operators in terms of *spinless fermions*. Such a representation requires to recover the fermion commutation relations from spin operators. However, spin operators anticommute at the same site and commute at different sites, namely

$$\{\sigma_n^-, \sigma_n^+\} = 1\,, \{\sigma_n^-, \sigma_n^-\} = \{\sigma_n^+, \sigma_n^+\} = 0\,, \tag{3.25a}$$

$$[\sigma_n^-, \sigma_m^+] = [\sigma_n^-, \sigma_m^-] = [\sigma_n^+, \sigma_m^+] = 0\,, \ \text{with} \quad n \neq m\,, \tag{3.25b}$$

---

[17] It projects onto the one-dimensional subspace spanned by the eigenvectors of $i\tilde{A}(\mathbf{q})$ corresponding to negative eigenvalues.

[18] The formation of a different type of anyon by braiding together two anyons is called fusion.

where $\sigma_n^{\pm} = \sigma_n^x \pm i\sigma_n^y$ are the spin ladder operators, and $2\sigma_n^z = [\sigma_n^+, \sigma_n^-]$. Hence, one cannot simply have $\sigma_n^{(+)} = f_n^{(\dagger)}$, but rather one may perform a transformation to get fully anticommuting operators. In 1D systems the problem has been solved [117] introducing a *phase* along 1D chains of fermions, namely

$$\sigma_1^- = f_1, \quad \sigma_n^- = \exp\left(\pm i\pi \sum_{j=1}^{n-1} f_j^\dagger f_j\right) f_n = \prod_{j=1}^{n-1} \left(1 - 2f_j^\dagger f_j\right) f_n = \prod_{j=1}^{n-1} (-1)^j \sigma_j^z f_n\,,\ n{=}2,\ldots,N, \tag{3.26a}$$

$$\sigma_1^+ = f_1^\dagger, \quad \sigma_n^+ = \exp\left(\pm i\pi \sum_{j=1}^{n-1} f_j^\dagger f_j\right) f_n^\dagger = \prod_{j=1}^{n-1} (1 - 2f_j^\dagger f_j) f_n^\dagger = \prod_{j=1}^{n-1} (-1)^j \sigma_j^z f_n^\dagger\,,\ n{=}2,\ldots,N. \tag{3.26b}$$

The equalities in (3.26a) and (3.26b) follow from series expansion of the exponential function. The phase for the fermion on the n^{th} site is determined by the number of occupied fermionic states at sites $j = 1, \ldots, n-1$. The spin operators in terms of fermions then can be nonlocal since one has to deal with a *string* of $n-1$ operators. The transformed operators fulfill the anticommuting relations, i.e., $\{f_n^\dagger, f_m\} = \delta_{m,n}$, $\{f_n^\dagger, f_m^\dagger\} = \{f_n, f_m\} = 0$. As an example, equations (3.26a) and (3.26b) can be applied to transform a 1D spin-$\frac{1}{2}$ isotropic XY Heisenberg chain into a chain of noninteracting spinless fermions,

$$\mathcal{H}_{\text{XY}} = \sum_{j=1}^{N-1} \frac{J}{2}(\sigma_{j+1}^+ \sigma_j^- + \sigma_{j+1}^- \sigma_j^+)\,, \;\rightarrow\; \mathcal{H}_{\text{XY}} = \sum_{j=1}^{N-1} \frac{J}{2}(f_j^\dagger f_{j+1} + f_{j+1}^\dagger f_j)\,. \tag{3.27}$$

In general, applications of the JWT do not provide always simple models in the fermionic language – as for the case in (3.27). The reason is that the phase introduced is not always simple to treat. For instance, JWT on 2D models [120] may return nonlocal fermionic operators, where the phase is seen as a gauge field, and for which approximations are required [121, 122].

The 2D-KH model that follows from a JWT [118, 119] is still an exactly solvable model with no need for approximations. In the form of a topologically equivalent brick-wall lattice – see Fig. 3.6(a) – the model is build up by x-y chains connected by vertical z bonds. Therefore, one can perform a 1D JWT along a path that snakes through the whole 2D lattice and that visits each site once – see Fig. 3.6(b). The JWTs to represent the spin ladder operators read

$$\sigma_{i,j}^+ = 2f_{i,j}^\dagger e^{i\pi\hat{\theta}_{i,j}} = 2\left[\prod_{j'<j}\prod_{i'} \sigma_{i'j'}^z\right]\left[\prod_{i'<i} \sigma_{i'j}^z\right] f_{i,j}^\dagger\,, \tag{3.28a}$$

$$\sigma_{i,j}^- = 2e^{i\pi\hat{\theta}_{i,j}} f_{i,j} = 2\left[\prod_{j'<j}\prod_{i'} \sigma_{i'j'}^z\right]\left[\prod_{i'<i} \sigma_{i'j}^z\right] f_{i,j}\,, \tag{3.28b}$$

$$\sigma_{i,j}^z = 2f_{i,j}^\dagger f_{i,j} - 1\,, \tag{3.28c}$$

with

$$\hat{\theta}_{i,j} = \sum_{j'<j}\sum_{i'} f_{i',j'}^\dagger f_{i',j'} + \sum_{i'<i} f_{i',j'}^\dagger f_{i',j'}. \tag{3.29}$$

Operators in (3.28) act on all spins located at site (i, j) of the 1D path – see Fig. 3.6(b). Equations (3.28a) and (3.28b) are twice the spin ladder operator for a given site. The operator

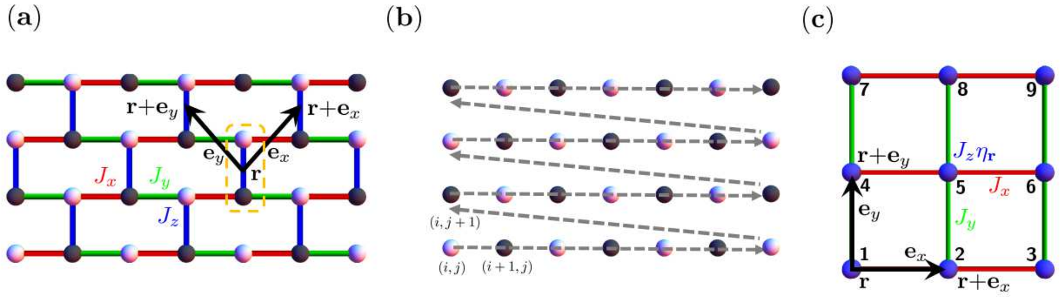

Figure 3.6: (a) Brick-wall lattice obtained by a deformation of the honeycomb lattice in Fig. 3.2(a). (b) Contour for the JW transformation used in the brick-wall lattice. (c) 2D-KH shrunk onto a square lattice. The exchange interactions $J_{x,y}$ (red, green edges) run along the lattice vectors $\mathbf{e}_{x,y}$, whereas J_z exchange coupling and the η_r gauge field tune the on-site potential of the r^{th} site of the lattice (blue vertices).

in (3.29), and thus $\exp(i\pi\hat{\theta}_{i,j})$, are rephrased in terms of $\sigma^z_{i,j}$, as similarly done in (3.26a) and (3.26b). Thus, one can use operators in (3.28) to represent the Pauli matrices in the Hamiltonian of (3.6), which terms are given by

$$
\begin{aligned}
\sigma^x_{i,j}\sigma^x_{i+1,j} &= \prod_{i\prime<i}\sigma^z_{i\prime,j}\big(f^\dagger_{i,j}+f_{i,j}\big)\prod_{i\prime<i+1}\sigma^z_{i\prime,j}\big(f^\dagger_{i+1,j}+f_{i+1,j}\big)\\
&= \big(f^\dagger_{i,j}+f_{i,j}\big)\sigma^z_{i\prime,j}\big(f^\dagger_{i+1,j}+f_{i+1,j}\big)\\
&\overbrace{=}^{(\mathbf{19})} -\big(f^\dagger_{i,j}-f_{i,j}\big)\big(f^\dagger_{i+1,j}+f_{i+1,j}\big) \qquad (3.30a)\\
\sigma^y_{i-1,j}\sigma^y_{i,j} &= \prod_{i\prime<i-1}\sigma^z_{i\prime,j}\big(f^\dagger_{i-1,j}-f_{i-1,j}\big)\prod_{i\prime<i}\sigma^z_{i\prime,j}\big(f^\dagger_{i,j}-f_{i,j}\big)\\
&= -\big(f^\dagger_{i-1,j}-f_{i-1,j}\big)\sigma^z_{i-1\prime,j}\big(f^\dagger_{i,j}-f_{i,j}\big)\\
&\overbrace{=}^{(\mathbf{19})} \big(f^\dagger_{i-1,j}+f_{i-1,j}\big)\big(f^\dagger_{i,j}-f_{i,j}\big) \qquad (3.30b)\\
\sigma^z_{i,j}\sigma^z_{i,j-1} &= \big(2f^\dagger_{i,j}f_{i,j}-1\big)\big(2f^\dagger_{i,j-1}f_{i,j-1}-1\big) \qquad . \qquad (3.30c)
\end{aligned}
$$

Performing all these substitutions, the Hamiltonian of (3.6) reads

$$
\begin{aligned}
\mathcal{H} = J_x &\sum_{x-bonds}\big(f^\dagger_{i,j}-f_{i,j}\big)\big(f^\dagger_{i+1,j}+f_{i+1,j}\big)\\
-J_y &\sum_{y-bonds}\big(f^\dagger_{i-1,j}+f_{i-1,j}\big)\big(f^\dagger_{i,j}-f_{i,j}\big)\\
-J_z &\sum_{z-bonds}\big(2f^\dagger_{i,j}f_{i,j}-1\big)\big(2f^\dagger_{i,j-1}f_{i,j-1}-1\big). \qquad (3.31)
\end{aligned}
$$

Equation (3.31) consists of *local* bilinear terms along the x-y chain. The z terms, instead, lead to some density-density interactions – that are quartic in the fermion modes. Terms in (3.31) can be further simplified. Indeed, one may introduce two Majorana fermions, $c_{i,j}$ and

---

[19] The relation $(f^\dagger_\alpha+f_\alpha)\sigma^z_\alpha = (f^\dagger_\alpha+f_\alpha)(2f^\dagger_\alpha f_\alpha-1) = -f^\dagger_\alpha+f_\alpha-2f^\dagger_\alpha f_\alpha f_\alpha+2f_\alpha f^\dagger_\alpha f^\dagger_\alpha = -(f^\dagger_\alpha-f_\alpha)$ has been used.

$g_{i,j}$, per each fermion $f_{i,j}$

$$\begin{aligned} c_{i,j} &= i(f^\dagger_{i,j} - f_{i,j}), \qquad & g_{i,j} &= f^\dagger_{i,j} + f_{i,j} \qquad & i+j &= \text{even} \equiv \circ \\ c_{i,j} &= f^\dagger_{i,j} + f_{i,j}, \qquad & g_{i,j} &= i(f^\dagger_{i,j} - f_{i,j}) \qquad & i+j &= \text{odd} \equiv \bullet . \end{aligned} \tag{3.32}$$

In the following, I adopt the notation $(\circ, \bullet)$ as in (3.32) to indicate the (even,odd) sites of the bipartite lattice shown in Fig. 3.6(a). Thus, the Hamiltonian in (3.31) in terms of Majorana fermions is given by

$$\mathcal{H} = -iJ_x \sum_{x-bonds} c_\circ c_\bullet + iJ_y \sum_{y-bonds} c_\bullet c_\circ - iJ_z \sum_{z-bonds} \big(ig_\circ g_\bullet\big) c_\circ c_\bullet \,. \tag{3.33}$$

Let us consider N unit cells in the brick-wall lattice at the position $\mathbf{r}$. Each of these consists of one even ($\circ$) and one odd ($\bullet$) lattice site. The unit vectors $\mathbf{e}_x$ and $\mathbf{e}_y$ connect the unit cells, and span the whole lattice – see Fig. 3.6(a). The sum over all x, y, and z bonds in (3.33) turns into a sum over all the unit cells. Therefore, the Hamiltonian reads

$$\mathcal{H} = \sum_{\mathbf{r}} i\big[J_x c_{\bullet,\mathbf{r}} c_{\circ,\mathbf{r}+\mathbf{e}_x} + J_y c_{\bullet,\mathbf{r}} c_{\circ,\mathbf{r}+\mathbf{e}_y} - J_z \big(\underbrace{ig_{\bullet,\mathbf{r}} g_{\circ,\mathbf{r}}}_{\hat{\eta}_\mathbf{r}}\big) c_{\bullet,\mathbf{r}} c_{\circ,\mathbf{r}}\big] \,, \tag{3.34}$$

where the operator $\hat{\eta}_\mathbf{r} = (ig_{\bullet,\mathbf{r}} g_{\circ,\mathbf{r}})$ is defined on each z bond of the lattice and located by the vector $\mathbf{r}$. Operators $\hat{\eta}_\mathbf{r}$ commute with each other and with the Hamiltonian. This is verified for the x and y terms since $\{c_\mathbf{r}, g_{\mathbf{r}'}\} = 0$, but it is also true for the z terms, even at the same site $\mathbf{r}$, for which one has

$$\big[g_\bullet g_\circ c_\bullet c_\circ, g_\bullet g_\circ\big]_\mathbf{r} = g_\bullet g_\circ \big[c_\bullet c_\circ, g_\bullet g_\circ\big]_\mathbf{r} = 0. \tag{3.35}$$

Therefore, $\mathcal{H}$ and $\hat{\eta}_\mathbf{r}$ have common eigenstates. The Hilbert space can be decomposed into common eigenspaces of $\hat{\eta}_\mathbf{r}$, which are labeled by eigenvalues $\eta_\mathbf{r} = \pm 1$. Thus, one can diagonalize $\mathcal{H}$ within each eigenspace with a fixed configuration of eigenvalues $\{\eta_\mathbf{r}\} = (\eta_1, \ldots, \eta_N)$. The restriction of $\mathcal{H}$ in (3.34) to

$$\mathcal{H}_{\{\eta_\mathbf{r}\}} = \sum_{\mathbf{r}} i\big[J_x c_{\bullet,\mathbf{r}} c_{\circ,\mathbf{r}+\mathbf{e}_x} + J_y c_{\bullet,\mathbf{r}} c_{\circ,\mathbf{r}+\mathbf{e}_y} - J_z \eta_\mathbf{r} c_{\bullet,\mathbf{r}} c_{\circ,\mathbf{r}}\big] \,, \tag{3.36}$$

describes a problem of free Majorana fermions with static $\mathbb{Z}_2$ gauge fields. The Hamiltonian of (3.36) has the same form as for the Kitaev's solution in (3.14). However, the JW fermionization gives rise to a particular realization of Majorana fermionization, where the gauge fields along the 1D x-y chains are fixed to $+1$. One may wonder whether there exists a gauge transformation on the lattice which renders (3.14) to that of (3.36). It exists, and referring to the JW path of Fig. 3.6(b), it leads to

$$c_n \to \prod_{j=1}^{n-1} \eta_{j,j+1} c_n, \qquad n = 2, \ldots, N, \tag{3.37}$$

where $\eta_{j,j+1}$ are the gauge fields living on the bond joining the j^{th} and $(j+1)^{\text{th}}$ site along the JW path, if one applies the Majorana fermionizaton. The gauge transformation in (3.37) implies that the gauge fields $\eta_\mathbf{r} = \pm 1$ live only on the z bonds. In other words, the JW fermionization evades the gauge redundancy arising from the unphysical states [20] in the

---

[20] Now it should be clearer that the *unphysical* states are 2^{2N} *gauge copies* arising from the $2N$ different operators $\{D_j\}$ for each lattice site $j = 1, \ldots, 2N$, introduced in Sec.3.3.

Majorana representation. Indeed, the JWT maps the 2-dimensional Hilbert space of spins onto the 2-dimensional Hilbert space of spinless fermions. The advantage is that there is no need to project out states in solving the Hamiltonian. The operators $\hat{\eta}_{\mathbf{r}}$ are related to the plaquette operators $\hat{w}_p$ of (3.7) via the JWTs in (3.28a) and (3.28b)

$$\begin{aligned}\hat{w}_p &= \sigma_1^y\sigma_2^z\sigma_3^x\sigma_4^y\sigma_5^z\sigma_6^x \\ &= \frac{1}{i}(f_1^\dagger - f_1)\sigma_2^z(f_3^\dagger + f_3)\sigma_1^z\sigma_2^z\frac{1}{i}(f_4^\dagger - f_4)\sigma_5^z\sigma_6^z\sigma_5^z(f_6^\dagger + f_6) \\ &= i(f_1^\dagger + f_1)(f_3^\dagger + f_3)\frac{1}{i}i(f_4^\dagger - f_4)\frac{1}{i}(f_6^\dagger - f_6) \\ &\underbrace{=}_{(3.32)}(ig_{\circ,1}g_{\circ,3})(ig_{\bullet,4}g_{\bullet,6}) \\ &= \hat{\eta}_{61}\hat{\eta}_{43},\end{aligned} \tag{3.38}$$

with $\hat{\eta}_{61}$ and $\hat{\eta}_{43}$ living on the z bonds of the plaquette p – see Fig. 3.2(a). Thus *vortices* $w_p = \pm 1$ arise from the product of two consecutive gauge variables $\eta_{\mathbf{r}}$ on z bonds, i.e., vortices are *domain walls* in terms of $\eta_{\mathbf{r}}$. The inversion of $\eta_{\mathbf{r}} \to -\eta_{\mathbf{r}}$ for all the sites $\mathbf{r}$ lying along an horizontal row of plaquettes on the brick-wall lattice, does not change the vorticity content of the system [123]. Therefore, all the eigenstates of the Hamiltonian in (3.36) are at least 2^R-fold degenerate, with R the number of rows. Since the conserved quantities $\hat{\eta}_{\mathbf{r}}$ live on the z bonds of the lattice, one may introduce complex fermions on each z bond

$$d_{\mathbf{r}} = \frac{1}{2}\big(c_{\bullet,\mathbf{r}} - ic_{\circ,\mathbf{r}}\big)\ ,\ d_{\mathbf{r}}^\dagger = \frac{1}{2}\big(c_{\bullet,\mathbf{r}} + ic_{\circ,\mathbf{r}}\big), \tag{3.39}$$

to rewrite the Hamiltonian in (3.36) as

$$\begin{aligned}\mathcal{H}_{\{\eta_{\mathbf{r}}\}} = \sum_{\mathbf{r}} & J_x(d_{\mathbf{r}}^\dagger + d_{\mathbf{r}})(d_{\mathbf{r}+\mathbf{e}_x}^\dagger - d_{\mathbf{r}+\mathbf{e}_x}) + J_y(d_{\mathbf{r}}^\dagger + d_{\mathbf{r}}) \\ & \times(d_{\mathbf{r}+\mathbf{e}_y}^\dagger - d_{\mathbf{r}+\mathbf{e}_y}) + J_z\eta_{\mathbf{r}}(2d_{\mathbf{r}}^\dagger d_{\mathbf{r}} - 1)\,,\end{aligned} \tag{3.40}$$

where $\mathbf{e}_x$ and $\mathbf{e}_y$ connect two z-bonds that cross x- and y-bonds, respectively, and form a unit vector basis of a square lattice (SL). The SL is obtained by shrinking the z bonds of the brick-wall lattice into SL sites located by $\mathbf{r}$, as shown in Fig. 3.6(c). Equation (3.40) describes a matter fermion Hamiltonian with an on-site dependent gauge potential, containing both hopping and pairing terms. As for the Kitaev's solution in Sec. 3.3.1, the ground state is given by the vortex-free state. To find the energy spectrum one can fix the gauge configuration $\{\eta_{\mathbf{r}}\}$ to one which does not contain vortices, e.g., $\eta_{\mathbf{r}} = 1\ \forall\,\mathbf{r}$ – as similarly done in Sec. 3.3.2. The sector is translational invariant, thus one Fourier transforms (3.40), to obtain

$$d_{\mathbf{r}} = \frac{1}{\sqrt{N}}\sum_{\mathbf{q}} e^{i(\mathbf{qr})}d_{\mathbf{q}} \implies \tilde{\mathcal{H}}_{\{\eta=1\}} = \frac{1}{2}\sum_{\mathbf{q}} \overbrace{\begin{pmatrix} d_{\mathbf{q}}^\dagger d_{-\mathbf{q}}\end{pmatrix}}^{\mathbf{D}_{\mathbf{q}}^\dagger}\begin{pmatrix} e_{\mathbf{q}} & i\Delta_{\mathbf{q}} \\ i\Delta_{-\mathbf{q}} & -e_{-\mathbf{q}}\end{pmatrix}\overbrace{\begin{pmatrix} d_{\mathbf{q}} \\ d_{-\mathbf{q}}^\dagger\end{pmatrix}}^{\mathbf{D}_{\mathbf{q}}}, \tag{3.41}$$

where $e_{\mathbf{q}} = 2(J_z - J_x\cos q_x - J_y\cos q_y)$, and $\Delta_{\mathbf{q}} = 2(J_x\sin q_x + J_y\sin q_y)$. The Hamiltonian in (3.41) recalls the BCS Hamiltonian found in (3.20). Its diagonalized form follows from a Bogoliubov transformation $\mathbf{B}$ – I refer to Appendix A.1 for further details – that gives rise to

$$\tilde{\mathcal{H}}_{\{\eta=1\}} = \sum_{\mathbf{q}} E(\mathbf{q})\Big(2a_{\mathbf{q}}^\dagger a_{\mathbf{q}} - 1\Big). \tag{3.42}$$

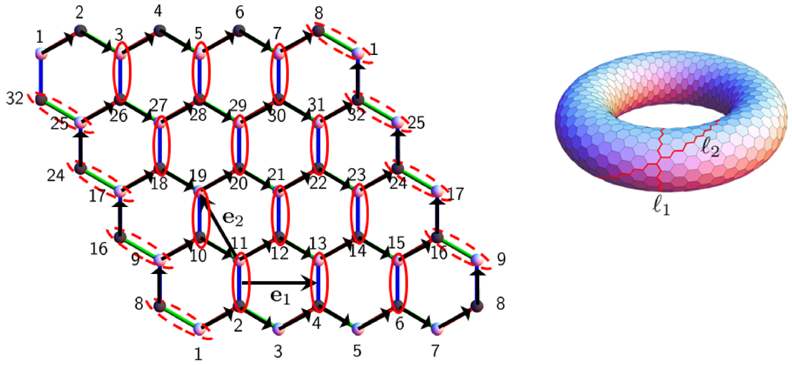

Figure 3.7: 2D Kitaev honeycomb 4×4 lattice – $N = 32$ sites – on a torus. Red solid loops ℓ_1 and ℓ_2 run along the $\mathbf{e}_1$ and $\mathbf{e}_2$ directions. Ellipsis mark the normal bonds $\mathbf{n}_i$, according to the winding direction $\mathbf{e}_1$ of JW path from 1 to N.

Equation (3.42) is identical to (3.21), where $E(\mathbf{q}) = |f(\mathbf{q})| = \sqrt{e_{\mathbf{q}}^2 + \Delta_{\mathbf{q}}^2}$ is the energy of quasiparticles $\mathbf{A}_{\mathbf{q}}^\dagger = (a_{\mathbf{q}}^\dagger, a_{-\mathbf{q}})$, with $\mathbf{A}^\dagger = \mathbf{D}^\dagger \mathbf{B}$. The properties of the related phases and excitations remain as described in Secs. 3.3.3 and 3.3.4.

3.4.1 Boundary terms

The JW mapping in (3.34) is limited to the *bulk* system. If *boundaries* are considered, a nonvanishing phase term follows from the JWT along the 1D path. It is important to study the boundary conditions to recover the topological ground-state degeneracy discussed in Sec. 3.3.1. One may consider the lattice in Fig. 3.7, with $N = 32$ sites, embedded onto a torus. The whole lattice is spanned by the 1D JW path, according to the winding direction $\mathbf{e}_1$, and following the numbering of sites. One may refer to the construction adopted by Mandal *et al.* [119] to recover the gauge transformation in (3.37) that fixes $\eta_{\mathbf{r}} = 1$ along the 1D chain, and leaves $\eta_{\mathbf{r}} = \pm 1$ on z bonds. Such a construction implies that the 1D path goes through two of the three bonds connected to each site. These are called *tangential bonds*, $\mathbf{t}_{1i}, \mathbf{t}_{2i}$, where the third bond $\mathbf{n}_i = \mathbf{t}_{1i} \times \mathbf{t}_{2i}$ is called *normal bond.* For any path or closed loop, the operator in (3.7), $\hat{w}_p = \prod_i (\mathbf{n}_i \cdot \sigma_i^{\lambda_{\mathbf{n}}})$, i.e., $\eta_{\mathbf{r}} = \pm 1$ lies only on normal bonds – which agrees with (3.38). Internal (boundary) normal bonds are marked by solid (dashed) ellipsis in Fig. 3.7. The Hamiltonian that describes the system in Fig. 3.7 can be split into three terms

$$\mathcal{H}_{\text{bulk}} = \sum_{j,k} -iJ_x c_{\circ(j,k)} c_{\bullet(j+1,k+1)} - iJ_y c_{\circ(j,k)} c_{\bullet(j,k+1)} - iJ_z \hat{\eta}^{(|)}_{j,k} c_{\circ(j,k)} c_{\bullet(j,k)} \,, \tag{3.43a}$$

$$\mathcal{H}_{\text{bound}} = \sum_{j,k \,\in\, \text{boundary}} -iJ_y \hat{\eta}^{(\backslash)}_{\substack{j,k \\ j,k+1}} c_{\circ(j,k)} c_{\bullet(j,k+1)} - iJ_z c_{\circ(j,k)} c_{\bullet(j,k)} \,, \tag{3.43b}$$

$$\mathcal{H}_{\text{end}} = i\mathcal{S} J_z c_{\circ(N,N)} c_{\bullet(N,N)} . \tag{3.43c}$$

In equations (3.43) indices (j, k) relate to the 1D JW path in Fig. 3.7, and $c_{\circ(\bullet)}$ is the Majorana fermion located on the $\circ(\bullet)$ sublattice site. Equation (3.43a) contains the *bulk* terms , with $\hat{\eta}^{(|)}$ the conserved operator on the internal normal z bonds $(|)$ – as for (3.34). All the *boundary* terms – except one where the JW end points meet each other – are contained in (3.43b), with $\hat{\eta}^{(\backslash)}$ living on the boundary normal y bonds $(\backslash)$. The *end* points boundary term is given by (3.43c). The quantity $\mathcal{S}$ is defined as

$$\mathcal{S} = \prod_{i=1}^{N} (\mathbf{n}_i \cdot \sigma_i^{\lambda_\mathbf{n}}) = \prod_{i=1}^{N} (-i\hat{\eta}_{i+1,i} c_{i+1} c_i) \underbrace{=}_{\text{at } i=N,\ i+1=1} \pm 1 \ . \tag{3.44}$$

Equation (3.44) retrieves the conserved quantity defined in (3.18). $\mathcal{S}$ determines the gauge variable on the tangential bond at the end point of the chosen JW path – the only one not fixed to 1 – and it refers to the aforementioned nonvanishing nonlocal phase term in the JW string with boundary conditions. From Fig. 3.7 one can note that every plaquette has two normal bonds, i.e., for every plaquette $\hat{w}_p = \hat{\eta}_{ij}\hat{\eta}_{kl}$, with $(i,j),(k,l) \in p$. For the end plaquette where the JW path terminates, $\hat{w}_p = \mathcal{S}\hat{\eta}_{ij}\hat{\eta}_{kl}$. Considering these quantities, one can compute the Wilson loops $\hat{w}_{\ell_1}$ and $\hat{w}_{\ell_2}$ – as done for (3.18) – along the two essential paths on a torus. It is possible to show that the four distinct topological sectors found in Sec. 3.3.1 arise from distinct combination of $\mathcal{S}$ and η, leading to four different kinds of boundary conditions [21]. A discussion on all possible scenarios goes beyond the purpose of this work, for which I would refer the reader to the work of Mandal *et al.* [119]. What described above relates to a proper way of treating boundary conditions, which is clearly important to get the proper ground state degeneracy, and to study the topological quantities arising from the model. For the purpose of this work – which aims to investigate *bulk* transport properties of the model – I consider boundary conditions onto the square lattice in Fig. 3.6(c), geometry which the system has been reduced to in (3.40). These boundary conditions are *periodic* along the $\mathbf{e}_x$ and $\mathbf{e}_y$ directions of the lattice – see Fig. 3.6(c). These conditions do not take into account the arising end points term of (3.43c), as required for any JW mapping. However, this is not a real issue since in this work I will not discuss about topological quantities of the system. In particular, the term in (3.43c) has no relevant effects on the bulk transport properties, thus I will discard it. Nevertheless, one may worry whether different choices for boundary conditions imply different results for the bulk quantities, due to finite size corrections $\mathcal{O}(1/L)$ for a system with $N = L \times L$ sites. In this context, in Chapter 5, Sec. 5.5, I will contrast two different ways to map boundaries against each other, and I will show that results are qualitatively the same regardless of which boundaries I consider.

---

[21] One of the four possible sectors arises from all $\{\eta\} = 1$ and $\mathcal{S} = -1$. The Wilson loop's eigenvalues are $w_{\ell_1} = 1$ and $w_{\ell_2} = 1$, with periodic boundary conditions in both directions.

CHAPTER 4

Evaluation of dynamical heat current correlation functions

In this chapter, I will show the analytical and numerical methods employed in this work to compute the heat transport coefficients for the two-dimensional Kitaev model. These coefficients are derived within the linear response theory, and thus, according to equations (2.13) and (2.14), they can be computed via the energy-current auto-correlation functions. Since the model is analytically solved in the vortex-free state, I will provide an analytical expression for the correlation functions. The analytical findings are valid only in the zero-temperature limit. A finite-temperature study includes thermal fluctuations of the static gauge fields, i.e., a nonzero content of vortices. Therefore, to investigate the influence of vortices on mobile heat carriers, I will show the numerical methods employed to deal with the finite-temperature problem.

4.1 Analytical calculations in the vortex-free state

To compute the energy-current auto-correlation function in the vortex-free state, first one needs to evaluate the energy current. According to (2.6), the energy current follows from the continuity equation as, $\partial_l j_h^l = -\partial_t h(\mathbf{r})$. The right hand side of the equation refers to the time derivative of the *local energy density.* In the vortex-free state, and at zero magnetic field $B = 0$, one may define this energy density as

$$\begin{aligned} h(\mathbf{r})_{\{\eta_{\mathbf{r}}=1\}} &= J_x(d_{\mathbf{r}}^\dagger + d_{\mathbf{r}})(d_{\mathbf{r}+\mathbf{e}_x}^\dagger - d_{\mathbf{r}+\mathbf{e}_x}) + J_y(d_{\mathbf{r}}^\dagger + d_{\mathbf{r}})(d_{\mathbf{r}+\mathbf{e}_y}^\dagger - d_{\mathbf{r}+\mathbf{e}_y}) \\ &\quad + J_z(2d_{\mathbf{r}}^\dagger d_{\mathbf{r}} - 1)\,, \end{aligned} \tag{4.1}$$

where $\int d\mathbf{r}\, h(\mathbf{r}) = \mathcal{H}_{\{\eta_{\mathbf{r}}=1\}}$ retrieves the Hamiltonian of (3.40) in terms of matter fermions $d^{(\dagger)}$ located at sites $\mathbf{r}$ of the square lattice – as shown in Fig. 3.6(c). The time derivative of (4.1) is given by the commutator $i\big[\mathcal{H}, h(\mathbf{r})\big]$. This latter – hence the current, and its related correlation function – can be evaluated analytically. Equation (4.1) is translational invariant, and thus it can be studied in the momentum space via a Fourier transformation. One may recall the Hamiltonian in the momentum space evaluated in (3.41),

$$\tilde{\mathcal{H}} = \sum_{\mathbf{q}} \overbrace{\begin{pmatrix} d_{\mathbf{q}}^\dagger d_{-\mathbf{q}} \end{pmatrix}}^{\mathbf{D}_{\alpha,\mathbf{q}}^\dagger} \overbrace{\begin{pmatrix} \frac{e_{\mathbf{q}}}{2} & i\frac{\Delta_{\mathbf{q}}}{2} \\ i\frac{\Delta_{-\mathbf{q}}}{2} & -\frac{e_{-\mathbf{q}}}{2} \end{pmatrix}}^{\mathrm{H}(\mathbf{q})_{\alpha\beta}} \underbrace{\begin{pmatrix} d_{\mathbf{q}} \\ d_{-\mathbf{q}}^\dagger \end{pmatrix}}_{\mathbf{D}_{\beta,\mathbf{q}}}, \text{ with } \begin{cases} e_{\mathbf{q}} = 2(J_z - J_x \cos q_x - J_y \cos q_y) \\ \Delta_{\mathbf{q}} = 2(J_x \sin q_x + J_y \sin q_y) \end{cases} . \tag{4.2}$$

Similarly, one may Fourier transform the energy density $h(\mathbf{r})$ in (4.1)

$$\tilde{h}(\mathbf{r}) = h_{\mathbf{p}} = \sum_{\mathbf{q}'} \overbrace{\begin{pmatrix} d^\dagger_{\mathbf{q}'} d_{-\mathbf{q}'} \end{pmatrix}}^{\mathbf{D}^\dagger_{\mu,\mathbf{q}'}} \overbrace{\begin{pmatrix} a_{\mathbf{q}',\mathbf{p}} & ib_{\mathbf{q}',\mathbf{p}} \\ -ib_{\mathbf{q}',\mathbf{p}} & -a_{\mathbf{q}',\mathbf{p}} \end{pmatrix}}^{\mathrm{R}(\mathbf{q}',\mathbf{p})_{\mu\nu}} \underbrace{\begin{pmatrix} d_{\mathbf{q}'+\mathbf{p}} \\ d^\dagger_{-\mathbf{q}'-\mathbf{p}} \end{pmatrix}}_{\mathbf{D}_{\nu,\mathbf{q}'+\mathbf{p}}},$$

$$\text{with } \begin{cases} a_{\mathbf{q}',\mathbf{p}} = J_z - J_x e^{i\frac{p_x}{2}} \cos(q'_x + \frac{p_x}{2}) - J_y e^{i\frac{p_y}{2}} \cos(q'_y + \frac{p_y}{2}) \\ b_{\mathbf{q}',\mathbf{p}} = (J_x e^{i\frac{p_x}{2}} \sin(q'_x + \frac{p_x}{2}) + J_y e^{i\frac{p_y}{2}} \sin(q'_y + \frac{p_y}{2})) \end{cases} . \tag{4.3}$$

The energy current in the momentum space follows from a Fourier transformation of (2.6) and from (4.2) and (4.3),

$$\mathbf{p} \cdot \mathbf{j}(\mathbf{p}) = \left[\tilde{\mathcal{H}}, h_{\mathbf{p}}\right]. \tag{4.4}$$

In (4.4) I dropped off the index "h" since (4.1) is considered at zero magnetic field. Indeed, the energy current $\mathbf{j}_h = \mathbf{j}_{th} = \mathbf{j}$ consists only of the thermal current, without any coupling with the spin current $\mathbf{j}_S$ – see Sec. 2.1. Thus, one needs to compute the right hand side of (4.4), which is given by

$$\begin{aligned} \left[\tilde{\mathcal{H}}, h_{\mathbf{p}}\right] &= \sum_{\mathbf{q}\alpha\beta} \sum_{\mathbf{q}'\mu\nu} \left[d^\dagger_{\alpha,\mathbf{q}} \mathrm{H}(\mathbf{q})_{\alpha\beta} d_{\beta,\mathbf{q}}, d^\dagger_{\mu,\mathbf{q}'} \mathrm{R}(\mathbf{q}',\mathbf{p})_{\mu\nu} d_{\nu,\mathbf{q}'+\mathbf{p}}\right] \\ &= \sum_{\mathbf{q}\alpha\beta} \sum_{\mathbf{q}'\mu\nu} \mathrm{H}(\mathbf{q})_{\alpha\beta} \mathrm{R}(\mathbf{q}',\mathbf{p})_{\mu\nu} \Big(d^\dagger_{\alpha,\mathbf{q}} d_{\beta,\mathbf{q}} d^\dagger_{\mu,\mathbf{q}'} d_{\nu,\mathbf{q}'+\mathbf{p}} - d^\dagger_{\mu,\mathbf{q}'} d_{\nu,\mathbf{q}'+\mathbf{p}} d^\dagger_{\alpha,\mathbf{q}} d_{\beta,\mathbf{q}} \Big) \\ &= \sum_{\mathbf{q}\alpha\beta} \sum_{\mathbf{q}'\mu\nu} \mathrm{H}(\mathbf{q})_{\alpha\beta} \mathrm{R}(\mathbf{q}',\mathbf{p})_{\mu\nu} \Big(d^\dagger_{\alpha,\mathbf{q}} d_{\nu,\mathbf{q}'+\mathbf{p}} \delta_{\mu,\beta} \delta_{\mathbf{q},\mathbf{q}'} - d^\dagger_{\mu,\mathbf{q}'} d_{\beta,\mathbf{q}} \delta_{\alpha,\nu} \delta_{\mathbf{q},\mathbf{q}'+\mathbf{p}} \Big) \\ &= \sum_{\mathbf{q}} \mathbf{D}^\dagger_{\mathbf{q}} \Big(\mathrm{H}(\mathbf{q}) \mathrm{R}(\mathbf{q},\mathbf{p}) - \mathrm{R}(\mathbf{q},\mathbf{p}) \mathrm{H}(\mathbf{q}+\mathbf{p}) \Big) \mathbf{D}_{\mathbf{q}+\mathbf{p}} . \end{aligned} \tag{4.5}$$

To get an expression for $\mathbf{j}$, one can expand both sides of (4.4) in Taylor's series of $\mathbf{p} = (p_x, p_y)$ about zero up to the 1^{st} order. In such a way, one is considering the energy current of (4.4) in the long-wavelength limit $\mathbf{p} \to 0$, that reads

$$j^\mu = \sum_{\mathbf{q}} \begin{pmatrix} d^\dagger_{\mathbf{q}} d_{-\mathbf{q}} \end{pmatrix} \overbrace{\begin{pmatrix} l_{\mathbf{q},\mu} & l_{\mathbf{q},\mu} \\ l_{\mathbf{q},\mu} & l_{\mathbf{q},\mu} \end{pmatrix}}^{\mathrm{L}^\mu(\mathbf{q})} \begin{pmatrix} d_{\mathbf{q}} \\ d^\dagger_{-\mathbf{q}} \end{pmatrix}, \tag{4.6}$$

with $l_{\mathbf{q},\mu} = 2\big(J_\mu J_z \sin(q_\mu) - J_x J_y \sin(q_\mu - q_{\bar{\mu}})\big)$ and $\bar{\mu} = y(x)$ for $\mu = x(y)$. After that, one performs a standard Bogoliubov transformation $\mathbf{B}$ – as discussed in Sec. 3.4 – which makes the matrix in (4.2) diagonal in the Bogoliubov basis $\mathbf{A}^\dagger = \mathbf{D}^\dagger \mathbf{B}$. The result is obviously identical to that in (3.42), with the quasiparticle energy $E(\mathbf{q}) = \sqrt{e^2_{\mathbf{q}} + \Delta^2_{\mathbf{q}}}$. One can use yet the quasiparticle basis of the diagonal Hamiltonian to transform the energy current operator in (4.6), which possibly become diagonal. The transformed current operator reads $j^\mu = \sum_{\mathbf{q}} \mathbf{A}^\dagger_{\mathbf{q}} \tilde{\mathrm{L}}^\mu(\mathbf{q}) \mathbf{A}_{\mathbf{q}}$, with $\tilde{\mathrm{L}}^\mu(\mathbf{q}) = \mathrm{L}^\mu(\mathbf{q})$. In the quasiparticle basis the current matrix remains not diagonal, and thus the energy current displays both diagonal (quasiparticle) terms, and off-diagonal (pair-breaking) terms. It can be also written as

$$j^\mu = \sum_{\mathbf{q}} E(\mathbf{q}) \frac{\partial E(\mathbf{q})}{\partial q_\mu} a^\dagger_{\mathbf{q}} a_{\mathbf{q}} + \text{pair-breaking terms}, \tag{4.7}$$

with the quasiparticle contribution $E(\mathbf{q})\partial E(\mathbf{q})/\partial q_\mu = 2l_{\mathbf{q},\mu}$. The latter relation follows from the definition of the local energy density in (4.1). The next step consists in the evaluation of the energy-current auto-correlation function (2.14), which in the quasiparticle basis reads as [1]

$$C_{\mu\nu}(t) = \langle j^\mu(t) j^\nu \rangle = \frac{1}{N}\sum_{\mathbf{q}\alpha\beta}\sum_{\mathbf{k}\gamma\delta}\langle \mathbf{A}^\dagger_{\alpha,\mathbf{q}}\mathrm{L}^\mu_{\alpha\beta}(\mathbf{q})\mathbf{A}_{\beta,\mathbf{q}}\mathbf{A}^\dagger_{\gamma,\mathbf{k}}\mathrm{L}^\nu_{\gamma\delta}(\mathbf{k})\mathbf{A}_{\delta,\mathbf{k}}\rangle e^{i(E(\mathbf{q})_\alpha - E(\mathbf{q})_\beta)t} . \tag{4.8}$$

In (4.8) the time evolution is considered in the Heisenberg picture [2], and N is the system size. To calculate (4.8) one may perform a Wick's decomposition to compact the four-point correlator in products of simpler two-point correlators. Without loss of generality, one may assume for simplicity that $\mu = \nu$ – which refers to the longitudinal correlation function. The latter can be written as

$$\begin{aligned}
C(t) &= \frac{1}{N}\sum_{\mathbf{q},\mathbf{k}}\langle l_\mathbf{q}\Big(2a^\dagger_\mathbf{q}a_\mathbf{q} + a^\dagger_\mathbf{q}a^\dagger_{-\mathbf{q}}e^{i2E(\mathbf{q})t} + a_{-\mathbf{q}}a_\mathbf{q}e^{-i2E(\mathbf{q})t}\Big)l_\mathbf{k}\Big(2a^\dagger_\mathbf{k}a_\mathbf{k} + a^\dagger_\mathbf{k}a^\dagger_{-\mathbf{k}} + a_{-\mathbf{k}}a_\mathbf{k}\Big)\rangle \\
&= \frac{1}{N}\sum_{\mathbf{q},\mathbf{k}} l_\mathbf{q}l_\mathbf{k}\Big(4\langle a^\dagger_\mathbf{q}a_\mathbf{q}a^\dagger_\mathbf{k}a_\mathbf{k}\rangle + 2\langle a^\dagger_\mathbf{q}a_\mathbf{q}a^\dagger_\mathbf{k}a^\dagger_{-\mathbf{k}}\rangle + 2\langle a^\dagger_\mathbf{q}a_\mathbf{q}a_{-\mathbf{k}}a_\mathbf{k}\rangle \\
&+ e^{i2E(\mathbf{q})t}(2\langle a^\dagger_\mathbf{q}a^\dagger_{-\mathbf{q}}a^\dagger_\mathbf{k}a_\mathbf{k}\rangle + \langle a^\dagger_\mathbf{q}a^\dagger_{-\mathbf{q}}a^\dagger_\mathbf{k}a^\dagger_{-\mathbf{k}}\rangle + \langle a^\dagger_\mathbf{q}a^\dagger_{-\mathbf{q}}a_{-\mathbf{k}}a_\mathbf{k}\rangle) \\
&+ e^{-i2E(\mathbf{q})t}(2\langle a_{-\mathbf{q}}a_\mathbf{q}a^\dagger_\mathbf{k}a_\mathbf{k}\rangle + \langle a_{-\mathbf{q}}a_\mathbf{q}a^\dagger_\mathbf{k}a^\dagger_{-\mathbf{k}}\rangle + \langle a_{-\mathbf{q}}a_\mathbf{q}a_{-\mathbf{k}}a_\mathbf{k}\rangle)\Big) \\
&= \frac{1}{N}\sum_{\mathbf{q},\mathbf{k}} l_\mathbf{q}l_\mathbf{k}\Big(4\langle a^\dagger_\mathbf{q}a_\mathbf{k}\rangle\langle a_\mathbf{q}a^\dagger_\mathbf{k}\rangle + e^{i2E(\mathbf{q})t}(\langle a^\dagger_\mathbf{q}a_\mathbf{k}\rangle\langle a^\dagger_{-\mathbf{q}}a_{-\mathbf{k}}\rangle - \langle a^\dagger_\mathbf{q}a_{-\mathbf{k}}\rangle\langle a^\dagger_{-\mathbf{q}}a_\mathbf{k}\rangle) \\
&+ e^{-i2E(\mathbf{q})t}(\langle a_{-\mathbf{q}}a^\dagger_{-\mathbf{k}}\rangle\langle a_\mathbf{q}a^\dagger_\mathbf{k}\rangle - \langle a_{-\mathbf{q}}a^\dagger_\mathbf{k}\rangle\langle a_\mathbf{q}a^\dagger_{-\mathbf{k}}\rangle)\Big) .
\end{aligned} \tag{4.9}$$

Equation (4.9) can be further simplified, and it reads

$$C(t) = \frac{1}{N}\sum_\mathbf{q} 2l^2_\mathbf{q}\Big[2f_\mathbf{q}(1-f_\mathbf{q}) + f^2_\mathbf{q}e^{i2E(\mathbf{q})t} + (1-f_\mathbf{q})^2 e^{-i2E(\mathbf{q})t}\Big] , \tag{4.10}$$

where $\langle a^\dagger_\mathbf{q}a_\mathbf{q}\rangle \to f_\mathbf{q}$, with $f_\mathbf{q} = \big(\exp(\beta E(\mathbf{q})) + 1\big)^{-1}$ the Fermi-Dirac distribution. Equation (4.10) contains both particle-hole, and particle-particle (hole-hole) contributions. To relate (4.10) to the transport coefficients – see equations (2.15 - 2.17) – it would be appropriate to Fourier transform (4.10) in the frequency space, which returns

$$\begin{aligned}
C(\omega) &= \int_{-\infty}^{\infty} dt e^{-i\omega t}C(t) \\
&= \frac{2\pi}{N}\sum_\mathbf{q} 2l^2_\mathbf{q}\Big[2f_\mathbf{q}(1-f_\mathbf{q})\delta(\omega) + f^2_\mathbf{q}\delta(\omega + 2E(\mathbf{q})) + (1-f_\mathbf{q})^2\delta(\omega - 2E(\mathbf{q}))\Big] .
\end{aligned} \tag{4.11}$$

The first term in (4.11) is the quasiparticle contribution. It relates to the zero-frequency transport coefficient, i.e., the Drude weight in (2.18). The remaining two contributions arise from pair-breaking terms in (4.6), and they refer to the finite-frequency coefficients, i.e., the regular part in (2.19).

---

[1] In the remainder of the chapter $\hbar = k_B = 1$

[2] In the Heisenberg picture, $\dot{A}(t) = i\big[H, A(t)\big]$, where A is the operator which incorporates a dependency on time, whilst state vectors $|\psi\rangle$ are time-independent.

The analytical finding arising from (4.11) for the energy-current correlation function is meaningful only in the limit of $T/\Delta_w \to 0$ – with Δ_w the vortex energy gap as defined in Sec. 3.3.2 – where no gauge excitations are present. Yet, these results can be used to check and to interpret the numerical findings in their low-temperature limit. In this context, they are also useful to contrast a fictitious heat conductivity at finite temperature – arising from the vortex-free state – with that one including the effects of thermal gauge excitations, i.e., with a finite content of vorticity.

4.2 Exact diagonalization

Let us consider a finite-temperature scenario with thermal gauge fluctuations and vortices. This problem is no longer analytically solvable because of the distribution of the gauge fields $\eta_{\mathbf{r}}$ in real space. However, one may attack the problem via numerical calculations. The local energy density is similar to (4.1), but it has to include an on-site dependent gauge potential $\eta_{\mathbf{r}} = \pm 1$. This points out that the system is no more translational invariant. In view of this, to determine the energy current one can make use of a version of the continuity equation (2.6) that takes into account the real space site-dependent gauge variables. The energy current follows from (2.7) by using the polarization operator $\mathbf{P}$ [53]. I remind (2.7) in the following for the purposes of this section,

$$\mathbf{j} = \partial_t \mathbf{P} = i\big[\mathcal{H}, \mathbf{P}\big] \qquad \text{with} \qquad \mathbf{P} = \sum_{\mathbf{r}} \mathbf{r} h(\mathbf{r}). \tag{4.12}$$

Thus, the current can be obtained by computing the commutator in (4.12), and it follows as

$$\begin{aligned} j^\mu &= i \sum_{\mathbf{s},\mathbf{r}} \hat{\mu} \cdot \big[h(\mathbf{s}), \mathbf{r} h(\mathbf{r})\big] \\ &= i \sum_{\mathbf{s},\mathbf{r}} \hat{\mu} \cdot \mathbf{r} \big[J_x b_{\mathbf{s}} g_{\mathbf{s}+\mathbf{e}_x} + J_y b_{\mathbf{s}} g_{\mathbf{s}+\mathbf{e}_y} - J_z \eta_{\mathbf{s}} b_{\mathbf{s}} g_{\mathbf{s}} \, , \, J_x b_{\mathbf{r}} g_{\mathbf{r}+\mathbf{e}_x} + J_y b_{\mathbf{r}} g_{\mathbf{r}+\mathbf{e}_y} - J_z \eta_{\mathbf{r}} b_{\mathbf{r}} g_{\mathbf{r}}\big] \, , \end{aligned} \tag{4.13}$$

where $\mu = x, y$ refers to the specific component of the energy current on the 2D square lattice. The unit vectors $\mathbf{e}_x$ and $\mathbf{e}_y$ refer to those of Fig. 3.6(c). In (4.13), the operators $b_{\mathbf{r}} = (d^\dagger_{\mathbf{r}} + d_{\mathbf{r}})$, and $g_{\mathbf{r}} = (d^\dagger_{\mathbf{r}} - d_{\mathbf{r}})$ are used to compact the notation in the commutator. It can be verified that $b_{\mathbf{r}}$ and $g_{\mathbf{r}}$ satisfy the algebraic relations $\{b_{\mathbf{r}}, g_{\mathbf{s}}\} = 0$, $\{b_{\mathbf{r}}, b_{\mathbf{s}}\} = 2\delta_{\mathbf{r},\mathbf{s}}$, and $\{g_{\mathbf{r}}, g_{\mathbf{s}}\} = -2\delta_{\mathbf{r},\mathbf{s}}$. Considering these relations, one can compute the commutator, which leads to

$$\begin{aligned} j^\mu = i \sum_{\mathbf{r}} \hat{\mu} \cdot \Big\{ &- J_x J_z \big[\eta_{\mathbf{r}+\mathbf{e}_x} (\mathbf{r} + \mathbf{e}_x) b_{\mathbf{r}} b_{\mathbf{r}+\mathbf{e}_x} + \eta_{\mathbf{r}} (\mathbf{r} - \mathbf{e}_x) b_{\mathbf{r}} b_{\mathbf{r}-\mathbf{e}_x}\big] \\ &- J_y J_z \big[\eta_{\mathbf{r}+\mathbf{e}_y} (\mathbf{r} + \mathbf{e}_y) b_{\mathbf{r}} b_{\mathbf{r}+\mathbf{e}_y} + \eta_{\mathbf{r}} (\mathbf{r} - \mathbf{e}_y) b_{\mathbf{r}} b_{\mathbf{r}-\mathbf{e}_y}\big] \\ &+ J_x J_y \big[(\mathbf{r} + \mathbf{e}_x - \mathbf{e}_y) b_{\mathbf{r}} b_{\mathbf{r}+\mathbf{e}_x-\mathbf{e}_y} + (\mathbf{r} + \mathbf{e}_y - \mathbf{e}_x) b_{\mathbf{r}} b_{\mathbf{r}+\mathbf{e}_y-\mathbf{e}_x}\big] \Big\} \end{aligned} \tag{4.14}$$

Equation (4.14) can be further simplified, and it can be written as

$$j^\mu = 2 i J_\mu \sum_{\mathbf{r}} \Big(J_z \eta_{\mathbf{r}} b_{\mathbf{r}} b_{\mathbf{r}-\mathbf{e}_\mu} + \tau_\mu J_{\bar{\mu}} b_{\mathbf{r}} b_{\mathbf{r}+\mathbf{e}_x-\mathbf{e}_y} \Big) \, , \tag{4.15}$$

where $\bar{\mu} = y(x)$, and $\tau_\mu = +(-)$, when $\mu = x(y)$. The energy current is diagonal in the gauge field, thus one can write the energy-current auto-correlation function as follows,

$$C(t) = \frac{1}{ZN} \operatorname{Tr}_\eta \left(Z_{d(\eta)} \underbrace{\langle j(t) j \rangle_{d(\eta)}}_{C(\eta,t)} \right). \tag{4.16}$$

In (4.16) I consider the longitudinal correlation function, dropping off indices $\mu = \nu$ of the current operators. The subscript $d(\eta)$ relates to a trace over matter fermions for a fixed gauge field sector $\eta = (\eta_1, \ldots, \eta_N)$. The $\langle \cdots \rangle_{d(\eta)}$ provides the correlation function $C(\eta, t)$ related to the gauge sector η. Each of these functions is weighted by its sector's partition function $Z_{d(\eta)}$, which sum up to the total partition function Z – I would refer the reader to Appendix C.1 for further insights on the thermodynamic of the model.

To evaluate numerically each $C(\eta, t)$, and thus (4.16), I resort to exact diagonalization (ED) in the *fermion* basis. The method yields all eigenenergies and eigenvectors of the Hamiltonian in (3.40). The ED allows the evaluation of ground state properties as well as finite temperature static or dynamic quantities. The method can treat systems with limited dimension of the Hilbert space $\propto K^N$, where K is the number of local quantum states, and N the lattice size. Indeed, the processing time of ED routines scales exponentially with the dimension d of the Hamilton matrix to diagonalize as $\sim \mathcal{O}(d^3)$.

For instance, the Kitaev honeycomb model in (3.6) has 2^{2N} states. Thus, the ED in the *spin* basis turns to be restricted to a modest number of unit cells $N \lesssim 10$. In the fermion basis, one can define a $2N$ component operator $\mathbf{D}^\dagger = (d_1^\dagger, \ldots, d_N^\dagger, d_1, \ldots, d_N)$. The indices $\{1, \ldots, N\}$ refer to all sites $\mathbf{r}$ of the square lattice in Fig. 3.6(c). In terms of $\mathbf{D}^\dagger$ the Hamiltonian and the energy current operator are set up in real space as

$$\mathcal{H} = \underbrace{\begin{pmatrix} d_1^\dagger \\ \vdots \\ d_N^\dagger \\ d_1 \\ \vdots \\ d_N \end{pmatrix}^{\mathbf{T}}}_{\mathbf{D}^\dagger} \big[\mathrm{H}(\eta)\big]_{2N\times 2N} \overbrace{\begin{pmatrix} d_1 \\ \vdots \\ d_N \\ d_1^\dagger \\ \vdots \\ d_N^\dagger \end{pmatrix}}^{\mathbf{D}}, \qquad j = \underbrace{\begin{pmatrix} d_1^\dagger \\ \vdots \\ d_N^\dagger \\ d_1 \\ \vdots \\ d_N \end{pmatrix}^{\mathbf{T}}}_{\mathbf{D}^\dagger} \big[\mathrm{L}(\eta)\big]_{2N\times 2N} \overbrace{\begin{pmatrix} d_1 \\ \vdots \\ d_N \\ d_1^\dagger \\ \vdots \\ d_N^\dagger \end{pmatrix}}^{\mathbf{D}}. \tag{4.17}$$

Both the Hamiltonian $\mathcal{H}$ and the energy current j in (4.17) have $2N \times 2N$ matrices that depend on the gauge field sector considered $\eta = (\eta_1, \ldots, \eta_N)$. For each given η, one can perform a numerical Bogoliubov transformation $\mathbf{B}$ which maps the Hamiltonian in (4.17) to $\tilde{\mathcal{H}} = \frac{1}{2}\mathbf{A}^\dagger \mathbf{E} \mathbf{A}$, where $\mathbf{A}^\dagger = (a_1^\dagger, \ldots, a_N^\dagger, a_1, \ldots, a_N)$ are quasiparticle fermions introduced via $\mathbf{A}^\dagger = \mathbf{D}^\dagger \mathbf{B}$. The matrix $\mathbf{E}$ is diagonal with $\operatorname{diag}(\mathbf{E}) = (E_1, \cdots, E_N, -E_1, \ldots, -E_N)$, where E_j are the quasiparticle energies.

Performing this transformation requires to account for some facts. $\mathbf{B}$ is a *linear transformation* combining creation and annihilation operators, which must preserve the algebraic relations among them. It means that for any given operator $a_j^{(\dagger)}$ the fermion anticommuting relations $\{a_j, a_k^\dagger\} = \delta_{j,k}$ and $\{a_j, a_k\} = \{a_j^\dagger, a_k^\dagger\} = 0$ must hold.

Yet, in case of degenerate eigenspaces, there is an issue with standard Gram-Schmidt orthogonalized transformation matrix usually adopted to diagonalize $\mathcal{H}$. The algorithm does not consider such a mixing of particle-hole states. It provides an unphysical transformation which does not preserve the algebraic relations aforementioned.

To deal with this numerical issue, one needs to modify the transformation matrix **T** provided by standard diagonalization routines. In this work, I resort to the EISPACK linear algebra libraries [124] for the aforementioned routines, in particular to *tred2* [125] and *tql2* [126]. The former reduces the real symmetric matrix $\mathrm{H}(\eta)$ to a symmetric tridiagonal one, with an orthogonal transformation matrix arising from the reduction. The latter finds the eigenvalues and eigenvectors of the tridiagonal matrix obtained via the *tred2* algorithm. The transformation matrix **T** has to be adapted to the Bogoliubov problem, in particular it turns out that

$$\mathbf{T} \to \mathbf{B} = \left(\begin{array}{c|c} U_{\alpha,\beta} & V_{\alpha,\beta+N} \\ \hline V_{\alpha+N,\beta} & U_{\alpha+N,\beta+N} \end{array}\right) , \tag{4.18}$$

with $\alpha, \beta = 1, \dots, N$, and U, V being $N \times N$ coefficients matrices. The modification of **T** into **B** in (4.18) satisfies

$$\begin{aligned} \{a_j^\dagger, a_k^\dagger\} &= \left\{ \sum_{i=1}^{N} \Big(u_{i,j} d_i^\dagger + v_{i+N,j} d_i \Big) , \sum_{m=1}^{N} \Big(u_{m,k} d_m^\dagger + v_{m+N,k} d_m \Big) \right\} \\ &= \sum_{i,m=1}^{N} \big[u_{i,j} v_{m+N,k} \delta_{i,m} + v_{i+N,j} u_{m,k} \delta_{i,m} \big] = \sum_{i=1}^{N} \big[u_{i,j} v_{i+N,k} + v_{i+N,j} u_{i,k} \big] = 0 , \end{aligned} \tag{4.19}$$

$$\begin{aligned} \{a_j, a_k^\dagger\} &= \left\{ \sum_{i=1}^{N} \Big(v_{i,j} d_i^\dagger + u_{i+N,j} d_i \Big) , \sum_{m=1}^{N} \Big(u_{m,k} d_m^\dagger + v_{m+N,k} d_m \Big) \right\} \\ &= \sum_{i,m=1}^{N} \big[v_{i,j} v_{m+N,k} \delta_{i,m} + u_{i+N,j} u_{m,k} \delta_{i,m} \big] = \sum_{i=1}^{N} \big[v_{i,j} v_{i+N,k} + u_{i+N,j} u_{i,k} \big] = \delta_{j,k} , \end{aligned} \tag{4.20}$$

such that the Bogoliubov diagonalization is well defined and physically meaningful. Therefore, the energy-current auto-correlation function at a fixed gauge sector η, in the quasiparticle basis, reads as

$$C(\eta, t) = \frac{1}{N} \sum_{nm} \sum_{n'm'} \langle \mathbf{A}_n^\dagger(t) L_{nm} \mathbf{A}_m(t) \mathbf{A}_{n'}^\dagger L_{n'm'} \mathbf{A}_{m'} \rangle , \tag{4.21}$$

where $L = \mathbf{B}^\dagger \mathrm{L}(\eta) \mathbf{B}$. In order to compute (4.21), a Wick's decomposition is performed. The idea is – as for (4.9) – to reduce (4.21) into a sum of products of single-particle propagators. I report in the following the result of contractions – I refer the reader to the Appendix A.2 for further details – which reads as

$$\begin{aligned} C(\eta, t) = \frac{1}{N} \sum_{n,m=1}^{N} \Big[& e^{-i(E_n - E_m)t} f_n (1 - f_m) L^{(\mathbf{1})}(n, m) + e^{i(E_n - E_m)t} f_m (1 - f_n) L^{(\mathbf{2})}(n, m) \\ & + e^{-i(E_n + E_m)t} f_n f_m L^{(\mathbf{3})}(n, m) + e^{i(E_n + E_m)t} (1 - f_n)(1 - f_m) L^{(\mathbf{4})}(n, m) \Big] , \end{aligned} \tag{4.22}$$

where $L^{(\mathbf{k})}(n, m)$ refer to four distinct combinations of current matrix elements related to the four possible contractions arising from (4.21), and $\langle a_n^\dagger a_n \rangle \to f_n$, with $f_n = \big(\exp(\beta E_n) + 1\big)^{-1}$

the Fermi-Dirac distribution. Equation (4.22) is weighted with its related sector's partition function $Z_{a(\eta)}$. The evaluation of the energy-current auto-correlation function as in (4.16) is completed summing up over all contributions given by (4.22) for all the gauge sectors η. Relations with the transport coefficient derived in (2.15 - 2.17) can be shown by Fourier transform (4.22) in the frequency space, which reads

$$\begin{aligned} C(\eta,\omega) = \frac{2\pi}{N} \sum_{n,m=1}^{N} \Big[& L^{(\mathbf{1})}(n,m) f_n (1-f_m) \delta\big(\omega - (E_n - E_m)\big) \\ & + L^{(\mathbf{2})}(n,m) f_m (1-f_n) \delta\big(\omega + (E_n - E_m)\big) \\ & + L^{(\mathbf{3})}(n,m) f_n f_m \delta\big(\omega - (E_n + E_m)\big) \\ & + L^{(\mathbf{4})}(n,m) (1-f_n)(1-f_m) \delta\big(\omega + (E_n + E_m)\big) \Big] . \end{aligned} \tag{4.23}$$

Equation (4.23) relates to the quantity $\langle \cdots \rangle \langle \cdots \rangle \delta(\omega + \varepsilon_l - \varepsilon_m)$ in (2.16). Two contributions arise from (4.23) : quasiparticle – with $E_n E_m > 0$ – and pair-breaking – with $E_n E_m < 0$ – contribution. The zero-frequency Drude weight D can be acquired from a degeneracy plateau, i.e., for E_n and E_m such that $\mid E_n - E_m \mid < \delta\omega^*$, where $\delta\omega^*$ is the numerical energy window used as degeneracy cut-off.
Finite-frequency terms in (4.23) recover the regular part of (2.16).

To compute the Dirac's delta function $\delta(\omega - E_{nm})$ in (4.23) I use *binning* of δ functions in a window of size $\delta\omega$ – see further details in Appendix A.3. This window sets the resolution of the spectra, and it has been adjusted to reduce finite size effects best – see Appendix B.2. The numerical findings via the ED method allows to study exactly the transport coefficients for systems up to $N = 36$ fermion sites. This system size corresponds to a huge Hilbert space dimension of the underlying spin model in (3.6) which consists of 2^{72} states.

The achievement of such a large Hilbert space has required the use of lattice symmetry to reduce the computational effort – I refer the reader to Appendix B.1 for further details. Indeed, for each given gauge sector, one can have a certain number of flipped gauge fields $\eta_{\mathbf{r}}$ with respect the uniform gauge sector. Translations along the lattice vectors $\mathbf{e}_x$ and $\mathbf{e}_y$ of the flipped gauge fields provide translational invariant gauge sectors. The invariant gauge sectors show degenerate energy spectra, as well as same correlation spectra, and one can collect all of these invariant sectors in a single gauge sector η having a multiplicity $m^\star_\eta$ – results from this analysis are reported in Appendix B.1.

Therefore, the trace over all gauge sectors in (4.16) is reduced to a trace over not equivalent gauge sectors under translational symmetry, where each $C(\eta, t)$ from (4.22) is counted $m^\star_\eta$-times.
Results from the ED method suffers from finite-size effects, and a study of systems approaching the thermodynamic limit is desirable. In this context, I will introduce in the next section an approximate numerical approach to study larger systems.

4.3 Average gauge configuration

In this section, I present an approximate way to calculate the energy-current auto-correlation function. The approximate method – also employed in Ref. [127] to study the quasi-1D Kitaev ladder – will allow to reach much larger system sizes, up to $\sim \mathcal{O}(100)$ larger than the

systems studied via the ED approach, and shown in Sec. 4.2. This method will be used to get closer to the thermodynamic limit, aiming to suppress possible finite-size effects.
The approximation consists of replacing the full trace over all gauge sectors η in (4.16) by a trace only over dominant set of gauge sectors. The term *dominant* means fixing the number of excited gauge fields to its *mean value* $n(T)$, which can in principle be temperature dependent. The $n(T)$ can be thought as a mean density of thermal gauge excitations off the vortex-free state. In view of this, the evaluation of (4.16) by tracing over all the gauge sectors turns out to be reduced to a *disorder problem* with an emergent temperature-dependent defect density set by the excited gauge fields, and given by

$$C(t) \approx \frac{1}{N} \langle \underbrace{\langle j(t) j \rangle_{a(\eta)}}_{C(\eta,t)} \rangle_{n(T)} \,. \tag{4.24}$$

In (4.24) I consider as in (4.16) an expression for the longitudinal energy-current autocorrelation function, and I drop off indices for the current components. The energy current is considered in the quasiparticle basis $a^{(\dagger)}$, hence $\langle \cdots \rangle_{a(\eta)}$. Because of the *average* over gauge configurations with $n(T)$ – given as $\langle \cdots \rangle_{n(T)}$ in (4.24)– the method has been referred to as average gauge configuration (AGC) method [128, 129].

The nature of the mean value $n(T)$ is only meaningful if the fluctuations around it are not too large, i.e., $\delta n(T) \ll n(T)$. Therefore, the latter sets a constraint on the temperature range within which the AGC method can be applied. To estimate this temperature range, I resort to ED to evaluate exactly the mean density of gauge excitations $n(T)$

$$n(T) = \frac{1}{ZN} \, \mathrm{Tr}_{\eta} \, Z_{a(\eta)} n_{\eta} \ , \tag{4.25}$$

and its fluctuations $\delta n(T)$. In (4.25) n_η is the number of the flipped gauge fields off the vortex-free sector, excluding degenerate vortex-free configurations – I refer the reader to Appendix C.1 for further details. Yet, I also evaluate the flux density $\Phi(T)$

$$\Phi(T) = \frac{1}{ZN} \, \mathrm{Tr}_{\eta} \, Z_{a(\eta)} \sum_{\mathbf{r}} w_{\mathbf{r}} \ , \quad \text{with} \ w_{\mathbf{r}} = \eta_{\mathbf{r}} \eta_{\mathbf{r}+\mathbf{e}_x-\mathbf{e}_y} \ , \tag{4.26}$$

and its temperature derivative $\Phi'(T)$. In (4.26) $w_{\mathbf{r}}$ relates to the flux (vortex) of the square-lattice plaquette in between of $\mathbf{r}$ and $\mathbf{r}+\mathbf{e}_x-\mathbf{e}_y$ sites. Indeed, one can note that a mean-field description in terms of thermally excited *vortices* using $\Phi(T)$ would be more appropriate than a mean-field description in terms of excited gauge fields [3]. In the quasi-1D Kitaev ladder model, this is possible treating vortices as 1D domain walls in terms of gauge fields [128]. On the 2D Kitaev model I am not aware of a simple mapping between $n(T)$ and $\Phi(T)$. Thus, I study both to confine the method to temperatures where either $n(T)$ or $\Phi(T)$ behave similarly.
Figures 4.1(a) and 4.1(b) show the ED results for systems with $N = 6 \times 6$ lattice sites, in the isotropic regime – that lies in the gapless phase of the 2D Kitaev model.
In the following – referring to the phase diagram of Fig. 3.3(b) – I make use of a parameter α to tune the exchange couplings in the Kitaev Hamiltonian of (3.40), such that $J_x = J_y = \alpha$, and $J_z = 3 - 2\alpha$. The fermion energy scale $(J_x + J_y + J_z)/3 = 1 \equiv J$ is kept constant while

---

[3] Due to Kitaev model degeneracy under inversion of all gauge fields $\eta_{\mathbf{r}}$ of z bonds along any $x-y$ chains [123, 128] – see Sec. 3.4 – vortex-free states also arise from configurations with a finite number of gauge excitations. This makes $n(T)$ not completely well defined at all temperatures.

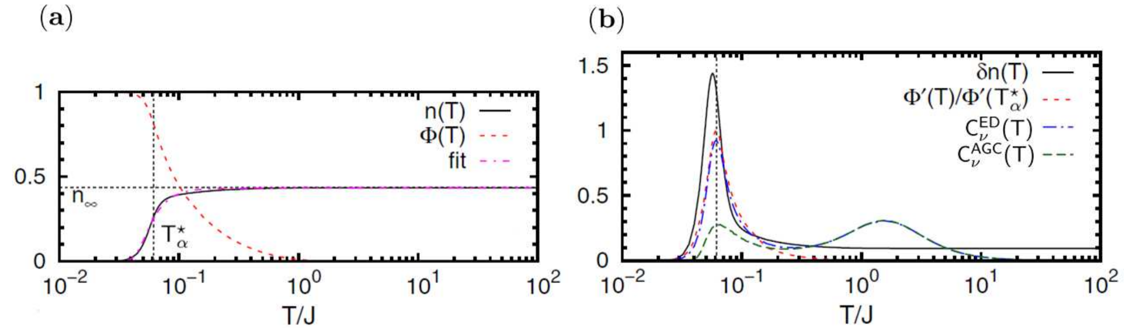

Figure 4.1: (a) Mean density of gauge excitations $n(T)$ and flux density $\Phi(T)$ vs. T for $\alpha = 1.0$. A fit function used in the crossover region, $n(T) \sim 1/[\exp(\Delta/T)^b + 1]$, is shown, with $\Delta = 0.06$, and $b = 3.5$. The limit mean value, $n_\infty = 0.434$ is displayed (horizontal grey-dashed line). The ED calculations relate to $N = 6 \times 6$ lattice sites. (b) Fluctuations of mean density of gauge excitations $\delta n(T)$, and derivative of flux density $\Phi'(T)$ normalized to its minimum value at $T^\star_\alpha$, $\Phi'(T^\star_\alpha) = -15.16$. The specific heat C_ν from both the ED and AGC methods is shown. The fit function $n(T)$ in (a) is considered for the AGC calculations. For the AGC, $N = 20 \times 20$ sites are considered, with a number of gauge sets $N_R = 20000$. The vertical grey-dashed line indicates the location of $T^\star_\alpha \sim 0.06\,J$. Figure adapted from Ref. [128]

exploring both the gapless and the gapped regime, for $1 > \alpha > 0.75$, and $0.75 > \alpha > 0$, respectively. The *isotropic* regime is set by $\alpha = 1$.

In Fig. 4.1(a), at very low temperatures, $n(T)$ and $\Phi(T)$ reproduce the expected vortex-free state. Upon increasing the temperature, around $T \sim 0.03\,J$ – which is yet below the $\mathbb{Z}_2$-flux energy gap $\Delta_w \simeq 0.26\,J$ [14] – collective thermal gauge excitations give rise to a rapid increase of $n(T)$, followed by a downturn of $\Phi(T)$, and a region of large fluctuations $\delta n(T) > n(T)$ – see Fig. 4.1(b). For $T \geq 0.1\,J \equiv T_R$, the system is set in a *fully random* gauge sector, where in the limit of infinite temperature $n(T \to \infty) = n_\infty \simeq 0.434$ **[4]**, and $\Phi(T \to \infty) = 0$. Within the latter regime, the system can be considered as free matter fermions scattering from a completely random binary potential.
In the *crossover* region, $n(T) \sim \big(\exp(\Delta/T)^b + 1\big)^{-1}$, with $\Delta = 0.06$, and $b = 3.5$ for the finite system considered. This kind of abrupt transition may likely arise from gauge-gauge interactions **[5]**.

In view of the ratio $\delta n(T)/n(T)$, and of $\Phi'(T)$ as a function of temperature – see Figs. 4.1(a,b), the AGC method will work quite well for $T > T_R$. An indication for this can be provided by contrasting the specific heat $C_\nu(T)$ evaluated via both the ED and the AGC method, as a function of temperature – see Appendix C.1 for further details. For the AGC calculations, one can use the mean density $n(T)$ as from ED, and to perform an average over N_R gauge fields sets that fulfill $n(T)$ – which for this calculation will be $N_R = 2 \cdot 10^4$. The two specific heat are compared in Fig. 4.1(b). The agreement to the exact result is very good down to $T \approx T_R$, below which the AGC fails to reproduce the ED result.

---

[4] For $T \to \infty$, (4.25) leads to a mean density of gauge excitations arising from combinatorial calculation, i.e., $n_\infty = \sum_{k=0}^{N} n_\eta(k)\binom{N}{k}/(N2^N)$. The latter for finite system size $N = 6 \times 6$ yields $n_\infty \simeq 0.434$.

[5] Noninteracting gauge excitations in a free lattice gas are gapped by $\Delta_w \simeq 0.26\,J$, thus one would expect $n(T) \sim \big(\exp(\Delta_w/T) + 1\big)^{-1}$ – see Ref. [127]

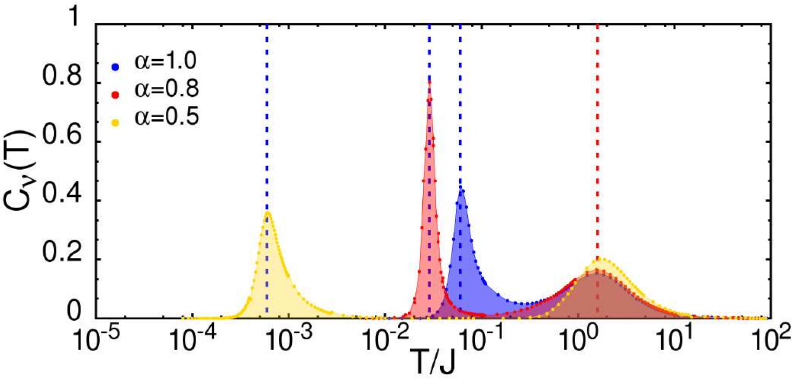

Figure 4.2: Temperature dependence of the specific heat $C_\nu(T)$ for anisotropy values $\alpha = 1.0, 0.8, 0.5$, with $J_x = J_y = \alpha$ and $J_z = 3 - 2\alpha$, based on ED thermodynamics performed on $N = 6 \times 6$ sites system. Blue-dashed lines locate the position of the low-temperature crossover $T^\star_\alpha$, whereas the red-dashed line indicates the position of the high-temperature crossover T_M. Figure taken from Ref. [129]

The specific heat $C_\nu = T\partial S/\partial T$ provides a measure of the release of entropy $S(T)$. For the Kitaev model, the specific heat consists of two-peak structure [130]. This structure is related to the release of entropy at two different energy scales: from the gauge degrees of freedom (vortices) and the matter fermions, at $T^\star_\alpha$ and $T_M \sim J$, respectively.

The ED specific heat in Fig. 4.1(b) shows both the characteristic peaks, that develop at $T^\star_\alpha \simeq 0.06\,J$, and $T_M \sim J$ – one might also see consistency of this finding with the specific heat arising from QMC calculations of Ref. [130], and shown in Sec. 5.4.

The AGC specific heat shown in Fig. 4.1(b) – by construction – does not account for all the entropy release, due to large gauge fluctuations at the low-temperature crossover.

Therefore, for the isotropic regime of the model, one can conclude that the AGC calculations are reliable for $T_R < T < \infty$. For this temperature range, the energy-current autocorrelation function in (4.24) can be computed by averaging over fully random gauge sets, i.e., for $n(T) = 0.5$. The number of gauge fields sets N_R used for the average has been adjusted *a posteriori* to reduce finite-size effects best. Simulations with different N_R have been contrasted to each other, and I report results in the Appendix B.2.

Finally, one may wonder whether the *anisotropy* of couplings may play some role in the conclusions derived on the AGC applicability for the isotropic regime.

In this context, I have computed and contrasted to each other the specific heat for different values of α, for either gapless or gapped phases of the model – I refer the reader to Sec. 5.4 for a comparison with QMC findings in Ref. [130].

I resort to the ED – as for the isotropic case – considering systems with $N = 6 \times 6$ sites. Results are shown in Fig. 4.2. Three cases are plotted with colored shaded curves: $\alpha = 1$ (blue), $= 0.8$ (red), and $= 0.5$ (yellow). The former two lie in the gapless phase, whilst the last one in the gapped phase. The expected two peaks develop at $T^\star_\alpha$ (blue dashed line) and T_M (red dashed line).

Some comments about findings. First, the high-temperature peak at T_M remains rather insensitive to the degree of anisotropy α, and weakly affected by the gauge disorder. This feature is consistent with the fermion energy scale set by J – as discussed in Sec. 3.3.3. Second, the low-temperature peak at $T^{\star}_{\alpha}$ is strongly shifted to smaller temperatures, upon increasing the anisotropy, with $T^{\star}_{1.0} \sim 0.06\,J$, $T^{\star}_{0.8} \sim 0.029\,J$, and $T^{\star}_{0.5} \sim 0.00064\,J$. This is consistent to the scaling of the energy to excite a single pair of vortices in the system entering in the gapped phase A - see Sec. 3.3.3. Therefore, while in principle $T^{\star}_{\alpha}$ sets a specific temperature scale for each α – above which averaging over fully random gauge sets is reliable – I will refer to the maximum of these, i.e., $T^{\star,\mathrm{max}}_{\alpha} \sim \mathcal{O}(0.1)\,J$ as the lowest temperature to apply AGC for all calculations, independent of α.

CHAPTER 5

Heat transport results

In this chapter, I will show the results obtained for thermal transport in the Kitaev honeycomb model. These results are based on the formal developments from the preceding chapters. The strategy pursued is to evaluate the longitudinal dynamical energy-current auto-correlation function, from which various transport properties are extracted, in particular, the dc-limit of heat conductivity. These quantities are studied in a wide range of temperatures, which allows to explore the impact of thermal gauge disorder. Also the role of anisotropic exchange couplings on heat transport is considered. This allows to cover heat conductivity for both gapless and gapped phases of the model. In this context, results from both analytical calculations in the uniform gauge (vortex-free) sector, and numerical calculations for the system with vortices are presented. The numerical results are obtained via a complementary use of both the ED and the AGC methods. The related sets of results are compared and discussed. A comparison with recent heat transport results from quantum Monte Carlo investigations [131] is also presented. Results from contrasting bulk transport quantities – for two distinct boundary conditions in the model – are also shown.

5.1 Analytical results

As discussed in Sec. 4.1, the vortex-free state allows for analytical expression of correlation functions. I recall in the following the expression found as in (4.11), which is used to compute the longitudinal transport coefficients,

$$C(\omega) = \frac{2\pi}{N}\sum_{\mathbf{q}} 2l_{\mathbf{q}}^2\Big[2f_{\mathbf{q}}(1-f_{\mathbf{q}})\delta(\omega) + f_{\mathbf{q}}^2\delta(\omega+2E(\mathbf{q})) + (1-f_{\mathbf{q}})^2\delta(\omega-2E(\mathbf{q}))\Big]\,. \tag{5.1}$$

In (5.1), $N = 10^6$ is the system size, $l_{\mathbf{q}}$ are the current matrix elements from (4.6), $f_{\mathbf{q}}$ is the Fermi-Dirac distribution, and $E(\mathbf{q})$ the quasiparticle energy. Three contributions arise from (5.1): a zero-frequency term, i.e., $\sim \delta(\omega)$, which is the quasiparticle contribution. The latter is related to the spectral weight of the *ballistic* channel, i.e., $\sim T^2 D$, where D is the Drude weight – see equation (2.18). The remaining two finite-frequency contributions arise from pair-breaking terms in (4.6). These latter relate to the regular part of the spectrum, and thus to the spectral weight of the *dissipative* channel – see equation (2.19). Findings from (5.1) in principle only represent the limit $T \to 0$. At such temperature limit, the number of occupied quasiparticle states at energy $E(\mathbf{q})$ goes to zero, i.e., $f_{\mathbf{q}} \to 0$. Therefore, the

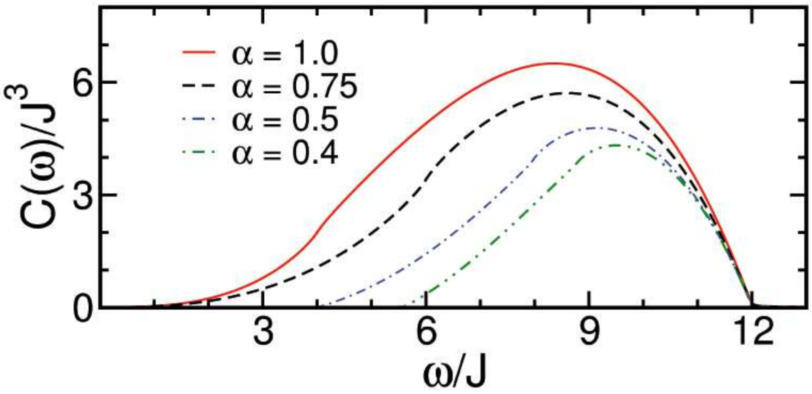

Figure 5.1: Regular part of the dynamical energy-current auto-correlation function $C(\omega)$ vs. frequency $\omega > 0$ at $T = 0$, in the vortex-free state, for various $\alpha = 1 \cdots 0.4$, ranging from gapless to gapped phases.

correlation function in (5.1) is given by

$$C(\omega, T = 0) = \frac{2\pi}{N} \sum_{\mathbf{q}} 2 l_{\mathbf{q}}^2 \delta(\omega - 2E(\mathbf{q})) \,. \tag{5.2}$$

I show the results from (5.2) in Fig. 5.1. It displays the regular part of the dynamical energy-current auto-correlation function versus frequency. It is considered for various values of anisotropy α of exchange couplings – α defined as in Sec. 4.3, covering both gapless and gapped phases of the model.
Only the spectrum at $\omega > 0$ is shown, since $C(-\omega) = e^{-\beta\omega} C(\omega)$, as required by detailed balance. The latter relation follows from the periodicity of the correlation function $C_{\mu\nu}(-t) = C_{\nu\mu}(t - i\tau)$ [53, 132] – where τ is the imaginary time, having units of β – and its Fourier transform. [1] . It covers the relation between the correlation spectrum and the imaginary part of the linear response function $\chi_{\mu\nu}$ in (2.8) – i.e., $\mathbb{Im}\{\chi_{\mu\nu}(\omega)\} = \frac{1}{2}(1 + e^{-\beta\omega}) C_{\mu\nu}(\omega)$ [53, 132] – i.e., between the *fluctuations* and *dissipation*, respectively.
The low-frequency part of the spectrum in Fig. 5.1 reflects the structure of the low-energy quasiparticle density of states [130] combined with the energy current. In particular, for $\alpha = 1, 0.75$ the matter fermion spectrum is gapless [130], which gives rise to a power-law behavior as $C(\omega) \sim \omega^3$. The opening of a one-particle energy gap Δ_f in the matter fermion spectrum for $\alpha = 0.5, 0.4$, leads to a linear onset above a finite two-particle excitation gap $\xi \simeq 2\Delta_f$. Moreover, the spectra show a weak van-Hove singularity related to a saddle point in the energy dispersion $E(\mathbf{q})$, which is barely noticeable on the scale of plotted spectra. For instance, the gapless cases at $\alpha = 1$ and $\alpha = 0.75$ – shown in Fig. 5.1 – have a logarithmic-singular derivative of $C(\omega)$ at $\omega \approx 4\,J$ and $\omega \approx 6\,J$, respectively.

In the vortex-free state, the totality of quasiparticle transport is accumulated into the Drude weight $D(T)$, which depends on the temperature. The latter is proportional to the zero-frequency coefficient in (5.1) divided by T^2 – according to (2.18).

In Fig. 5.2 I show the temperature dependence of the Drude weight for the same anisotropies as in Fig. 5.1. Within the temperature range considered, it follows that $D(T)$ is finite either in gapless or gapped phases. $D(T)$ has a peak – regardless of anisotropy – around the fermion

---

[1] $C_{\mu\nu}(-\omega) = \int dt e^{i\omega t} C_{\mu\nu}(-t) = \int dt e^{i\omega t} C_{\nu\mu}(t - i\tau) = \int dt e^{i\omega(t+i\tau)} C_{\nu\mu}(t) = e^{-\tau\omega} C_{\nu\mu}(\omega)$.

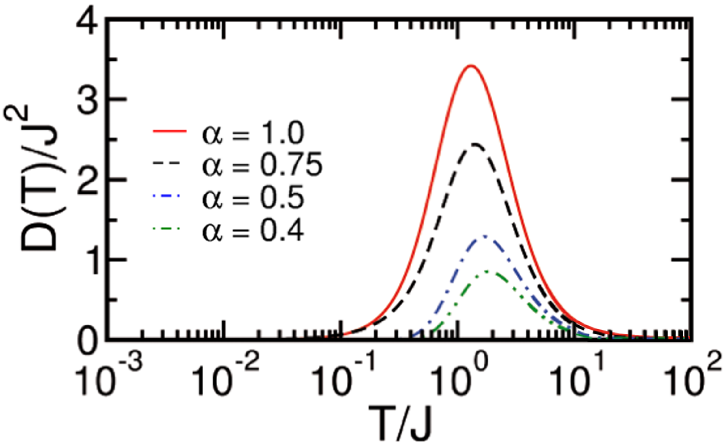

Figure 5.2: Drude weight $D(T)$ vs. temperature T, in the vortex-free state, for various $\alpha = 1 \cdots 0.4$, ranging from gapless to gapped phases.

energy scale J. There is a qualitative change in the low-temperature dependence of $D(T)$, as systems cross over from gapless to gapped phases. In the former, the Drude weight shows a power-law behavior as $D(T) \sim T^2$, while in the latter it shows an exponential behavior with $D(T) \sim \exp(-\Delta/T)$, and $\Delta \simeq \Delta_f$.

Figures 5.3(a,b) help to fortify the previous statements. In particular, Fig. 5.3(a) shows $D(T)/T^2$ versus T, for $\alpha = 1$ (gapless), and $\alpha = 0.5$ (gapped). The plot verifies two facts: a nonzero $D(T)$ at finite temperature for both phases, and the two distinct low-temperature behaviors. The inset in Fig. 5.3(a) emphasizes the exponential activation for the gapped case. A fit curve (light blue) $\propto T^{-2}\exp(-\Delta/T)$ is superimposed onto data, with $\Delta = 2.09$ – where for $\alpha = 0.5$ the one-particle energy gap is $\Delta_f = 2$. The low-temperature behavior of $D(T)$ can be also roughly estimated via a power counting from (5.1),

$$
\begin{aligned}
D(T) \propto \frac{C(\omega=0,T)}{T^2} &\approx \frac{1}{T^2}\int dE\rho(E)l(E)^2 f(E)\big(1-f(E)\big) \\
\propto &\begin{cases} \dfrac{T^4}{T^2}\displaystyle\int dx\rho(x)l(x)^2\frac{e^x}{(1+e^x)^2}\,, & \text{if} \quad E{=}E(\mathbf{q}){\sim}\mathbf{q},\ x{=}\dfrac{E}{T} \\ \dfrac{T^2e^{-\Delta/T}}{T^2}\displaystyle\int dx\rho(x)l(x)^2\frac{e^x}{(1+e^x)^2}\,, & \text{if} \quad E{=}E(\mathbf{q}){\sim}(\mathbf{q}^2{+}\Delta^2)^{\frac{1}{2}},\ x{=}\dfrac{(E{-}\Delta)}{T}. \end{cases}
\end{aligned}
\tag{5.3}
$$

In (5.3) $\rho(E)$ is the density of states, and $\sum_{\mathbf{q}} \to \int dE\rho(E)$. The energy current matrix elements follow from (4.7). Moreover, I assume that for $T \to 0$ the quasiparticle energy dispersion can be approximated as in (5.3) – which, at least in the gapless case, describes acceptably well the Dirac-cone like dispersion at the isotropic point.
Finally, in Fig. 5.3(b) I show results for the ratio of the ballistic spectral weight, $T^2D(T)$, with the integrated regular spectrum $I_0(T)$, as a function of temperature. The latter is given by integrating all finite-frequency spectral contributions at temperature T, i.e., $⨍_{-\infty}^{\infty} C(\omega,T)d\omega$. The ballistic spectral weight displays a similar size to that of the integrated regular spectral weight. This fact, together with the other aspects above discussed, suggest that within the vortex-free state, the system is a *ballistic heat conductor* at $T > 0$.

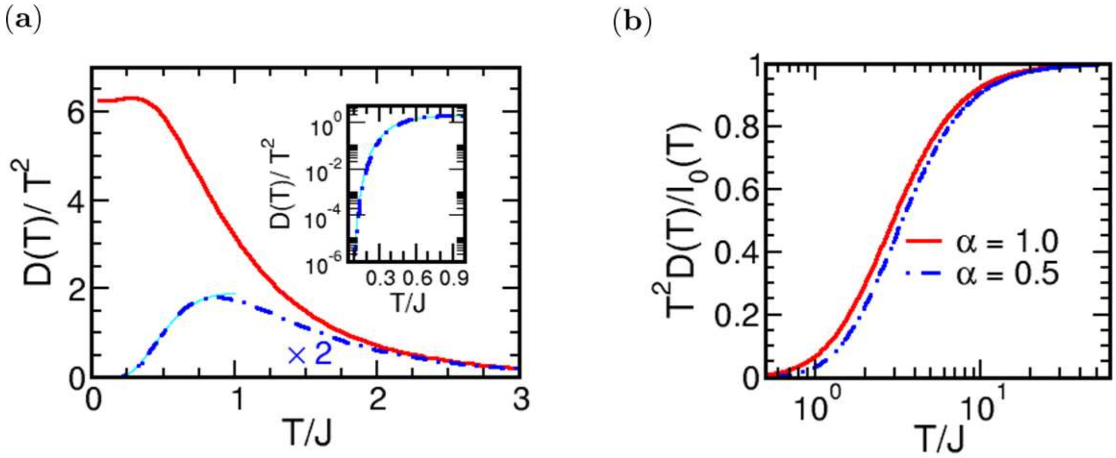

Figure 5.3: (a) Drude weight $D(T)/T^2$ vs. T for $\alpha = 1$ (gapless) and $\alpha = 0.5$ (gapped), in the vortex-free state. Inset: low-T zoom-in with fitting curve superimposed onto data for the gapped phase. (b) Ballistic weight $T^2D(T)$ normalized to the weight of the regular part $I_0(T) = ⨍_{-\infty}^{\infty} C(\omega,T)d\omega$ vs. T, for same anisotropies as in (a).

5.2 Numerical results: isotropic case

In the following, I present numerical results obtained via both the ED and the AGC approach. The results refer only to the isotropic point of the Kitaev honeycomb model. Thus, the heat transport properties extracted relate to the gapless phase of the model.

5.2.1 ED results

I recall – for the purpose of this section – the expression for the dynamical energy-current auto-correlation function as in (4.16), provided in Sec. 4.2,

$$C(t) = \frac{1}{ZN}\,\mathrm{Tr}_\eta\left(Z_{a(\eta)}\underbrace{\langle j(t)j\rangle_{a(\eta)}}_{C(\eta,t)}\right), \tag{5.4}$$

where $C(\eta, t)$ is the correlation function for each given gauge sector η, as in (4.22). Each function $C(\eta, t)$ is Fourier transformed in the frequency space – see equation (4.23) – and adding up all over the contributions from all gauge sectors completes the evaluation of (5.4) in the frequency space. Each contribution is weighted by its sector's partition function $Z_{a(\eta)}$. The method allows for a finite-temperature study of the correlation function, and it takes into account thermal gauge excitations.

In Fig. 5.4(a) I show the frequency dependence of the energy-current auto-correlation function from (5.4) evaluated for systems with $N = 36$ lattice sites. It is presented for three temperature regimes, from $T = 0.1\,J$ to $T = 100\,J$.

Let us start by commenting on the spectrum at the lowest temperature $T = 0.1\,J$. For this case, the δ function in (4.23) is binned in windows of $\delta\omega = 0.02$, which fixes the energy resolution of the spectrum. The spectrum somewhat recovers that one in the limit for $T \to 0$ arising from the vortex-free state, and shown in Fig. 5.1, with some sharp peaks for $\omega \geq 4\,J$ likely due to finite-size effects – which are expected to vanish in the thermodynamic limit.

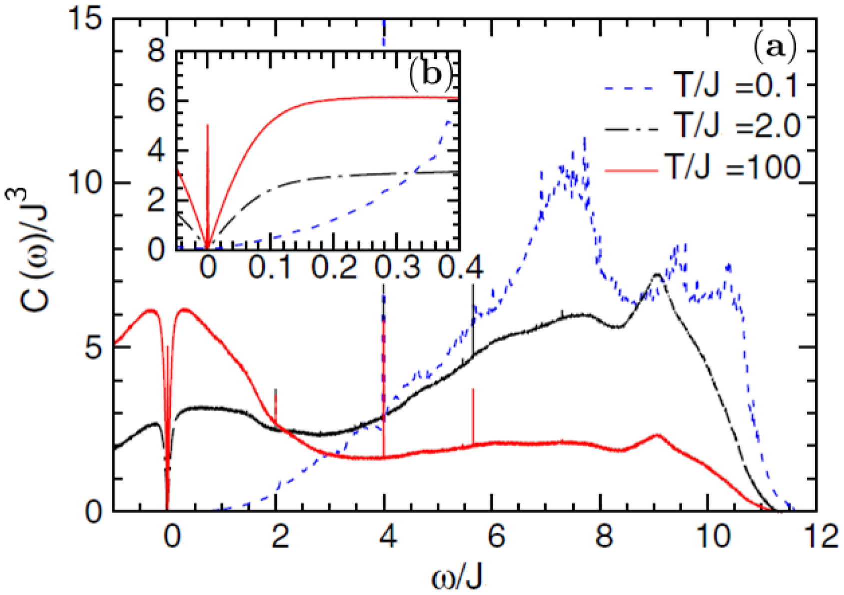

Figure 5.4: (a) $C(\omega)$ from ED calculations, versus frequency ω, at three different temperatures $T/J = 0.1, 2, 100$, for $N = 6 \times 6$ system. (b) Zoom-in of (a) at low-frequency range. Figure adapted from Ref. [128].

The spectral weight mostly arises from pair-breaking transport – i.e., $E_n E_m < 0$ in (4.23) – since at this temperature quasiparticle contributions are very small. Indeed, the quasiparticle transport is proportional to $f(E_n)\big(1 - f(E_m)\big)$ in (4.23) – with $E_n E_m > 0$ – and $f(E)$ is the Fermi-Dirac function related to the matter fermion occupation number. The spectrum structure also suggests that for $T \ll 0.1\,J$ – at which temperature the gauge excitations start to freeze-out – the correlation function should approach the form in Fig. 5.1. Unfortunately, such a low-temperature regime is numerically unfeasible since it suffers from large finite-size effects.

Upon increasing the temperature, both pair-breaking and quasiparticle terms contribute to the spectra – see spectra at $T = 2, 100\,J$. For these temperatures, the δ function in (4.23) is binned in windows of $\delta\omega = 0.001$.

I would like to recall that the quasiparticle contribution in the vortex-free state is completely accumulated into only a temperature-dependent Drude weight – see equation (5.1) and Fig. 5.2.
At finite temperature, in the presence of thermal gauge excitations and randomly distributed vortices [2] , most of the Drude weight broadens over a finite frequency range, also exhibiting a very low-frequency depletion – look at the low-ω spectra at $T = 2, 100\,J$. Thus, the spectra at $T \gtrsim J$ are qualitatively different from those shown in Fig. 5.1 where gauge excitations are discarded.

This result has been interpreted as an indication of *fractionalization*, where the randomly distributed gauge field degrees of freedom act as a thermally activated disorder for the sys-

---

[2] For $T > 0.1\,J$ the mean density of gauge excitations tends to $n(T) \sim 0.5$, see Fig. 4.1.

tem. Since the quasiparticle contribution is related to the matter fermion density relaxation, it is strongly affected by scattering from the gauge excitations. Thus, the low-ω hump $-$ at $\omega \lesssim J$ $-$ in the finite-temperature spectra shown in Fig. 5.4(a) would arise from scattering of matter fermions with excited gauge fields.

Moreover, the quasiparticle contribution shows a spectral weight which is strongly temperature-dependent. It becomes larger with increasing temperature, fact which reflects the temperature dependence of the matter fermion occupation number. The high-frequency part of the spectrum $-$ $\omega \gtrsim 6\,J$ $-$ in Fig. 5.4(a) is solely provided by the pair-breaking transport $-$ see the quasiparticle density of states in Fig. 5.9(a-b). Its spectral weight is depleted with increasing temperature $-$ since the sum rule does not change with temperature $-$ due to accumulation of spectral weight at low frequencies.

The low-frequency spectral hump in the correlation functions shown in Fig. 5.4(a) leads to a visible, abrupt dip as $\omega \to 0$. In particular, it suggests that $C(\omega \to 0, T) \simeq 0$, as can be read off from Fig. 5.4(b), especially evident from high-temperature curves.

In the following, I will make use of the term *pseudogap* to indicate the approaching to zero $-$ only at the single point $\omega = 0$ $-$ of the regular part of the correlation spectrum. According to (2.20), the zero-frequency limit of the regular part $C(\omega \to 0)$ refers to the so called *dc heat conductivity*. The latter is a transport coefficient which characterizes $-$ together with the Drude weight $-$ the system as conducting or insulating in the thermodynamic limit. In particular, one may deal either with a closing pseudogap in the thermodynamic limit $-$ and hence a system having a dissipative conducting dc channel $-$ or with pseudogap which remains open. In this latter case, the system turns out to be an ideal conductor (insulator) in the presence (absence) of a finite Drude weight at $T > 0$. In view of this, the low-frequency pseudogap requires an accurate *finite-size* analysis.

Results from ED in Figs. 5.4(a,b) highlight the impact of thermal gauge excitations on finite-temperature dynamical correlation spectra. However, a conclusive statement about the behavior of the pseudogap with the system size can not be provided as long as one sticks to the ED method. The largest system size studied via ED, i.e., $N = 36$ sites, is not large enough, and one may worry about the impact of finite-size effects on the pseudogap structure. The finite-size analysis requires larger systems, which will be considered via the AGC method in Sec. 5.2.2.

In Fig. 5.5 I show the results for the temperature dependence of the the ballistic contribution to heat transport, i.e., the Drude weight $D(T)$. It is acquired from the so called degeneracy plateau $-$ as discussed in Sec. 4.2 $-$ selecting only degenerate states according to a fixed numerical energy degeneracy cut-off. This allows to exclude non-degenerate contributions from the regular part of the spectrum.

Figure 5.5 displays $D(T)$ for three different system sizes, aiming to a reasonable understanding of the scaling of $D(T)$ with the system size. $D(T)$ shows a general peak centered around the fermion energy scale J. This is reminiscent of the Drude peak in the vortex-free state shown in Fig. 5.2. Even though they have no comparable spectral weights, they both show this feature.
The peak location is yet almost independent on the system size. However, the magnitude of $D(T)$ decreases upon increasing the system size. Although the sizes at hand for the ED

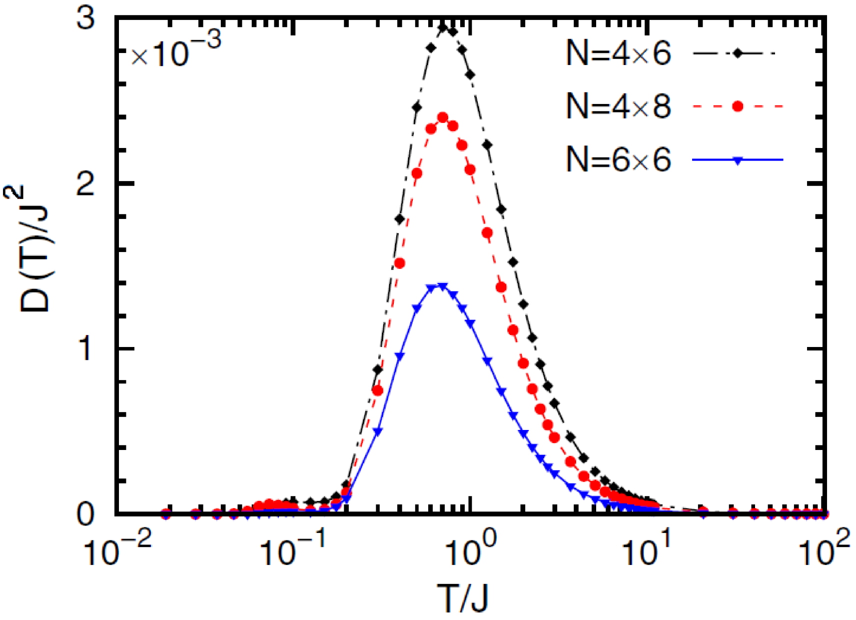

Figure 5.5: Temperature dependence of Drude weight, $D(T)$ for three different system sizes, from ED calculations. Figure adapted from Ref. [128].

method can not provide a convincing finite-size scaling of $D(T)$, these findings may be assumed as a hint for a vanishing Drude weight in the thermodynamic limit. A possible argument for the latter statement might be that among the 2^N gauge sectors, only a small bunch contribute to $D(T)$. The size of this bunch grows linearly with the system size, $\propto N$. This needs to be normalized to the number of total sectors, which in the thermodynamic limit leads to $D(T) \sim N/2^N \to 0$.

5.2.2 AGC results

The approximate AGC method is employed to extend results from ED to larger systems. I recall the expression in (4.24) – provided in Sec. 4.3 – which is used to evaluate the dynamical energy-current auto-correlation function,

$$C(t) \approx \frac{1}{N} \langle \underbrace{\langle j(t) j \rangle_{a(\eta)}}_{C(\eta,t)} \rangle_{n(T)} \,. \tag{5.5}$$

The correlation function in (5.5) is evaluated at $n(T) = 0.5$ for any temperature – with $T \gtrsim T_R = 0.1\,J$, as discussed in Sec. 4.3 – which allows to compute (5.5) by averaging over fully random gauge sectors. Equation (5.5) is therefore Fourier transformed and studied in the frequency space.

In Fig. 5.6(a-f), I show the results for the frequency dependence of $C(\omega)$ from (5.5). The correlation spectrum is studied ranging from low- to high-temperature regimes : $T = 0.1\,J$ (a-b), $T = 2.1\,J$ (c-d), and $T = 100\,J$ (e-f). Results for several system sizes are reported for each temperature, to study the dependence of $C(\omega)$ with the system size. In particular, $N = 256, \cdots, 3600$ lattice sites. The number of gauge sectors N_R used for the average in (5.5) depends on the system size. It goes from $N_R = 20000$ for the smallest size, to $N_R = 1000$ for the biggest one. This choice have reduced acceptably well finite-size effects – as can be read

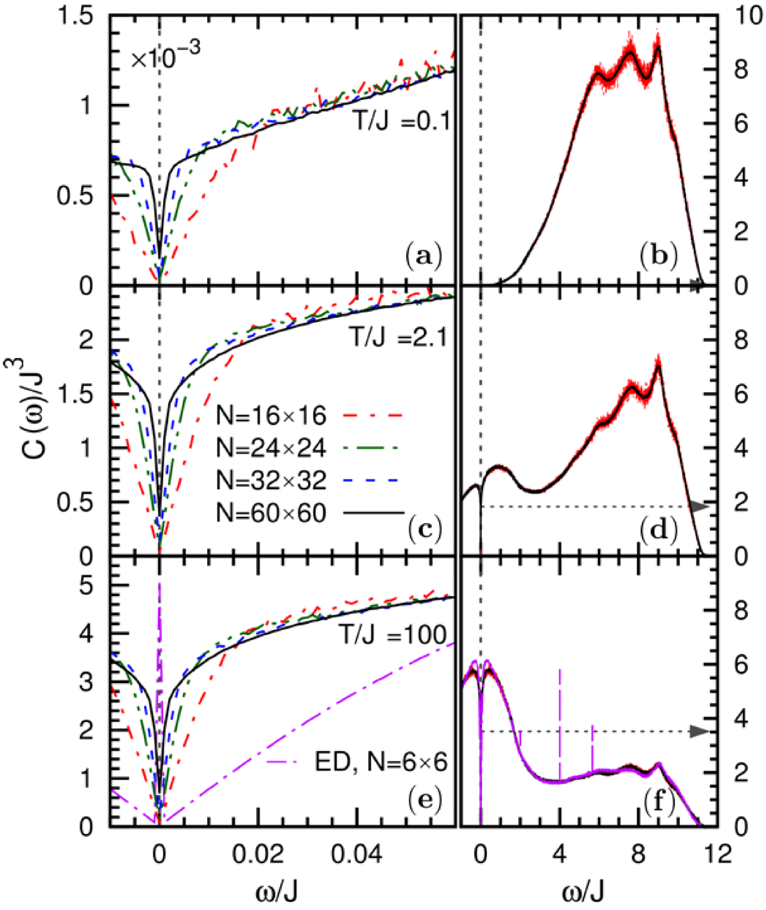

Figure 5.6: $C(\omega)$ vs. ω from AGC calculations, ranging over different system sizes $N = L \times L$, $\{L = 16, 24, 32, 60\}$. (a,c,e) Low-ω range for three different temperatures $T/J = 0.1, 2.1, 100$, respectively. Focus on the low-ω pseudogap behavior. (b,d,f) Correlation spectra for the entire scanned frequency range, for $T/J = 0.1, 2.1, 100$, respectively. The smallest (red) and the biggest (black) sizes are compared . Arrows indicate the zero-frequency extrapolation value for κ^{dc} (see Sec. 5.2.3). For the highest temperature $T/J = 100$ AGC results are contrasted against ED results for $N = 6 \times 6$ (purple). Figure adapted from Ref. [128].

off from smooth spectra in Fig. 5.6(b,d,f). The δ function in (4.23) is binned in windows of $\delta\omega = 0.001$ for all temperatures and sizes considered.

Let us start by commenting the overall behavior of spectra in the entire frequency range, as shown in Figs. 5.6(b,d,f). In these panels, two system sizes are contrasted for each given temperature: $N = 256$ (red) and $N = 3600$ (black). The spectra for the two sizes match quite well, with smoother spectra for the biggest system.
One may also compare these spectra from AGC to those shown in Fig. 5.4 arising from ED calculations, at the same temperatures. For $T = 2.1\,J$ in Fig. 5.6(d) and $T = 100\,J$ in Fig. 5.6(f), there is a qualitative agreement with the ED spectra. For $T = 0.1\,J$ case shown in Fig. 5.6(b), results from AGC do not fully capture the exact high-frequency structure of the ED spectrum. This part of the correlation spectrum – as discussed in Sec. 5.2.1 – arises mostly from the pair-breaking terms. It is only quantitatively influenced by the gauge excitations. Thus, it turns out that averaging over fully random gauge sectors does not completely preserve the physics content arising from the gauge background, at least for $T \lesssim J$.

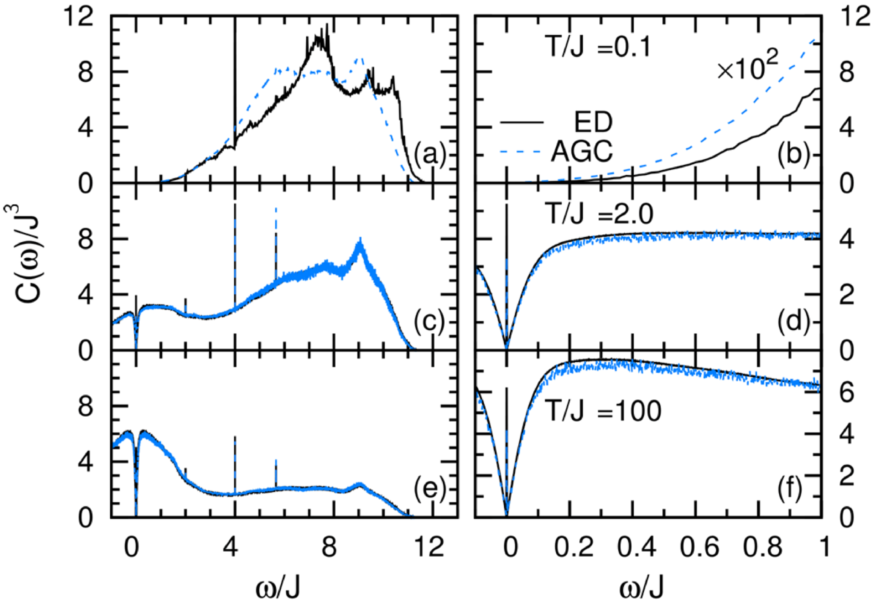

Figure 5.7: $C(\omega)$ vs. ω evaluated via the ED and the AGC method contrasted against each other, for $N = 36$ lattice sites, at three temperatures $T/J = 0.1, 2, 100$. (a,c,e) Overall frequency dependence of the correlation spectra for each given temperature. (b,d,f) Low-frequency range. Figure adapted from Ref. [128].

The low-ω hump observed in Fig. 5.4(a) is reproduced by the AGC calculations, with the characteristic temperature-dependent spectral weight related to the temperature-dependent matter fermion occupation number – as discussed in Sec. 5.2.1.
In Fig. 5.6(f) the ED spectrum (purple) at $T = 100\,J$ is superimposed onto the AGC spectrum. They show a similar overall frequency dependence, except for some sharp peaks arising only from the ED results, and for a distinct low-frequency behavior.

In Figs. 5.6(a,c,e) I show the spectra in the low-ω range for $T = 0.1\,J$, $T = 2.1\,J$, and $T = 100\,J$, respectively. It is important to look carefully at this frequency range – i.e., $\omega \ll J$ – because of the open-question left on the system-size dependence of the pseudogap observed in the ED spectra. The abrupt dip structure for $\omega \ll J$ is covered by the AGC results, independent of temperature. Even though the spectrum for frequencies $\omega \gtrsim 0.02\,J$ – at a given temperature – shows a magnitude almost independent of the system size, for $\omega < 0.02\,J$ the spectrum is strongly system-size dependent. It is possible to note that upon increasing the size of the systems, the pseudogap moves towards finite value on the y-axis. Thus, it seems to suggest a closing pseudogap in the thermodynamic limit.
Moreover, focusing on the high-temperature case in Fig. 5.6(e), I show the spectra from AGC contrasted with that from ED for $N = 36$ lattice sites. It is interesting to note that the system-size dependent pseudogap is not reproduced by the ED result. Such feature is in fact completely out of reach of the ED method, even for the largest system size considered, apparently because of finite-size effects.

To further fortify the results from AGC, I present in Figs. 5.7(a-f) a comparison of correlation spectra from ED with those obtained via the AGC method for the same system size. The spectra are evaluated for a relatively small system with $N = 36$ sites. They are also computed at three distinct temperature: $T = 0.1\,J$ (a,b), $T = 2\,J$ (c,d), and $T = 100\,J$ (e-f). To reduce the impact of finite-size effects, led by the large mean level spacing between quasiparticle states for this small system, I average (5.5) over $N_R = 50000$. The δ function in (4.23) is binned in a window $\delta\omega = 0.02$ for $T = 0.1\,J$, and $\delta\omega = 0.001$ for the rest of temperatures.

As already observed in Fig. 5.6(b) – but for larger systems – at $T = 0.1\,J$ shown in Fig. 5.7(a-b) the AGC method fails in capturing the exact high-frequency part of the correlation spectrum from ED results – for $\omega \gtrsim 4\,J$. Because of the small system considered, finite-size effects enhance differences between the two spectra, as shown in Fig. 5.7(a).

Upon increasing the temperature – see Figs. 5.7(c,d) and 5.7(e,f) – results from both methods are in a very good agreement. They show not only a qualitative agreement on the overall frequency dependence of $C(\omega)$, but also the fine structure of the spectra is covered by the AGC method. For instance, the peaks yielded by singularities in the density of states are reproduced by AGC spectra.

There are two important facts to be stressed. First, results in Figs. 5.7(b,d,f) further support findings in Fig. 5.6 for a *closing* low-frequency pseudogap in the thermodynamic limit.

I have shown that the ED low-frequency dip structure in Fig. 5.6(e) does not endorse the notion of a closing pseudogap. Thus, one may wonder whether this closing pseudogap is only an artifact arising from the AGC method. However, it is shown in Figs. 5.7(b,d,f) that the AGC method also reproduces an open dip structure $C(\omega \to 0) \simeq 0$ for $N = 36$ lattice sites.

Therefore, one can conclude that the open pseudogap is solely due to the small systems considered. In view of this, the AGC approach turns out to be essential to reveal such a feature, which can not be captured via ED results.

Second, Figs. 5.7(b,d,f) show that the AGC method is also able to detect the existence of a finite Drude weight, although its correct weight is not properly predicted. This because its evaluation involves only degenerate states, whereas the AGC method randomly averages over states.

The absence of any remnants of the Drude weight in the spectrum for the larger systems shown in Fig. 5.6 could be related to its fast decay upon increasing the system size. Thus, in the thermodynamic limit, one may expect the ballistic spectral weight to completely disappear – similarly to what conjectured in Sec. 5.2.1.

5.2.3 dc-limit of heat conductivity

In the preceding sections, it has been observed that the energy-current auto-correlation spectrum for $\omega \to 0$ yields a finite value in the thermodynamic limit. The latter is in principle temperature dependent. According to (2.20), a finite zero-frequency limit of the regular spectrum of $C(\omega, T)$ corresponds to a finite dc heat conductivity $\kappa^{dc}(T)$. Thus, one could think to extract the latter as a function of temperature from $C(\omega \to 0, T)$ obtained via the AGC calculations.

In this section, I show the approach adopted to extract $\kappa^{dc}(T)$, and the related results. First, the static transport coefficient follows as $\kappa^{dc}(T) \sim C(\omega \to 0, T)/T^2$ – see equation (2.20). Second, a way to extrapolate the limit value of the energy correlation function needs to be determined.

Figures 5.6(a,c,e) show two distinct behavior of $C(\omega)$ for $\omega \lesssim 0.02\,J$, and $\omega > 0.02\,J$: a

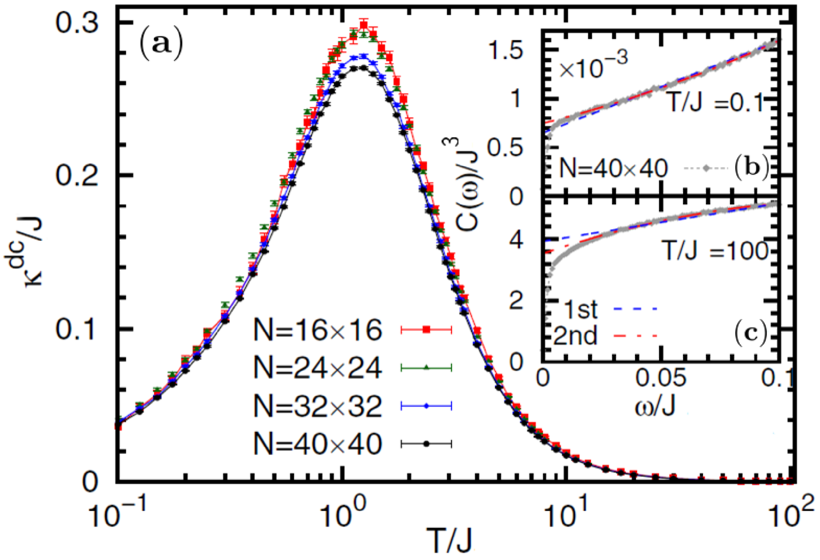

Figure 5.8: (a) Temperature dependence of the dc-limit of heat conductivity, $\kappa^{dc}(T)$, for various system sizes. $\kappa^{dc}(T)$ is obtained by fitting $C(\omega \to 0, T)$ data via second order polynomials. Insets show the low-frequency of $C(\omega)$ for $N = 1600$, at temperature $T/J = 0.1$ (b), and $T/J = 100$ (c). Linear and quadratic fit functions are superimposed onto data. Figure adapted from Ref. [128].

system-size dependent spectral weight, and a smooth spectral plateau independent of the size of systems, respectively.
In the following, I will rely on a least-square fitting procedure to extrapolate $\kappa^{dc}(T)$. To proceed, I fix a frequency range within which to fit data. The fitting range adopted for the extrapolation is $0.02\,J \lesssim \omega \lesssim 0.12\,J$. This choice allows to get the limit value for ω quite small, but at the same time not too small, such that fit results are not biased by the strongly system-size dependent range.
Several functions can be used to fit the data. In particular, I have used both polynomial and exponential functions for some trial extrapolations. The best results – in terms of fit parameters – are obtained by using polynomial functions. I consider either first order ($\alpha + \beta\omega$), or second order ($\alpha' + \beta'\omega + \gamma\omega^2$) polynomials, with a slightly different output at any temperature. The zero-frequency limit would correspond to the intercept α (α') of the linear (quadratic) fit function.

Results of this fitting procedure are shown in Fig. 5.8(b) and 5.8(c), for two sample-temperatures, $T = 0.1\,J$ and $T = 100\,J$, respectively. The size of the system considered in Figs. 5.8(b,c) is fixed to $N = 1600$. It is possible to note that both polynomials well fit $C(\omega \to 0, T)$, with the second order polynomial better fitting the high-temperature case. The number of data points taken into account in the fit frequency range is one hundred – since $C(\omega, T)$ is computed by binning the δ function with a resolution $\delta\omega = 0.001$. This number of points can be considered large enough to obtain reliable fit parameters. In the following, I stick with the second order polynomial fitting, with $\alpha' = C(\omega \to 0)$, and $\delta\alpha'$ being its error arising from the fit procedure.

In Fig. 5.8(a) I present the temperature dependence of the dc heat conductivity $\kappa^{dc}(T)$ based on the discussed least-square fitting procedure, for four different system sizes.
Each point of the plot shows an error bar proportional to the fit error $\delta\alpha'$. The error bar is

quite small and thus hardly visible with respect the size of the related symbol displayed. The small error on fit parameters is indicative of a rather good extrapolation.

Based on the quality of fit results, I am going to comment on $\kappa^{dc}(T)$. First, it shows minimal finite-size effects for most of the temperatures, despite the variety of different sizes displayed. The maximum of the curve shows a general systematic correction, with a decreasing magnitude upon increasing the system size. One can assume this feature as an indication of the tendency of $\kappa^{dc}(T)$ approaching the thermodynamic limit.

Second, $\kappa^{dc}(T)$ shows a system-size independent peak, centered around the fermion energy scale $T \sim J$. This feature has been already encountered for the Drude weight evaluated via ED calculations – see Fig. 5.5.
One might coarsely comment on this feature recalling that the heat conductivity $\kappa(T)$ can be also expressed in terms of quasiparticle properties, based on the kinetic theory, i.e., $\kappa_\nu(T) \propto \sum_\nu C_\nu(T) v_\nu(T) \ell_\nu(T)$ – I refer the reader to Sec. 5.3.4 for further insights – with $C_\nu(T)$ the specific heat, $v_\nu(T)$ the velocity, and $\ell_\nu(T)$ the mean-free path of the ν^{th} quasiparticle. Resorting to the specific heat computed via ED calculations, shown in Fig. 4.2, there is a peak of $C_\nu(T)$ at the high-temperature crossover $T \approx J$ that refers to a maximum of the energy fluctuations of matter fermions, which are mobile quasiparticles for the model. In fact, one might conclude that the peak location in Fig. 5.8(a) – as well as in Fig. 5.5 – is related to the exchange energy of heat carriers, i.e., the mobile matter fermions [3].

Finally, the dc heat conductivity in Fig. 5.8(a) gives a measure of dissipative mechanisms involved in the heat transport. In particular, a measure of the impact of thermally-induced gauge disorder in the model.
To appreciate it, one might compare the dc heat conductivity in Fig. 5.8(a) with the fictitious finite-temperature heat conductivity of Fig. 5.2 arising from analytical calculations in the vortex-free state. While in the former, thermal gauge excitations are considered, the latter discards them. Even though both $\kappa^{dc}(T)$ and $D(T)$ show qualitatively a similar shape, the low-temperature behavior of the two curves is different. $D(T)$ for $\alpha = 1.0$ increases as $\sim T^2$, while $\kappa^{dc}(T) \sim T^\gamma$, with $\gamma \lesssim 1$ [128, 129] – see also Fig. 5.11. The distinct low-temperature dependence for κ^{dc} has been interpreted as a consequence of the intrinsic disorder arising from the thermally excited gauge fields – see low-ω correlation spectrum in Figs. 5.4(a) and 5.6 – absent in the vortex-free state.

To conclude, results arising from both ED and AGC numerical calculations presented in Sec. 5.2.1, 5.2.2, and 5.2.3, have shown several properties led by the interplay between matter fermions and gauge degrees of freedom in the context of heat transport. In particular, it turns out that – in the thermodynamic limit and at finite temperature – the isotropic 2D Kitaev systems have a vanishing Drude weight, and a nonzero dc conductivity, which classify these systems as *dissipative heat conductors*.

---

[3] One has to consider, however, that in such a coarse phenomenological connection between specific heat and heat conductivity, I have not considered the temperature dependence of velocity v_ν, and mean-free path ℓ_ν. Yet, these may play a role in the form of $\kappa(T)$ as arises from (2.2).

5.3 Numerical results: anisotropic regime

So far, transport coefficients have been numerically evaluated for the isotropic point of the Kitaev honeycomb model, putting the system in the gapless phase. In the following, I present the numerical results for *anisotropic* exchange couplings in the model. The anisotropy allows to explore heat transport in both the gapless and the gapped phase.

5.3.1 Density of states of matter fermions

In the following, I show results for the density of states (DOS) of matter fermions $\rho(\omega)$, computed to determine the impact of gauge excitations $\eta_{\mathbf{r}}$ on the matter fermion DOS. The DOS is evaluated at finite temperatures and for different values of anisotropy α, via both the ED method,

$$\rho(\omega) = \frac{1}{NZ} \sum_{\eta=1}^{2^N} \sum_{j=1}^{N} Z_{a(\eta)} \delta(\omega - E_j(\eta)) \,, \tag{5.6}$$

and the AGC method,

$$\rho(\omega) = \frac{1}{N} \frac{1}{N_R} \sum_{\eta=1}^{N_R} \sum_{j=1}^{N} \delta(\omega - E_j(\eta)) \,. \tag{5.7}$$

While the ED DOS from (5.6) is evaluated considering all 2^N gauge sectors of the system, each one weighted by its related partition function $Z_{a(\eta)}$, the AGC DOS from (5.7) is computed via an average over N_R random gauge sectors.
In both (5.6) and (5.7), $E_j(\eta)$ are the quasiparticle energies for the given gauge sector η. The δ function is evaluated binning in windows of $\delta\omega = 0.001$, for both methods, at any temperature and anisotropy.

Figure 5.9 shows the frequency dependence of $\rho(\omega)$. The AGC DOS evaluated for $N = 3600$ and over $N_R = 1000$, and the ED DOS for $N = 36$ are contrasted against each other. The AGC DOS (black line) for the isotropic point $\alpha = 1$ (gapless matter fermions) is displayed at $T = 0.1\,J$ and $T = 100\,J$, in Fig. 5.9(a) and Fig. 5.9(b), respectively. The AGC DOS (red line) for the anisotropic point $\alpha = 0.5$ (gapped matter fermions) is displayed at $T = 0.1\,J$ and $T = 100\,J$, in Fig. 5.9(c) and Fig. 5.9(d), respectively. In Figs. 5.9(a-d) the ED DOS (blue dashed line) is superimposed onto the AGC DOS.

Let us start by commenting on the isotropic DOS. In Fig. 5.9(a) one can note a qualitative disagreement between the AGC and ED results. First, the larger system approached by the AGC yields smoother DOS than that from ED, missing the fine structures shown by the latter.

Second, in this low-temperature regime, while the ED results can somewhat reflect the influence of thermal gauge excitations on the DOS, the AGC hardly can do it. This because the density of excited gauge fields is fixed to $n(T) = 0.5$ independent of the temperature considered. The latter imposes an average DOS over fully random gauge excitations, which does not capture low-temperature gauge fluctuations.

Finally, although the aforementioned mismatch between ED and AGC results, both exhibit a *metallic* behavior, i.e., $\rho(\omega = 0) \neq 0$, against the *semimetallic* behavior – i.e., $\rho(\omega) \sim \omega$ for small ω, as one would expect from the Dirac-cone like dispersion in the gapless case at $T = 0$ [130]. This fact indicates that thermal gauge excitations have a relevant impact on the

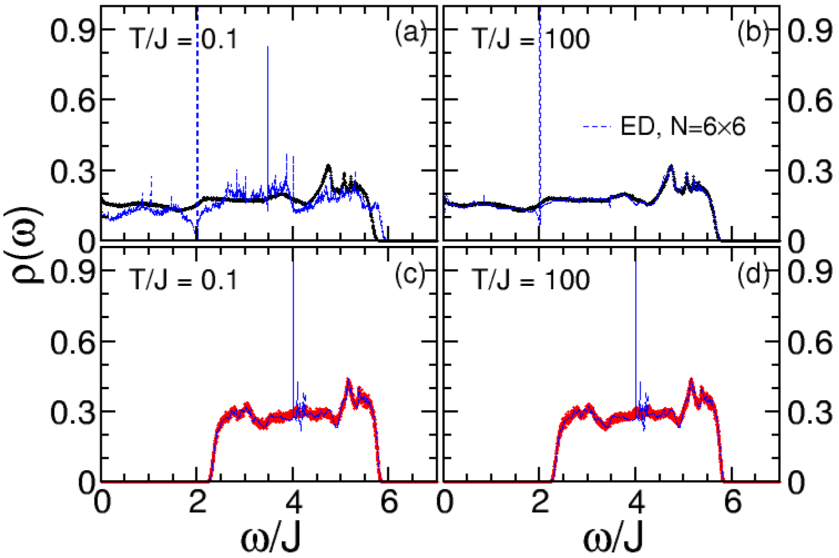

Figure 5.9: Density of states (DOS) $\rho(\omega)$ vs. ω for $N = 3600$-site systems, for different anisotropies $\alpha = 1.0(0.5)$, obtained via the AGC method averaging over $N_R = 10^3$ gauge sectors. (a,b): Variation with temperature, $T/J = 0.1$ (a), and $T/J = 100$ (b), for $\alpha = 1$. (c,d): Variation with temperature, $T/J = 0.1$ (c), and $T/J = 100$ (d), for $\alpha = 0.5$. The DOS obtained via ED calculations (blue dashed) for $N = 36$ is superimposed onto the DOS from AGC, for each given temperature and anisotropy.

low-energy spectrum of gapless mobile matter fermions. Upon increasing the temperature, gauge excitations lead to a filling of the semimetallic dip of DOS, giving rise to a metallic DOS. This observation is in agreement to what reported by quantum Monte-Carlo (QMC) calculations of DOS in Ref. [130].

At higher temperature in Fig. 5.9(b), the ED and AGC spectra resemble to each other. The metallic behavior is held. The peak at $\omega \sim 2\,J$ – also present in Fig. 5.9(a) – is visible only from the ED spectrum, and it is related to a van-Hove singularity arising from a saddle point in the quasiparticle energy dispersion.

In Fig. 5.9(c) the DOS for gapped matter fermions is shown for the low-temperature case. There is a very good correspondence between ED and AGC spectra – even at this temperature – contrarily to the gapless case shown in Fig. 5.9(a). This can be intuitively explained keeping in mind that the anisotropy considered is $\alpha = 0.5$, and having a look on the temperature dependence of the specific heat in Fig. 4.2. The specific heat displays a low-temperature crossover for C_ν at $T^\star_{0.5} \sim 0.0006\,J$, which corresponds to the energy scale of flux (gauges) proliferation. This energy scale is rather far apart with respect to the matter fermion energy scale at $T \sim J$. In view of this energy separation, and since results in Fig. 5.9(c) arise from calculations at $T \gg T^\star_{0.5}$, thermal gauge excitations do not strongly affect the DOS.

Even more, no in-gap states from thermal gauge excitations arise in the DOS of both low- and high-temperature cases in Fig. 5.9(c) and 5.9(d), respectively. The energy gap Δ_f extends

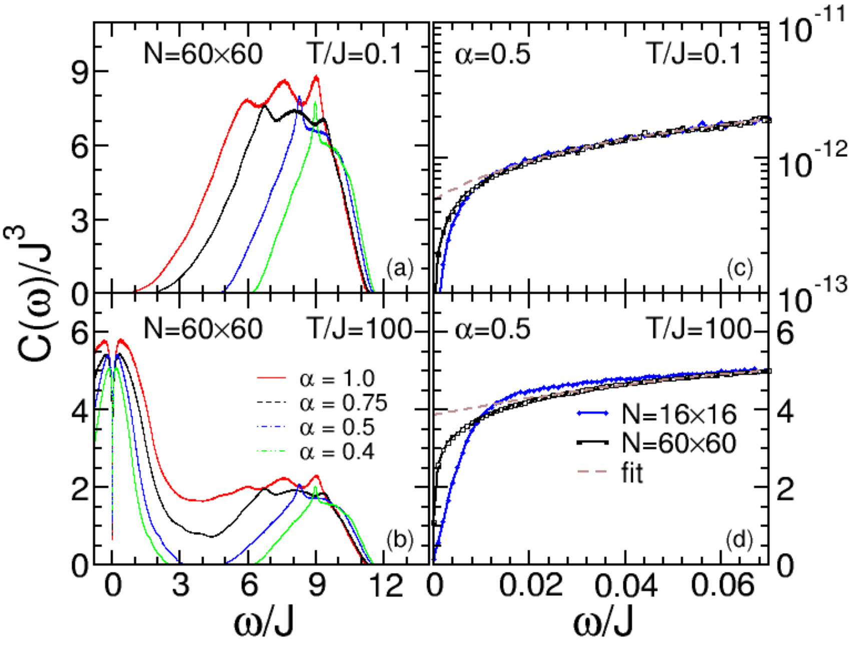

Figure 5.10: $C(\omega)$ vs. ω, obtained via the AGC method, for two temperatures $T = 0.1\,J$ (a,c), and $T = 100\,J$ (b,d). (a,b) Anisotropies $\alpha = 1, \cdots, 0.4$ refer to the gapless ($\alpha = 1$), and gapped ($\alpha = 0.75, 0.5, 0.4$) phases. Spectra are displayed for the entire frequency range considered, for $N = 3600$-sites system. (c,d) Two different system sizes, $N = 256$ (blue), and $N = 3600$ (black) in the low-ω range, for $\alpha = 0.5$. Brown-dashed lines in (c,d) depict the fitting polynomial for $C(\omega)$ of the largest size, to extrapolate κ^{dc}.

up to $\omega \simeq 2\,J$ for $\alpha = 0.5$, and it results robust against gauge excitations at any temperature. From ED a peak at $\omega \sim 4\,J$ shows up, which is related to a van-Hove singularity of the energy spectrum.

5.3.2 AGC results

In this section, I show results for the dynamical energy-current auto-correlation function arising from AGC calculations. These calculations are performed analogously to those presented in Sec. 5.2.2, computing (5.5) in the frequency space, for fully random gauge sectors, in a temperature range above T_R. However, in the following, I consider anisotropic exchange couplings in the Hamiltonian by tuning the anisotropy parameter α. This allows to range from gapless to gapped phases of the matter sector, and thus to study the anisotropy influence on transport coefficients.

In Fig. 5.10 I show the frequency dependence of the correlation spectra. In particular, Figs. 5.10(a,b) display $C_\alpha(\omega)$ with $\alpha = 1, \cdots, 0.4$, at $T = 0.1\,J$ in Fig. 5.10(a), and at $T = 100\,J$ in Fig. 5.10(b), for system with $N = 3600$ lattice sites. The δ function in (4.23) is binned in windows of $\delta\omega = 0.001$, for all temperatures. The correlation function from (5.5) is computed by averaging over $N_R = 1000$ gauge sectors.

All the anisotropic cases $\alpha \neq 1$ considered set the system in the gapped phase. The energy correlation spectra in the gapped phase are contrasted against the isotropic correlation spectra in the gapless phase, obtained in Sec. 5.2.2, and shown in Fig. 5.6(b) and Fig. 5.6(f).

At $T = 0.1\,J$, $C_{\alpha\neq 1}(\omega)$ displays a major contribution to transport led by pair-breaking terms in (4.23), due to a rather small fermion occupation number at this temperature – as similarly found for the isotropic case. The opening of a single-particle energy gap Δ_f is reflected as well in the correlation spectrum. For instance, at $\alpha = 0.5$, the energy gap is $\Delta_f \sim 2\,J$ – as it has been observed in Fig. 5.9(c). Hence, the correlation spectrum $C_{0.5}(\omega)$ in Fig. 5.10(a) shows a corresponding two-particle excitation gap $\xi \sim 2\Delta_f \approx 4\,J$.

A peculiar spectrum arises for systems at $\alpha = 0.75$. At $\alpha = 0.75$ and $T = 0$, systems lie at the phase boundary between the gapless (B) and the gapped (A) phase [130] – see Fig. 3.3(b). Moreover, the DOS is $\rho(\omega) \sim \omega$ – as observed from QMC calculations in Ref. [130]. However, while at $T = 0$ and $\alpha = 0.75$ systems are gapless, it turns out that upon increasing the temperature, these systems belong to an intermediate region in terms of α where thermal gauge excitations gap out the low-energy matter fermions.
A finite-temperature renormalization of phase boundaries induced by gauge excitations is the possible argument provided in Ref. [130]. This would explain the opening of an energy gap Δ_f in the DOS at $\alpha = 0.75$ – as arising from QMC calculations in Ref. [130]. Indeed, differently from the correlation spectrum $C_{0.75}(\omega)$ of the zero-temperature vortex-free state in Fig. 5.1 – which low-frequency part scales as $\sim \omega^3$ – $C_{0.75}(\omega)$ at finite-temperature in Fig. 5.10(a) displays an onset above a two-particle excitation gap $\xi \sim 2\Delta_f$.

Moving to higher temperatures, the correlation spectra $C_\alpha(\omega)$ in Fig. 5.10(b), show the characteristic temperature-dependent quasiparticle transport at $\omega \lesssim J$. Some comments about these high-temperature results.
First, due to thermal gauge disorder, the Drude weight peak smears over a range of finite frequencies $\sim \mathcal{O}(J)$.

Second, one can realize – contrasting $C_{\alpha\neq 1}(\omega)$ with $C_1(\omega)$ – that while the latter has a finite intensity all over the frequency range, the former do not, except for $C_{0.75}(\omega)$ which however displays an evident depletion of spectral weight. The lowering of intensity is consistent with the opening of the energy gap Δ_f, and it continues to decrease as Δ_f increases.

Finally, fully random gauge excitations are not sufficient to fill in the excitation gap completely. This can be observed from the zero-spectral weight of $C_{0.5}(\omega)$ and $C_{0.4}(\omega)$ in Fig. 5.10(b), for $3\,J \lesssim \omega \lesssim 5\,J$ and $3\,J \lesssim \omega \lesssim 6\,J$, respectively. Surprisingly, the spectrum $C_{0.75}(\omega)$ shows a finite spectral intensity at all frequencies.
The two-particle excitation gap at $\alpha = 0.75$ is not robust against thermal gauge excitations – contrarily to $\alpha = 0.5, 0.4$ cases – and thus it is filled in at high temperatures. This difference is likely due to the nature of the gauge-induced energy gap at $\alpha = 0.75$.

Analogously to the isotropic spectra, $C_{\alpha\neq 1}(\omega)$ display a sharp zero-frequency dip – similarly as in Figs. 5.6(a,e). The dip structure of $C_{\alpha\neq 1}(\omega)$ is further studied considering different system sizes. For instance, I show the results for $C_{0.5}(\omega \ll J)$ in Fig. 5.10(c) at $T = 0.1\,J$, and in Fig. 5.10(d) at $T = 100\,J$, for systems with $N = 256$ (blue), and $N = 3600$ (black) lattice sites. It turns out that even in the anisotropic regime, the dip shows a strongly system-size dependent width. The latter fact suggests that the dip closes in onto the y-axis in the thermodynamic limit. This feature can be read off best from Fig. 5.10(d).
Interestingly, the spectral intensity of $C_{0.5}(\omega \ll J)$ in Fig. 5.10(c) is several order of magni-

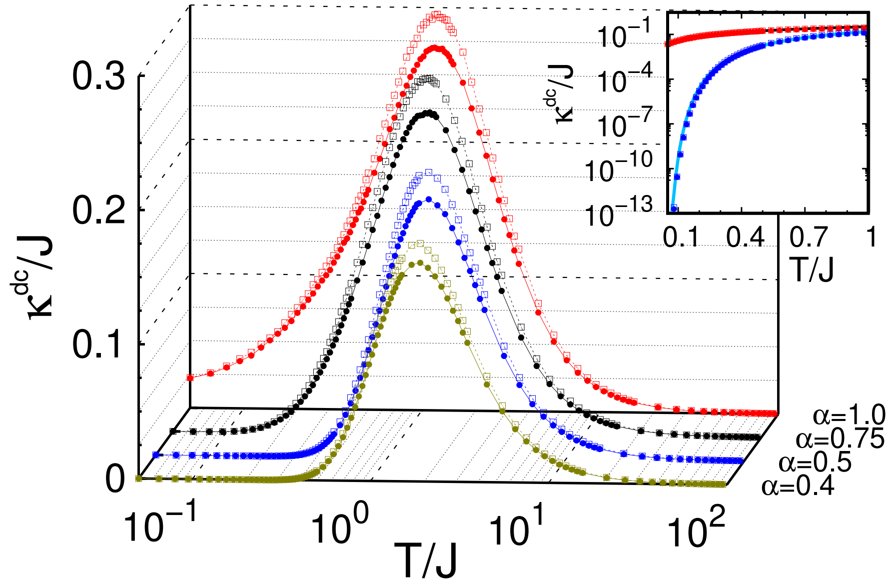

Figure 5.11: Thermal conductivity $\kappa^{dc}(T)$ vs. T for various anisotropies $\alpha = 1, ..., 0.4$, displayed on the lower right axis, going from gapless to gapped phases. Two system sizes, $N = 256$ (dashed with empty squares), and $N = 3600$ (solid with solid circles), are compared. Inset: low-temperature behavior for $\alpha = 1$ with red solid circles (red empty squares), and $\alpha = 0.5$ with blue solid circles (blue empty squares), for $N = 3600\,(256)$. Data are superimposed onto two different fit functions, $\sim T^{\gamma}$, with $\gamma = 0.92$ (black solid), and $\sim e^{-\Delta/T}$, with $\Delta = 2.3$ (blue solid), for the gapless and the gapped cases, respectively. Figure taken from Ref. [129].

tude lower than that of Fig. 5.10(d). Indeed, the very small, but finite, spectral weight of $C_{0.5}(\omega \ll J)$ at $T = 0.1\,J$ relates to a thermally activated behavior of heat transport in the gapped case.

The results on the dynamical correlation spectra presented for an anisotropic Kitaev Hamiltonian extends those obtained for the isotropic case. In particular, a finite $C_\alpha(\omega \to 0) \neq 0$ is reproduced at any α and temperature. Thus, finite dc transport coefficients can be extracted as similarly done in Sec. 5.2.3 for $\alpha = 1$. The latter will be presented in the next section.

5.3.3 dc-limit of heat conductivity

Based on the calculations of $C_\alpha(\omega, T)$ in a wide range of temperatures and for several anisotropies – as shown in Fig. 5.10 – in the following I show results of the extrapolated dc-limit $C_\alpha(\omega \to 0, T)$. It has already been observed in Sec. 5.2.3 that this limit corresponds to the dc heat conductivity $\kappa_\alpha^{dc}(T) \sim C_\alpha(\omega \to 0, T)/T^2$ – as required by (2.20).
The extrapolation procedure is analogous to that shown in Sec. 5.2.3: least-square fitting of the low-frequency plateau of $C_\alpha(\omega \ll J, T)$ – see Figs. 5.10(c,d) for $0.02\,J \lesssim \omega \lesssim 0.12\,J$ with $\alpha = 0.5$ – by using second order polynomials. The brown dashed lines in Figs. 5.10(c,d) refer to the extrapolation procedure applied to the system with $N = 3600$ sites and $\alpha = 0.5$. The same is done for each given pair (T, α) for two system sizes, $N = 256$ and $N = 3600$, also to obtain some form of finite-size scaling.

Figure 5.11 displays all the $\kappa_\alpha^{dc}(T)$. The $\kappa_1^{dc}(T)$ at the isotropic point is contrasted with $\kappa_{\alpha\neq1}^{dc}(T)$ for anisotropic cases. Many aspects of the isotropic case are reproduced by the

anisotropic ones.
First, despite the two system sizes $N = L \times L$ shown in Fig. 5.11 differ by almost a factor of 4 in their linear dimension, the dc heat conductivity $\kappa_\alpha^{dc}(T)$ shows minimal differences for any temperature, except at $T \approx J$, where the absolute error between the two systems becomes the largest. But even there, there is only a small systematic correction which provides lower values of $\kappa_\alpha^{dc}(T)$ as the size of system increases. Thus, visible but rather small finite-size effects exist, which presumably yield the largest system close enough to the thermodynamic limit.

Second, the peak of $\kappa_\alpha^{dc}(T)$ is located around $T \approx J$ independent of system size. The phenomenological relation of $\kappa_\alpha^{dc}(T)$ to the specific heat peak from matter fermions – used in Sec. 5.2.3 as an argument to justify the location of the peak of $\kappa_1^{dc}(T)$ – still holds for the anisotropic case. Indeed, the high-temperature peak in the specific heat shown in Fig. 4.2 is located around the fermion energy scale $T \approx J$ independent of the anisotropy α.

Interestingly, Fig. 5.11 shows a qualitative change of the low-temperature dependence of $\kappa_\alpha^{dc}(T)$ as systems cross over from the gapless to the gapped matter fermion spectrum. While the dc heat conductivity in the gapless phase roughly scales with a power law as $\kappa_1^{dc}(T) \sim T^\gamma$, with $\gamma \lesssim 1$ – as discussed in Sec. 5.2.3 – in the gapped phase an exponential behavior as $\kappa_{\alpha\neq 1}^{dc}(T) \sim \exp(-\Delta/T)$ gives a reasonable description. The latter cases are consistent with the notion of quasiparticle transport, since the activation energy gap Δ corresponds to the matter fermion energy gap Δ_f.

As an example, I show in the inset of Fig. 5.11 the low-temperature dependence of $\kappa_1^{dc}(T)$ and $\kappa_{0.5}^{dc}(T)$ superimposed onto two distinct fit functions, T^γ, and $\exp(-\Delta/T)$, respectively.
First, it is clearer from the inset the very small magnitude of $\kappa_{0.5}^{dc}(T)$ upon decreasing the temperature. This is compatible with the rapid low-temperature suppression by the thermal activation, and with the very low spectral weight reported for $C_{0.5}(\omega \ll J, T \ll J)$ in Fig. 5.10(c).
Second, the fit parameter found for the gapped case at $\alpha = 0.5$ is $\Delta = 2.3$, which is remarkably close to the value of $\Delta_f \sim 2\,J$.

Finally, one may wonder how the heat transport changes including (discarding) gauge excitations, for any anisotropy considered. For this purpose, it is interesting to make a comparison between the dc heat conductivity $\kappa_\alpha^{dc}(T)$ shown in Fig. 5.11, and the Drude weight $D_\alpha(T)$ displayed in Fig. 5.2.

The overall temperature dependence of $\kappa_\alpha^{dc}(T)$ for most of temperatures is qualitatively similar to that of $D_\alpha(T)$. However, at low temperatures some differences arise.
First, as already observed and discussed in Sec. 5.2.3, the isotropic $\kappa_1^{dc}(T)$ shows a sub-linear behavior, against the quadratic behavior for $D_1(T)$.
Second, contrarily to the polynomial onset exhibited by $D_{0.75}(T)$, $\kappa_{0.75}^{dc}(T)$ shows an exponential activation. As argued in Sec. 5.3.2, at $\alpha = 0.75$, thermal gauge excitations imply a modification of the finite-temperature phase boundaries. Because of this, systems with this anisotropy move to the gapped phase. As a consequence of gapped matter fermions, the low-frequency $C_{0.75}(\omega)$ displays an excitation gap – as seen in Fig. 5.10(a) – and thus the low-temperature dc conductivity shows the aforementioned thermal activation. From the comparison, it is hence evident the importance of considering gauge degrees of freedom in thermal transport properties of Kitaev systems.

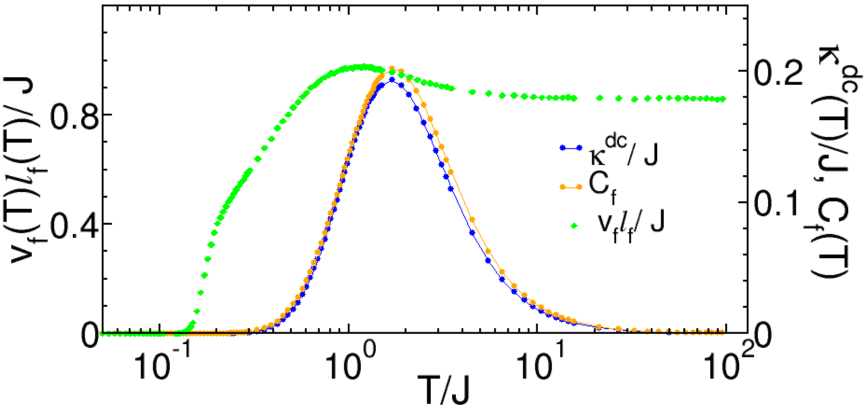

Figure 5.12: Green solid circles: $\kappa^{dc}(T)/C_f(T) \equiv v_f(T)\ell_f(T)$ vs. T at $\alpha = 0.5$. Solid lines with solid circles refer to the dc heat conductivity $\kappa^{dc}(T)$ (blue) and the specific heat $C_f(T)$ (yellow) computed via the AGC method at $\alpha = 0.5$ for $N = 1024$ lattice sites. Figure adapted from Ref. [129].

To conclude, results arising from ED and AGC calculations – extended to the anisotropic regime of exchange couplings, and presented in Sec. 5.3.1, 5.3.2 and 5.3.3 – have shown once again a fundamental interplay between matter fermions and gauge degrees of freedom. The inclusion of anisotropy has allowed to explore both gapless and gapped phases of the model. For anisotropies describing gapped systems, the gap in the matter fermion spectrum is reflected as well in the dynamical energy auto-correlation function. Moreover, transport coefficients derived for the gapped systems describe thermally activated heat conductors.

From these findings, it turns out that – in the thermodynamic limit and at finite temperature – the two-dimensional Kitaev systems are *dissipative heat conductors* at any value of anisotropy α, which extends the conclusion for the isotropic case in Sec. 5.2.3.

Remarkably, the dissipative nature found for two-dimensional Kitaev systems is in strong contrast with results for the quasi one-dimensional Kitaev ladder – I refer the reader to the Ref. [127] for further insights. The ladder turns out to be an *heat insulator* with a vanishing Drude weight and a zero-dc conductivity [4] – despite showing a similar emergent thermally activated gauge disorder, and signatures of fractionalization.

As conclusive remark, I want to stress that the characterization of the 2D Kitaev systems as dissipative heat conductors can be considered robust for $T \gtrsim T^{\star}_{\alpha}$ – as a consequence of the AGC method restriction in temperature.

5.3.4 Kinetic model of thermal conductivity

As an additional remark, I want to report in this section some results from a phenomenological treatment of $\kappa^{dc}_{\alpha}(T)$ as obtained via the AGC method and shown in Fig. 5.11. According to (2.2), one may perform a kinetic modeling of thermal conductivities expressing $\kappa^{dc}_{\alpha}(T)$ in

---

[4] The thermally activated gauge disorder leads to the opening of a similar pseudogap in $C(\omega \to 0)$, however not closing in the thermodynamic limit.

terms of quasiparticles properties,

$$\kappa_\alpha^{dc}(T) \approx \sum_{\mathbf{q},\nu} C_{\mathbf{q},\nu}(T) v_{\mathbf{q},\nu}(T) \ell_{\mathbf{q},\nu}(T), \tag{5.8}$$

where $C_{\mathbf{q},\nu}(T)$, $v_{\mathbf{q},\nu}(T)$, and $\ell_{\mathbf{q},\nu}(T)$ relate to the specific heat, velocity, and mean-free path at momentum $\mathbf{q}$ of the ν^{th} kind of quasiparticle. This modeling based on (5.8) might be interesting both because recalled in Sec. 5.2.3 and 5.3.3 to argue on the origin of the peak's location for κ^{dc}, but above all because of several experiments on thermal transport – e.g., shown in Sec. 2.2.1 – which theoretical estimates of thermal conductivity rely on the kinetic theory [25].

In Kitaev systems, one deals with two types of quasiparticles, namely vortices $\nu = v$, and matter fermions, $\nu = f$. Thus, for this two-fluid model, it turns out convenient to disentangle the contributions to $\kappa_\alpha^{dc}(T)$ arising from the two degrees of freedom, in order to discern between them. However, this operation is feasible only if their spectral supports are well separated in energy.

In this context, it is helpful to have a look on the specific heat from ED calculations reported in Fig. 4.2. In the figure, at $\alpha = 1$, the specific heat $C_\nu(T)$ shows two peaks – related to the energy fluctuation of gauge fluxes at $T_\alpha^\star$, and of matter fermions at T_M, respectively – rather close in the energy scale. This makes hard to completely separate the two degrees of freedom from each other.
However, upon increasing the anisotropy – e.g., at $\alpha = 0.5$ – the flux peak at $T_\alpha^\star$ is well separated from the contribution provided by the matter fermions.
Yet, the Kitaev honeycomb model is described in terms of *static* gauge fields, from which follows that the velocity of vortices $v_{\mathbf{q},v} = 0$.

Thus, sticking with the $\alpha = 0.5$ case, one may adopt the standard approximation to drop the momentum dependence in the sum in (5.8) in favor of momentum integrated quantities. Under such considerations, it follows that (5.8) reads as $\kappa_\alpha^{dc}(T) \sim C_f(T)v_f(T)\ell_f(T)$ – for $T > T_\alpha^\star$. From the latter relation, one might be interested into analyze the ratio $\kappa_\alpha^{dc}(T)/C_f(T)$, as obtained from AGC calculations at $\alpha = 0.5$.

For the ratio, I computed the specific heat $C_f(T)$ resorting to the AGC method – to use quantities arising from the same method – which result is reliable as much as that from the ED. This is also shown in Fig. 4.1(b) where the ED and AGC thermodynamic quantities coincide for $T > T_\alpha^\star$.

Figure 5.12 shows both $\kappa_{0.5}^{dc}(T)$ and $C_f(T)$, as well as their ratio. Quantities are evaluated for systems with $N = 1024$ lattice sites, averaging over $N_R = 5000$ gauge sectors. The ratio refers to this variation of $v_f(T)\ell_f(T)$ as a function of temperature – which Fig. 5.12 is meant to speculate on.
First, at temperatures $T > T_{0.5}^\star$ the distribution of vortices is fully random. This means that the matter fermion mean-free path is temperature independent.
Second, at large enough temperatures – $T \gtrsim J$ – the matter fermions velocity is set to be equal to the temperature-independent Fermi velocity, by fermions far up in the Dirac-cone like energy dispersion.
Finally, as the temperature decreases, matter fermions close to the energy gap have velocity $v_f(T)$. In the limit of $T \to 0$, the latter tends to zero. Remarkably, the features discussed are roughly captured by the ratio $v_f(T)\ell_f(T)$ displayed in Fig. 5.12.

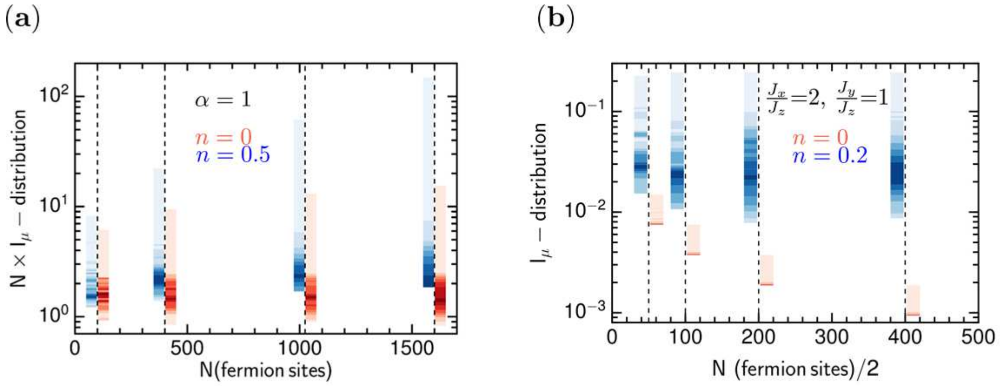

Figure 5.13: (a) Contour plot of IPR I_μ distribution as a function of the system size N for the 2D isotropic Kitaev model ($\alpha = 1$). The disorder is given in terms of the mean density of gauge excitations n as in (4.25). Cases with no disorder $n = 0$ (reddish), and with disorder $n = 0.5$ (blueish) are both shown. (b) As in (a) the I_μ distribution is shown, but for the quasi-1D Kitaev ladder in the gapless regime, in both clean and disordered cases, for $n = 0$ (reddish) and $n = 0.2$ (blueish) gauge excitations density, respectively. For both (a) and (b), a single random gauge configuration is considered.

5.3.5 Notes on disorder and localization

Results from AGC calculations shown in the preceding sections describe the 2D Kitaev systems as dissipative heat conductors, due to an emergent thermal gauge disorder. In this context, one may wonder how this relates to a possible (de)localization of states, as in Anderson localization (AL) [133].

In 1958 P. W. Anderson published a seminal paper [133] dealing with disorder in tight-binding systems. This work raised the question, whether electronic states can be localized by disorder, yielding an insulating behavior. If disorder is strong *enough*, indeed quantum amplitudes related to the hopping paths cancel each other [5], providing localized wave-functions – i.e., $|\psi(\mathbf{r})| \sim \exp(|\mathbf{r} - \mathbf{r}_0|/\xi)$ with ξ the *localization length*.

For disordered 1D systems, there exists a mathematically rigorous proof that for diagonal disorder all noninteracting electron wave-functions localize at any energy regardless of the disorder strength [135]. In 2D and 3D systems, unfortunately, no rigorous theory of localization exists. Theoretical progresses have been made based on the renormalization group theory [136] – introducing a one-parameter scaling hypothesis of localization – and on a self-consistent diagrammatic theory [137]. From these studies, *conventional* AL for noninteracting free electrons is well understood: no extended states exist in 2D, while 3D systems show a metal-insulator transition at a critical disorder [6].

Studies of AL in novel 2D systems – e.g., Dirac semimetals, Weyl semimetals, and p- or d-wave superconductors – are far from complete. For instance, two-dimensional d-wave superconductors have been shown to have localized low-energy excitations, with peculiar effects

---

[5] An equivalent wave model has been proposed [134], where the incoming wave is scattered off potentials led by disorder. The scattered wavelets interfere destructively in the forward direction for strong disorder, giving rise to the exponential decay of the wave.

[6] I refer the reader to Refs. [138, 139] for further insights

on mobility of nodal fermions dependent on the kind of disorder [140]. Moreover, 2D massless Dirac fermion systems subject to a random disorder have been shown to have delocalized states even in the strong disorder regime [141].

To learn more about the question of localization in the 2D Kitaev honeycomb model, I have preliminarily studied a quantity known as *inverse participation ratio* (IPR),

$$I_\mu = \sum_{i=1}^{N} |\psi_\mu(i)|^4 \qquad \text{with} \qquad \lim_{N\to\infty} I_\mu = \begin{cases} 1/N & \Rightarrow \text{extended} \\ \text{const.} & \Rightarrow \text{localized} \end{cases} . \tag{5.9}$$

The IPR is a quantity frequently used [142, 143] to characterize the localization of normalized eigenfunctions $\psi_\mu(i)$ of the Hamiltonian $\mathcal{H}$, where i is a lattice site, and μ labels the eigenfunctions.
Indeed, if $\psi_\mu(i)$, for a given μ is fully localized, i.e., confined to a single site i, then $I_\mu = 1$. Conversely, if $\psi_\mu(i)$ is fully delocalized, i.e., spread over the whole lattice, then $I_\mu = 1/N$, with N the system size.

In Fig. 5.13(a) I show the results for the IPR distribution of the isotropic 2D Kitaev model. The contour plot can be seen as top sight histogram of I_μ from (5.9), showing the distribution of μ eigenfunctions according to the value of I_μ − note that I_μ is multiplied by the number of fermion sites N. Four system sizes are considered, $N = 100, \cdots, 1600$, and two cases: (i) *clean* systems − i.e., the vortex-free state with a mean density of gauge excitations $n = 0$ (reddish), and (ii) *disordered* systems with $n = 0.5$ (blueish). For (i) wave-functions ψ_μ are mostly located around $I_\mu \to 1/N$, regardless of the size N. For (ii) systems show a distribution of ψ_μ at $I_\mu \gtrsim 1/N$, slightly dependent on N. A long tail of ψ_μ distributed at $I_\mu \gg 1/N$ is also displayed, which length seems to increase upon increasing N.

I also report the IPR data in Fig. 5.13(b) for the quasi-1D Kitaev ladder in the gapless regime − which I_μ from (5.9) is computed considering data from the work of Metavitsiadis and Brenig [127]. Both (i) clean and (ii) disordered cases have been considered − same color code of Fig. 5.13(a). While for (i) the majority of ψ_μ distribute around $I_\mu \to 1/N$, for (ii) ψ_μ distribute around $I_\mu \sim$ const.

The findings from Fig. 5.13 are consistent with heat transport results for both the 2D [128, 129, 131] and 1D Kitaev systems [127] − see Sec. 5.3.3. On the one hand, the 2D system shows extended states in both the clean case and the disordered case, allowing for finite conductivity.
On the other hand, the 1D system has extended versus localized states for the clean versus the disordered case, consistent with insulating behavior in finite-temperature 1D Kitaev systems.

Finally, some caution is required using the IPR diagnostic since it may suffer from finite-size effects − which makes it hard to provide conclusive statements on localization in the thermodynamic limit.

5.4 Comparison to QMC thermal transport results

The interest in thermal conductivity from emergent fractional excitations in the 2D Kitaev systems − used as a tool to explore the related quantum spin liquid state − has recently led to other theoretical investigations.

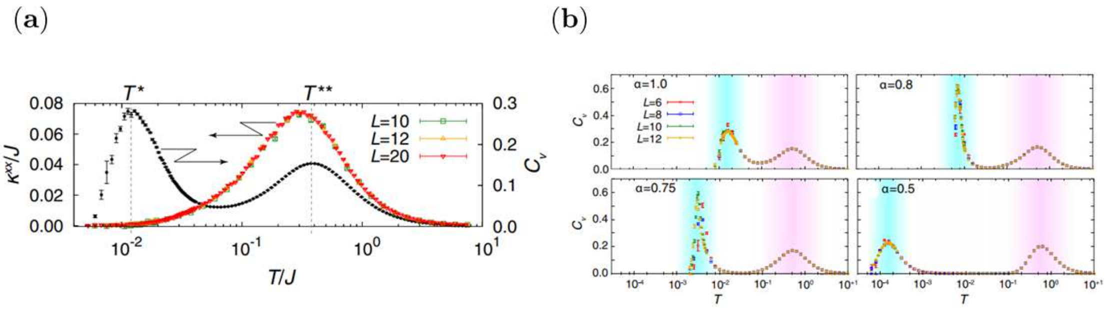

Figure 5.14: (a) Thermal conductivity κ^{xx} vs. T from QMC calculations carried out in Ref. [131], for $\alpha = 1$ and cluster size $L = 10, 12, 20$ – with $2L^2$ lattice sites. The specific heat C_V vs. T for $\alpha = 1$ and $L = 20$ is also plotted. (b) Temperature dependencies of the specific heat from QMC calculations carried out in Ref. [130], for various anisotropies $\alpha = 1, \cdots, 0.5$, and sizes L. The anisotropy α is defined from $J_x = J_y = \alpha/3$ and $J_z = 1 - 2\alpha/3$. The low- and high-temperature crossovers are displayed with blue and pink shaded regions, respectively. Figure (a) is adapted from Ref. [131] and (b) is reproduced from Ref. [130].

In this section, I will compare aspects of the quantum Monte Carlo (QMC) data obtained by Nasu *et al.* [131] for the thermal conductivity in the 2D Kitaev honeycomb model with the results of my work – arising from AGC and ED calculations, and shown in the preceding sections.

The work carried out in Ref. [131] has investigated the thermal transport in the 2D *isotropic* Kitaev honeycomb model. The work relies on QMC calculations, and it evaluates the temperature dependences of both longitudinal and transverse thermal conductivities κ, in the presence and absence of magnetic field.
For the purpose of this section, I am going to focus only on the zero-field data for the longitudinal component of κ, based on results in Ref. [131] [7].

I show Nasu *et al.* QMC findings for the temperature dependence of the isotropic – i.e., at $\alpha = 1$ – dc-limit of heat conductivity $\kappa^{xx} = \lim_{\omega\to 0} \kappa^{xx}(\omega)$ [131] in Fig. 5.14(a), and for the temperature dependence of the specific heat at various anisotropies [130] in Fig. 5.14(b).

Remarkably, these results are consistent with those arising from AGC and ED calculations, and presented in Secs. 5.2.3 and 4.3.
Compared to $\kappa_1^{dc}(T)$ shown in Fig. 5.8, $\kappa^{xx}(T)$ is finite at $T > 0$, and similarly exhibits a single broad peak close to the high-temperature crossover – in Fig. 5.14(a) marked by $T^{**} \simeq 0.375\,J$ – as well as minimal finite-size effects.
Moreover, the estimate of κ^{xx} follows from an extrapolation in the low-ω range [8] – as similarly done in Secs. 5.2.3 and 5.3.3 .
Nasu *et al.* have also observed a system-size dependent dip for $C^{xx}(\omega)$ close to $\omega \sim 0$, which approaches nonzero values in the thermodynamic limit – similarly to the pseudogap structure described and discussed in the preceding sections.

---

[7] I refer the reader to the related supplemental material of Ref. [131] for further details on the formulation of thermal conductivity.

[8] See the supplemental material of Ref. [131].

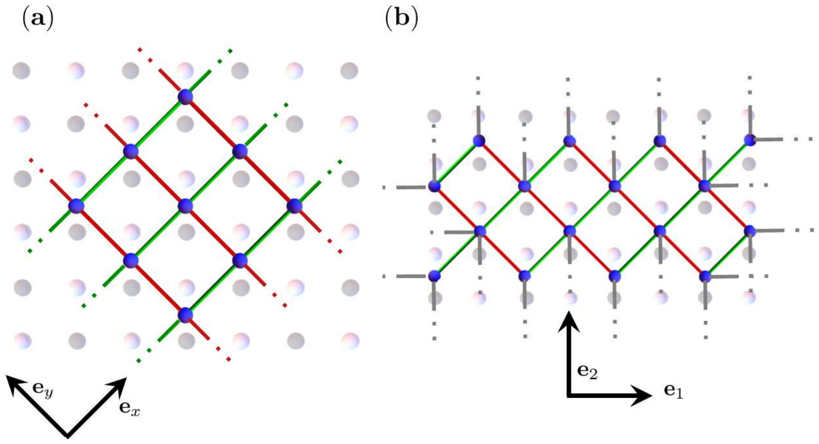

Figure 5.15: Boundary conditions for finite-size systems on the brick-wall lattice (BWL). (a) Type-I boundary condition: periodic boundary conditions (PBCs) in the $\mathbf{e}_x$ and $\mathbf{e}_y$ directions – i.e., along the edges of the dual square lattice – for a system with $N = 9$ lattice sites (blue bullets). (b) Type-II boundary condition: PBCs in the $\mathbf{e}_1$ and $\mathbf{e}_2$ directions – along the $x - y$ chains, and the z-bonds, respectively – for a system with $N = 16$ sites.

Quantitative differences between this thesis and Nasu *et al.*'s results arise, for instance, in the high-ω conductivity $\kappa^{xx}(\omega, T)$ possibly due to a different choice of the local energy density used to derive the energy current operator. Possible differences in κ^{xx} may also arise from details of the fitting procedure. Finally, the QMC method allows to study the system with no restriction in temperatures – going even to $T < T^*$ – as long as finite-size effects are not too large.

As in the present thesis – see Appendix C.1 – Nasu *et al.* have analyzed the thermodynamics of Kitaev systems. Figure 5.14(a) displays the specific heat C_V for $\alpha = 1$. Figure 5.14(b) shows C_V for $\alpha = 1$ – as in Fig. 5.14(a) – but also for other anisotropies with $\alpha = 0.8 \cdots 0.5$, and for several system sizes.
The specific heat C_V shows the characteristic two-peak structure, with two well-separated energy scales T^{**} and T^* related to the entropy release of mobile matter fermions and localized gauge fluxes, respectively.

Comparing findings in Fig. 5.14(b) with those reported in Fig. 4.2 and Fig. C.1, there is a good qualitative agreement. In particular, the low-temperature peak at T^* is dependent on α, while the high-temperature peak at T^{**} is independent on α [9].

To conclude – despite a different numerical method, and slightly different definitions employed to study Kitaev systems – results from QMC for the isotropic heat conductivity, as well as for the thermodynamics of 2D Kitaev systems, obtained in Refs. [130, 131] are consistent with results of this thesis.

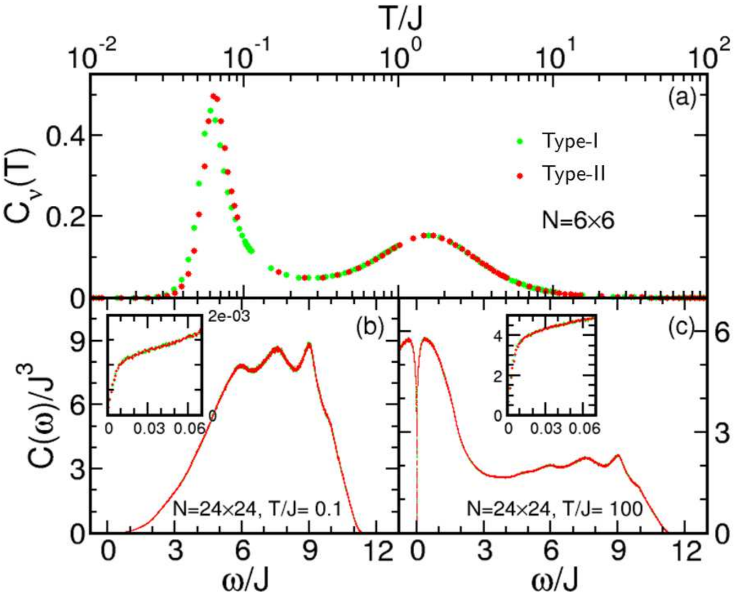

Figure 5.16: (a) Specific heat $C_\nu(T)$ vs. T computed via the ED method for $N = 6\times 6$-sites systems. Boundary conditions Type-I (green solid circles) are contrasted to Type-II (red solid circles). (b,c) $C(\omega)$ vs. ω evaluated via the AGC method for $N = 24 \times 24$-sites systems, at two different temperatures, $T/J = 0.1$ (b), and $T/J = 100$ (c). Type-I (green) and Type-II (red) contrasted to each other. Insets: low-frequency range of $C(\omega)$.

5.5 Periodic boundary conditions

In this section, I show results from different mapping of boundary conditions for the Kitaev honeycomb model. As discussed in Sec. 3.4.1, calculations in this work have been carried out considering the model in (3.40) put onto a square lattice – shown in Fig. 3.6(c) – with periodic boundary conditions (PBCs) along the square lattice vectors $\mathbf{e}_x$ and $\mathbf{e}_y$.
This type of boundary conditions – in the following referred to as *Type-I* – is depicted in Fig. 5.15(a).

In the following, I also report on calculations of specific heat and dynamical energy-current auto-correlation functions based on the model constructed onto a lattice with a different arrangement of boundary conditions. These latter are considered along the unit vectors $\mathbf{e}_1$ and $\mathbf{e}_2$, pointing along the $x - y$ chains, and the z-bonds of the brick-wall lattice, respectively – see Fig. 3.6(a). This type of boundary conditions – referred to as *Type-II* – is shown in Fig. 5.15(b).

Note that for both boundary conditions *Type-I* and *Type-II* imposed, the boundary problem intrinsic to the Jordan-Wigner transformation – discussed in Sec. 3.4.1 – arising from term in (3.43c) is omitted. For both *Type-I* and *Type-II*, I construct the Hamiltonian as in (3.40) and the energy current operator as in (4.15). The energy spectra and the energy-current auto-correlation function are computed according to the formal developments presented in the preceding chapters.

---

[9] One might note that $T^\star_\alpha \approx 4T^*$ and $T_M \approx 4T^{**}$. This factor 4 arises from expressing the Kitaev spin Hamiltonian in terms of operators $S_j = \frac{\hbar}{2}\sigma_j$, with σ_j the related Pauli matrix, and $\hbar = 1$.

In Fig. 5.16 I contrast results at the isotropic point $\alpha = 1$ for systems with *Type-I* and *Type-II* boundary conditions. Figure 5.16(a) shows the temperature dependence of the specific heat $C_\nu(T)$ obtained via the ED method for systems with $N = 6 \times 6$ lattice sites. The thermodynamic observable is related to the energy spectrum of the system. Thus, it may yield possible differences arising from the two distinct boundary conditions. There are yet no qualitative changes shown in the specific heat crossing over from *Type-I* to *Type-II.* It shows only slightly quantitative changes within the low-temperature crossover at $T^{\star}_{\alpha}$, which peak is barely shifted at a higher temperature. For the rest of temperatures − including the peak at the high-temperature crossover − the specific heat is rather insensitive to the change of boundary conditions.

Figures 5.16(b,c) display the frequency dependence of $C(\omega)$ computed via the AGC method for $N = 24 \times 24$ lattice sites. It is evaluated averaging over $N_R = 5000$ fully random gauge sectors, and binning δ in windows of $\delta\omega = 0.001$. Variations of temperatures are shown in 5.16(b) for $T = 0.1\,J$, and 5.16(c) for $T = 100\,J$. Insets in both panels zoom-in the low-frequency range close to $\omega \sim 0$. For this system size, there are no evident changes in the spectra crossing over *Type-I* to *Type-II.* A good agreement is held even in the low-frequency range. From this latter feature, one can assume that also the dc heat conductivity $\kappa^{dc}(T)$, for systems with both types of boundary conditions, is the same independent of the boundary mapping.

To conclude, systems with distinct types of boundary conditions, do not show any relevant change in the *bulk* quantities of interest for this work.

Summary

In this doctoral thesis work, I presented a study of thermal transport properties of a two-dimensional quantum spin liquid. The latter represents a novel phase of matter based on topological order, which shows features, such as fractionalization, emerging gauge theories, and unconventional magnetism. The indisputable observation of a spin liquid remains an outstanding goal in modern condensed matter physics, due to its elusive nature. Experiments can access indirectly properties of spin liquid states, looking at their magnetic excitations. Thermal transport investigations hence become a powerful mean to explore such phase of matter.

Frustrated, and frequently low-dimensional magnets are the prime material basis for spin liquids. Therefore, in chapter 1, I provided an introduction to magnetic frustration, and its signatures in magnetic materials. This is followed by a description of the ingredients of a quantum spin liquid, and its working definition, together with a list of possible experimental techniques used in the literature to explore this novel phase.

The thesis work focused on the study of longitudinal heat transport coefficients, based on the formalism of linear response theory which is described in chapter 2. Transport coefficients − within this theoretical framework − can be evaluated by studying the dynamical energy-current auto-correlation functions.

In my study, I considered the two-dimensional Kitaev spin model on the honeycomb lattice. The model describes local moments subject to frustrated Ising-type compass exchange. As shown in chapter 3, the model stands out as one of the few in which a quantum spin liquid can be exactly shown to exist. The model's ground state can be found exactly.
Kitaev's original solution is based on a representation of spin degrees of freedom in terms of Majorana fermions. Further approaches to solve the model exist in the literature. In particular, I used a Jordan-Wigner transformation to map the spin model to a spinless fermion model. These transformations are described in chapter 3.
Independent of the approach used, the exact solution of the model yields a quantum spin liquid ground state which supports two kinds of fractional excitations: spinless itinerant matter fermions, and localized flux excitations of $\mathbb{Z}_2$ gauge fields.
Many properties arising from the topological nature of the model are presented and discussed as well in chapter 3.
Interestingly, the system displays distinct gapless and gapped phases of matter fermions, depending on the anisotropy of exchange couplings in the model. This aspect has been taken into account in my thermal transport analysis.

In chapter 4, I described three methods which I used to calculate the aforementioned dynamical energy-current auto-correlation functions, in order to extract thermal transport properties

of the model.
First, I presented an analytical approach which is used to study thermal transport in the uniform gauge (flux-free) sector, where no gauge excitations are present.
Second, I studied thermal transport at finite temperatures, considering thermal gauge excitations off the uniform gauge sector. For this purpose, I made use of two complementary numerical methods able to treat finite-temperature systems.
First, the exact diagonalization method (ED) in the fermion basis has been used to exactly compute correlation functions in systems up to 36 lattice sites. This corresponds to a very large Hilbert space dimension of the underlying spin model which consists of 2^{72} states.
To approach these sizes, I developed a numerical routine that exploits translational invariance of gauge sectors. The routine allowed to reduce the number of gauge sectors to consider in the calculation of the correlation functions, and thus the computational effort.
Second, in order to reach larger systems − which is desirable to study transport in the thermodynamic limit − I used a method based on a mean-field treatment of gauge fluctuations − dubbed average gauge configuration (AGC). This method made possible to approach systems with up to $\sim \mathcal{O}(10^4)$ spinful sites.
It allowed to perform calculations of approximate correlation functions, reducing the trace over all gauge sectors − as required by the former exact method − to an average over dominant gauge sectors suited to a given temperature range. Indeed, the approximation is valid only for temperatures where fluctuations of gauge excitations are small.
To estimate this range, I resorted to the thermodynamics of the system to study the mean density of gauge excitations and its fluctuations. Results from this analysis have been completed by studying the temperature dependence of the specific heat via both numerical methods. I found that the specific heat shows characteristic features arising from the fractional degrees of freedom of the model. Moreover, the comparative analysis of thermodynamics has supported the validity of the approximate method over a wide temperature range, independent of the exchange coupling regime considered.

My results based on these formal developments have been reported in chapter 5. Thermal transport coefficients have been extracted from the longitudinal energy-current autocorrelation spectrum. The latter has been studied for varying sets of exchange couplings of the model, by tuning a related anisotropy parameter. This allowed to study heat transport for both the gapless and the gapped phase.
Furthermore, the investigation has been carried out in a wide range of temperatures, to highlight the impact of thermal gauge excitations on the heat transport from matter fermions. In the following, I will summarize and discuss such findings.

Analytical calculations in the uniform gauge sector provided the frequency dependence of the energy correlation spectra. The zero-frequency Drude weight at finite temperatures refers to the ballistic channel for matter fermions. It reflects the gapless (gapped) nature of fermions, showing a low-temperature power-law (exponential) behavior. The analytical findings imply that discarding gauge excitations, the two-dimensional Kitaev systems are ballistic heat conductors at finite temperatures and for any exchange coupling regime.

Numerical results from ED calculations showed several interesting features.
First, an indication of spin fractionalization − describing the system in terms of a "gas" of matter fermions interacting with thermally excited gauge fields − pertains to a spectral hump arising in the low-energy part of spectra. This hump stems from a broadening of the quasiparticle transport − which in the uniform gauge sector is entirely accumulated in the

Drude weight – to finite frequencies. The latter is presumably due to the scattering of matter fermions on thermal gauge excitations, which act as a thermally activated disorder.
Second, this low-energy hump is strongly temperature dependent, which is related to the matter fermions temperature-dependent density.
Third, the same spectral hump shows a structure in the zero-frequency limit of the spectra – dubbed pseudogap, due to its apparent gap-like behavior. The thermodynamic limit of this pseudogap is of interest to extract the dc transport coefficient, but it remains out of reach of the ED method.
Finally, the Drude weight is calculated. It shows a decreasing spectral intensity upon increasing the system size. From these results it has been conjectured that the ballistic channel decays exponentially fast in the thermodynamic limit.

Numerical results from the AGC method completed the picture provided by those from ED calculations.
First, the approximate correlation spectra show an overall qualitative agreement – at any temperature and for any system size – with the exact results, except for the lowest temperature, where strong gauge fluctuations influence the high-frequency part of spectra.
However, above a characteristic temperature the findings from the ED agree qualitatively with results from the AGC. The AGC spectra – compared with the ED ones for the same system size – well reproduces the ED results, being even able to capture remnants of the Drude weight, which disappears in the thermodynamic limit. The AGC spectra also show a two-particle excitation gap upon entering the gapped phase – as also observed from analytical results.
Moreover, it turns out – from ED and AGC calculations of the density of states (DOS) of matter fermions – that the matter fermion energy gap is robust against thermal gauge excitations. In the gapless phase, gauge excitations instead contribute to suppress a semimetallic DOS in favor of a metallic one.
Second, and going beyond a comparison to ED, the larger systems accessible to the AGC method answer the open-question on the nature of the pseudogap structure in the infinite system-size limit. Based on finite-size scaling, it turns out that – at any temperatures and anisotropy – the pseudogap has a strongly system-size dependent width, which suggests its closing onto finite values in the thermodynamic limit.
Using this finite zero-frequency limit of the correlation spectra I extracted the static dc heat conductivity as a function of temperatures and anisotropy, for various system sizes.
Interestingly, the conductivity features a form independent of the exchange coupling regime, with minimal finite-size corrections. However, the low-temperature behavior of the heat conductivity crosses over from a power-law to an exponentially activated behavior upon opening of the matter fermion gap by tuning the anisotropy. This is consistent with the notion of quasiparticle transport, where the activation energy corresponds to the energy gap of matter fermions.
Findings for the gapless matter-fermions heat conductivity in the isotropic regime have been also contrasted with those arising from QMC calculations of other authors [10]. Remarkably, the comparison shows many similarities, which makes these findings robust and independent of the numerical technique used to study the problem.
Finally, I tested the impact of altering boundary conditions on bulk transport in the system studied, and I found my results to be insensitive with respect to them.

To conclude, numerical findings – which consider the impact of gauge degrees of freedom

---

[10] I refer to the work in Ref. [131].

on heat transport – stress that there is a relevant interplay between matter fermions and gauge excitations.
This interplay displays important signatures in the dynamical energy-current correlation functions. As a consequence, dc transport coefficients are influenced as well. I have shown this by comparing the uniform gauge sector with sectors having randomly distributed gauge excitations. The former completely neglects gauge degrees of freedom – leading to a solely ballistic dc transport – while the latter show dissipative mechanisms which stem from an intrinsic thermal gauge disorder, leading to finite dc conductivities and a vanishing Drude weight in the thermodynamic limit.
Therefore, I have shown that two-dimensional Kitaev systems are dissipative heat conductors at finite temperature and for any exchange coupling regime.

Remarkably, the dissipative nature found for two-dimensional Kitaev systems is in strong contrast with results for the quasi one-dimensional Kitaev ladder [11] – which turns out to be an insulator with a vanishing Drude weight and a zero-dc conductivity – despite similar emergent thermally activated gauge disorder, and signatures of fractionalization.

Finally, the analysis carried out in this work does not access the very low-temperature regime, and it might neglect possible effects induced by strong gauge fluctuations, or their interactions in such a temperature range. Moreover, the results shown arise from a finite-size study, which can not exclude scenarios where transport coefficients might change, for system sizes way beyond the reach of the methods used. For instance, the pseudogap might acquire a different frequency dependence, such as to give rise to a different finite-size scaling in the thermodynamic limit.

---

[11] I refer to the work in Ref. [127].

Appendices

APPENDIX A

Mathematical supplement

A.1 Bogoliubov transformation

Given a quadratic Hamiltonian, in the specific case, the BCS Hamiltonian of (3.20, 3.41)

$$\mathcal{H} = \sum_{\mathbf{q}} \left[e_{\mathbf{q}} d^\dagger_{\mathbf{q}} d_{\mathbf{q}} + i \frac{\Delta_{\mathbf{q}}}{2} d^\dagger_{\mathbf{q}} d^\dagger_{-\mathbf{q}} - i \frac{\Delta_{\mathbf{q}}}{2} d_{-\mathbf{q}} d_{\mathbf{q}} \right] , \tag{A.1}$$

$d^{(\dagger)}_{\mathbf{q}}$ is a basis of complex fermion operators, $e_{\mathbf{q}}$ is the energy of the particle at momentum $\mathbf{q}$, and $\Delta_{\mathbf{q}}$ is a real function of the momentum which is related to the BCS pairing. Physical meaning is provided by symmetric particle energy, and antisymmetric pairing relation, i.e. $e_{\mathbf{q}} = e_{-\mathbf{q}}$ and $\Delta_{\mathbf{q}} = -\Delta_{-\mathbf{q}}$. A global gauge transformation applied to the basis can remove the imaginary unit i, as

$$d^\dagger_{\mathbf{q}} \to e^{-i\frac{\pi}{4}} d^\dagger_{\mathbf{q}} \qquad d_{\mathbf{q}} \to e^{i\frac{\pi}{4}} d_{\mathbf{q}} \, , \tag{A.2}$$

rendering (A.1) in this form

$$\mathcal{H} = \sum_{\mathbf{q}} \left[\frac{e_{\mathbf{q}}}{2} \Big(d^\dagger_{\mathbf{q}} d_{\mathbf{q}} + d^\dagger_{-\mathbf{q}} d_{-\mathbf{q}} \Big) + \frac{\Delta_{\mathbf{q}}}{2} \Big(d^\dagger_{\mathbf{q}} d^\dagger_{-\mathbf{q}} + d_{-\mathbf{q}} d_{\mathbf{q}} \Big) \right] . \tag{A.3}$$

The Hamiltonian in (A.3) can be diagonalized by means of a Bogoliubov transformation. To do this, (A.3) can be rewritten in this form

$$\mathcal{H} = \sum_{\mathbf{q}} \left[\varepsilon_0 \Big(\alpha^\dagger_{\mathbf{q}} \alpha_{\mathbf{q}} + \beta^\dagger_{\mathbf{q}} \beta_{\mathbf{q}} \Big) + \varepsilon_1 \Big(\alpha^\dagger_{\mathbf{q}} \beta^\dagger_{\mathbf{q}} + \beta_{\mathbf{q}} \alpha_{\mathbf{q}} \Big) \right] , \tag{A.4}$$

with $\alpha_{\mathbf{q}} = d_{\mathbf{q}}$ and $\beta_{\mathbf{q}} = d_{-\mathbf{q}}$. Using a matrix transformation $\mathbf{U}$, a new set of fermionic operators is obtained, in particular

$$A_{\mathbf{q}} = u_{\mathbf{q}} \alpha_{\mathbf{q}} + v_{\mathbf{q}} \beta^\dagger_{\mathbf{q}} \qquad A^\dagger_{\mathbf{q}} = u_{\mathbf{q}} \alpha^\dagger_{\mathbf{q}} + v_{\mathbf{q}} \beta_{\mathbf{q}} \tag{A.5a}$$

$$B_{\mathbf{q}} = v_{\mathbf{q}} \alpha^\dagger_{\mathbf{q}} - u_{\mathbf{q}} \beta_{\mathbf{q}} \qquad B^\dagger_{\mathbf{q}} = v_{\mathbf{q}} \alpha_{\mathbf{q}} - u_{\mathbf{q}} \beta^\dagger_{\mathbf{q}} . \tag{A.5b}$$

where $u_{\mathbf{q}}$ and $v_{\mathbf{q}}$ are real coefficients of this linear transformation $\mathbf{U}$ applied to α, β basis set. The diagonal form of the Hamiltonian follows from a proper choice of these coefficients, such that they have to preserve the algebraic relation given by the anticommutation relations of $A_{\mathbf{q}}$ and $B_{\mathbf{q}}$, namely

$$u^2_{\mathbf{q}} + v^2_{\mathbf{q}} = 1 = \Big\{ A_{\mathbf{q}}, A^\dagger_{\mathbf{q}} \Big\} = \Big\{ B_{\mathbf{q}}, B^\dagger_{\mathbf{q}} \Big\} \tag{A.6}$$

Using (A.6), it is possible to get the old basis set expressed in terms of $A_{\mathbf{q}}$ and $B_{\mathbf{q}}$,

$$\alpha_{\mathbf{q}} = u_{\mathbf{q}} A_{\mathbf{q}} + v_{\mathbf{q}} B^{\dagger}_{\mathbf{q}} \qquad \alpha^{\dagger}_{\mathbf{q}} = u_{\mathbf{q}} A^{\dagger}_{\mathbf{q}} + v_{\mathbf{q}} B_{\mathbf{q}} \tag{A.7a}$$

$$\beta_{\mathbf{q}} = v_{\mathbf{q}} A^{\dagger}_{\mathbf{q}} - u_{\mathbf{q}} B_{\mathbf{q}} \qquad \beta^{\dagger}_{\mathbf{q}} = v_{\mathbf{q}} A_{\mathbf{q}} - u_{\mathbf{q}} \beta^{\dagger}_{\mathbf{q}}. \tag{A.7b}$$

and thus inserting these into (A.4), the Hamiltonian in the new basis reads

$$\mathcal{H} = \sum_{\mathbf{q}} \Bigg\{ \left[\frac{e_{\mathbf{q}}}{2}(u^2_{\mathbf{q}} - v^2_{\mathbf{q}}) + \Delta_{\mathbf{q}} u_{\mathbf{q}} v_{\mathbf{q}} \right] \Big(A^{\dagger}_{\mathbf{q}} A_{\mathbf{q}} - B_{\mathbf{q}} B^{\dagger}_{\mathbf{q}} \Big) + \left[e_{\mathbf{q}} u_{\mathbf{q}} v_{\mathbf{q}} - \frac{\Delta_{\mathbf{q}}}{2}(u^2_{\mathbf{q}} - v^2_{\mathbf{q}}) \right] \Big(A^{\dagger}_{\mathbf{q}} B^{\dagger}_{\mathbf{q}} + B_{\mathbf{q}} A_{\mathbf{q}} \Big) \Bigg\}. \tag{A.8}$$

Diagonalization imposes that non-diagonal terms have to vanish, and this can follow from (A.8) as

$$e_{\mathbf{q}} u_{\mathbf{q}} v_{\mathbf{q}} - \frac{\Delta_{\mathbf{q}}}{2}(u^2_{\mathbf{q}} - v^2_{\mathbf{q}}) = 0 \ . \tag{A.9}$$

Moreover, exploiting the constraint of (A.6), it is possible to parametrize the set of two coefficients in terms of just one parameter to be determined,

$$u_{\mathbf{q}} = \cos\theta_{\mathbf{q}} \quad , v_{\mathbf{q}} = \sin\theta_{\mathbf{q}}. \tag{A.10}$$

Substituting (A.10) in (A.9), one obtains

$$\tan 2\theta_{\mathbf{q}} = \frac{\Delta_{\mathbf{q}}}{e_{\mathbf{q}}} \tag{A.11}$$

Solving for the diagonal part of (A.8), it turns out that $u^2_{\mathbf{q}} - v^2_{\mathbf{q}} = e_{\mathbf{q}}/\varepsilon_{\mathbf{q}}$, and $u_{\mathbf{q}} v_{\mathbf{q}} = \frac{1}{2}\Delta_{\mathbf{q}}/\varepsilon_{\mathbf{q}}$, where $\varepsilon_{\mathbf{q}} = \sqrt{e^2_{\mathbf{q}} + \Delta^2_{\mathbf{q}}}$ is the quasiparticle excitation energy. Both relations give important information on the nature of the coefficients solving the model, in particular (*i*) an expression for them in terms of momentum relations and energy dispersion, and (*ii*) from symmetries of $\varepsilon_{\mathbf{q}} = \varepsilon_{-\mathbf{q}}$, and $\Delta_{\mathbf{q}} = -\Delta_{-\mathbf{q}}$, it follows that $u_{-\mathbf{q}} = -u_{\mathbf{q}}$, and $v_{-\mathbf{q}} = v_{\mathbf{q}}$. With this choice of coefficients, and with their expression, the diagonal part of (A.8) reads as

$$\mathcal{H} = \sum_{\mathbf{q}} \frac{\varepsilon_{\mathbf{q}}}{2} \Big(A^{\dagger}_{\mathbf{q}} A_{\mathbf{q}} - B_{\mathbf{q}} B^{\dagger}_{\mathbf{q}} \Big) \underbrace{=}_{B^{\dagger}_{-\mathbf{q}} = A^{\dagger}_{\mathbf{q}}\, ,\, B_{-\mathbf{q}} = A_{\mathbf{q}}} \sum_{\mathbf{q}} \varepsilon_{\mathbf{q}} \Big(A^{\dagger}_{\mathbf{q}} A_{\mathbf{q}} - \frac{1}{2} \Big). \tag{A.12}$$

A.2 Wick's contractions

The basic idea of using Wick's theorem is to compact big complicated correlation functions in terms of *products* of the simplest *two-point* correlation functions, i.e. single-particle propagators. In Chapter 4, independently by the method employed, the following energy-current auto-correlation function has been considered, which is a 4-point correlator

$$C(\eta,t) = \frac{1}{N}\sum_{nmn'm'} L_{nm}L_{n'm'}\Big(\langle \mathbf{A}_n^\dagger(t)\mathbf{A}_m(t)\mathbf{A}_{n'}^\dagger\mathbf{A}_{m'}\rangle\Big)\,, \tag{A.13}$$

with $\mathbf{A}_n^\dagger = (a_1^\dagger, ..., a_N^\dagger, a_1, ..., a_N)$ the $2N$ components operator, and $L_{\alpha\beta}$ the current matrix elements. To evaluate (A.13) a Wick's decomposition has to be performed. Considering the time-evolution of operators in (A.13) within the Heisenberg picture, then

$$a_i^\dagger(t) = e^{-i\varepsilon_i t}a_i^\dagger \tag{A.14a}$$

$$a_i(t) = e^{i\varepsilon_i t}a_i\,. \tag{A.14b}$$

The possible meaningful contractions of the correlator in (A.13) are two, giving rise to

$$C(\eta,t) = \frac{1}{N}\sum_{nmn'm'} L_{nm}L_{n'm'}\Bigg(\underbrace{\langle \mathbf{A}_n^\dagger(t)\mathbf{A}_{m'}\rangle\langle \mathbf{A}_m(t)\mathbf{A}_{n'}^\dagger\rangle}_{(1)} - \underbrace{\langle \mathbf{A}_n^\dagger(t)\mathbf{A}_{n'}^\dagger\rangle\langle \mathbf{A}_m(t)\mathbf{A}_{m'}\rangle}_{(2)}\Bigg)\,, \tag{A.15}$$

where the 4-point correlator has been written as sum of products of 2-point correlators. Now, to make clearer the relation among the current matrix elements and these propagators, is useful to write explicitly these products $\langle\cdots\rangle\langle\cdots\rangle$. One may start considering the term (1) in (A.15), this can be read as

$$\begin{aligned}&\langle \overbrace{\Big[a_1^\dagger(t), a_2^\dagger(t), ..., a_N^\dagger(t), a_1(t), a_2(t), ..., a_N(t)\Big]}^{\mathbf{A}_n^\dagger(t)}\overbrace{\Big[a_1, a_2, ..., a_N, a_1^\dagger, a_2^\dagger, ..., a_N^\dagger\Big]}^{\mathbf{A}_{m'}}\rangle \times \\ &\quad\langle \underbrace{\Big[a_1(t), a_2(t), ..., a_N(t), a_1^\dagger(t), a_2^\dagger(t), ..., a_N^\dagger(t)\Big]}_{\mathbf{A}_m(t)}\underbrace{\Big[a_1^\dagger, a_2^\dagger, ..., a_N^\dagger, a_1, a_2, ..., a_N\Big]}_{\mathbf{A}_{n'}^\dagger}\rangle\end{aligned} \tag{A.16}$$

Looking at the structure of each $\big[\cdots\big]$, N annihilation operators follows N creation operators, or viceversa. Thus, $\langle\cdots\rangle$ reduces to only combinations among creation-annihilation pairs per each lattice site. For instance, running the index $i = 1, ..., N$, possible combinations among $\mathbf{A}_n^\dagger(t)$ and $\mathbf{A}_{m'}$ are only if $n = m'$ and $n + N = m' + N$. Similarly for $\mathbf{A}_m(t)$ and $\mathbf{A}_{n'}^\dagger$, with $m = n'$ and $m + N = n' + N$. Such selection of pairs suppresses sum over n' and m' in (A.15). Thus, considering (A.14a) and (A.14b) for the time evolution, (1) reads as

$$(1) = \Big[\langle a_n^\dagger a_n\rangle e^{-i\varepsilon_n t} + \langle a_n a_n^\dagger\rangle e^{+i\varepsilon_n t}\Big]\cdot\Big[\langle a_m a_m^\dagger\rangle e^{+i\varepsilon_m t} + \langle a_m^\dagger a_m\rangle e^{-i\varepsilon_m t}\Big]\,, \tag{A.17}$$

where the sign $+(-)$ in the exponential function is related to the time evolution of the annihilation (creation) operator in the brackets. One may further simplify the expression in (A.17), leading to

$$\begin{aligned}(1) &= f_n(1-f_m)e^{-i(\varepsilon_n-\varepsilon_m)t} + f_m(1-f_n)e^{i(\varepsilon_n-\varepsilon_m)t}\\ &\quad + f_n f_m e^{-i(\varepsilon_n+\varepsilon_m)t} + (1-f_n)(1-f_m)e^{i(\varepsilon_n+\varepsilon_m)t}\,,\end{aligned} \tag{A.18}$$

where $f_n = 1/(\exp(\beta\varepsilon_n) + 1)$ is the Fermi-Dirac distribution. Following the same procedure, a similar result is obtained for the contraction (2). One difference arises from the structure of creation/annihilation operators inside the brackets. Because of this, different combinations of N operators, compared to (1), are possible – e.g., between $\mathbf{A}_n^\dagger(t)$ and $\mathbf{A}_{n'}^\dagger(t)$, with $n = n' + N$, and $n + N = n'$.

Therefore, summing up (1) and (2), with their proper related current matrix elements in (A.13), $C(\eta, t)$ reads as

$$\begin{aligned} C(\eta,t) = \frac{1}{N}\sum_{n,m=1}^{N} \Bigg[& e^{-i(\varepsilon_n-\varepsilon_m)t} f_n(1-f_m)\Big(L_{n,m}L_{m,n} - L_{n,m}L_{n+N,m+N}\Big) \\ & + e^{i(\varepsilon_n-\varepsilon_m)t} f_m(1-f_n)\Big(L_{n+N,m+N}L_{m+N,n+N} - L_{n+N,m+N}L_{n,m}\Big) \\ & + e^{-i(\varepsilon_n+\varepsilon_m)t} f_n f_m\Big(L_{n,m+N}L_{m+N,n} - L_{n,m+N}L_{n+N,m}\Big) \\ & + e^{i(\varepsilon_n+\varepsilon_m)t}(1-f_n)(1-f_m)\Big(L_{n+N,m}L_{m,n+N} - L_{n+N,m}L_{n,m+N}\Big)\Bigg] . \end{aligned} \tag{A.19}$$

A.3 Computation of Dirac δ function

The numerical study of the energy-current auto-correlation function in Chapter 4 requires a way to compute the Dirac's delta function in the frequency space. It shows up in equation (4.23) − which I recall,

$$C(\eta,\omega) = \int_{-\infty}^{\infty} e^{i\omega t} C(\eta,t)\, dt = \frac{2\pi}{N} \sum_{n,m=1}^{N} (\cdots)^{\eta}_{n,m} \delta(\omega - \omega_{nm}) \ , \tag{A.20}$$

where $(\cdots)^{\eta}_{n,m}$ contains the product of the current matrix elements and the Wick-decomposition's terms, per each gauge sector η. $\delta(\omega - \omega_{mn})$ is the Dirac's delta function, with $\omega_{nm} = \mp(E_n \pm E_m)$, and E_n, E_m the eigenenergies of the system ($\hbar = 1$). Among all the possible representations of δ, I present in the following two ways to compute it, and thus to evaluate (A.20).

- **Sokhotski-Plemelj representation** : the Sokhotski-Plemelj theorem relates the delta function to the distribution of the Cauchy principal value of the function $1/x$, defined by

  $$\langle \mathcal{P}\frac{1}{x}, f\rangle = \lim_{\chi\to 0^+} \int_{|x|>\chi} \frac{f(x)}{x} dx \ , \tag{A.21}$$

  with the Sokhotski's formula stating that

  $$\lim_{\chi\to 0^+} \frac{1}{x \pm i\chi} = \mathcal{P}\frac{1}{x} \mp i\pi\delta(x) \, . \tag{A.22}$$

  The limit is understood in the *distribution* sense, for all smooth functions f,

  $$\lim_{\chi\to 0^+} \int_{-\infty}^{\infty} \frac{f(x)}{x \pm i\chi} = \mathcal{P}\frac{f(x)}{x} \mp i\pi f(0) \, . \tag{A.23}$$

  Therefore, $\delta(x)$ function can be obtained from (A.22) as

  $$\begin{aligned} 2i\pi\delta(x) &= \lim_{\chi\to 0^+} \left(\frac{1}{x - i\chi} - \frac{1}{x + i\chi} \right) = \lim_{\chi\to 0^+} \frac{2i\chi}{x^2 + \chi^2} \ \to \\ &\to \delta(x) = \lim_{\chi\to 0^+} \frac{1}{\pi} \frac{\chi}{x^2 + \chi^2} \ , \end{aligned} \tag{A.24}$$

  with x its argument, and χ the full width at half-maximum of the related Cauchy-Lorentz distribution in (A.24). As smaller the value of χ, as smaller the broadening of the distribution around x, and finer the resolution of δ in the x-space.

  Going back to (A.20), the argument of δ function is $x = \omega \mp (E_n \pm E_m)$, where '$\mp$' sign refers to the sign in front of exponents in (A.18), which follows from the time evolution. The '$\pm$' sign depends on the contribution considered in (A.18), if the pair-breaking, or the quasiparticle one, respectively. Thus, all four possible contributions of (A.24) are considered as a function of x_i, leading to

  $$C(\eta,\omega) = \lim_{\chi\to 0^+} \frac{2\pi}{N} \sum_{n,m=1}^{N} (\cdots)^{\eta}_{n,m} \sum_{\omega=\omega_{min}}^{\omega_{max}} \sum_{i=1}^{4} \frac{1}{\pi} \frac{\chi}{x_i^2 + \chi^2} \, . \tag{A.25}$$

  The energy resolution of correlation spectra can depend by several details. First, the limit of $\chi \to 0$ is implemented considering very small, but finite values of χ, which can provide different resolutions. Second, once found the best χ, the correlation spectrum is studied in an energy range $\omega \in [\omega_{min}, \omega_{max}]$. A smooth shape of the spectrum depends by the grid width, i.e. the width of discrete number of energy intervals, $\delta\omega = (\omega_{max} - \omega_{min})/n$. As smaller is $\delta\omega$, as larger the resolution and the number of intervals considered, and in the end also the computational effort.

- **Discrete binning representation** : considering the energy range of interest, and dividing it into *bins* of width $\delta\omega$, the correlation spectrum spanning the total energy range will read

$$\begin{aligned}\tilde{C}(\eta,\omega) &= \int_{\omega-\delta\omega/2}^{\omega+\delta\omega/2} C(\eta,\omega)d\omega = \int_{\omega-\delta\omega/2}^{\omega+\delta\omega/2} \frac{2\pi}{N}\sum_{n,m=1}^{N}(\cdots)^{\eta}_{n,m}\delta(\omega-\omega_{nm})d\omega \\ &= \frac{2\pi}{N}\sum_{n,m=1}^{N}(\cdots)^{\eta}_{n,m}\int_{\omega-\delta\omega/2}^{\omega+\delta\omega/2}\delta(\omega-\omega_{nm})d\omega\,. \end{aligned} \tag{A.26}$$

Terms inside $(\cdots)^{\eta}_{n,m}$ can be integrated out because do not depend on ω. Integral of Dirac's delta in (A.26) refers to δ as a *measure*, i.e., a way that assigns a value to each subsets in the integral. In other words, $\int_{\omega-\delta\omega/2}^{\omega+\delta\omega/2}\delta(\omega-\omega_{nm})d\omega$ is the integral of 1 with respect to the δ measure in the interval $A = [\omega - \delta\omega/2, \omega + \delta\omega/2]$. The $\delta(\omega - \omega_{nm})$ assigns 'volume' 1 to the set $\{\omega_{nm}\}$ and to every set which contains ω_{nm}. While, it assigns 'volume' 0 to every other set, i.e., those ones not containing ω_{nm}. This means that,

$$\int_A d\delta = \begin{cases} 1, & \text{if } \omega_{nm} \in A \\ 0, & \text{if } \omega_{nm} \notin A \end{cases}. \tag{A.27}$$

This allows to collect all the contributions to the energy-current correlation function at each specific bin of energy $\omega_{nm} \pm \delta\omega/2$, leading to

$$\tilde{C}(\eta,\omega) = \frac{2\pi}{N}\sum_{n,m=1}^{N}(\cdots)^{\eta}_{n,m}\int_{\omega-\delta\omega/2}^{\omega+\delta\omega/2}\delta(\omega-\omega_{nm})d\omega = \frac{2\pi}{N}\sum_{n,m=1}^{N}\sum_{i=1}^{4}(\cdots)^{\eta}_{n,m|A_i}\,, \tag{A.28}$$

where the position of set A_i depends on the possible four combinations of sign of $\omega_{nm} = \pm(E_n \pm E_m)$. The numerical energy resolution in is set only by the size of $\delta\omega$.

APPENDIX B

Numerical remarks

B.1 Translational invariant gauge sectors

Calculations via the ED method introduced in Sec. 4.2 have an upper limit in the number of lattice sites N that can be treated. This because one needs to trace over all the possible 2^N gauge sectors of the system. Thus, the computational effort grows exponentially fast. Progress can be made considering lattice symmetry.

In particular, each gauge sector is due to a specific combination of $\eta_{\mathbf{r}}$ gauge fields sitting on each lattice site, i.e., $\{\eta_{\mathbf{r}}\} = \{\eta_0, \eta_1, \cdots, \eta_j, \cdots, \eta_{N-1}\}$, with $\eta_j = \pm 1$, and $j = 0, 1, \dots, N-1$. One can represent each $\{\eta_{\mathbf{r}}\}$ on a lattice with N sites via a binary vector of size N. Each element of the vector is related to a corresponding lattice site, which value can be "0" ($\eta_j = -1$), or "1" ($\eta_j = +1$). This leads to 2^N different possible binary vectors, related to the 2^N gauge sectors. Fig. B.1 shows an example of such a construction.

The idea is that for each given gauge sector, there exists a certain number of redundant translational invariant gauge sectors. For instance, one may take a lattice with N sites and a single gauge-flip – i.e., one deviating gauge variable from the uniform gauge sector – at position $(0, 0)$. This single-flip gauge sector has exactly N redundant copies produced via all possible translations of the single gauge-flip along the x and y direction on the square lattice. In general, for a system with N lattice sites, collecting the gauge flips in k ways, provides the number of possible combinations without repetitions of gauge configurations,

$$C_k(N) = \binom{N}{k} = \frac{N!}{k!(N-k)!}, \qquad \text{where} \qquad \sum_{k=0}^{N} C_k(N) = 2^N. \tag{B.1}$$

Fig. B.2 shows an example of what discussed above but for a double gauge-flip, i.e., for $k = 2$ in a system with $N = 9$ sites. It turns out that only 4 over 36 possible gauge sectors arising from (B.1) are not invariant gauge sectors under translational symmetry. Each of these 4 sector appears with a *multiplicity* $m^\star = 9$ – which in the end covers the total 36 combinations.

Unfortunately, $C_k(N)$ in (B.1) says only the total amount of combinations arising from the number of gauge flips k on the lattice, but nothing about how many of these gauge sectors are *irreproducible* by any discrete translational operation, neither on their multiplicity.
Thus, the task is to find the $N^\star$ not invariant gauge sectors, and in the end to evaluate their

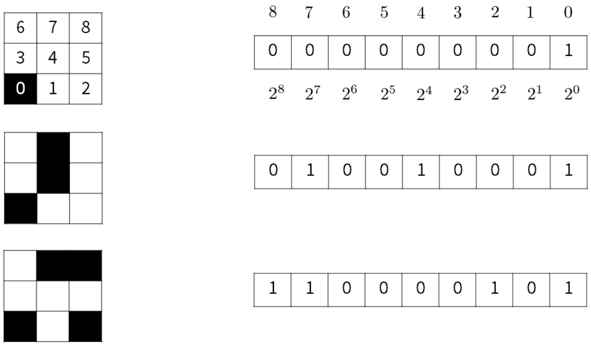

Figure B.1: Scheme of binary representations of gauge flips on a square lattice with $N = 9$ sites. Black (white) cells indicate lattice sites with $\eta_j = +1$ ($\eta_j = -1$). Lattice sites are numbered along a snake-pattern on the square lattice, from left to right. On the right side, the corresponding binary vectors : each element of the array has value 1(0) related to the gauge field value.

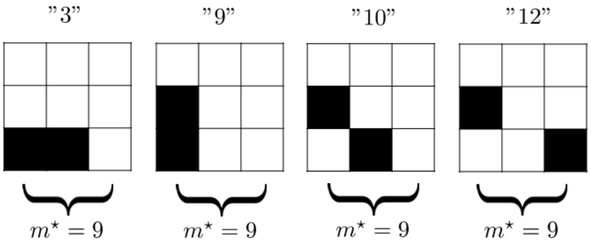

Figure B.2: Schemes of not equivalent gauge representations for $N = 9$ and double gauge-flips ($k = 2$). Number in quotation marks indicates the decimal value of the corresponding binary vector. On the bottom, the multiplicity $m^\star$ of each sector is reported.

multiplicity, $m^\star_\eta$. The number $N^\star$, and each $m^\star_\eta$ found, have to satisfy the following constraint,

$$\sum_{\eta=1}^{N^\star} m^\star_\eta = \sum_{k=0}^{N} C_k(N) = 2^N. \tag{B.2}$$

In the following, I provide a description of the code used to find $N^\star$ and $m^\star_\eta$. The code aims to find the smallest decimal label related to the binary representation of the not invariant gauge sector − see for instance Fig. B.2 − which is stored in a vector *ireps(i)*, with $i = 1, \ldots, N^\star$. One can summarize the code in the following few-step operative diagram flow:

- One initializes the lattice with the j^{th} gauge configuration, looping $j = 0, 2^N - 1$.
- For each starting j^{th} gauge sector, one performs lattice translations along x, y directions, or a combination of the two.
- One compares each translated sector's decimal label with the starting one. If they are equal, then one continues to translate the sector up to reach all the possible moves. If it is greater, then one updates the multiplicity counter *imlt(i)*, and adds the invariant sector to a temporary storage vector. If it is smaller, one quits the j-loop, increasing the counter. Therefore, one takes the new smaller decimal value, and starts from its related gauge sector again the translations' loop.
- One collects all the not invariant gauge sectors in the array *ireps(i)*, with their respective multiplicities *imlt(i)*.

N=16	**i**	**ireps(i)**	**imlt(i)**	**$\{\eta_\mathbf{r}\}$(i)**
	1	0	1	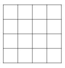
	2	1	16	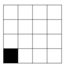
	3	3	16	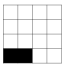
	···	···	···	···
	305	771	8	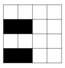
	306	773	16	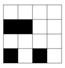
	···	···	···	···
	4156	65535	1	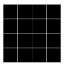

Table B.1: Results for the not invariant gauge sectors under translational symmetry for systems with $N = 16$ sites. The index i refers to the i^{th} sector found, with $i = 1, \cdots, N^\star$, and $N^\star$ equal to 4156. The corresponding decimal value of the gauge sector is stored in *ireps(i)*, and its multiplicity in *imlt(i)*. The corresponding arrangement of $\{\eta_\mathbf{r}\}$ is shown in the last column.

In Tab. B.1, I show the results from this analysis for a lattice with $N = 16$ sites. The totality of gauge configurations are $2^{16} = 65536$. Remarkably, only $N^\star = 4156$ not invariant sectors have been found. Each of these has a specific multiplicity $m^\star_\eta$ tracked by the code. The sum of all these, in the end, fulfills (B.2).

One may wonder whether this symmetry argument applies to the study of the dynamical energy current auto-correlation function. To verify this fact, I show in Fig. B.3 the spectra of $C^{\{\eta\}}(\omega)$ evaluated for a given gauge sector $\{\eta\}$, for two different system sizes $N = 36$ (a-b), and $N = 100$ (c-d), at $T = \infty$, and for the isotropic point $\alpha = 1$.

In particular, Figs. B.3(a,c) show $C(\omega)$ for the gauge sector "1" and "2" – having a single gauge-flip at site $(0, 0)$ and $(0, 1)$, respectively. These two are translational invariant, and energy-degenerate, sectors obtained as single-flip from the vortex-free sector. What is shown in Figs. B.3(a,c) is that also the related correlation spectra are degenerate. The inset in Fig. B.3(a) displays the difference $C^{\{1\}}(\omega) - C^{\{2\}}(\omega)$, which is finite but satisfyingly small. This difference decreases as the size of the system increases, as can be observed in the inset of Fig. B.3(c).

Figs. B.3(b,d) instead point out that not invariant gauge sectors, "1" and "5" – with "5" arising from a double gauge-flip at $(0, 0)$ and $(0, 2)$ – have both different energy spectrum and correlation spectra. This is evident from a finite spectral difference shown in the insets of Figs. B.3(b,d). In other words, these independently contribute to $C(\omega)$.

In view of these results, one can compute (4.16) reducing the full gauge trace to a smaller num-

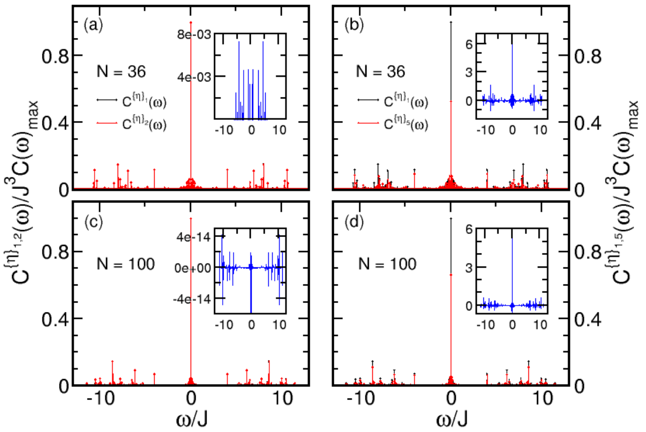

Figure B.3: Single gauge sectors $C^{\{\eta\}}(\omega)$ vs. ω at $T = \infty$ for two different system sizes, $N = 36$ (a,b), and $N = 100$ (c,d), for $\alpha = 1.0$. (a,c): Gauge sectors “1” and “2” are considered. Insets: difference $C^{\{1\}}(\omega) - C^{\{2\}}(\omega)$. (b,d): Gauge sectors “1” and “5” are considered. Insets: difference $C^{\{1\}}(\omega) - C^{\{5\}}(\omega)$.

ber of not invariant gauge sectors under translational symmetry. Results are still exact, up to small deviations due to finite-size effects, which are suppressed in the thermodynamic limit.

Fig. B.4(a) shows the $C(\omega)$ spectra obtained employing both the full-trace (black solid line with solid triangles), and the reduced trace (red empty circles) version of (4.16), for $N = 16$ lattice sites, at $\alpha = 1.0$, and $T = \infty$. Fig. B.4(b) shows the low-frequency range of Fig. B.4(a) , and Fig. B.4(c) shows $\mid C_{\text{full-trace}}(\omega) - C_{\text{reduced-trace}}(\omega) \mid$, which turns out to be very small.

B.2 Random average and energy resolution

In order to get smooth correlation spectra from AGC calculations – as shown in the main text – one deals with two degrees of freedom. These are the energy resolution of spectra – fixed by the energy window $\delta\omega$ in binning Dirac's δ functions – and the number of gauge sectors N_R for the average in (4.24). It turns out that a good balance between the two is enough to reduce best finite-size effects in the spectra. In the following, I show results from calculations of spectra via the AGC method, tuning both $\delta\omega$ and N_R.

I have performed several numerical “experiments” aiming to get smooth spectra with the highest energy resolution (smallest $\delta\omega$) and the lowest computational effort (smallest N_R). The following calculations have been carried out at fixed temperature $T = \infty$, and at the isotropic point $\alpha = 1.0$.

One may start by seeing the effect of tuning N_R at fixed $\delta\omega$ on $C(\omega)$, and viceversa, the effect of changing $\delta\omega$ for a fixed number N_R. These are reported in Fig. B.5 for $N = 100$ lattice sites.

Each panel of Figs. B.5(a-d) shows the spectrum $C(\omega)$ for different numbers of fully random gauge sectors N_R chosen with $n(T) = 0.5$, in the range $N_R = [100, 2000]$. Going from (a) to (d) different $\delta\omega$ are considered, from $\delta\omega = 10^{-3}$(a) to $\delta\omega = 5 \cdot 10^{-2}$(d). They show

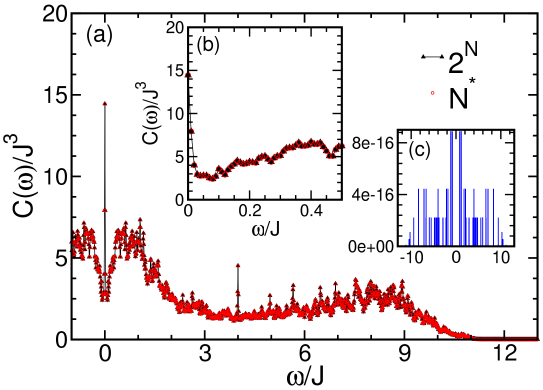

Figure B.4: (a) $C(\omega)$ vs. ω from ED calculations via a full trace over gauge sectors (black solid with solid triangles), and a reduced trace (red empty circles), for $N = 16$ lattice sites, $\alpha = 1.0$, and at $T = \infty$. (b) Low-frequency zoom-in of (a). (c) Difference among the resulting spectra of (a).

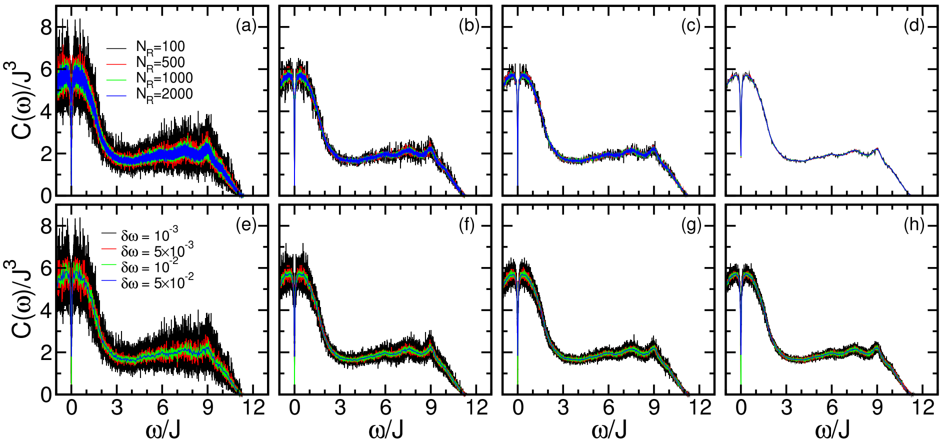

Figure B.5: $C(\omega)$ versus frequency via AGC, for $N = 100$-sites systems. (a-d) Variations with $\delta\omega = 10^{-3}, 5\cdot10^{-3}, 10^{-2}, 5\cdot10^{-2}$ from (a) to (d). Each panel shows four different number of realizations N_R. (e-h) Variations with number of realizations $N_R = 100, 500, 1000, 2000$ from (e) to (h). Each panel shows four different binning resolutions $\delta\omega$.

that once the energy resolution is fixed the spectrum becomes smoother as N_R increases – see Fig. B.5(a). Moreover, decreasing the energy resolution (b-d), the spectrum sensitivity to the N_R used becomes less evident. This means that for low energy resolutions, finite-size effects are well reduced even by using a small N_R, i.e., one can obtain low-resolution smooth spectra with low computational effort.

Each panel of Figs. B.5(e-h) shows the spectrum $C(\omega)$ for varying $\delta\omega$ – in the same range of Figs. B.5(a-d) –, and going from (e) to (h) different N_R are used, from $N_R = 100$ (e) to $N_R = 2000$ (h). They, consistently with Figs. B.5(a-d), show the impact of changing $\delta\omega$ for fixed N_R on the spectra.

One may also wonder, how much the choice of N_R – at a fixed $\delta\omega$ – is dependent on the system size N. Fig. B.6 shows $C(\omega)$ as a function of frequency at fixed $\delta\omega = 10^{-3}$, for many system sizes N and different N_R.

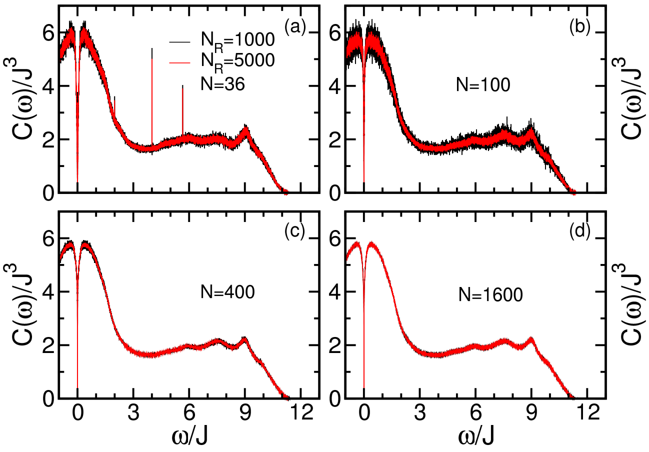

Figure B.6: $C(\omega)$ versus frequency via AGC, for two possible numbers of realizations $N_R = 1000\,(5000)$ in black (red) lines, at fixed $\delta\omega = 10^{-3}$. From (a) to (d) is displayed a variation with the number of lattice sites $N = 36, 100, 400,$ and 1600.

It is shown that for relatively small systems – see Figs. B.6(a,b) – a larger N_R is important to obtain a smoother spectrum. However, as N increases it becomes indifferent what N_R is used – as shown progressively in Figs. B.6(c,d). For the largest N, the results might be considered almost independent of N_R.

To conclude, by means of this numerical analysis I have found the energy resolution $\delta\omega$ which reduces best finite-size effects – also taking into account the computational effort – and which is used for the AGC calculations presented in the main text.
Yet, it turns out that one needs to choose N_R dependently on the system size N considered. Interestingly, for $N \gtrsim 900$, the quality of numerical results becomes almost independent of N_R. Thus, N_R can be very small, which further minimizes the computational effort.

APPENDIX C

Thermodynamics

C.1 Thermodynamics of the Kitaev honeycomb model on a square lattice

In this section I provide a description of thermodynamics of the Kitaev model on the square lattice, and also further details on all the thermodynamic quantities discussed in the main text. Before going into details of calculations, one needs to keep track of the Hilbert space dimension, in the step from the spin Hamiltonian on the brick-wall lattice (BWL) to the spinless fermion Hamiltonian on the square lattice (SL). For this purpose, one can recall the spin Hamiltonian in (3.6)

$$\mathcal{H} = J_x \sum_{\langle ij \rangle_x} \sigma_i^x \sigma_j^x + J_y \sum_{\langle ij \rangle_y} \sigma_i^y \sigma_j^y + J_z \sum_{\langle ij \rangle_z} \sigma_i^z \sigma_j^z, \tag{C.1}$$

which on the BWL is studied for $M = M_x M_y$ sites. M_x runs along the $x-y$ chains of the BWL, while M_y along the z-bonds. Therefore, it counts 2^M states. The corresponding SL − whose each single vertex contains one black and one white site connected by a z-bond on the bipartite BWL − has $N = N_x N_y$ sites. Since there is one z-bond every second site, $N_x = M_x/2$, and $N_y = M_y$, and one recovers the spinless Hamiltonian in (3.40) − which I recall for the purpose of the section,

$$\begin{aligned}\mathcal{H}_{\{\eta\}} = \sum_{\mathbf{r}} & J_x(d_{\mathbf{r}}^\dagger + d_{\mathbf{r}})(d_{\mathbf{r}+\mathbf{e}_x}^\dagger - d_{\mathbf{r}+\mathbf{e}_x}) + J_y(d_{\mathbf{r}}^\dagger + d_{\mathbf{r}}) \\ & \times(d_{\mathbf{r}+\mathbf{e}_y}^\dagger - d_{\mathbf{r}+\mathbf{e}_y}) + J_z \eta_{\mathbf{r}}(2d_{\mathbf{r}}^\dagger d_{\mathbf{r}} - 1)\,. \end{aligned} \tag{C.2}$$

The latter has consistently $2^M = 2^{2N}$ states. Indeed, on the SL with N sites, there are 2^N different gauge configurations − in the following referred to as $\{\eta\}$. The Hamiltonian in (C.2) is one of the 2^N different single-particle Hamiltonians, $\mathcal{H}_{\{\eta\}}$, each of which has a dimension of $2N \times 2N$ − because of the pairing terms, see Sec. 4.2 − and which reads in the Bogoliubov quasiparticle basis as

$$\mathcal{H}_{\{\eta\}} = \sum_{j=1}^{N} \varepsilon_j a_j^\dagger a_j - \varepsilon_j a_j a_j^\dagger = \sum_{j=1}^{N} 2\varepsilon_j (a_j^\dagger a_j - \frac{1}{2}) \ , \ \varepsilon_j > 0. \tag{C.3}$$

From these N single-particle states of energy ε_j one can build 2^N many-body particle states. Thus, the Hilbert space dimension counts for 2^N many-body particle states for 2^N gauge sectors, i.e., 2^{2N} states. The many-particle eigenenergies are given by

$$E_i(\{\eta\}) = \sum_{l=1}^{N} 2\varepsilon_l(\theta_{il} - \frac{1}{2}), \tag{C.4}$$

where $\theta_{il} = 0, 1$ indicates the occupation number in the quasiparticle basis. The 2^N possible values of θ_{il} give rise to the 2^N different E_i. These latter span in the range $E_i(\{\eta\}) = [E^0(\{\eta\}), -E^0(\{\eta\})]$, with $E^0(\{\eta\})$ being the *local* many-body ground state energy for the given gauge sector $\{\eta\}$, obtained from (C.4) with $\theta_{il} = 0$,

$$E^0(\{\eta\}) = -\sum_{j=1}^{N} \varepsilon_j < 0. \tag{C.5}$$

One may consider an operator A, which is also diagonal in the gauge fields $\eta_{\mathbf{r}}$. The expectation value can be evaluated as

$$\langle A \rangle = \frac{\operatorname{Tr} e^{-\beta\mathcal{H}} A}{\operatorname{Tr} e^{-\beta\mathcal{H}}} = \frac{1}{Z} \sum_{\eta=0}^{2^N-1} Z_\eta \langle A \rangle_\eta, \tag{C.6}$$

with $\langle \cdots \rangle_\eta$ evaluated in the single-particle sector within the given gauge sector $\{\eta\}$, and Z the total partition function of the system. The latter reads as

$$Z = \operatorname{Tr}_{\{\eta\}} \operatorname{Tr}_{a_j(\eta)} e^{-\beta\mathcal{H}_{\{\eta\}}} = \sum_{\eta=0}^{2^N-1} Z_\eta\,, \tag{C.7}$$

which is obtained tracing over all gauge sectors $\{\eta\}$, and over matter fermions at each fixed gauge sector. In (C.6) and (C.7) Z_η is the partition function of matter fermions in the given gauge sector. This latter can be expressed as,

$$Z_\eta = \sum_{i=1}^{2^N} e^{-\beta E_i(\{\eta\})} = \prod_{j=1}^{N} (e^{\beta\varepsilon_j} + e^{-\beta\varepsilon_j}) = 2^N \prod_{j=1}^{N} \cosh(\beta\varepsilon_j)\,. \tag{C.8}$$

Thermodynamic quantities hence can be evaluated by means of the partition function Z. Numerically it is useful to scale the local partition function by the Boltzmann factor arising from the *global* many-body ground state energy E_G [1], i.e., $Z_\eta \to e^{\beta E_G} Z_\eta$. Scaling by the constant $e^{\beta E_G}$ does not change the result of (C.6). Thus, one can rewrite (C.8) as

$$\begin{aligned} Z_\eta = e^{\beta E_G} \prod_{j=1}^{N} e^{\beta\varepsilon_j}(1 + e^{-2\beta\varepsilon_j}) = e^{\beta E_G}\, \overbrace{e^{\beta\sum_{i=1}^{N}\varepsilon_i}}^{-\beta E^0(\eta)} \prod_{j=1}^{N}(1 + e^{-2\beta\varepsilon_j}) = \\ e^{-\beta(E^0(\eta) - E_G)} \prod_{j=1}^{N}(1 + e^{-2\beta\varepsilon_j}) = e^{-\beta\Delta\varepsilon(\eta)} \prod_{j=1}^{N}(1 + e^{-2\beta\varepsilon_j})\,. \end{aligned} \tag{C.9}$$

In (C.9) $\Delta\varepsilon(\eta) = E^0(\eta) - E_G$ is the difference between the local and global many-body ground state energies. The value of $\Delta\varepsilon(\eta)$ also says how close the sector considered is from being

---

[1] The global many-body ground state energy can be seen as the lowest local many-body ground state energy arising from all the gauge sectors of the system, i.e. $\min_{\{\eta\}} E^0(\{\eta\})$.

degenerate to that with energy E_G. Generally, one may assume that the latter is represented by the vortex-free sector ($\eta_{\mathbf{r}} = -1 \ \forall \mathbf{r}$). This has been accurately checked by comparing all the $E^0(\eta)$ found in the calculations, and considering in the end the lowest among them. The $\Delta\varepsilon(\eta)$ is important for the computation of Z. This partition function Z in the zero-temperature limit reads as

$$Z(\beta \to \infty) = \sum_{\eta=0}^{2^N-1} e^{-\beta(E^0(\eta)-E_G))} + \cdots = \mathcal{D}_G \ , \tag{C.10}$$

where $\mathcal{D}_G$ is the degree of degeneracy of the ground state. Indeed, in the zero-temperature limit the Boltzmann weights in (C.9) tend to zero. Thus, only sectors degenerate to the global ground state contribute to Z, i.e., those for which $|\Delta\varepsilon(\eta)| \ll 1$. A numerical cut-off for the energy degeneracy of the states is required. Numerical calculations performed in this work count sectors as degenerate to the global ground state only if $|\Delta\varepsilon(\eta)| < 10^{-8}$. In the opposite infinite-temperature limit, the total partition function is given by

$$Z(\beta \to 0) = \sum_{\eta=0}^{2^N-1} 2^N = 2^{2N} \ , \tag{C.11}$$

which makes each gauge sector equally probable, and contributing to the thermodynamics of the system. At intermediate temperatures ($0 < \beta < \infty$), two possible cases arise :

- $|\Delta\varepsilon(\eta)| < 10^{-8}$: $Z(\beta)$ will be returned from the sum of $Z_\eta(\beta)$ of (C.9) with the exponential factor $e^{-\beta\Delta\varepsilon(\eta)} \approx 1$.
- $|\Delta\varepsilon(\eta)| > 10^{-8}$: $Z(\beta)$ will be the sum of $Z_\eta(\beta)$ of (C.9), which also considers the weight provided by the exponential factor. As greater $|\Delta\varepsilon(\eta)|$, as smaller the contribution of the related gauge sector to the thermodynamic of the system.

To evaluate the thermodynamic observables of interest, one may start deriving fundamental quantities. In particular,

- Average energy

$$U_1(T) = \langle \mathcal{H} \rangle = \frac{1}{N}\left[\frac{1}{Z}\sum_{\eta=0}^{2^N-1} Z_\eta \langle \mathcal{H} \rangle_\eta\right] \tag{C.12}$$

with

$$\begin{aligned}\langle \mathcal{H} \rangle_\eta &= \left\langle \sum_{j=1}^{N} 2\varepsilon_j \left(a_j^\dagger a_j - \frac{1}{2}\right)\right\rangle_\eta = \\ &= \sum_{j=1}^{N} 2\varepsilon_j \langle a_j^\dagger a_j \rangle_\eta - \frac{1}{2}\sum_{j=1}^{N} 2\varepsilon_j = \\ &= \sum_{j=1}^{N} 2\varepsilon_j f_j(T) + E^0(\{\eta\}) \ . \end{aligned} \tag{C.13}$$

The expectation value of the occupation number in (C.13) − which follows from the quadratic form of the Hamiltonian (C.3) − is given by the Fermi-Dirac distribution,

$$f_j(T) = \langle a_j^\dagger a_j \rangle_\eta = \frac{1}{1 + e^{2\beta\varepsilon_j}} \ . \tag{C.14}$$

- Average energy square

$$U_2(T) = \langle \mathcal{H}^2 \rangle = \frac{1}{N}\left[\frac{1}{Z}\sum_{\eta=0}^{2^N-1} Z_\eta \langle \mathcal{H}^2 \rangle_\eta\right] \tag{C.15}$$

with

$$\begin{aligned}
\langle \mathcal{H}^2 \rangle_\eta &= \left\langle \sum_{j=1}^{N}\sum_{k=1}^{N} 2\varepsilon_j \cdot 2\varepsilon_k \left(a_j^\dagger a_j - \frac{1}{2}\right)\left(a_k^\dagger a_k - \frac{1}{2}\right)\right\rangle_\eta = \\
&= \sum_{j=1}^{N}\sum_{k=1}^{N} 2\varepsilon_j 2\varepsilon_k \left[\langle a_j^\dagger a_j a_k^\dagger a_k\rangle_\eta - \frac{1}{2}\langle a_j^\dagger a_j\rangle_\eta - \frac{1}{2}\langle a_k^\dagger a_k\rangle_\eta + \frac{1}{4}\right] = \\
&= \sum_{j=1}^{N}(2\varepsilon_j)^2 f_j(T)\big[1 - f_j(T)\big] + \sum_{j=1}^{N}\left[4\varepsilon_j^2 f_j^2(T) - 4\varepsilon_j^2 f_j(T) + \varepsilon_j^2\right] = \\
&= \sum_{j=1}^{N}(2\varepsilon_j)^2 f_j(T)\big[1 - f_j(T)\big] + \langle \mathcal{H}\rangle_\eta^2 \,,
\end{aligned} \tag{C.16}$$

where the last line of (C.16) is obtained by applying a Wick's contraction to $\langle \cdots \rangle_\eta$, and making use of (C.13). Importantly, in the construction of $U_1(T)$ and $U_2(T)$ the total partition function Z arises from (C.9) and (C.7), taking into account the scaling $Z \to e^{\beta E_G} Z$. Many observables can be calculated by computing the free energy of the system, and using the quantities defined in (C.12) and (C.15). In particular,

$$F(T) = -\frac{1}{N}(T \ln Z - E_G)\,, \tag{C.17}$$

is the free energy of the system, with Z from (C.9) and (C.7). First, one may start evaluating the entropy $S(T)$ of the system, which is given by

$$S(T) = \frac{1}{T}(U_1(T) - F(T))\ . \tag{C.18}$$

In Sec. 4.3, it has been observed that the entropy of the model is released in two stages at two separated temperature scales, as a consequence of the thermal fractionalization [130]. Therefore, one may continue computing the specific heat $C_\nu(T)$, since it is related to the release of the entropy, that reads as

$$C_\nu(T) = \underbrace{T\frac{\partial S}{\partial T}}_{\textbf{(a)}} = \overbrace{\frac{1}{T^2}(U_2(T) - U_1^2(T))}^{\textbf{(b)}}\ , \tag{C.19}$$

which results have been shown in Fig. 4.2. Results shown in the main text have been obtained by using the first equality of (C.19) − and they are consistent with QMC findings in Ref. [130], as shown in in Sec. 5.4. Equations (C.19)(**a**) and (C.19)(**b**) describe the same quantity. However, one might have some numerical issue in computing the specific heat from (C.19)(**a**) which are reduced best by using (C.19)(**b**), or viceversa. One the one hand, (C.19)**(a)** comes out from the Maxwell's relations for thermodynamics potentials. Computing $C_\nu(T)$ via a numerical derivative of the entropy leads to possible sharp peaks due to the finite difference approximation, i.e. $S(T+\Delta T) - S(T-\Delta T)/2\Delta T$, depending on the width of the increment

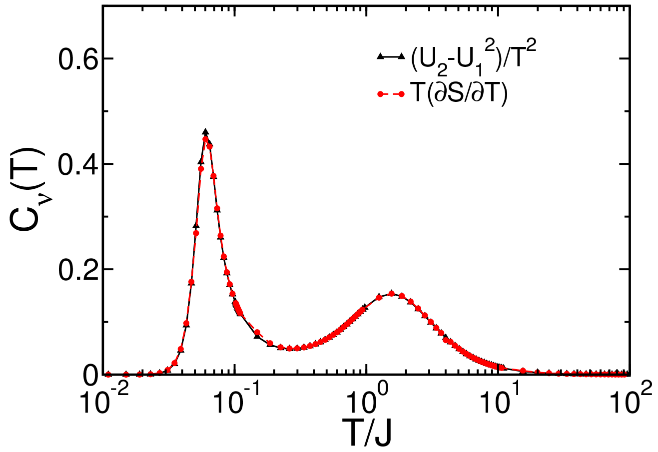

Figure C.1: Specific heat versus temperature for a system with $N = 36$ sites ($N_x = N_y = 6$) in the isotropic regime of Kitaev couplings $\alpha = 1.0$. $C_\nu(T)$ is evaluated using both the **(a)** and **(b)** of (C.19).

ΔT. On the other hand, (C.19)**(b)** arises from the fluctuation-dissipation theorem [144], where $C_\nu(T)$ is a measure of the energy fluctuation of the system, in particular

$$\begin{aligned} C_\nu(T) = \frac{\partial\langle\mathcal{H}\rangle}{\partial T} = \frac{-\beta}{T}\frac{\partial\langle\mathcal{H}\rangle}{\partial\beta} = \\ = \frac{1}{T^2}\frac{\partial^2 \ln Z}{\partial\beta^2} = \frac{1}{T^2}\frac{\partial}{\partial\beta}\left(\frac{1}{Z}\frac{\partial Z}{\partial\beta}\right) = \\ = \frac{1}{T^2}\left[\frac{1}{Z}\frac{\partial^2 Z}{\partial\beta^2} - \frac{1}{Z^2}\left(\frac{\partial Z}{\partial\beta}\right)^2\right] = \frac{1}{T^2}(U_2(T) - U_1^2(T)) \; . \end{aligned} \tag{C.20}$$

Equation (C.20) outlines that (C.19)(**b**) follows from the partition function of the system. The numerical challenge using (C.19)(**b**) is to compute correctly the partition function from (C.9). Especially in the very low-temperature limit, due to the temperature dependence of (C.19)(**b**) as T^{-2}, some anomalous oscillation of $C_\nu(T)$ can arise, which suppression requires an accurate balance between the numerical cut-off for the energy degeneracy and the temperature in (C.9). A comparison of the $C_\nu(T)$ obtained from (C.19)(**a**) and (C.19)(**b**) is shown in Fig. C.1 for the isotropic regime $\alpha = 1$, which displays a rather well agreement between the two numerical approaches.

For the sake of completeness, I show in Fig. C.2 the analytical specific heat C_f at $\alpha = 1$ for the vortex-free sector – i.e., discarding any gauge excitations and arising only from matter-fermions energy fluctuations – evaluated as

$$C_f = \int d\varepsilon_{\mathbf{q}}\,(2\varepsilon_{\mathbf{q}})\rho(\varepsilon_{\mathbf{q}})\frac{\partial f(\varepsilon_{\mathbf{q}})}{\partial T} \underbrace{\propto}_{x=\frac{\varepsilon_{\mathbf{q}}}{T}} T^2 \int dx \frac{x^3 \exp(x)}{(\exp(x)+1)^2} \, , \tag{C.21}$$

with $\varepsilon_{\mathbf{q}}$ the quasiparticle energy, $\rho(\varepsilon_{\mathbf{q}})$ the related density of states (DOS), and $f(\varepsilon_{\mathbf{q}})$ the Fermi-Dirac distribution – see Sec. 4.1 for references. Interestingly, the peak of Fig. C.2 has the same location of the high-temperature peak in Fig. C.1 arising from matter fermions, which thus has no relations with the gauge induced disorder. Yet, at low temperatures [2],

---

[2] Specifically for $T_\alpha^\star \lesssim T \lesssim T_M$.

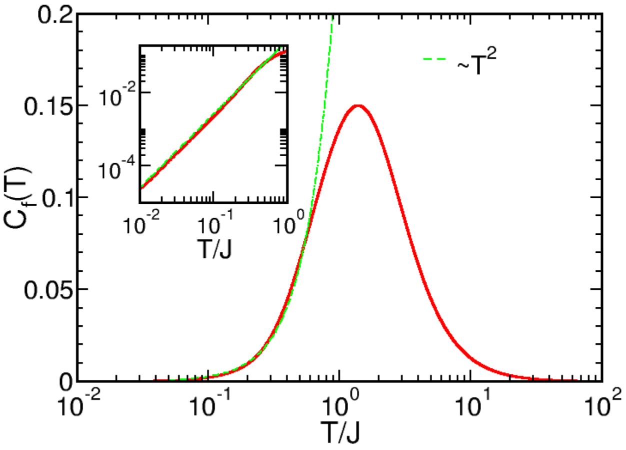

Figure C.2: Specific heat versus temperature for a system with $N = 320 \times 320$ sites in the isotropic regime of Kitaev couplings $\alpha = 1.0$, analytically evaluated from (C.21). Inset: low-T fit function.

$C_f(T) \sim T^2$ shows the effects of neglecting thermal gauge excitations: with no gauge fluxes, matter-fermions specific heat recalls the typical behavior expected for semimetallic systems **[3]**, which is well reproduced by the fit function in the inset of Fig. C.2. The same behavior can be also derived by a power counting – as shown in (C.21). Conversely, $C_\nu(T)$ of Fig. C.1 scales as $\sim T$ [130], which originates from the metallic DOS induced by thermally excited gauge fluxes [130] – see also Sec. 5.3.1.

In the main text, the mean density of gauge excitations has been also introduced in (4.25) of Sec. 4.3. In detail, it is given by

$$n(T) = \frac{1}{N}\left[\frac{1}{Z}\sum_{\eta=0}^{2^N-1} Z_\eta \mathcal{M}_\eta\right], \quad \text{with } \mathcal{M}_\eta = \begin{cases} n_\eta & \text{if } n_\eta \leq \frac{N}{2} \\ N - n_\eta & \text{if } n_\eta > \frac{N}{2} \end{cases}, \tag{C.22}$$

where n_η counts the number of positive gauge fields in the gauge sector $\{\eta\}$, and $\mathcal{M}_\eta$ indicates the average number of deviating gauge fields from the uniform gauge sector. The fluctuations $\delta n(T)$ of $n(T)$ in (C.22) are evaluated via a numerical temperature derivative, which reads as $\delta n(T) = \big[n(T+\Delta T) - n(T-\Delta T)\big]/2\Delta T$.

---

[3] At least in the gapless regime, e.g., at $\alpha = 1$, $\varepsilon_{\mathbf{q}} \sim \mathbf{q}$ for $\mathbf{q} \to 0$, as for Dirac semimetals.

Bibliography

[1] P.W. Anderson. *Resonating valence bonds: A new kind of insulator ? Materials Research Bulletin*, 8(2):153 – 160, 1973. ISSN 0025-5408. URL `http://www.sciencedirect.com/science/article/pii/0025540873901670`.

[2] L. D. Landau. *On the theory of phase transitions. Zh. Eksp. Teor. Fiz.*, 7:19–32, 1937.

[3] V. L. Ginzburg and L. D. Landau. *On the Theory of superconductivity. Zh. Eksp. Teor. Fiz.*, 20:1064–1082, 1950.

[4] D. C. Tsui, H. L. Stormer, and A. C. Gossard. *Two-Dimensional Magnetotransport in the Extreme Quantum Limit. Phys. Rev. Lett.*, 48:1559–1562, May 1982. URL `https://link.aps.org/doi/10.1103/PhysRevLett.48.1559`.

[5] R. B. Laughlin. *Quantized Hall conductivity in two dimensions. Phys. Rev. B*, 23:5632–5633, May 1981. URL `https://link.aps.org/doi/10.1103/PhysRevB.23.5632`.

[6] X.-G. Wen and Q. Niu. *Ground-state degeneracy of the fractional quantum Hall states in the presence of a random potential and on high-genus Riemann surfaces. Phys. Rev. B*, 41:9377–9396, May 1990. URL `https://link.aps.org/doi/10.1103/PhysRevB.41.9377`.

[7] X.-G. Wen. *Vacuum degeneracy of chiral spin states in compactified space. Phys. Rev. B*, 40:7387–7390, Oct 1989. URL `https://link.aps.org/doi/10.1103/PhysRevB.40.7387`.

[8] F. Wilczek. *Magnetic Flux, Angular Momentum, and Statistics. Phys. Rev. Lett.*, 48:1144–1146, Apr 1982. URL `https://link.aps.org/doi/10.1103/PhysRevLett.48.1144`.

[9] F. Wilczek. Fractional Statistics and Anyon Superconductivity. International journal of modern physics. World Scientific, 1990. ISBN 9789810200497. URL `https://books.google.de/books?id=mCgy_y8PAkoC`.

[10] A. Kitaev and C. Laumann. *Topological phases and quantum computation.* Les Houches Summer School: Exact methods in low-dimensional physics and quantum computing, Volume: 89, (2008). Oxford University Press, 2009. ISBN 0199574618.

[11] J. K. Pachos. *Quantum computation with abelian anyons on the honeycomb lattice. International Journal of Quantum Information*, 04(06):947–954, 2006. URL `https://doi.org/10.1142/S0219749906002328`.

[12] M. H. Freedman, A. Kitaev, M. J. Larsen, and Z. Wang. *Topological quantum computation. Bull. Amer. Math. Soc. (N.S.)*, 40(1):31–38, 2003. ISSN 0273-0979. URL `https://doi.org/10.1090/S0273-0979-02-00964-3`.

[13] A.Y. Kitaev. *Fault-tolerant quantum computation by anyons. Annals of Physics*, 303 (1):2 – 30, 2003. ISSN 0003-4916. URL `http://www.sciencedirect.com/science/article/pii/S0003491602000180`.

[14] A. Kitaev. *Anyons in an exactly solved model and beyond. Annals of Physics*, 321(1):2 – 111, 2006. ISSN 0003-4916. URL `http://www.sciencedirect.com/science/article/pii/S0003491605002381`.

[15] L. Balents. *Spin liquids in frustrated magnets. Nature*, 464:199 EP –, Mar 2010. URL `http://dx.doi.org/10.1038/nature08917`.

[16] H.T. Diep. Frustrated Spin Systems. World Scientific, 2004. ISBN 9789812567819. URL `https://books.google.de/books?id=eVZmj0vkelUC`.

[17] A. Banerjee, C. A. Bridges, J.-Q. Yan, A. A. Aczel, L. Li, M. B. Stone, G. E. Granroth, M. D. Lumsden, Y. Yiu, J. Knolle, S. Bhattacharjee, D. L. Kovrizhin, R. Moessner, D. A. Tennant, D. G. Mandrus, and S. E. Nagler. *Proximate Kitaev quantum spin liquid behaviour in a honeycomb magnet. Nature Materials*, 15:733 EP –, Apr 2016. URL `http://dx.doi.org/10.1038/nmat4604`.

[18] A. Banerjee, J. Yan, J. Knolle, Craig A. Bridges, M. B. Stone, M. D. Lumsden, D. G. Mandrus, D. A. Tennant, R. Moessner, and S. E. Nagler. *Neutron scattering in the proximate quantum spin liquid* $\alpha - \mathrm{RuCl}_3$. *Science*, 356(6342):1055–1059, 2017. ISSN 0036-8075. URL `http://science.sciencemag.org/content/356/6342/1055`.

[19] J. Knolle, G.-W. Chern, D. L. Kovrizhin, R. Moessner, and N. B. Perkins. *Raman Scattering Signatures of Kitaev Spin Liquids in* $A_2\mathrm{IrO}_3$ *Iridates with* $A = \mathrm{Na}$ *or* Li. *Phys. Rev. Lett.*, 113:187201, Oct 2014. URL `https://link.aps.org/doi/10.1103/PhysRevLett.113.187201`.

[20] Y. Li, D. Adroja, P. K. Biswas, P. J. Baker, Q. Zhang, J. Liu, A. A. Tsirlin, P. Gegenwart, and Q. Zhang. *Muon Spin Relaxation Evidence for the U(1) Quantum Spin-Liquid Ground State in the Triangular Antiferromagnet* $\mathrm{YbMgGaO}_4$. *Phys. Rev. Lett.*, 117:097201, Aug 2016. URL `https://link.aps.org/doi/10.1103/PhysRevLett.117.097201`.

[21] S.-H. Baek, S.-H. Do, K.-Y. Choi, Y. S. Kwon, A. U. B. Wolter, S. Nishimoto, J. van den Brink, and B. Büchner. *Evidence for a Field-Induced Quantum Spin Liquid in* α-RuCl_3. *Phys. Rev. Lett.*, 119:037201, Jul 2017. URL `https://link.aps.org/doi/10.1103/PhysRevLett.119.037201`.

[22] J. Zheng, K. Ran, T. Li, J. Wang, P. Wang, B. Liu, Z.-X. Liu, B. Normand, J. Wen, and W. Yu. *Gapless Spin Excitations in the Field-Induced Quantum Spin Liquid Phase of* $\alpha{-}\mathrm{RuCl}_3$. *Phys. Rev. Lett.*, 119:227208, Dec 2017. URL `https://link.aps.org/doi/10.1103/PhysRevLett.119.227208`.

[23] M. Yamashita, N. Nakata, Y. Kasahara, T. Sasaki, N. Yoneyama, N. Kobayashi, S. Fujimoto, T. Shibauchi, and Y. Matsuda. *Thermal-transport measurements in a quantum*

spin-liquid state of the frustrated triangular magnet $\kappa-(\mathrm{BEDT}-\mathrm{TTF})_2\mathrm{Cu}_2(\mathrm{CN})_3$. *Nature Physics*, 5:44 EP –, Nov 2008. URL `http://dx.doi.org/10.1038/nphys1134`.

[24] M. Yamashita, T. Shibauchi, and Y. Matsuda. *Thermal-Transport Studies on Two-Dimensional Quantum Spin Liquids. ChemPhysChem*, 13(1):74–78, 2012. URL `https://onlinelibrary.wiley.com/doi/abs/10.1002/cphc.201100556`.

[25] C. Hess. *Heat conduction in low-dimensional quantum magnets. The European Physical Journal Special Topics*, 151(1):73–83, Dec 2007. ISSN 1951-6401. URL `https://doi.org/10.1140/epjst/e2007-00363-8`.

[26] P. Chandra and B. Doucot. *Possible spin-liquid state at large S for the frustrated square Heisenberg lattice. Phys. Rev. B*, 38:9335–9338, Nov 1988. URL `https://link.aps.org/doi/10.1103/PhysRevB.38.9335`.

[27] H. Rosner, R. R. P. Singh, W. H. Zheng, J. Oitmaa, and W. E. Pickett. *High-temperature expansions for the* $J_1 - J_2$ *Heisenberg models: Applications to ab initio calculated models for* $\mathrm{Li_2VOSiO_4}$ *and* $\mathrm{Li_2VOGeO_4}$. *Phys. Rev. B*, 67:014416, Jan 2003. URL `https://link.aps.org/doi/10.1103/PhysRevB.67.014416`.

[28] S. Trebst. *Kitaev Materials. ArXiv e-prints*, Jan 2017. URL `https://arxiv.org/abs/1701.07056v1`.

[29] G. Jackeli and G. Khaliullin. *Mott Insulators in the Strong Spin-Orbit Coupling Limit: From Heisenberg to a Quantum Compass and Kitaev Models. Phys. Rev. Lett.*, 102:017205, Jan 2009. URL `https://link.aps.org/doi/10.1103/PhysRevLett.102.017205`.

[30] Z. Nussinov and J. van den Brink. *Compass models: Theory and physical motivations. Rev. Mod. Phys.*, 87:1–59, Jan 2015. URL `https://link.aps.org/doi/10.1103/RevModPhys.87.1`.

[31] A. P. Ramirez. *Strongly Geometrically Frustrated Magnets. Annual Review of Materials Science*, 24(1):453–480, 1994. URL `https://doi.org/10.1146/annurev.ms.24.080194.002321`.

[32] J. T. Chalker. *Spin liquids and frustrated magnetism.* Topological Aspects of Condensed Matter Physics: Lecture Notes of the Les Houches Summer School: Volume 103, August 2014. Oxford University Press, 2017. ISBN 9780198785781. URL `http://www.oxfordscholarship.com/view/10.1093/acprof:oso/9780198785781.001.0001/acprof-9780198785781-chapter-3`.

[33] G. H. Wannier. *Antiferromagnetism. The Triangular Ising Net. Phys. Rev.*, 79:357–364, Jul 1950. URL `https://link.aps.org/doi/10.1103/PhysRev.79.357`.

[34] N. H. March, R. Street, and Tosi M. P. *Amorphous Solids and the Liquid State.* Physics of Solids and Liquids. Springer US, 1985. ISBN 9781475791563. URL `https://www.springer.com/la/book/9780306419478`.

[35] L. Savary and L. Balents. *Quantum spin liquids: a review. Reports on Progress in Physics*, 80(1):016502, 2017. URL `http://stacks.iop.org/0034-4885/80/i=1/a=016502`.

[36] N. D. Mermin and H. Wagner. *Absence of Ferromagnetism or Antiferromagnetism in One- or Two-Dimensional Isotropic Heisenberg Models. Phys. Rev. Lett.*, 17:1133–1136, Nov 1966. URL `https://link.aps.org/doi/10.1103/PhysRevLett.17.1133`.

[37] J. B. Fouet, P. Sindzingre, and C. Lhuillier. *An investigation of the quantum* $J_1 - J_2 - J_3$ *model on the honeycomb lattice. Eur. Phys. J. B*, 20, 2001. URL `https://link.springer.com/article/10.1007%2Fs100510170273`.

[38] C. Lacroix, P. Mendels, and F. Mila. Introduction to Frustrated Magnetism: Materials, Experiments, Theory. Springer Series in Solid-State Sciences. Springer Berlin Heidelberg, 2011. ISBN 9783642105890. URL `https://books.google.de/books?id=utSV09Zuh0kC`.

[39] H. Kageyama, K. Yoshimura, R. Stern, N. V. Mushnikov, K. Onizuka, M. Kato, K. Kosuge, C. P. Slichter, T. Goto, and Y. Ueda. *Exact Dimer Ground State and Quantized Magnetization Plateaus in the Two-Dimensional Spin System* $\mathrm{SrCu_2(BO_3)_2}$. *Phys. Rev. Lett.*, 82:3168–3171, Apr 1999. URL `https://link.aps.org/doi/10.1103/PhysRevLett.82.3168`.

[40] B. S. Shastry and B. Sutherland. *Exact ground state of a quantum mechanical antiferromagnet. Physica B+C*, 108(1):1069 – 1070, 1981. ISSN 0378-4363. URL `http://www.sciencedirect.com/science/article/pii/037843638190838X`.

[41] A. Koga and N. Kawakami. *Quantum Phase Transitions in the Shastry-Sutherland Model for* $\mathrm{SrCu_2(BO_3)_2}$. *Phys. Rev. Lett.*, 84:4461–4464, May 2000. URL `https://link.aps.org/doi/10.1103/PhysRevLett.84.4461`.

[42] S. Liang, B. Doucot, and P. W. Anderson. *Some New Variational Resonating-Valence-Bond-Type Wave Functions for the Spin-*$\frac{1}{2}$ *Antiferromagnetic Heisenberg Model on a Square Lattice. Phys. Rev. Lett.*, 61:365–368, Jul 1988. URL `https://link.aps.org/doi/10.1103/PhysRevLett.61.365`.

[43] D. S. Rokhsar and S. A. Kivelson. *Superconductivity and the Quantum Hard-Core Dimer Gas. Phys. Rev. Lett.*, 61:2376–2379, Nov 1988. URL `https://link.aps.org/doi/10.1103/PhysRevLett.61.2376`.

[44] R. Moessner and S. L. Sondhi. *Resonating Valence Bond Phase in the Triangular Lattice Quantum Dimer Model. Phys. Rev. Lett.*, 86:1881–1884, Feb 2001. URL `https://link.aps.org/doi/10.1103/PhysRevLett.86.1881`.

[45] S. Furukawa, G. Misguich, and M. Oshikawa. *Reduced density matrices and topological order in a quantum dimer model. Journal of Physics: Condensed Matter*, 19(14):145212, 2007. URL `http://stacks.iop.org/0953-8984/19/i=14/a=145212`.

[46] A. Kitaev and J. Preskill. *Topological Entanglement Entropy. Phys. Rev. Lett.*, 96:110404, Mar 2006. URL `https://link.aps.org/doi/10.1103/PhysRevLett.96.110404`.

[47] J. Wildeboer, A. Seidel, and R. G. Melko. *Entanglement entropy and topological order in resonating valence-bond quantum spin liquids. Phys. Rev. B*, 95:100402, Mar 2017. URL `https://link.aps.org/doi/10.1103/PhysRevB.95.100402`.

[48] C. Kittel. *Introduction to solid state physics.* New York Wiley London, Chapman and Hall, 1953.

[49] R. Franz and G. Wiedemann. *Ueber die Wärme-Leitungsfähigkeit der Metalle. Annalen der Physik*, 165(8):497–531, 1853. URL `https://onlinelibrary.wiley.com/doi/abs/10.1002/andp.18531650802`.

[50] N.W. Ashcroft and N.D. Mermin. *Solid State Physics.* HRW international editions. Holt, Rinehart and Winston, 1976. ISBN 9780030839931. URL `https://books.google.de/books?id=1C9HAQAAIAAJ`.

[51] P. G. Klemens. *The Scattering of Low-Frequency Lattice Waves by Static Imperfections. Proceedings of the Physical Society A*, 68:1113–1128, December 1955.

[52] P. D. Thacher. *Effect of Boundaries and Isotopes on the Thermal Conductivity of* LiF. *Phys. Rev.*, 156:975–988, Apr 1967. URL `https://link.aps.org/doi/10.1103/PhysRev.156.975`.

[53] G. D. Mahan. *Many-Particle Physics.* Number 2 in Plenum Press. Springer US, Plenum Press, New York, 1990. ISBN 978-0-306-43423-5. URL `https://www.springer.com/us/book/9780306434235`.

[54] R. Kubo. *Statistical-Mechanical Theory of Irreversible Processes. I. General Theory and Simple Applications to Magnetic and Conduction Problems. Journal of the Physical Society of Japan*, 12(6):570–586, 1957. URL `https://doi.org/10.1143/JPSJ.12.570`.

[55] L. Onsager. *Reciprocal Relations in Irreversible Processes. I. Phys. Rev.*, 37:405–426, Feb 1931. URL `https://link.aps.org/doi/10.1103/PhysRev.37.405`.

[56] H. Mori. *Collective Motion of Particles at Finite Temperatures. Progress of Theoretical Physics*, 28(5):763–783, 11 1962. ISSN 0033-068X. URL `https://dx.doi.org/10.1143/PTP.28.763`.

[57] X. Zotos and P. Prelovšek. *Transport in one dimensional quantum systems. arXiv e-prints*, art. cond-mat/0304630, Apr 2003. URL `https://ui.adsabs.harvard.edu/#abs/2003cond.mat..4630Z`.

[58] J. Sirker, R. G. Pereira, and I. Affleck. *Conservation laws, integrability, and transport in one-dimensional quantum systems. Phys. Rev. B*, 83:035115, Jan 2011. URL `https://link.aps.org/doi/10.1103/PhysRevB.83.035115`.

[59] X. Zotos, F. Naef, and P. Prelovšek. *Transport and conservation laws. Phys. Rev. B*, 55:11029–11032, May 1997. URL `https://link.aps.org/doi/10.1103/PhysRevB.55.11029`.

[60] P. Mazur. *Non-ergodicity of phase functions in certain systems. Physica*, 43(4):533 – 545, 1969. ISSN 0031-8914. URL `http://www.sciencedirect.com/science/article/pii/0031891469901852`.

[61] F. W. Gorter, L. J. Noordermeer, A. R. Kop, and A. R. Miedema. *Observation of heat transport by magnons. Physics Letters A*, 29(6):331 – 332, 1969. ISSN 0375-9601. URL `http://www.sciencedirect.com/science/article/pii/0375960169901546`.

[62] H. N. De Lang, H. van Kempen, and P. Wyder. *Energy Transport above* T_c *by Paramagnetic Magnons in Two-Dimensional Ferromagnetic Heisenberg Systems.* *Phys. Rev. Lett.*, 39:467–470, Aug 1977. URL `https://link.aps.org/doi/10.1103/PhysRevLett.39.467`.

[63] A. V. Sologubenko, K. Giannó, H. R. Ott, U. Ammerahl, and A. Revcolevschi. *Thermal Conductivity of the Hole-Doped Spin Ladder System* $Sr_{14-x}Ca_xCu_{24}O_{41}$. *Phys. Rev. Lett.*, 84:2714–2717, Mar 2000. URL `https://link.aps.org/doi/10.1103/PhysRevLett.84.2714`.

[64] A. V. Sologubenko, E. Felder, K. Giannò, H. R. Ott, A. Vietkine, and A. Revcolevschi. *Thermal conductivity and specific heat of the linear chain cuprate* Sr_2CuO_3 : *Evidence for thermal transport via spinons.* *Phys. Rev. B*, 62:R6108–R6111, Sep 2000. URL `https://link.aps.org/doi/10.1103/PhysRevB.62.R6108`.

[65] A. V. Sologubenko, K. Giannò, H. R. Ott, A. Vietkine, and A. Revcolevschi. *Heat transport by lattice and spin excitations in the spin-chain compounds* $SrCuO_2$ *and* Sr_2CuO_3. *Phys. Rev. B*, 64:054412, Jul 2001. URL `https://link.aps.org/doi/10.1103/PhysRevB.64.054412`.

[66] C. Hess, C. Baumann, U. Ammerahl, B. Büchner, F. Heidrich-Meisner, W. Brenig, and A. Revcolevschi. *Magnon heat transport in* $(Sr, Ca, La)_{14}Cu_{24}O_{41}$. *Phys. Rev. B*, 64: 184305, Oct 2001. URL `https://link.aps.org/doi/10.1103/PhysRevB.64.184305`.

[67] M. Hofmann, T. Lorenz, K. Berggold, M. Grüninger, A. Freimuth, G. S. Uhrig, and E. Brück. *Evidence for a large magnetic heat current in insulating layered cuprates.* *Phys. Rev. B*, 67:184502, May 2003. URL `https://link.aps.org/doi/10.1103/PhysRevB.67.184502`.

[68] X. F. Sun, J. Takeya, S. Komiya, and Y. Ando. *Thermal conductivity of lightly* Sr- *and* Zn-*doped* La_2CuO_4 *single crystals.* *Phys. Rev. B*, 67:104503, Mar 2003. URL `https://link.aps.org/doi/10.1103/PhysRevB.67.104503`.

[69] C. Hess, B. Büchner, U. Ammerahl, L. Colonescu, F. Heidrich-Meisner, W. Brenig, and A. Revcolevschi. *Magnon Heat Transport in Doped* La_2CuO_4. *Phys. Rev. Lett.*, 90:197002, May 2003. URL `https://link.aps.org/doi/10.1103/PhysRevLett.90.197002`.

[70] C. Hess, H. ElHaes, A. Waske, B. Büchner, C. Sekar, G. Krabbes, F. Heidrich-Meisner, and W. Brenig. *Linear Temperature Dependence of the Magnetic Heat Conductivity in* $CaCu_2O_3$. *Phys. Rev. Lett.*, 98:027201, Jan 2007. URL `https://link.aps.org/doi/10.1103/PhysRevLett.98.027201`.

[71] T. Kawamata, N. Takahashi, T. Adachi, T. Noji, K. Kudo, N. Kobayashi, and Y. Koike. *Evidence for Ballistic Thermal Conduction in the One-Dimensional S=1/2 Heisenberg Antiferromagnetic Spin System* Sr_2CuO_3. *Journal of the Physical Society of Japan*, 77 (3):034607, 2008. URL `https://doi.org/10.1143/JPSJ.77.034607`.

[72] N. Hlubek, P. Ribeiro, R. Saint-Martin, A. Revcolevschi, G. Roth, G. Behr, B. Büchner, and C. Hess. *Ballistic heat transport of quantum spin excitations as seen in* $SrCuO_2$. *Phys. Rev. B*, 81:020405, Jan 2010. URL `https://link.aps.org/doi/10.1103/PhysRevB.81.020405`.

[73] R. Hentrich, A. U. B. Wolter, X. Zotos, W. Brenig, D. Nowak, A. Isaeva, T. Doert, A. Banerjee, P. Lampen-Kelley, D. G. Mandrus, S. E. Nagler, J. Sears, Y.-J. Kim, B. Büchner, and C. Hess. *Unusual Phonon Heat Transport in* $\alpha-\mathrm{RuCl}_3$*: Strong Spin-Phonon Scattering and Field-Induced Spin Gap. Phys. Rev. Lett.*, 120:117204, Mar 2018. URL `https://link.aps.org/doi/10.1103/PhysRevLett.120.117204`.

[74] Y. J. Yu, Y. Xu, K. J. Ran, J. M. Ni, Y. Y. Huang, J. H. Wang, J. S. Wen, and S. Y. Li. *Ultralow-Temperature Thermal Conductivity of the Kitaev Honeycomb Magnet* $\alpha-\mathrm{RuCl}_3$ *across the Field-Induced Phase Transition. Phys. Rev. Lett.*, 120:067202, Feb 2018. URL `https://link.aps.org/doi/10.1103/PhysRevLett.120.067202`.

[75] Y. Kasahara, T. Ohnishi, Y. Mizukami, O. Tanaka, S. Ma, K. Sugii, N. Kurita, H. Tanaka, J. Nasu, Y. Motome, T. Shibauchi, and Y. Matsuda. *Majorana quantization and half-integer thermal quantum Hall effect in a Kitaev spin liquid. Nature*, 559(7713):227–231, 2018. ISSN 1476-4687. URL `https://doi.org/10.1038/s41586-018-0274-0`.

[76] M. Goiran, M. Costes, J. M. Broto, F. C. Chou, R. Klingeler, E. Arushanov, S.-L. Drechsler, B. Büchner, and V. Kataev. *High-field ESR studies of the quantum spin magnet* $\mathrm{CaCu_2O_3}$. *New Journal of Physics*, 8(5):74–74, May 2006. URL `https://doi.org/10.1088%2F1367-2630%2F8%2F5%2F074`.

[77] K. Ishii, K. Tsutsui, T. Tohyama, T. Inami, J. Mizuki, Y. Murakami, Y. Endoh, S. Maekawa, K. Kudo, Y. Koike, and K. Kumagai. *Momentum-dependent charge excitations of a two-leg ladder: Resonant inelastic x-ray scattering of* $(\mathrm{La,Sr,Ca})_{14}\mathrm{Cu}_{24}\mathrm{O}_{41}$. *Phys. Rev. B*, 76:045124, Jul 2007. URL `https://link.aps.org/doi/10.1103/PhysRevB.76.045124`.

[78] H. Hosono, K. Tanabe, E. Takayama-Muromachi, H. Kageyama, S. Yamanaka, H. Kumakura, M. Nohara, H. Hiramatsu, and S. Fujitsu. *Exploration of new superconductors and functional materials, and fabrication of superconducting tapes and wires of iron pnictides. Science and Technology of Advanced Materials*, 16(3):033503, Jun 2015. URL `https://doi.org/10.1088%2F1468-6996%2F16%2F3%2F033503`.

[79] J. Sirker. *The Luttinger liquid and integrable models. International Journal of Modern Physics B*, 26(22):1244009, 2012. URL `https://doi.org/10.1142/S0217979212440092`.

[80] J. M. Luttinger. *An Exactly Soluble Model of a Many Fermion System. Journal of Mathematical Physics*, 4(9):1154–1162, 1963. URL `https://doi.org/10.1063/1.1704046`.

[81] A. Klümper and K. Sakai. *The thermal conductivity of the spin-*$\frac{1}{2}$ *XXZ chain at arbitrary temperature. Journal of Physics A: Mathematical and General*, 35(9):2173–2182, feb 2002. URL `https://doi.org/10.1088%2F0305-4470%2F35%2F9%2F307`.

[82] X. Zotos. *High Temperature Thermal Conductivity of Two-Leg Spin-*$1/2$ *Ladders. Phys. Rev. Lett.*, 92:067202, Feb 2004. URL `https://link.aps.org/doi/10.1103/PhysRevLett.92.067202`.

[83] E. Manousakis. *The spin-1/2 Heisenberg antiferromagnet on a square lattice and its application to the cuprous oxides. Rev. Mod. Phys.*, 63:1–62, Jan 1991. URL `https://link.aps.org/doi/10.1103/RevModPhys.63.1`.

[84] D. T. Morelli, J. Heremans, G. Doll, P. J. Picone, H. P. Jenssen, and M. S. Dresselhaus. *Thermal properties of single-crystal* $La_2CuO_{4-\Delta}$. *Phys. Rev. B*, 39:804–807, Jan 1989. URL `https://link.aps.org/doi/10.1103/PhysRevB.39.804`.

[85] Y. Nakamura, S. Uchida, T. Kimura, N. Motohira, K. Kishio, K. Kitazawa, T. Arima, and Y. Tokura. *In-plane and out-of-plane thermal conductivity of* $La_{2-x}Sr_xCuO_4$ *single crystals. Physica C: Superconductivity*, 185-189:1409–1410, 1991. ISSN 0921-4534. URL `http://www.sciencedirect.com/science/article/pii/092145349191928W`.

[86] D. Hirobe, M. Sato, Y. Shiomi, H. Tanaka, and E. Saitoh. *Magnetic thermal conductivity far above the Néel temperature in the Kitaev-magnet candidate* $\alpha-RuCl_3$. *Phys. Rev. B*, 95:241112, Jun 2017. URL `https://link.aps.org/doi/10.1103/PhysRevB.95.241112`.

[87] T. Isono, T. Terashima, K. Miyagawa, K. Kanoda, and S. Uji. *Quantum criticality in an organic spin-liquid insulator* $\kappa-(BEDT-TTF)_2Cu_2(CN)_3$. *Nature Communications*, 7:13494 EP –, Nov 2016. URL `https://doi.org/10.1038/ncomms13494`.

[88] Q. Q. Ge, H. C. Xu, X. P. Shen, M. Xia, B. P. Xie, F. Chen, Y. Zhang, R. Kato, T. Tsumuraya, T. Miyazaki, M. Matsunami, S. Kimura, and D. L. Feng. *Angle-resolved photoemission study of the electronic structure of the quantum spin liquid* $EtMe_3Sb[Pd(dmit)_2]_2$. *Phys. Rev. B*, 89:075105, Feb 2014. URL `https://link.aps.org/doi/10.1103/PhysRevB.89.075105`.

[89] Y. Shimizu, K. Miyagawa, K. Kanoda, M. Maesato, and G. Saito. *Spin Liquid State in an Organic Mott Insulator with a Triangular Lattice. Phys. Rev. Lett.*, 91:107001, Sep 2003. URL `https://link.aps.org/doi/10.1103/PhysRevLett.91.107001`.

[90] T. Itou, A. Oyamada, S. Maegawa, and R. Kato. *Instability of a quantum spin liquid in an organic triangular-lattice antiferromagnet. Nature Physics*, 6:673 EP –, Jul 2010. URL `https://doi.org/10.1038/nphys1715`.

[91] G. Misguich, C. Lhuillier, B. Bernu, and C. Waldtmann. *Spin-liquid phase of the multiple-spin exchange Hamiltonian on the triangular lattice. Phys. Rev. B*, 60:1064–1074, Jul 1999. URL `https://link.aps.org/doi/10.1103/PhysRevB.60.1064`.

[92] H. Morita, S. Watanabe, and M. Imada. *Nonmagnetic Insulating States near the Mott Transitions on Lattices with Geometrical Frustration and Implications for* $\kappa-(ET)_2Cu_2(CN)_3$. *Journal of the Physical Society of Japan*, 71(9):2109–2112, 2002. URL `https://doi.org/10.1143/JPSJ.71.2109`.

[93] D. Watanabe, M. Yamashita, S. Tonegawa, Y. Oshima, H. M. Yamamoto, R. Kato, I. Sheikin, K. Behnia, T. Terashima, S. Uji, T. Shibauchi, and Y. Matsuda. *Novel Pauli-paramagnetic quantum phase in a Mott insulator. Nature Communications*, 3: 1090 EP –, Sep 2012. URL `https://doi.org/10.1038/ncomms2082`.

[94] J. M. Ni, B. L. Pan, Y. Y. Huang, J. Y. Zeng, Y. J. Yu, E. J. Cheng, L. S. Wang, R. Kato, and S. Y. Li. *Absence of magnetic thermal conductivity in the quantum spin liquid candidate* $EtMe_3Sb[Pd(dmit)_2]_2$ *– revisited. arXiv e-prints*, art. arXiv:1904.10395, Apr 2019. URL `https://ui.adsabs.harvard.edu/abs/2019arXiv190410395N`.

[95] P. Bourgeois-Hope, F. Laliberté, E. Lefrançois, G. Grissonnanche, S. René de Cotret, R. Gordon, R. Kato, L. Taillefer, and N. Doiron-Leyraud. *Thermal conductivity of the quantum spin liquid candidate* $\mathrm{EtMe_3Sb[Pd(dmit)_2]_2}$*: No evidence of mobile gapless excitations. arXiv e-prints*, art. arXiv:1904.10402, Apr 2019. URL `https://ui.adsabs.harvard.edu/abs/2019arXiv190410402B`.

[96] I. Kimchi, A. Nahum, and T. Senthil. *Valence Bonds in Random Quantum Magnets: Theory and Application to* $\mathrm{YbMgGaO_4}$. *Phys. Rev. X*, 8:031028, Jul 2018. URL `https://link.aps.org/doi/10.1103/PhysRevX.8.031028`.

[97] S.-Y. Park, S.-H. Do, K.-Y. Choi, D. Jang, T.-H. Jang, J. Schefer, C.-M. Wu, J.S. Gardner, J.M.S. Park, J.-H. Park, and S. Ji. *Emergence of the Isotropic Kitaev Honeycomb Lattice with Two-dimensional Ising Universality in* $\alpha{-}\mathrm{RuCl_3}$. *arXiv:1609.05690*, 2016.

[98] S.-H. Do, S.-Y. Park, J. Yoshitake, J. Nasu, Y. Motome, Y.-S. Kwon, D. T. Adroja, D. J. Voneshen, K. Kim, T.-H. Jang, J.-H. Park, K.-Y. Choi, and S. Ji. *Majorana fermions in the Kitaev quantum spin system* $\alpha-\mathrm{RuCl_3}$. *Nature Physics*, 13:1079 EP –, Sep 2017. URL `http://dx.doi.org/10.1038/nphys4264`.

[99] K. W. Plumb, J. P. Clancy, L. J. Sandilands, V. V. Shankar, Y. F. Hu, K. S. Burch, H.-Y. Kee, and Y.-J. Kim. $\alpha-\mathrm{RuCl_3}$*: A spin-orbit assisted Mott insulator on a honeycomb lattice. Phys. Rev. B*, 90:041112, Jul 2014. URL `https://link.aps.org/doi/10.1103/PhysRevB.90.041112`.

[100] N. Read and D. Green. *Paired states of fermions in two dimensions with breaking of parity and time-reversal symmetries and the fractional quantum Hall effect. Phys. Rev. B*, 61:10267–10297, Apr 2000. URL `https://link.aps.org/doi/10.1103/PhysRevB.61.10267`.

[101] M. Stone. *Gravitational anomalies and thermal Hall effect in topological insulators. Phys. Rev. B*, 85:184503, May 2012. URL `https://link.aps.org/doi/10.1103/PhysRevB.85.184503`.

[102] H. Katsura, N. Nagaosa, and P. A. Lee. *Theory of the Thermal Hall Effect in Quantum Magnets. Phys. Rev. Lett.*, 104:066403, Feb 2010. URL `https://link.aps.org/doi/10.1103/PhysRevLett.104.066403`.

[103] J. Cookmeyer and J. E. Moore. *Spin-wave analysis of the low-temperature thermal Hall effect in the candidate Kitaev spin liquid* $\alpha-\mathrm{RuCl_3}$. *Phys. Rev. B*, 98:060412, Aug 2018. URL `https://link.aps.org/doi/10.1103/PhysRevB.98.060412`.

[104] Y. Vinkler-Aviv and A. Rosch. *Approximately Quantized Thermal Hall Effect of Chiral Liquids Coupled to Phonons. Phys. Rev. X*, 8:031032, Aug 2018. URL `https://link.aps.org/doi/10.1103/PhysRevX.8.031032`.

[105] M. Ye, G. B. Halász, L. Savary, and L. Balents. *Quantization of the Thermal Hall Conductivity at Small Hall Angles. Phys. Rev. Lett.*, 121:147201, Oct 2018. URL `https://link.aps.org/doi/10.1103/PhysRevLett.121.147201`.

[106] S. Simon. Lecture notes: Topological quantum, 2016. URL: `http://www-thphys.physics.ox.ac.uk/people/SteveSimon/topological2016/TopoBook.pdf`.

[107] A. Stern. *Anyons and the quantum Hall effect—A pedagogical review. Annals of Physics*, 323(1):204 – 249, 2008. ISSN 0003-4916. URL `http://www.sciencedirect.com/science/article/pii/S0003491607001674`.

[108] R. B. Laughlin. *Anomalous Quantum Hall Effect: An Incompressible Quantum Fluid with Fractionally Charged Excitations. Phys. Rev. Lett.*, 50:1395–1398, May 1983. URL `https://link.aps.org/doi/10.1103/PhysRevLett.50.1395`.

[109] E. Majorana. *Teoria simmetrica dell'elettrone e del positrone. Il Nuovo Cimento (1924-1942)*, 14(4):171, Sep 1937. ISSN 1827-6121. URL `https://doi.org/10.1007/BF02961314`.

[110] L. Carr. *Understanding Quantum Phase Transitions.* Condensed Matter Physics. CRC Press, 2010. ISBN 9781439802618. URL `https://books.google.de/books?id=tArMBQAAQBAJ`.

[111] S. Trebst. Lecture notes: Breakdown of a topological phase. URL: `https://www.thp.uni-koeln.de/trebst/Talks/ToricCode.pdf`.

[112] J. B. Kogut. *An introduction to lattice gauge theory and spin systems. Rev. Mod. Phys.*, 51:659–713, Oct 1979. URL `https://link.aps.org/doi/10.1103/RevModPhys.51.659`.

[113] Y.-J. Han, R. Raussendorf, and L.-M. Duan. *Scheme for Demonstration of Fractional Statistics of Anyons in an Exactly Solvable Model. Phys. Rev. Lett.*, 98:150404, Apr 2007. URL `https://link.aps.org/doi/10.1103/PhysRevLett.98.150404`.

[114] H. Weimer, M. Müller, I. Lesanovsky, P. Zoller, and H. P. Büchler. *A Rydberg quantum simulator. Nature Physics*, 6:382 EP –, Mar 2010. URL `https://doi.org/10.1038/nphys1614`.

[115] L. B. Ioffe, M. V. Feigel'man, A. Ioselevich, D. Ivanov, M. Troyer, and G. Blatter. *Topologically protected quantum bits using Josephson junction arrays. Nature*, 415:503 EP –, Jan 2002. URL `https://doi.org/10.1038/415503a`.

[116] M. Z. Hasan and C. L. Kane. *Colloquium: Topological insulators. Rev. Mod. Phys.*, 82:3045–3067, Nov 2010. URL `https://link.aps.org/doi/10.1103/RevModPhys.82.3045`.

[117] P. Jordan and E. P. Wigner. Über das paulische äquivalenzverbot. *Z. Physik*, 47: 631–651, 1928. URL `https://doi.org/10.1007/BF01331938`.

[118] H.-D. Chen and Z. Nussinov. *Exact results of the Kitaev model on a hexagonal lattice: spin states, string and brane correlators, and anyonic excitations. Journal of Physics A: Mathematical and Theoretical*, 41(7):075001, feb 2008. URL `https://doi.org/10.1088%2F1751-8113%2F41%2F7%2F075001`.

[119] S. Mandal, R. Shankar, and G. Baskaran. *RVB gauge theory and the topological degeneracy in the honeycomb Kitaev model. Journal of Physics A: Mathematical and Theoretical*, 45(33):335304, 2012. URL `http://stacks.iop.org/1751-8121/45/i=33/a=335304`.

[120] E. Fradkin. *Jordan-Wigner transformation for quantum-spin systems in two dimensions and fractional statistics. Phys. Rev. Lett.*, 63:322–325, Jul 1989. URL `https://link.aps.org/doi/10.1103/PhysRevLett.63.322`.

[121] Y. R. Wang. *Ground state of the two-dimensional antiferromagnetic Heisenberg model studied using an extended Wigner-Jordon transformation. Phys. Rev. B*, 43:3786–3789, Feb 1991. URL `https://link.aps.org/doi/10.1103/PhysRevB.43.3786`.

[122] O. Derzhko. *Jordan-wigner fermionization for spin-1/2 systems in two dimensions: A brief review. arXiv preprint cond-mat/0101188*, 2001. URL `https://arxiv.org/abs/cond-mat/0101188`.

[123] X.-Y. Feng, G.-M. Zhang, and T. Xiang. *Topological Characterization of Quantum Phase Transitions in a Spin-*1/2 *Model. Phys. Rev. Lett.*, 98:087204, Feb 2007. URL `https://link.aps.org/doi/10.1103/PhysRevLett.98.087204`.

[124] B. S. Garbow. *EISPACK — A package of matrix eigensystem routines. Computer Physics Communications*, 7(4):179 – 184, 1974. ISSN 0010-4655. URL `http://www.sciencedirect.com/science/article/pii/0010465574900861`.

[125] R. S. Martin, C. Reinsch, and J. H. Wilkinson. *Householder's tridiagonalization of a symmetric matrix. Numerische Mathematik*, 11(3):181–195, 1968.

[126] H. Bowdler, R. S. Martin, C. Reinsch, and J. H. Wilkinson. *The QR and QL algorithms for symmetric matrices.* In *Linear Algebra*, pages 227–240. Springer, 1971.

[127] A. Metavitsiadis and W. Brenig. *Thermal transport in a one-dimensional $\mathbb{Z}_2$ spin liquid. Phys. Rev. B*, 96:041115, Jul 2017. URL `https://link.aps.org/doi/10.1103/PhysRevB.96.041115`.

[128] A. Metavitsiadis, A. Pidatella, and W. Brenig. *Thermal transport in a two-dimensional $\mathbb{Z}_2$ spin liquid. Phys. Rev. B*, 96:205121, Nov 2017. URL `https://link.aps.org/doi/10.1103/PhysRevB.96.205121`.

[129] A. Pidatella, A. Metavitsiadis, and W. Brenig. *Heat transport in the anisotropic Kitaev spin liquid. Phys. Rev. B*, 99:075141, Feb 2019. URL `https://link.aps.org/doi/10.1103/PhysRevB.99.075141`.

[130] J. Nasu, M. Udagawa, and Y. Motome. *Thermal fractionalization of quantum spins in a Kitaev model: Temperature-linear specific heat and coherent transport of Majorana fermions. Phys. Rev. B*, 92:115122, Sep 2015. URL `https://link.aps.org/doi/10.1103/PhysRevB.92.115122`.

[131] J. Nasu, J. Yoshitake, and Y. Motome. *Thermal Transport in the Kitaev Model. Phys. Rev. Lett.*, 119:127204, Sep 2017. URL `https://link.aps.org/doi/10.1103/PhysRevLett.119.127204`.

[132] A.-M. Tremblay. *A refresher in many-body theory. Online document, updated May,* 2008.

[133] P. W. Anderson. *Absence of Diffusion in Certain Random Lattices. Phys. Rev.*, 109:1492–1505, Mar 1958. URL `https://link.aps.org/doi/10.1103/PhysRev.109.1492`.

[134] A. Aspect and M. Inguscio. *Anderson localization of ultracold atoms. Physics Today*, 62(8):30–35, 2009. URL `https://doi.org/10.1063/1.3206092`.

[135] J. Fröhlich, F. Martinelli, E. Scoppola, and T. Spencer. *Constructive proof of localization in the Anderson tight binding model. Comm. Math. Phys.*, 101(1):21–46, 1985. URL `https://projecteuclid.org:443/euclid.cmp/1104114065`.

[136] E. Abrahams, P. W. Anderson, D. C. Licciardello, and T. V. Ramakrishnan. *Scaling Theory of Localization: Absence of Quantum Diffusion in Two Dimensions. Phys. Rev. Lett.*, 42:673–676, Mar 1979. URL `https://link.aps.org/doi/10.1103/PhysRevLett.42.673`.

[137] D. Vollhardt and P. Wölfle. *Anderson Localization in* $d \leq 2$ *Dimensions: A Self-Consistent Diagrammatic Theory. Phys. Rev. Lett.*, 45:842–846, Sep 1980. URL `https://link.aps.org/doi/10.1103/PhysRevLett.45.842`.

[138] P. A. Lee and T. V. Ramakrishnan. *Disordered electronic systems. Rev. Mod. Phys.*, 57: 287–337, Apr 1985. URL `https://link.aps.org/doi/10.1103/RevModPhys.57.287`.

[139] M. Schreiber and M. Ottomeier. *Localization of electronic states in 2D disordered systems. Journal of Physics: Condensed Matter*, 4(8):1959–1971, feb 1992. URL `https://doi.org/10.1088%2F0953-8984%2F4%2F8%2F011`.

[140] P. A. Lee. *Localized states in a d-wave superconductor. Phys. Rev. Lett.*, 71:1887–1890, Sep 1993. URL `https://link.aps.org/doi/10.1103/PhysRevLett.71.1887`.

[141] K. Nomura, M. Koshino, and S. Ryu. *Topological Delocalization of Two-Dimensional Massless Dirac Fermions. Phys. Rev. Lett.*, 99:146806, Oct 2007. URL `https://link.aps.org/doi/10.1103/PhysRevLett.99.146806`.

[142] X. Cai, L.-J. Lang, S. Chen, and Y. Wang. *Topological Superconductor to Anderson Localization Transition in One-Dimensional Incommensurate Lattices. Phys. Rev. Lett.*, 110:176403, Apr 2013. URL `https://link.aps.org/doi/10.1103/PhysRevLett.110.176403`.

[143] S. Liu, X.-F. Zhou, G.-C. Guo, and Y.-S. Zhang. *Anderson localization in degenerate spin-orbit coupled Fermi gas with disorder. Scientific Reports*, 6:22623 EP –, Mar 2016. URL `https://doi.org/10.1038/srep22623`.

[144] D. Chandler and D. Wu. Introduction to Modern Statistical Mechanics. Oxford University Press, 1987. ISBN 9780195042764. URL `https://books.google.de/books?id=ep5yswEACAAJ`.

Publications

This doctoral thesis is based on the following publications:

- A. Metavitsiadis, A. Pidatella, and W. Brenig. Thermal transport in a two-dimensional $\mathbb{Z}_2$ spin liquid. Phys. Rev. B **96**, 205121 (2017).
- A. Pidatella, A. Metavitsiadis, and W. Brenig. Heat transport in the anisotropic Kitaev spin liquid. Phys. Rev. B **99**, 075141 (2019).

Acknowledgements

First and foremost, I would like to thank my PhD advisor, Wolfram Brenig. I have had the great pleasure of enjoying in recent years his enthusiasm for research, his passion for physics, and his unfailing sense of humor. His support, criticism, and incredible patience, guided me through the insidious paths of research, and to the completion of my doctoral studies. Thank you for always treating me with trust and respect, both as a scientist and as a person.

I am also really grateful to my other PhD advisor, Matthias Vojta, who gave me the chance to join his incredible research group. It was a great learning experience, and a privilege for me to work beside him in these last years. I express my gratitude for his excellent supervision, his advice, and his countless availability in whatever circumstances.

I want also to thank Carsten Timm, for his support during these years, and for having been a good PhD mentor.

I immensely thank Alexandros Metavitsiadis, who has given me an inestimable support throughout my doctoral studies. He has been always available for discussions, even if arising from my silliest questions. I am also really thankful for having continuously shared his expertise with me, but even more for his friendship.

I would also like to acknowledge fundings from the German Research Foundation (DFG), namely the DFG-SFB 1143 project "Correlated Magnetism: From Frustration to Topology" (247310070), which I have been affiliated to over the entire PhD period.

A heartfelt thank goes to Tatjana, for all the nice talks, going beyond physics and making me feel a little closer to home. Thanks also to Gudrun for her outstanding kindness and her support in my experience abroad, and to Kerstin for all the smiles and funny stories shared.

A huge thanks goes to the many people who have provided me with professional support during my PhD, but even more who have shared amazing time and fun with me: especially my colleagues from Dresden – Laura, Santanu, Urban, Heike, Madelynn, Tobias, Ankita, Janna, Chris, and Tim – and from Braunschweig – Benjamin, Niklas, Lena, and Evrard.

" *Nulla è piú utile del sale e del sole* " [1]

But *there is* yet *plenty of room at the bottom.* I want to say thanks to all the people that have brightened my time during my stay in Germany, thousand of miles away from home. My dearest friends – dubbed "The Dogs" – Giorgio, Emanuele, Luca, and Cipollino (Alessandro) for the daily amusement, to have let me feel continuously at home. And all my other friends – too many to be cited one by one – spread out in Catania, and all over Europe. Despite the distance which separates us, the echo of your affect and of your attentions have fed my spirit. I really owe you a lot.

---

[1] From Plinio il Vecchio, *Naturalis Historia*, 31, 102, literally : Nothing is more useful than salt and sun.

Without the trust, understanding, and love provided by my family, none of this would have been possible. Thanks to have let me take my choices, but even more to have supported them, never leaving me alone: grazie mamma, papá , Luca, e Simone.

And thank you Nancy. You are the salt of my time, and the sun on my way.

Erklärung

Hiermit versichere ich, dass ich die vorliegende Arbeit ohne unzulässige Hilfe Dritter und ohne Benutzung anderer als der angegebenen Hilfsmittel angefertigt habe. Die aus fremden Quellen direkt oder indirekt übernommenen Gedanken sind als solche kenntlich gemacht. Die Arbeit wurde bisher weder im Inland noch im Ausland in gleicher oder ähnlicher Form einer anderen Prüfungsbehörde vorgelegt. Die Dissertation wurde am Institut für Theoretische Physik der Technischen Universität Dresden unter der wissenschaftlichen Betreuung von Prof. Dr. Matthias Vojta und Prof. Dr. Wolfram Brenig angefertigt. Ich erkläre hiermit, dass keine früheren erfolglosen Promotionsverfahren stattgefunden haben. Ich erkenne die Promotionsordnung der Fakultät Mathematik und Naturwissenschaften der Technischen Universität Dresden vom 23.02.2011 an.

Angelo Pidatella

Dresden, 27.06.2019